

UC San Diego

UC San Diego Electronic Theses and Dissertations

Title

Exploring the Morphology Control and Formation Mechanisms of Ultra-High Temperature Ceramic Particles: A Study on Tantalum Carbide

Permalink

<https://escholarship.org/uc/item/83s6j6xt>

Author

Ren, Tianqi

Publication Date

2021

Peer reviewed|Thesis/dissertation

UNIVERSITY OF CALIFORNIA SAN DIEGO

Exploring the Morphology Control and Formation Mechanisms of Ultra-High Temperature
Ceramic Particles: A Study on Tantalum Carbide

A dissertation submitted in partial satisfaction

of requirements for the degree

Doctor of Philosophy

in

Materials Science and Engineering

by

Tianqi Ren

Committee in Charge:

Professor Olivia A. Graeve, Chair
Professor Robert E. Continetti
Professor Shirley Meng
Professor Marc A. Meyers
Professor Shyue Ping Ong

2021

©

Tianqi Ren, 2021
All rights reserved.

The dissertation of Tianqi Ren is approved, and is acceptable in quality and form for publication on microfilm or electronically.

University of California San Diego

2021

DEDICATION

This dissertation is dedicated to my parents, Zhishui Ren and Ping Chen, who supported me both materially and spiritually. You taught me how to think, learn and contribute.

And to my wife, Baihua Chen, who always stands by my side no matter how tough the obstacles are. You are my perfect lifelong partner. I will, as promised, spend the rest of my life by your side.

TABLE OF CONTENTS

DISSERTATION APPROVAL PAGE	iii
DEDICATION	iv
TABLE OF CONTENTS	v
LIST OF TABLES	vii
LIST OF FIGURES	viii
ACKNOWLEDGEMENTS	xv
VITA	xvii
ABSTRACT OF THE DISSERTATION	xviii
Chapter 1. Introduction	1
1.1. Ultra-high Temperature Ceramics	1
1.2. Tantalum Carbide	3
1.3. Crystal Growth and Morphology Control of Inorganic Materials	7
1.3.1. Growth of Bulk Crystals	7
1.3.2. Growth and Morphology Control of Nanoscale Crystalline Particles	9
1.3.2.1. Morphology Evolution of Nanoscale Crystalline Particles	12
1.3.2.2. Literature Review: Morphology Control of Metallic Nanoparticles	17
1.3.2.3. Literature Review: Morphology Control of Ceramic Particles	26
1.4. Motivation of Study	54
1.5. References	59
Chapter 2. Experimental Procedure	74
2.1. Experimental Design	74
2.2. Synthesis of Carbide Particles	76

2.3. Analytical Techniques	80
2.4. References	81
Chapter 3. Dopant-Dependent Morphology Selectivity of Tantalum Carbide Particles	82
3.1. Brief Introduction	82
3.2. Rationale of Dopant and Precursor Selection	84
3.3. Detailed Results and Discussion	97
3.3.1. Undoped TaC.....	97
3.3.2. Y-Doped TaC.....	110
3.3.3. Nb/Zr/Hf-Doped TaC.....	121
3.3.4. Ni-Doped TaC.....	128
3.3.5. Co-Doped TaC.....	141
3.3.6. Fe-Doped TaC.....	149
3.3.7. Ni-Ti Co-Doped TaC.....	159
3.3.8. Modeling-Assisted Discussion.....	171
3.4. Conclusions	182
3.5. References	184
Chapter 4. Prospects for Future Research	188
4.1. Selection of Growth Habit Modifier	188
4.2. Experimental Techniques	188
4.3. Study of Sintering Behaviors and Properties	190
4.4. Conclusions	190
4.5. References	191
Chapter 5. Conclusions	192

LIST OF TABLES

Table 2-1. List of major TaC-based samples investigated in this study.....	75
Table 3-1. Dopant concentrations of TaC powders determined from energy dispersive spectroscopy.....	173
Table 3-2. Dopant concentration of TaC powders determined from X-ray photoelectron spectroscopy. All values are in atomic percent.....	173
Table 3-3. Percentage of covalency for the dopant bonds at the surface and the corresponding metal atom that was substituted in the undoped surface. The remainder percentage represents metallicity. Ni* indicates Ni substituting Ti in $TiTa_3C_4$	180

LIST OF FIGURES

Figure 1-1. Blunt leading edge component used in the Space Shuttle. Typical radius of curvature at the tip is ~ 10 cm, made from SiC/carbon and carbon/carbon composites (adapted from http://www.pari.edu/shuttle-leading-wing-edge-web/).....	2
Figure 1-2. Phase diagram for the Ta-C system. “x” and “y” denote possible carbon substoichiometry in corresponding phases (reprinted with permission from Ref. 30).....	5
Figure 1-3. Crystal structure of TaC_{1-x} . Both Ta and C sublattices are in <i>fcc</i> arrangement. Carbon atoms sit in the interstitial sites within Ta lattice. (With color).....	6
Figure 1-4. Schematic of an industrial single crystal silicon puller using Czochralski process (reprinted with permission from Ref. 41).....	8
Figure 1-5. Typical truncated octahedron as the Wulff polyhedron of <i>fcc</i> single crystal under inert gas or vacuum at 0K. The index of each surface shown is labelled with Millar notations (reprinted and modified with permission from Ref. 47).....	10
Figure 1-6. The definition of F-, S- and K-faces according to the PBC theory by Hartman and Perlok. F-faces: (100), (010) and (001); S-faces: (101), (110) and (011); K-face: (111) (reprinted with permission from Ref. 48).....	11
Figure 1-7. Representation of clusters in an ideal and the densest atomic packing. Polyhedral shape of the cluster becomes more pronounced as the number of atoms increases (reprinted with permission from Ref. 46; original figure was modified with permission from Ref. 51).....	13
Figure 1-8. Schematic illustration of the evolution pathways that lead to the formation of polyhedrons for <i>fcc</i> crystals.....	14
Figure 1-9. (a) Morphologies of cubic crystals as a function of R , the ratio between the growth rates along $\langle 111 \rangle$ and $\langle 100 \rangle$ directions. (b) Evolution in shapes of a set of (111) based particles as the ratio of $\{111\}$ to $\{100\}$ increases. (c) Morphologies of multiply twinned decahedral and icosahedral particles.....	16
Figure 1-10. A summary of various metallic nanoparticles being synthesized with controlled morphologies using solution-based synthesis (reprinted with permission from Ref. 59).....	18
Figure 1-11. Electron micrographs of Pd nanoparticles with various sizes and morphologies: (a) Wulff polyhedrons, (b) nanocubes with average of 50 nm size, (c) nanocubes with average of 8 nm size, (d) nanobars, (e) nanorods and (f) octahedrons (reprinted with permission from Ref. 46).....	20
Figure 1-12. Schematic illustration of the growth mechanisms responsible for the formation of Pd nanobars and nanorods, as well as the thermodynamically controlled aging process (reprinted with permission from Ref. 68).....	22

Figure 1-13. Au nanocubes formed with 1/200 Ag/Au addition of AgNO ₃ obtained using a modified polyol process: (a-b) SEM micrographs with 45° tilt, scale bars are 500 nm and 200 nm respectively, (c-d) TEM micrographs of corresponding Au nanocubes, scales bars are 200 nm and 100 nm respectively (reprinted and modified with permission from Ref. 75).....	24
Figure 1-14. TEM micrographs of Au nanocubes illustrating the change in corner sharpness under different CTAB concentrations (reprinted with permission from Ref. 77).....	24
Figure 1-15. TEM micrographs of Pt nanoparticles produced by reduction of K ₂ PtCl ₄ with TTAB as the surfactant: (a) nanocubes (with NaBH ₄ at high pH) and (b) cuboctahedrons (with NaBH ₄ + H ₂ flow at low pH) (reprinted and modified with permission from Ref. 78).....	25
Figure 1-16. (a) Ideal surface structure of cubic NaCl crystal enclosed by {100} facets. Cl ⁻ ions in blue and Na ⁺ ions in red. (b-c) Surface structure of {110} facets. (d-e) Surface structure of {111} facets (reprinted and modified with permission from Ref. 111). (With color).....	28
Figure 1-17. (a) TiC nanoparticles synthesized from arc discharge method with low methane concentrations showing cubic-dominated morphology. (b) At high methane concentration (60% in this case), the morphology of TiC nanoparticles favors cuboctahedron (reprinted and modified with permission from Ref. 35).....	30
Figure 1-18. WO ₃ particles with different morphologies caused by Cr-doping. (a) monolithic WO ₃ . (b) 2.5 at.% Cr-WO ₃ . (c) 10 at.% Cr-WO ₃ (reprinted with permission from Ref. 117).....	33
Figure 1-19. Microscopy graph examples of (a) NiFe ₂ O ₄ porous nanocubes by Wang <i>et al.</i> ; (b) MgO nanocubes by Takahashi; (c) MgO nanocubes by Issa <i>et al.</i> ; (d) CaCu ₃ Ti ₄ O ₁₂ nanocubes by Maity <i>et al.</i> (reprinted with permission from Ref. 144, 148, 149, 150).....	35
Figure 1-20. TEM micrograph of BaTiO ₃ nanoparticles prepared at 240 °C for 18 hours using 40 vol.% 2-methoxy ethanol and 60 vol.% ethanol (reprinted with permission from Ref. 121).....	38
Figure 1-21. SEM micrographs of BaTiO ₃ nanocubes synthesized using hydrothermal method with different precursor concentrations at 220 °C for 72 hours: (a) 0.1 M, (b) 0.05 M, (c) 0.03 M and (d) 0.025 M of Ba(OH) ₂ and TALH (reprinted with permission from Ref. 123).....	39
Figure 1-22. SEM micrographs of BaTiO ₃ nanoparticles synthesized using hydrothermal method with different molar ratios (Ba(OH) ₂ : TALH : OLA) at 220 °C for 72 hours: (a) 1 : 1 : 6 and (b) 1 : 1 : 18 (modified and reprinted with permission from Ref. 123).....	40
Figure 1-23. Schematic illustration of possible mechanisms (<i>in situ</i> transformation) for the development of BaTiO ₃ nanocubes (reprinted with permission from Ref. 124).....	41
Figure 1-24. HRTEM micrographs of a cubic SrTiO ₃ particle. (a) The particle shown is pictured along the body diagonal of a cube. The inset shows the electron diffraction pattern of the particle.	

(b) Magnified image of one edge showing dislocations and misalignments of nanocrystals across some interfaces (reprinted with permission from Ref. 129).....43

Figure 1-25. SEM micrographs of SrTiO₃ particles synthesized using alcohols with different pK_a values and concentrations. Decreasing pK_a value from top to bottom and increasing concentration from left to right (reprinted with permission from Ref. 130).....45

Figure 1-26. SEM micrographs of NaNbO₃ microcrystals synthesized from ion exchange reaction with different reaction conditions showing morphological evolution from octahedron to cube. (reprinted with permission from Ref. 133).....47

Figure 1-27. SEM micrographs of NaTaO₃ particles obtained with 10 mmol of NaOH and different volumetric ratios of EG to water: (a) 1/13. (b) 3/11. (c) 5/9. (d) 11/3 (reprinted with permission from Ref. 137).....49

Figure 1-28. SEM micrographs of PrFeO₃ microcrystals grown under different urea concentration: (a) KOH/urea = 5.0 g/1.2 g, (b) KOH/urea = 5.0 g/1.5 g, (c) KOH/urea = 5.0 g/1.8 g, (d) KOH/urea = 5.0 g/2.0 g (reprinted with permission from Ref. 142).....51

Figure 1-29. SEM micrographs of LaFeO₃ microcrystals grown with 1.5 g urea under different KOH concentrations: (a-b) 4.5 g, (c-d) 5.0 g, (e-f) 5.5 g (reprinted with permission from Ref. 142).....52

Figure 1-30. Schematic illustration of the surface capping effect of NH₃ molecules (reprinted with permission from Ref. 141). (With color).....53

Figure 1-31. A schematic of typical SPS setup (reprinted with permission from Ref. 143).....55

Figure 1-32. A proposed comparison of the current pathways during SPS in powders with different particle morphologies: (a) highly faceted particles, point of discontinuity at corners/edges, (b) round-shaped particles, point of discontinuity at necks/grain boundaries.....56

Figure 1-33. (a) TEM micrographs for the CeO₂ nanocubes (inset b and d) and conventional nanoparticles (inset c and e); (b) The relative density of CeO₂ ceramics sintered from nanocubes and conventional nanoparticles at different sintering temperatures. (reprinted with permission from Ref. 152).....58

Figure 2-1. The Periodic Table highlighting the elements been screened as the dopants for morphology modification of TaC nanoparticles. Red: dopants showing no effect; Green: dopants showing effectiveness; Yellow: dopant showing effectiveness when co-doped with Ni. (With color).....74

Figure 2-2. Illustration of TaC-forming reaction. (a) Schematics of the solvothermal reaction. Ta and C atoms bond in molten lithium to form TaC in a highly-exothermic way. (b) Time-lapse photographs of the actual reaction.....78

Figure 2-3. Detailed powder washing procedures with a photograph of actual TaC sample produced.....	79
Figure 3-1. X-ray diffraction pattern of Y-doped TaC sample with 15 at% calculated Y amount using yttrium nitrate as the precursor.....	86
Figure 3-2. X-ray diffraction pattern of Y-doped TaC sample with 15 at% calculated Y amount using yttrium chloride as the precursor. Note the hump at the lower diffraction angles signals the presence of amorphous oxide phases.....	87
Figure 3-3. X-ray diffraction pattern of Y-doped TaC sample with 15 at% calculated Y amount using yttrium chloride as the precursor synthesized through improved reaction setups.....	88
Figure 3-4. X-ray diffraction pattern of Y-doped TaC sample with 15 at% calculated Y amount using metallic yttrium as the precursor synthesized through improved reaction setups.....	89
Figure 3-5. X-ray diffraction patterns of Nb-doped TaC samples with different Nb amount using metallic Nb as the precursor synthesized through improved reaction setups.....	90
Figure 3-6. X-ray diffraction pattern of Zr-doped TaC sample with 15 at% calculated Zr amount using metallic Zr as the precursor synthesized through improved reaction setups.....	91
Figure 3-7. X-ray diffraction pattern of Hf-doped TaC sample with 15 at% calculated Hf amount using metallic Hf as the precursor synthesized through improved reaction setups.....	92
Figure 3-8. Typical morphology of TiC particles synthesized from (a) non-Ni containing melts and (b) Ni-containing melts (reprinted with permission from Ref. 8).....	93
Figure 3-9. X-ray diffraction pattern of Ni-doped TaC sample with 15 at% calculated Ni amount using metallic Ni as the precursor synthesized through improved reaction setups.....	94
Figure 3-10. X-ray diffraction pattern of Co-doped TaC sample with 15 at% calculated Co amount using metallic Co as the precursor synthesized through improved reaction setups.....	95
Figure 3-11. X-ray diffraction pattern of Fe-doped TaC sample with 15 at% calculated Fe amount using metallic Fe as the precursor synthesized through improved reaction setups.....	96
Figure 3-12. X-ray diffraction pattern of Ni-Ti co-doped TaC sample with 20 at% calculated Ni amount and 5 at% calculated Ti amount using metallic Ni and Ti as the precursors synthesized through improved reaction setups.....	97
Figure 3-13. X-ray diffraction pattern of undoped TaC sample synthesized with improved reaction setups.....	98
Figure 3-14. Scanning electron micrographs of undoped TaC sample imaged at different magnifications (TaC-1).....	100

Figure 3-15. An illustration of various particles morphologies corresponding to the surface energy ratio ($R = \gamma_{111}/\gamma_{100}$).....	101
Figure 3-16. Scanning electron micrographs of commercial TaC powders imaged at different magnifications.....	103
Figure 3-17. Scanning electron micrographs of undoped TaC sample synthesized with the addition of 30 wt% commercial TaC powder as the reaction diluent imaged at different magnifications (TaC-2).....	105
Figure 3-18. Plot of surface energies for the TaC (100), (111), (110), and the face-centered cubic Ta (111) slabs as a function of the chemical potential of carbon ($\Delta\mu_C$).....	109
Figure 3-19. Scanning electron micrographs at different magnifications of Y-doped TaC sample with 15 at% calculated Y amount using yttrium nitrate (a)-(c) and yttrium chloride (d)-(g) as the precursors.....	111
Figure 3-20. Scanning electron micrographs of Y-doped TaC samples with different doping levels using metallic Y as the precursor.....	114
Figure 3-21. X-ray diffraction patterns of Y-doped TaC samples with different doping levels using metallic Y as the precursor.....	119
Figure 3-22. Statistical abundance of particle morphology for Y-doped TaC samples with different doping levels using metallic Y as the precursor. Color legends: Orange – non-faceted particles; Green – cubic/truncated cubic particles.....	120
Figure 3-23. Scanning electron micrographs of Nb-doped TaC samples with different doping levels using metallic Nb as the precursor.....	122
Figure 3-24. Scanning electron micrographs of Zr-doped TaC samples with different doping levels using metallic Zr as the precursor.....	125
Figure 3-25. Scanning electron micrographs of Hf-doped TaC samples with different doping levels using metallic Hf as the precursor: (a) and (b) 10 at% calculated Hf amount (Hf-1); (c) and (d) 15 at% calculated Hf amount (Hf-2).....	127
Figure 3-26. Scanning electron micrographs of Ni-doped TaC samples with different doping levels using metallic Ni as the precursor.....	131
Figure 3-27. X-ray diffraction patterns of Ni-doped TaC samples with different doping levels using metallic Ni as the precursor.....	138

Figure 3-28. Statistical abundance of particle morphology for Ni-doped TaC samples with different doping levels using metallic Ni as the precursor in comparison with the undoped TaC sample. Color legends: Orange – non-faceted particles; Blue – cuboctahedron particles.....139

Figure 3-29. Scanning electron micrographs of (a) undoped ZrC sample, (b) Ni-doped ZrC sample with 10 at% calculated amount of Ni, and (c) 15 at% calculated amount of Ni.....140

Figure 3-30. Scanning electron micrographs of Co-doped TaC samples with different doping levels using metallic Co as the precursor.....142

Figure 3-31. X-ray diffraction patterns of Co-doped TaC samples with different doping levels using metallic Co as the precursor.....148

Figure 3-32. Statistical abundance of particle morphology for Co-doped TaC samples with different doping levels using metallic Co as the precursor. Color legends: Orange – non-faceted particles; Blue – cuboctahedron particles.....149

Figure 3-33. Scanning electron micrographs of Fe-doped TaC samples showing both cuboctahedron and cubic particles with different doping levels using metallic Fe as the precursor.....150

Figure 3-34. X-ray diffraction patterns of Fe-doped TaC samples with different doping levels using metallic Fe as the precursor.....158

Figure 3-35. Statistical abundance of particle morphology for Fe-doped TaC samples with different doping levels using metallic Fe as the precursor. Color legends: Orange – non-faceted particles; Blue – cuboctahedron particles; Green – cubic/truncated cubic particles.....159

Figure 3-36. Scanning electron micrographs of Ni-Ti co-doped TaC samples showing both cuboctahedron and cubic particles with fixed amount of Ni (20 at% calculated) and different Ti doping levels using metallic Ni and Ti as the precursors.....160

Figure 3-37. X-ray diffraction patterns of Ni-Ti co-doped TaC samples with fixed Ni amount (20 at% calculated) and different Ti doping levels using metallic Ni and Ti as the precursors.....170

Figure 3-38. Statistical abundance of particle morphology for Ni-Ti co-doped TaC samples fixed Ni amount (20 at% calculated) and different Ti doping levels using metallic Ni and Ti as the precursors. Color legends: Orange – non-faceted particles; Blue – cuboctahedron particles; Green – cubic/truncated cubic particles.....171

Figure 3-39. Plot of the dopant concentrations detected by X-ray photoelectron spectroscopy with respect to the concentration detected by energy dispersive spectroscopy. The samples chosen for comparison have the highest abundance of modified particles in each system, namely, Ni-4, Co-3, Fe-4 and NiTi-5. Shape legends: Pentagon – $TiTa_3C_4$; Circle – TaC.....172

Figure 3-40. Slab models for (a) TaC (111) and (b) TaC (100) used to calculate segregation energies. Slab models for (c) TiTa₃C₄ (111) and (d) TiTa₃C₄ (100). The green (surface) and red (sub-surface) dashed boxes indicate the possible metallic (i.e., Ta and/or Ti) sites a dopant can substitute (courtesy of Richard Tran, co-first author of Ref. 21).....175

Figure 3-41. Calculated segregation energy for the (100) surface with respect to the (111) surface. Slab models for TaC (111), TaC (100), TiTa₃C₄ (111), and TiTa₃C₄ (100) used to calculate segregation energies are indicated in Figure 3-40. Shape legends: Pentagon – TiTa₃C₄; Circle – TaC (courtesy of Richard Tran, co-first author of Ref. 21).....176

Figure 3-42. Calculated enthalpy maps of R as a function of $\Delta\mu_C$ and $\Delta\mu_X$ for (a) Ni in TaC; (b) Co in TaC; (c) Fe in TaC; (d) Y in TaC; (e) Ti in TiTa₃C₄ with $\Delta\mu_{Ni} = 0 eV$ (courtesy of Richard Tran, co-first author of Ref. 21).....178

Figure 3-43. Scanning electron micrograph of Ti-doped TaC sample showing no sign of faceted particles with 15 at% calculated amount of Ti (Ti-2) using metallic Ti as the precursor.....179

Figure 3-44. Summary of the dopant-induced morphology selectivity of TaC nanoparticles.....183

ACKNOWLEDGEMENTS

This project was partially supported by the Frontiers of Innovation Scholars Program (FISP) from the University of California, San Diego. Major research experiments were performed at the CaliBaja Center for Resilient Materials and Systems at the University of California, San Diego. Scanning electron microscopy was performed at the Nano3 Facility at the University of California, San Diego. X-ray photoelectron spectroscopy was conducted by Dr. Manuel Herrera at the Centro de Nanociencias y Nanotecnología of the Universidad Nacional Autónoma de México.

I would like to thank Dr. Olivia Graeve with my greatest gratitude for serving as my research advisor and providing me with this unique opportunity to pursue scientific advancement and personal development. A very special thank-you to Richard Tran and Dr. Shyue Ping Ong for their dedication to carry out a seamless collaboration on this project with strong computational capabilities. I would also like to thank Dr. James Kelly, Dr. Ekaterina Novitskaya, Sebastian Lee, Aric Bandera, and all of my coworkers at the CaliBaja Center for Resilient Materials and Systems for their technical assistance and overall support beyond the laboratory to make this research happen. Finally, I would like to thank all of my friends along the way for their continuous encouragement and the fulfillments they brought to my life.

Chapter 2, in part, has been accepted for publication titled “Morphology Control of Tantalum Carbide Nanoparticles through Dopant Additions” in the Journal of Physical Chemistry C, 2021, where the dissertation author was the primary investigator and the co-first author of this paper. The paper is co-authored by R. Tran (co-first author), S. Lee, A. Bandera, M. Herrera, X.-G. Li, S.P. Ong, and O.A. Graeve. This chapter contains detailed description of the experimental procedures.

Chapter 3, in part, has been accepted for publication titled “Morphology Control of Tantalum Carbide Nanoparticles through Dopant Additions” in the Journal of Physical Chemistry C, 2021, where the dissertation author was the primary investigator and the co-first author of this paper. The paper is co-authored by R. Tran (co-first author), S. Lee, A. Bandera, M. Herrera, X.-G. Li, S.P. Ong, and O.A. Graeve. This chapter contains experimental results and discussions.

VITA

2012	Bachelor of Science, University of Illinois at Urbana-Champaign
2013 – 2014	Research Assistant, University of California San Diego
2013	Master of Science, University of California San Diego
2014 – 2018	Teaching Assistant, University of California San Diego
2021	Doctor of Philosophy, University of California San Diego
2018 – present	Process Development Engineer, Luminus Inc.

PUBLICATIONS

T. Ren, L.-N. Nforbi, R. Kanakala, and O.A. Graeve, “Phase Stability and Mechanisms of Transformation of La-Doped γ -Alumina” *Inorg. Chem.*, **57** [6] 3035-3041 (2018).

S. Qiao, E. Novitskaya, T. Ren, G. Pena, and O.A. Graeve, “Phase and Morphology Control of Magnesium Nanoparticles via Lithium Doping” *Cryst. Growth Des.*, **19** [7] 3626-32 (2019).

E.M. Bullard, I. Torres, T. Ren, O.A. Graeve, and K. Roy, “Shell Mineralogy of A Fundamental Marine Species, *Mytilus Californianus*, over Half A Century in A Changing Ocean,” *Proc. Natl. Acad. Sci. U.S.A.*, **118** [3] e2004769118 (2021).

T. Ren, R. Tran, S. Lee, A. Bandera, M. Herrera, X.-G. Li, S.P. Ong, and O.A. Graeve, “Morphology Control of Tantalum Carbide Nanoparticles through Dopant Additions,” Accepted (2021).

FIELD OF STUDY

Major Field: Materials Science and Engineering
Professor Olivia A. Graeve

ABSTRACT OF THE DISSERTATION

Exploring the Morphology Control and Formation Mechanisms of Ultra-High Temperature
Ceramic Particles: A Study on Tantalum Carbide

by

Tianqi Ren

Doctor of Philosophy in Materials Science and Engineering

University of California San Diego, 2021

Professor Olivia A. Graeve, Chair

Tantalum carbide (TaC) belongs to a class of materials known as ultra-high temperature ceramics (UHTCs) with unique combinations of physical, chemical and electronic properties. The following study presents for the first time the morphologically controlled synthesis of TaC nanoparticles using a modified solvothermal method. X-ray diffraction revealed that highly crystalline TaC can be obtained with excellent phase purity. Doping by metallic species is shown to have significant impact on the final morphology of TaC nanoparticles. The shape selectivity and morphology evolution from round/irregular shapes to cubes and cuboctahedrons varies with

the type of dopant, including Ni, Fe, Co, Y and Ni-Ti co-doping. Statistical abundance of over 80% particles with high-faceted morphologies were observed, significantly surpassing that of undoped samples (around 10%). Experimental interpretation was coupled by the Density Functional Theory (DFT) based calculation to probe the fundamental mechanisms responsible for the dopant-induced change in the growth habit of TaC nanoparticles. It was found that the major formation mechanisms include surface segregation of dopants, atomic orbital interaction between dopants and carbon, which caused the change in relative growth rate of facets. The probability of forming one type of faceted particles over another is governed by the surface energy distributions. The mechanisms and techniques explored herein are expected to be generally applicable to other transition metal-based ceramics thereby providing an unprecedented pathway towards the morphology tailoring of high-temperature materials. Principles of crystal growth and prior works for morphologically controlled synthesis of a variety of inorganic materials were also thoroughly reviewed.

Chapter 1

Introduction

1.1. Ultra-high Temperature Ceramics

Throughout history mankind has been striving to push the limits of materials for applications in harsh environments where high temperatures, high pressures and strong corrosivity often coexist. These environments typically require materials that possess high melting temperatures, high chemical stability, and other properties to achieve required durability and usability on a most cost-effective basis. Ultra-high temperature ceramics (UHTCs) are a class of materials that are promising to withstand such extreme conditions. Although the generally accepted definition of UHTCs states that these materials have melting temperatures greater than 2773 K, it is the high thermal conductivity that gives certain UHTC materials the advantage to be utilized in high-temperature applications, such as thermal protection for space re-entry vehicles and rocket nozzles.¹⁻² The use of UHTCs, specifically non-oxide ceramics, including transition metal carbides (TMCs), borides (TMBs) and nitrides (TMNs), in aviation industry has been pursued in the 1960's and early 70's primarily by the United States Air Force.³⁻¹⁰ Due to the nature of military-based research, the publications related to UHTCs remained dormant for decades until the National Aeronautics and Space Administration (NASA) regained interest in developing UHTC materials for application in sharp leading edge components in hypersonic flight conditions.¹¹⁻¹⁴ In the design of the Space Shuttle, a blunt nose and blunt leading edge were used mainly for the purpose of reducing the aerodynamic heating developed during atmospheric re-entry (Figure 1-1). This blunt configuration allows essentially the use of SiC/carbon or carbon/carbon composites, which are typically not considered UHTC materials, as the thermal protection layer.



Figure 1-1. Blunt leading edge component used in the Space Shuttle. Typical radius of curvature at the tip is ~ 10 cm, made from SiC/carbon and carbon/carbon composites (adapted from <http://www.pari.edu/shuttle-leading-wing-edge-web/>).

However, certain limitations are associated with this blunt configuration. This includes limited maneuverability, limited re-entry points, electromagnetic interference that causes blackouts in telecommunications, as well as high propulsion power requirements to account for the high drag.¹¹ To solve these problems, the concept of sharp leading edges with radii of curvature in the millimeter scale started to be applied in the design of next generation high-mach aircraft. Such sharp features enable flying at optimal angle of attack whose trajectory is more gently angled with respect to the ground level. This potentially enhances maneuverability and provides the vehicles with more trajectory options during the re-entry process. Meanwhile, the realization of this concept comes with the price of higher temperature on the leading edges due to lack of drag to reduce aerodynamic heating. Moreover, the smaller radius of curvature also creates higher local temperatures at the tip. The maximum temperature that is experienced by the leading edges can easily exceed 2073 K, beyond the capability of conventional SiC/carbon and carbon/carbon

composites.¹⁵⁻¹⁸ This requires the use of new high-temperature materials that are more robust to withstand such demanding temperatures. UHTC materials, including TMCs, TMBs and TMNs, are therefore being investigated extensively as promising candidates to answer the call for sharp leading edge applications.

Besides applications in the leading edge component, UHTC materials have the potential to be applied in many other demanding conditions.²⁰⁻²⁵ UHTCs that are able to withstand prolonged period of extreme conditions (minutes to hours compared to seconds for re-entry vehicles) could enable hypersonic flight. In these cases, UHTCs provide benefits mainly on the propulsion system where hotter combustion creates higher propulsion efficiency. On this aspect, it not only enhances the capability of military and national defense, but also potentially contributes to the development of commercial aircraft to have better physical and economical performance. Additionally, in advanced nuclear power generation, UHTC materials could also be attractive. Tantalum monocarbide (TaC), the focus in this study, remains one of the promising candidates to realize the applications described above. In the next section, general properties of TaC will be elaborated.

1.2. Tantalum Carbide

Tantalum carbide, as one of the commonly recognized transition metal carbides (TMCs), has several chemically stable polymorphs with different carbon stoichiometries according to the Ta-C phase diagram (Figure 1-2), among which the semi-carbide Ta_2C_{1-x} , ζ - Ta_4C_{3-x} , and monocarbide TaC_{1-x} are of particular research interests for a variety of applications. For example, TaC/ Ta_2C -based matrix with Ta_4C_3 laths provides the best overall strength compared to other carbide composites.²⁶ It has also been found that modifications in carbon stoichiometry can increase Vickers hardness of bulk tantalum carbide from 13.5 to 20 GPa upon the addition of Ta_4C_{3-x} phases.²⁷ The monocarbide phase (TaC_{1-x}) is primarily being focused in this study because

of its higher melting temperature as well as wide composition range. Structurally, the TaC_{1-x} phase has a highly symmetric face-centered cubic (*fcc*, space group $Fm\bar{3}m$) lattice with a reported lattice parameter of 4.45370 Å for stoichiometric TaC.²⁸ It has been determined that there is a definite relationship between the lattice parameter and carbon stoichiometry for the TaC_{1-x} phase and it is given by $C/\text{Ta} = 6.398a - 17.516$.²⁹ Practically, this allows the evaluation of carbon deficiency in TaC_{1-x} through the lattice parameter calculation from diffraction data. The lattice structure can be treated as two *fcc*-arranged lattices of Ta and C atoms where the *fcc*-arranged C lattice interstitially fits into the *fcc*-arranged Ta lattice (Figure 1-3), analogous to the Rocksalt structure. Many other TMCs (e.g., TiC, NbC, ZrC, etc.) possess this structure as well.

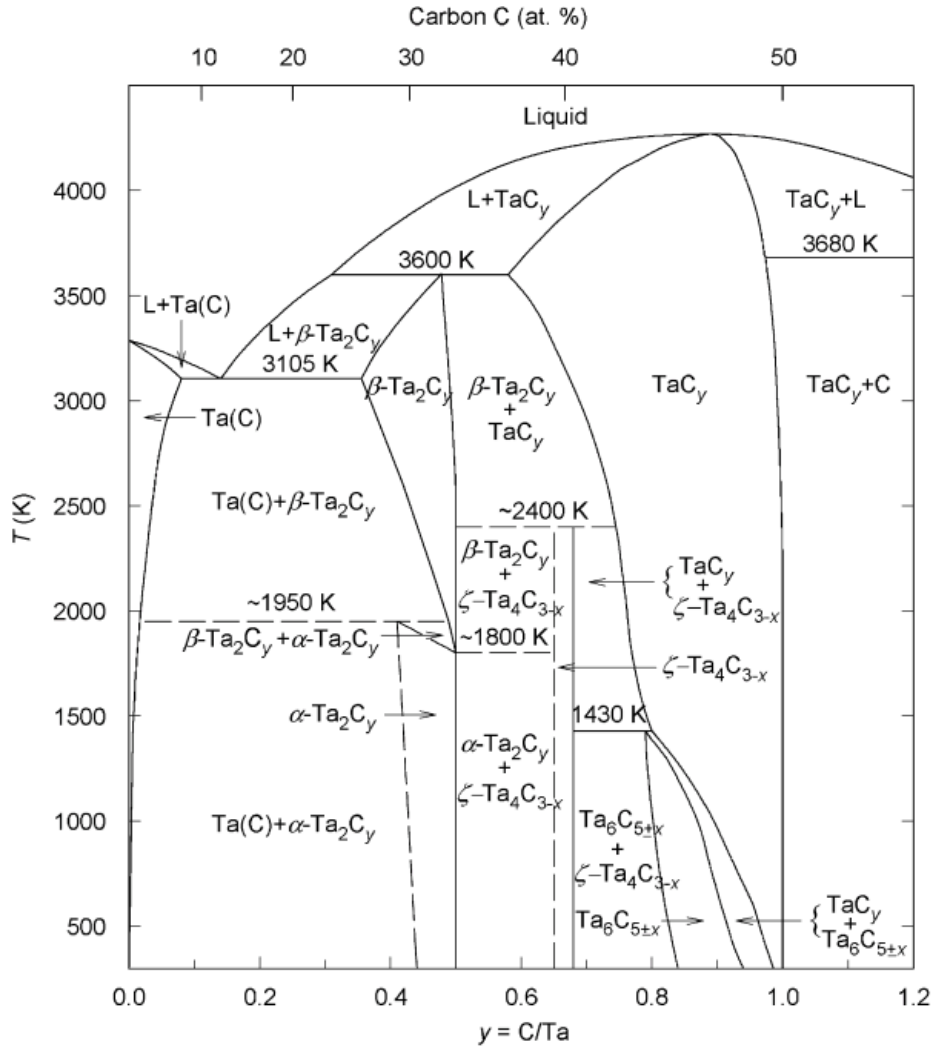


Figure 1-2. Phase diagram for the Ta-C system. “x” and “y” denote possible carbon sub-stoichiometry in corresponding phases (reprinted with permission from Ref. 30).

It is generally accepted that the bonding in TaC_{1-x} is dominated by the covalent bonds formed between Ta and C atoms through Ta-5d and C-2p orbital hybridization. While the metallic bonding arises from Ta-Ta interaction and the ionic contribution caused by charge transfer from Ta to C atoms coexist to give the overall bonding structure a complex mixture of covalent, metallic, and ionic characteristics.³¹⁻³³ Understanding the bonding characteristics of tantalum carbide is

essential for the purpose of this study because it serves as the most important intrinsic factor for the determination of particle morphologies. This aspect will be explained in detail in later chapters.

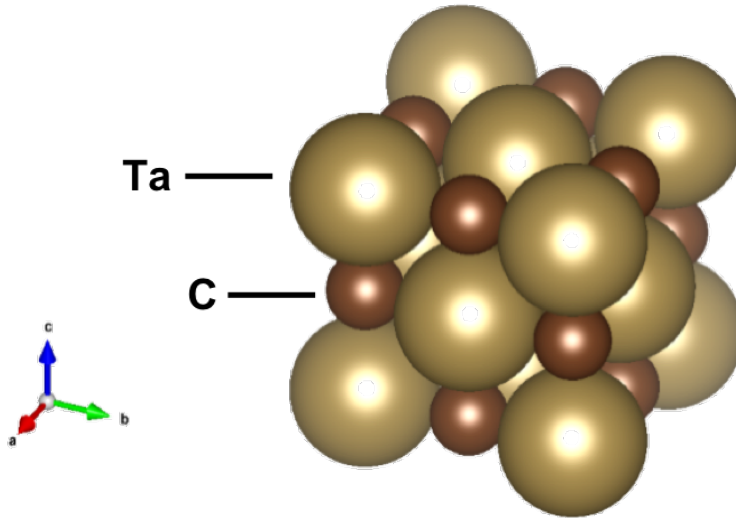


Figure 1-3. Crystal structure of TaC_{1-x}. Both Ta and C sublattices are in *fcc* arrangement. Carbon atoms sit in the interstitial sites within Ta lattice. (With color)

1.3. Crystal Growth and Morphology Control of Inorganic Materials

Modern scientific research has become more interested in revealing evolution phenomena from interpreting the equilibrium (or at least steady-state) conditions. Crystal growth and resultant morphology of the grown materials are two important aspects in the materials science community because many properties are morphology-specific. For example, structural, optical, and electrical properties can be largely augmented with the fabrication of composite materials with anisotropic microstructures or with anisotropic particles uniformly dispersed in an isotropic matrix.³⁴ Moreover, different crystal surfaces exhibit different physical and chemical characteristics due to their packing and coordination state. As an example, the TiC {111} surface has been shown to be highly active for dissociative adsorption of hydrogen at room temperature, while its {100} surface

has the ability to adsorb several other molecules, including methanol, ethanol, H₂O, NH₃ and CO.³⁵⁻⁴⁰ In this section, some fundamentals of crystal growth and methods developed for the control of morphology will be reviewed.

1.3. Crystal Growth and Morphology Control of Inorganic Materials

1.3.1. Growth of Bulk Crystals

The growth of crystals from the melt using a pulling mechanism was first demonstrated by Prof. Jan Czochralski dated back in 1916, and it was not until three decades later when the first single crystal silicon (Si) was grown using the Czochralski (Cz) technique.⁴¹ This essentially opened up a new horizon for developing semiconductors, microelectronics, and other related fields in information technology. A schematic illustration of the Cz process is shown below. In brief, a heated silica crucible in the middle melts polycrystalline silicon fed through the bottom. The crystal growth process is initiated by dipping a silicon seed crystal into the free surface of the silicon melt, and then the seed is slowly pulled up from the melt, causing the silicon atoms in the reservoir to crystallize at the melt-crystal interface. The diameter of the grown Si crystal increases to a nominal diameter and is kept constant until the most of melt is consumed. This gives the grown Si single crystal to have a cone geometry.

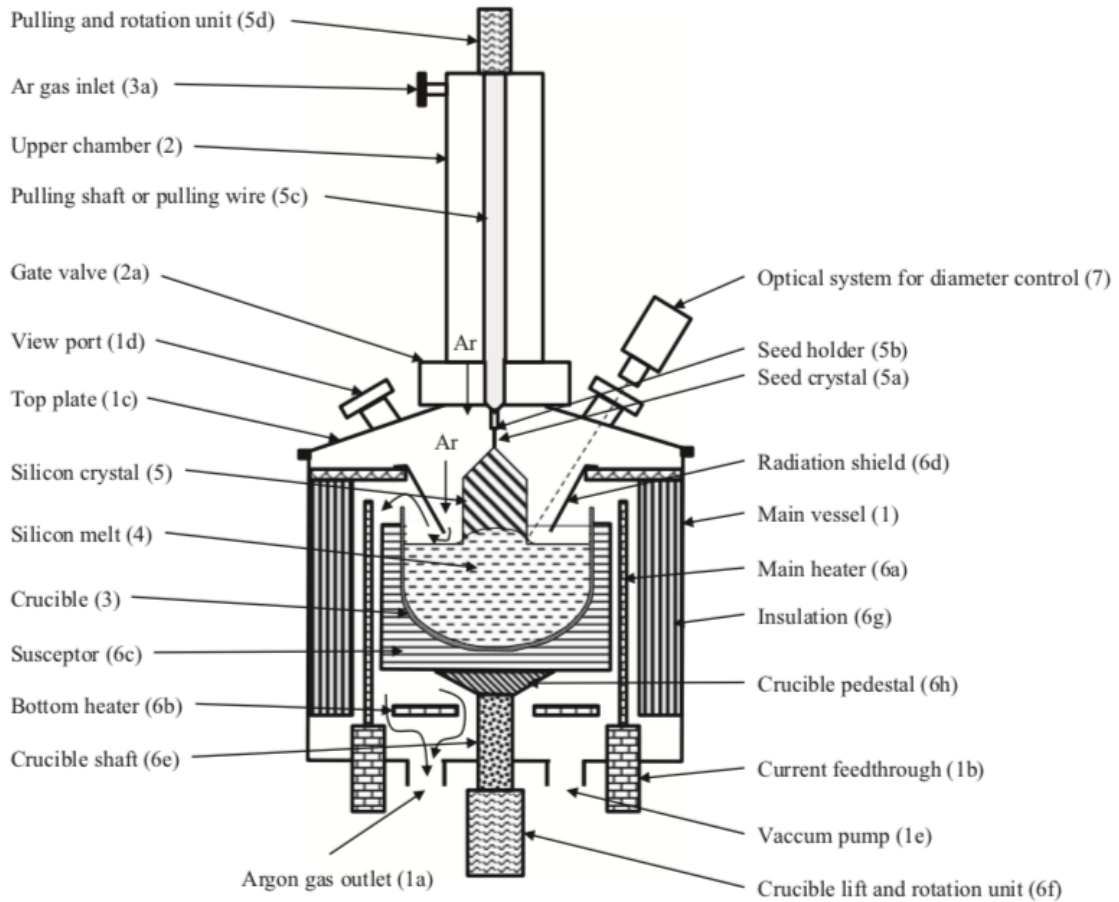


Figure 1-4. A schematic of an industrial single crystal silicon puller using Czochralski process (reprinted with permission from Ref. 41).

Many other inorganic crystals can be grown to bulk with high purity and production efficiency using the same principles. This includes, for example, sapphire single crystals (Al_2O_3), calcium fluoride (CaF_2) and other fluoride crystals, bismuth germinate ($\text{Bi}_4\text{Ge}_3\text{O}_{12}$), lead tungstate (PbWO_4), gadolinium silicate (Gd_2SiO_5), etc. These materials have wide applications in semiconductors, lasers, and radiation scintillators.⁴² Besides the Cz technique, several other common techniques are capable of fabricating bulk crystals, such as the floating zone method (for growing oxides and metal alloys) and the hydrothermal method (for growing quartz, phosphates, rare-earth vanadates, simple oxides, etc.).^{41,43} The technology development for the growth of bulk

crystals, especially those single crystals of semiconductor and functional oxides, enables people to create new devices and bring continuous advancements to the community. The fact that the 2014 Nobel Prize in Physics was awarded to Professors Isamu Akasaki, Hiroshi Amano, and Shuji Nakamura for their invention of blue light-emitting diodes sets another great example to indicate the importance of crystal growth. Nevertheless, the main message to be delivered here is that the growth of bulk crystals has been studied for decades with tremendous achievements. It is now the time to simultaneously make efforts towards microscopic scale where the growth phenomena of submicron/nano-sized particles are attracting increasing research attention. A thorough understanding of the growth behavior and controlling the particle shapes can help achieve material properties otherwise not possible by conventional methods.

1.3.2. Growth and Morphology Control of Nanoscale Crystalline Particles

According to Wulff's theorem first introduced in 1901, the equilibrium shape of a single crystal is unique from an energy minimization standpoint based on its crystal structures. More specifically, the equilibrium shape can be constructed by inscribing an in-polygon bounded by lines or planes of the internal tangent at the cusps of a raspberry form obtained by plotting the surface energies of facets. The growth rates of facets are proportional to the surface free energies.^{44,45} For example, *fcc* single crystal takes an equilibrium shape (Wulff polyhedron) of a truncated octahedron with minimization of its surface free energy (Figure 1-5). However, it should be noted that this equilibrium shape is valid only under the vacuum or inert gas atmosphere at 0K. Practically in a solution-based synthesis, the actual particle morphology can differ drastically from the Wulff polyhedron. The circumstances that cause the difference include: i) The equilibrium condition has never been reached during the entire synthesis; ii) Defects, impurities, surface capping agent, or the chemistry of the solvent may alter the surface energies of particle facets to

impact their relative growth rate.⁴⁶ The first circumstance is particularly true when the solution-based reaction involves a high-temperature or high-pressure environment.

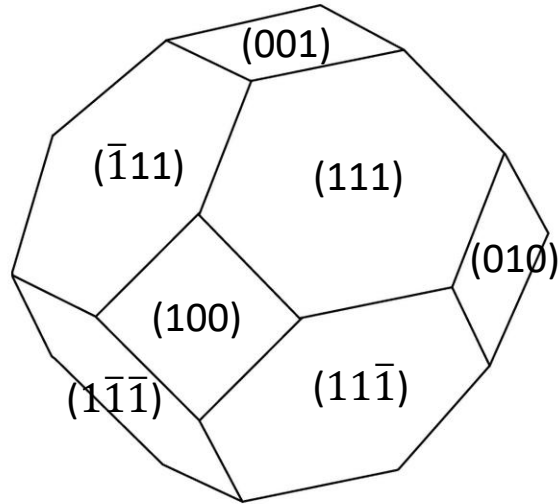


Figure 1-5. Typical truncated octahedron as the Wulff polyhedron of *fcc* single crystal under inert gas or vacuum at 0K. The index of each surface shown is labelled with Miller notations (reprinted and modified with permission from Ref. 47).

Besides Wulff's theorem, the Periodic Bond Chain (PBC) theory proposed by Hartman and Perdok is another model that correlates the internal crystal structure to the particle morphology.⁴⁸ In PBC analysis, crystal facets are classified into three types. Namely, F (flat), S (stepped), and K (kinked) faces, depending on the number of PBCs involved in each facet. They claimed that an F-face would develop into a large facet as it contains more than two PBCs. While an S- or K-faces would develop into small facets or does not appear at all because S-face contains only one PBC and K-face does not contain any PBC. A schematic representation of the PBC theory is presented in Figure 1-6. Although PBC analysis appears to be qualitative and even somewhat arbitrary, it was developed more quantitatively later by calculating the attachment energies of PBCs and has been applied as an important criterion for analyzing the growth behavior.

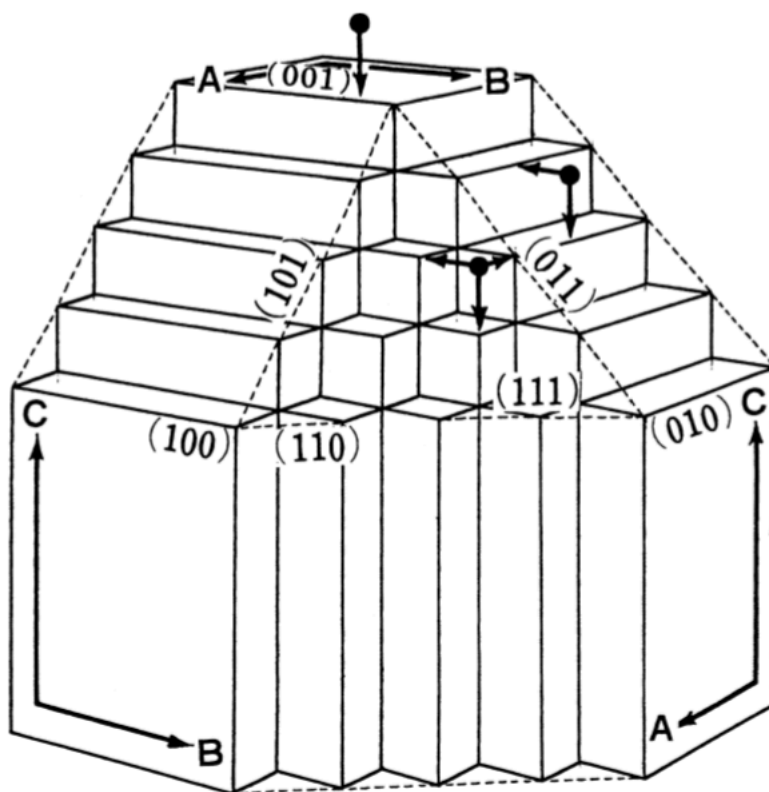


Figure 1-6. The definition of F-, S- and K-faces according to the PBC theory by Hartman and Perlok. F-faces: (100), (010) and (001); S-faces: (101), (110) and (011); K-face: (111) (reprinted with permission from Ref. 48).

The fabrication of submicron/nano-sized particles has been extensively reported in numerous literature, among which the solution-based methods are of particular interest because they are more powerful and versatile than other techniques (vapor-phase synthesis for instance) in terms of controlling the geometry of particles. Conventional solution-based methods generally involve aqueous or organic solvent with low viscosity, as well as relatively low reaction temperature. For certain ceramic compounds that cannot be straightforwardly fabricated using conventional solution-based routes, other synthesis techniques that involve solid-state reactions with high reaction temperatures can be employed (e.g., solvothermal synthesis, combustion synthesis, self-propagating high-temperature synthesis, etc.). Next, general principles of

morphology evolution of particles as well as several experimental examples on the synthesis of metallic and ceramic particles will be provided in the subsections below.

1.3.2.1. Morphology Evolution of Nanoscale Crystalline Particles

In a typical crystalline particle formation process, atomic nucleation can be treated as the starting point after individual atoms are generated in the solution. However, due to the small size of nuclei (i.e., a cluster made from several tens to hundreds of atoms), it is practically difficult to capture their internal structure and geometry. Using electrospray mass spectroscopy, researchers are able to quantify the mass of the small clusters.⁴⁹ By combining electrospray photoelectron spectroscopy and *ab initio* calculations, some information about the internal structure and geometry of clusters can also be obtained.⁵⁰ In an ideal case where the atoms are packed in the densest way possible, the shape of the cluster closely resembles that of single-crystal seed with a larger size and well-defined polyhedral shapes (Figure 1-6). Yet, the understanding of those atomic clusters formed during the initial stage is still insufficient. It will be very valuable to address the correlation between the shape of such clusters and the final morphology of crystalline particles with advancements in characterization tools and computational methods.





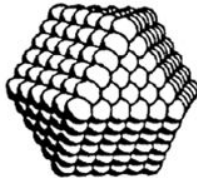
Full-shell "magic number" clusters					
Number of shells	1	2	3	4	5
Number of atoms in cluster	13	55	147	309	561
Percentage of surface atoms	92	76	63	52	45

Figure 1-7. Representation of clusters in an ideal and the densest atomic packing. Polyhedral shape of the cluster becomes more pronounced as the number of atoms increases (reprinted with permission from Ref. 46; original figure was modified with permission from Ref. 51).

Once the nuclei reach a critical size greater than which the overall shape fluctuation is no longer energetically favorable, single crystal seeds with certain three-dimensional geometry are formed. The formation of seeds is a critical step connecting the nuclei and particles, as their shape directs the development of final particle morphologies. Generally speaking, seeds may have a single-crystal, singly-twinned, multiply-twinned or plate-like structure for *fcc*-type nanocrystals. However, only single-crystal seed that leads to the formation of octahedron, cuboctahedron and cube, is within the scope of this study. Figure 1-7 illustrates schematically the evolutionary pathways that give births to such polyhedrons.

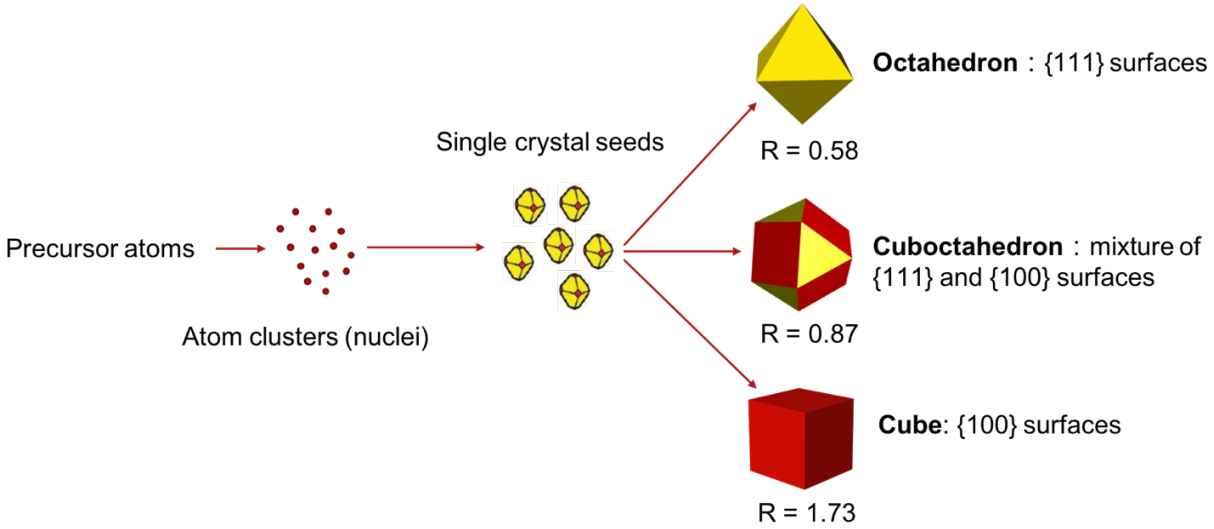


Figure 1-8. A schematic illustration of the evolution pathways that lead to the formation of polyhedrons for *fcc* crystals. The yellow- and red-colored regions represent {111} and {100} facets respectively. The value R is defined as the ratio between the growth rates along $\langle 111 \rangle$ and $\langle 100 \rangle$ directions. It should be noted that particle shapes out of actual experiments can deviate, to a variety of extent, from these ideal shapes shown here, depending on the actual growth rates along different crystallographic directions. (With color)

The population of seeds with different structures is controlled thermodynamically by their free energies, as well as certain experiment-specific kinetic factors. When an active system is under thermodynamic control, the population of particles will be dominated by the most energetically-stable products. To take a closer look at the Wulff theorem, which aims to minimize the total surface free energy of a system within a given volume, the shape of single crystal seeds with the largest popularity can be predicted. The surface free energy “ γ ” can be defined as:

$$\gamma = \left(\frac{\delta G}{\delta A} \right)_{n_i, T, P} \quad \text{Eq.1}$$

Where G is the total free energy, and A is the total surface area. Qualitatively, surface free energy is the energy required to create a new unit area of the surface. When a seed is newly formed, surface atoms tend to be attracted inward into the structure (i.e., atoms cluster together) due to

missing bonds at the surface. Therefore, a driving force on the surface is needed in order to pull the atoms back to their position to grow new surfaces and restore crystallographic symmetry. Surface free energy act as such driving force and can be thereby expressed as:

$$\gamma = \frac{1}{2} N_b \varepsilon \rho_a \quad \text{Eq.2}$$

Where N_b is the number of broken bonds, ε is the bond strength, ρ_a is the density of surface atoms. In the case of *fcc* crystals with lattice parameter a , the surface energies for three low-index crystallographic planes can be estimated as:

$$\gamma_{\{100\}} = \left(\frac{4\varepsilon}{a^2}\right); \quad \gamma_{\{110\}} = \left(\frac{4.24\varepsilon}{a^2}\right); \quad \gamma_{\{111\}} = \left(\frac{3.36\varepsilon}{a^2}\right); \quad \text{Eq.3}$$

Clearly, the overall surface energy follows a sequence of $\gamma_{\{111\}} < \gamma_{\{100\}} < \gamma_{\{110\}}$. This suggests that single-crystal seeds with *fcc* structure would take an octahedral or tetrahedral shape in attempt to minimize the total surface energy by maximizing the exposure of $\{111\}$ facets. On the other hand, however, both shapes have greater surface areas than a cube if given the same volume. By considering this, single-crystal seeds are expected to have truncated octahedron shape enclosed by the mixture of both $\{111\}$ and $\{100\}$ facets, which finalizes the minimization of total surface energy.⁴⁶

Besides thermodynamic control, kinetic effects on the seed formation are described in several studies, and most of them have been focused on the synthesis of inorganic nanoparticles.^{35,52-56} The population of seeds and particles can be controlled on a kinetic basis by varying the reduction or decomposition rate of precursors, or regulating the amount of precursor molecules. By using such kinetically-controlled synthesis, the seed can easily deviate from thermodynamically-favored shapes and exist in structures with higher free energies.

Once a seed is formed, it can grow into particles with larger sizes by the addition of new atoms. This is essentially a dynamic process during which the reduction of the bulk free energy (favored by growth) and the increase of surface free energy (favored by dissolution) mutually dictate the overall growth. The facets being exposed during the growth depend on their relative growth rate. As shown in Figure 1-8, for example, if the ratio between the growth rates of $\{111\}$ and $\{100\}$ facets is equal or greater than 1.73 (i.e., $R \geq 1.73$), cubes will be dominant in the final morphology, whereas octahedrons will be dominant if $R \leq 0.58$. More systematically, Figure 1-9 provides a summary of the geometrical shapes of nanoparticles that are possible to be grown by controlling the reaction parameters.⁵⁷

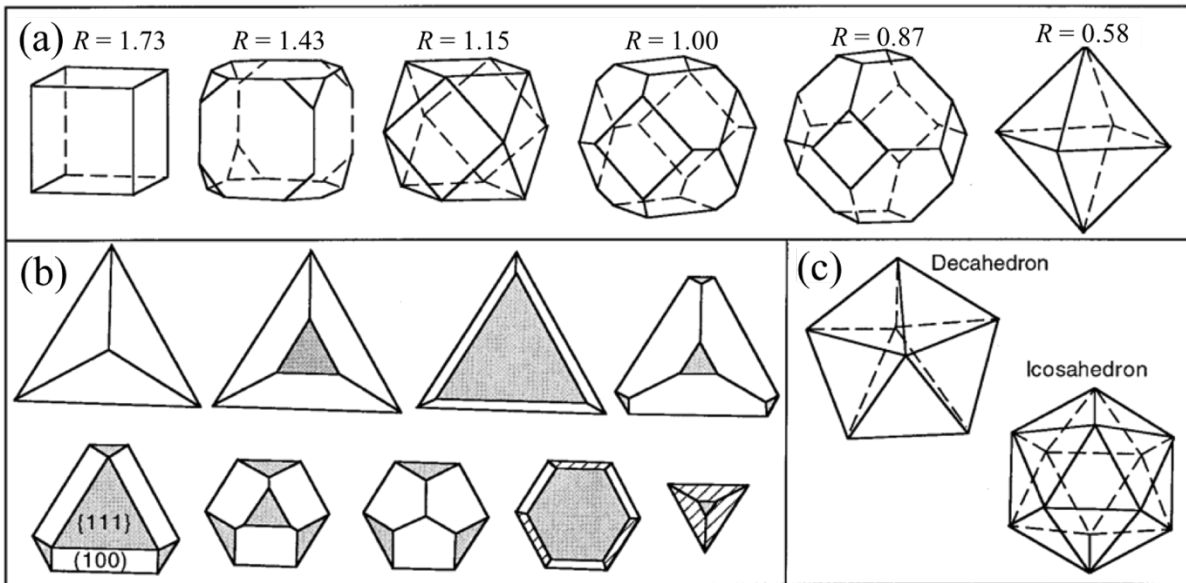


Figure 1-9. (a) Morphologies of cubic crystals as a function of R , the ratio between the growth rates along $\langle 111 \rangle$ and $\langle 100 \rangle$ directions. (b) Evolution in shapes of a set of $\{111\}$ based particles as the ratio of $\{111\}$ to $\{100\}$ increases. The beginning particle is bounded by three $\{100\}$ facets and a $\{111\}$ base, while the final particle is bounded by $\{111\}$ to form a tetrahedron. (c) Morphologies of multiply twinned decahedral and icosahedral particles (reprinted and modified with permission from Ref. 57).

Therefore, in principle, the morphology of particles can be altered through the control of the growth rates of different crystalline facets, and methods that realize this purpose vary significantly across the broad universe of materials. A number of examples of how this is practically achieved will be reviewed in the following.

1.3.2.2. Literature Review: Morphology Control of Metallic Nanoparticles

The shape-controlled synthesis of metallic nanoparticles was first demonstrated by Ahmadi *et al.* on Pt nanoparticles with tetrahedral, cubic, irregular-prismatic, icosahedral, and cuboctahedral shapes by varying the concentration ratio of the capping polymer materials to the Pt cation.⁵⁸ Since then, shape control of numerous metallic systems has been enabled, as summarized in Figure 1-10. In the past decades, the applications of metallic nanoparticles have been dramatically broadened, from catalysts, plasmonics, sensing, nanomedicine to electrochemistry, petroleum refining, as well as microelectronics.^{46,58} Many of these applications involve strong demand for morphology-dependent nanoparticle properties. For instance, in the case of localized surface plasmon resonance (LSPR) and surface-enhanced Raman scattering (SERS), the shape and structure of an Au or Ag nanocrystal are the most important factors in determining the number, position, and the intensity of LSPR modes, also the spectral region or polarization dependence for effective molecular detection via SERS.^{46,60-61} In the case of catalysis, the catalytic activity of metal nanoparticles increases with decreasing particle size. While the selectivity of adsorbing molecules depends mainly on the atomic packing on the surface or the exposed facets of a nanoparticle.^{46,62-63} Although the current study focuses heavily on ceramics, understanding the principles and methods of controlled crystal growth on structurally simpler metallic systems can provide fruitful guidance towards more complex ceramic materials.

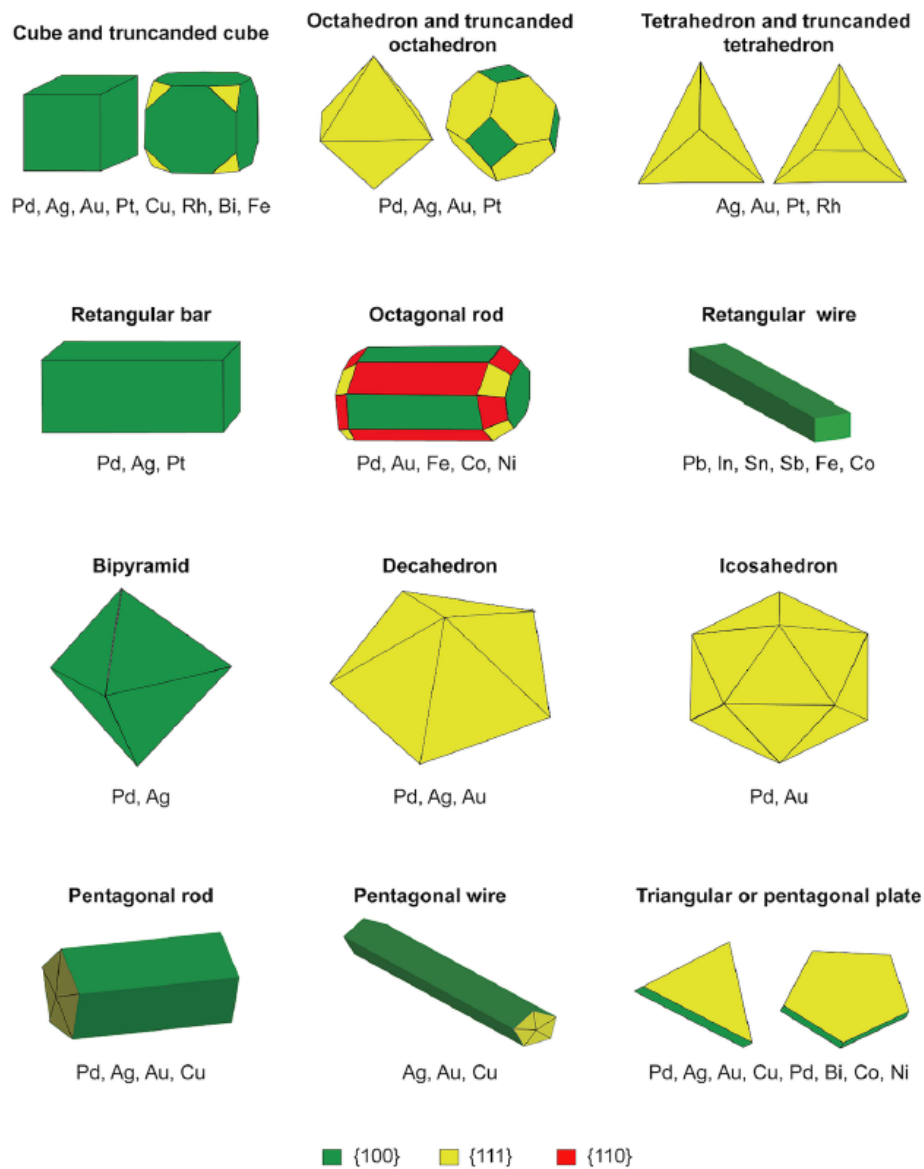


Figure 1-10. A summary of various metallic nanoparticles synthesized with controlled morphologies using solution-based synthesis (reprinted with permission from Ref. 59).

Palladium (Pd) is an ideal model system for understanding the shape control of nanoparticles as the general principles that direct the growth of Pd nanoparticles can be easily extended to other *fcc* structures.⁴⁶ Facet tailoring of Pd nanoparticles is essentially driven by the need to enhance its catalytic properties. Pd nanoparticles are usually synthesized by reducing Pd

precursors in solution (polyol synthesis), among which Na_2PdCl_4 is most commonly used as the precursor and alcohols, glycols, or hydrazine is the reductant. When prepared by rapid reduction or decomposition, Pd nanoparticles mostly form Wulff polyhedrons (refer to Figure 1-5) with the presence of poly(vinyl pyrrolidone) (PVP). Xiong *et al.* has shown that oxidative etching plays an important role in determining the population of polyhedrons.⁶⁴ It was found that oxidative etching of Pd nanoparticles by air leads to the removal of twinned particles in the early stage of growth and the dissolution of single-crystal cuboctahedra grown in the late stage. This means that in order to yield a high percentage of polyhedral nanoparticles with uniform size, one needs to utilize the former and eliminate the latter (Figure 1-11(a)).⁶⁴

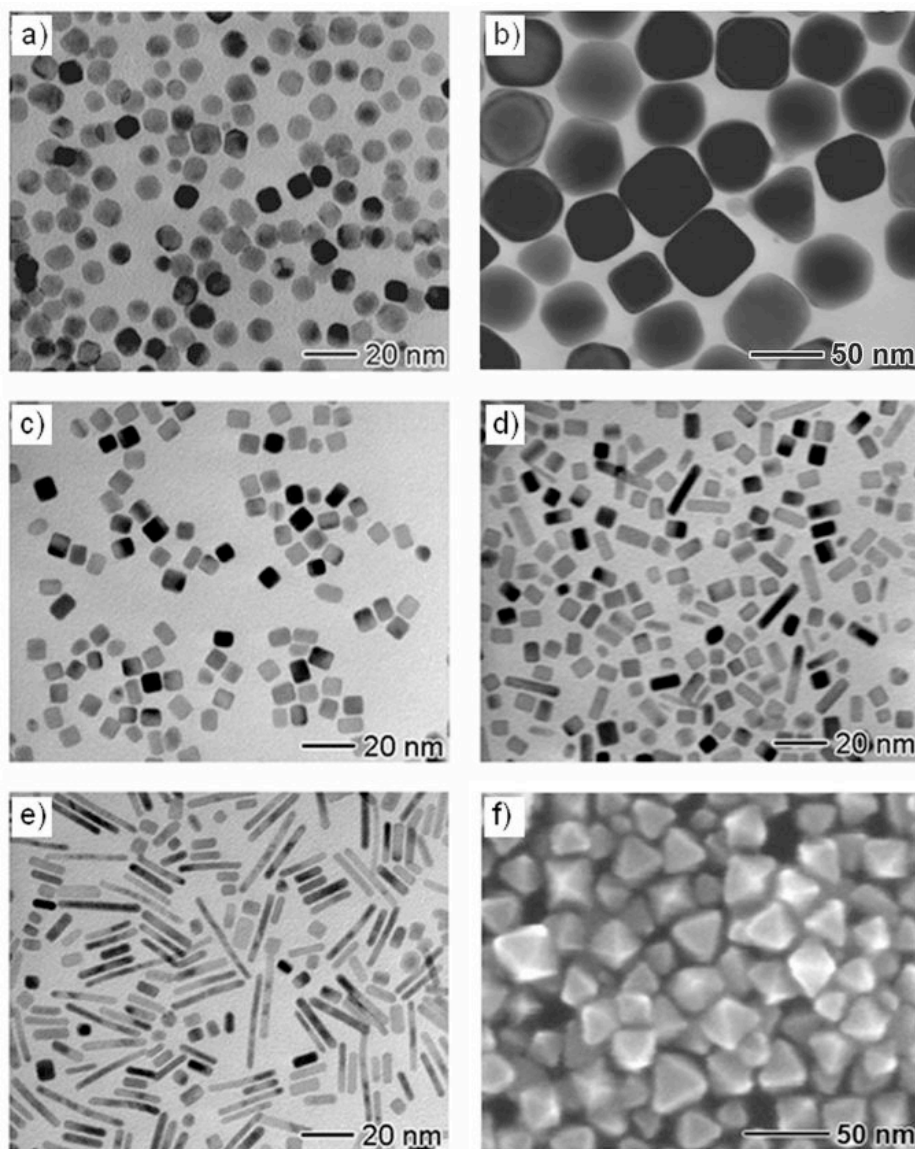


Figure 1-11. Electron micrographs of Pd nanoparticles with various sizes and morphologies: (a) Wulff polyhedrons, (b) nanocubes with average of 50 nm size, (c) nanocubes with average of 8 nm size, (d) nanobars, (e) nanorods and (f) octahedrons (reprinted with permission from Ref. 46).

As a step forward, Pd nanoparticles with a single type of facet are desired, especially for catalytic applications where cubes are preferred over Wulff polyhedrons.⁶⁵ To achieve this, surface capping agents such as PVP are introduced to the solution due to its strong adsorption onto the {100} facets. This preferential surface capping can drive the addition of metal atoms to other crystal surfaces when the size of seeds is considerably large.⁴⁶ In the case of surface capping by

PVP, metal atoms attach more preferably to the {111} facets and eventually form nanocubes with sizes greater than 25 nm.^{66,67} The formation of Pd nanocubes (including other metal nanocubes such as Ag and Au) through this route is in fact a combined effect from the oxidative etching of small seeds and surface capping by PVP in a relatively larger size. By adding FeCl₃ as the etchant, Pd nanocubes with sizes as large as 50 nm were produced (Figure 1-11(b)).⁶⁷ Due to the size of PVP molecules, it is not so effective in surface capping when the crystal seeds are smaller than 25 nm. Therefore, bromide (Br⁻) was employed as a smaller capping agent, allowing for the formation of Pd nanocubes with much smaller particle size. In another report by Xiong *et al.*, Pd nanocubes with an average size of 8 nm were synthesized using PVP as the reductant and KBr as the surface capping agent (Figure 1-11(c)).⁶⁸ Moreover, it was also illustrated in some work that elongated shapes of Pd crystals, including nanobars and nanorods can be grown with the addition of ethylene glycol (EG) as a result of anisotropic growth (Figure 1-11(d-e)). Anisotropic growth is usually seen in either crystal with highly anisotropic crystallographic structures (such as Se, Te, CdS, and CdSe) or twin/stacking faults in *fcc* metals.⁷⁰⁻⁷² As both characteristics are absent in the formation of Pd nanobars and nanorods, the mechanism involved in this anisotropic growth is attributed to the localized oxidative etching. Due to the capping effect by Br⁻ on the {100} facets, the surfaces need to be activated in some way for the growth process to continue, and this surface activation is done by oxidative etching. In a cubic crystal, oxidative etching can only activate one of the six crystal facets by the addition of atoms. In this sense, if Pd atoms can be supplied fast enough to surpass the atomic etching rate at that surface, the cubic symmetry will be broken, hence, the elongated shapes will be formed.^{46,68} This anisotropic growth set a nice example for kinetically controlled shape evolution. Such kinetically generated shapes, however, are not stable due to their high surface energies, and they will evolve into thermodynamically stable shapes over the time to

minimize the surface energies.⁶⁸ Figure 1-12 gives a schematic representation of how the shape of Pd nanoparticles is both kinetically and thermodynamically controlled.

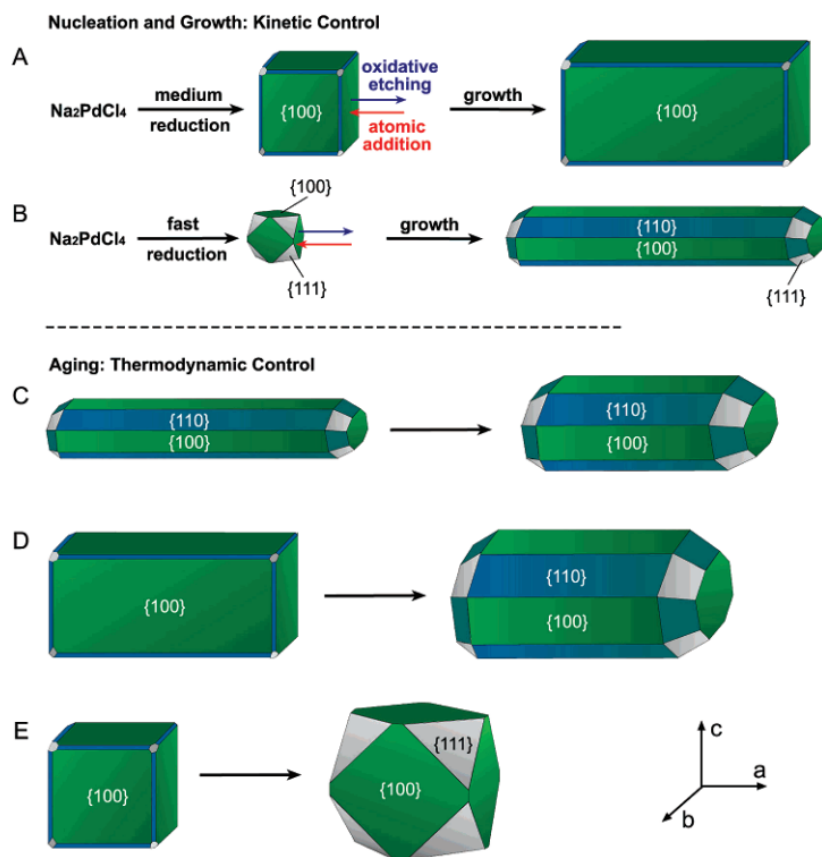


Figure 1-12. A schematic illustration of the growth mechanisms responsible for the formation of Pd nanobars and nanorods, as well as the thermodynamically controlled aging process (reprinted with permission from Ref. 68).

Using different surface capping agents, octahedral Pd nanoparticles can also be synthesized, as shown in Figure 1-11(f).⁷² With the application of a mild reductant and a suitable capping agent (citric acid serves as a dual-role additive in this case), plus a high concentration of Pd precursor, Pd octahedrons are produced for a greater than 90% yield.^{46,72} Same strategies can be used to generate Pd decahedrons and icosahedraons, thanks to the effective capping capability of the citric acid on the {111} facets.

Owing to the unique and tunable properties of Au nanoparticles, including LSPR, biocompatibility and easy surface modification, it has been one of the hottest research topics over the past couple of decades on the controllable synthesis of Au nanoparticles.⁴⁶ Although similar routes, such as polyol synthesis can be taken to synthesize Au nanoparticles in which a fast reduction also leads to the formation of thermodynamically favored polyhedral nanocrystals, notable differences exist in terms of the effect of surface capping agent, as well as the kinetically-controlled growth mechanisms compare to the Pd system described in preceding paragraphs. While PVP stabilizes the {100} facets of Pd crystals, in the case of Au, it helps stabilize the {111} facets to form octahedrons as demonstrated by Li *et al.*⁷³ Interestingly, when a small amount of AgNO₃ or cetyltrimethylammonium bromide (CTAB) is added to the precursor solution, Au nanocubes can be formed (Figure 1-13), indicating that Ag⁺ and Br⁻ preferentially attach to the {100} facets of Au and serve as the surface capping agent.⁷⁴⁻⁷⁷ Most recently, Park *et al.* reported that the concentration of CTAB controls the sharpness of Au nanocubes as the higher the concentration is, the sharper corners of nanocubes are (Figure 1-14, except for 200 mM CTAB due to the reduction in particle size). This further emphasized the effectiveness of Br⁻ in selective surface attachment on {100} and reduction of their growth rate.⁷⁷

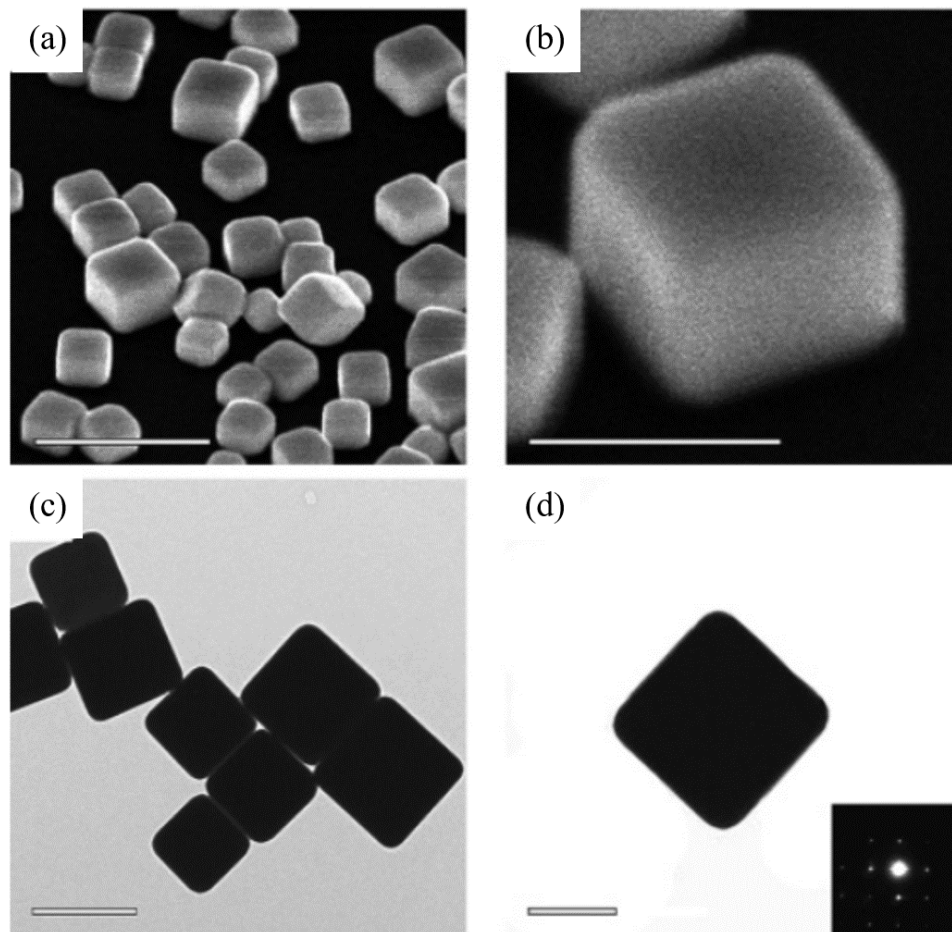


Figure 1-13. Au nanocubes formed with 1/200 Ag/Au addition of AgNO₃ obtained using a modified polyol process: (a-b) SEM micrographs with 45° tilt, scale bars are 500 nm and 200 nm respectively, (c-d) TEM micrographs of corresponding Au nanocubes, scales bars are 200 nm and 100 nm respectively (reprinted and modified with permission from Ref. 75).

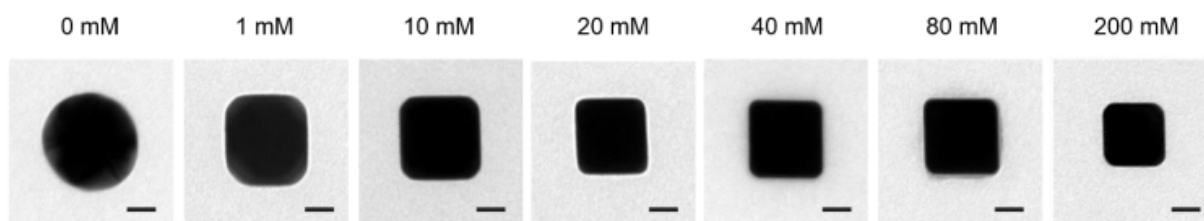


Figure 1-14. TEM micrographs of Au nanocubes illustrating the change in corner sharpness under different CTAB concentrations (reprinted with permission from Ref. 77).

Based on the similar consideration in promoting the catalytic properties, shape- and size-controlled synthesis of Pt nanoparticles are also extensively studied. It was shown by Yang's

research group that mono-dispersed cuboctahedral Pt nanoparticles with sizes 10 – 15 nm could be formed by reducing K_2PtCl_4 precursor by H_2 gas generated from the decomposition of $NaBH_4$. Further, with an increased pH value, cubic Pt nanoparticles were obtained due to the selective growth of the $\{100\}$ surfaces originated from decreased reduction rate (Figure 1-15). In their studies, tetradecyltrimethylammonium bromide (TTAB) was used as the surfactant.^{78,79}

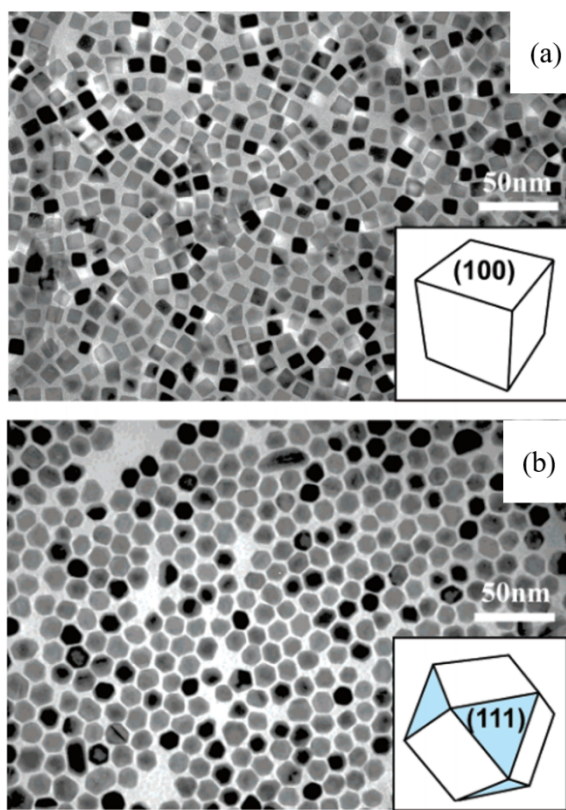


Figure 1-15. TEM micrographs of Pt nanoparticles produced by reduction of K_2PtCl_4 with TTAB as the surfactant: (a) nanocubes (with $NaBH_4$ at high pH) and (b) cuboctahedrons (with $NaBH_4 + H_2$ flow at low pH) (reprinted and modified with permission from Ref. 78).

The formation of Pt nanocubes has been realized in much smaller sizes, as reported by later studies by Lee *et al.* and Chen *et al.*^{80,81} Lee *et al.* prepared Pt nanocubes with an average size of 4.5 nm by thermal decomposition in the presence of PVP, while Chen *et al.* reduced platinum(II)2,4-pentanedionate ($Pt(acac)_2$) with ascorbic acid to yield Pt nanocubes with 3.5 nm

average size. The ascorbic acid is believed to accelerate the nucleation rate of Pt nanoparticles and the growth rate along $\langle 111 \rangle$ direction, although it was observed earlier in Yang's study that the use of ascorbic acid leads to the formation of Pt nanodendrites.^{79,81}

Many other metallic nanoparticles including Ag, Cu, Rh, Ir, Ru, Fe, Co, etc., have been investigated on their morphologically controlled synthesis.⁴⁶ Although the chemicals involved vary significantly across the systems, the principles and methodologies that facilitate the formation of different types of morphology are similar in general. By leveraging both kinetic and thermodynamic factors during the crystal growth, it is feasible to manipulate the particle morphology in a versatile way.

1.3.2.3. Literature Review: Morphology Control of Ceramic Particles

Ceramics are of great research interest mainly because of their structural/chemical robustness and diverse functionalities. Manipulation of particle morphology to desired shapes such as cubes and other types of polyhedrons has been investigated on a variety of advanced ceramic materials. These include, but not limited to, barium titanate (BaTiO_3)⁸²⁻⁸⁹, strontium titanate (SrTiO_3)⁹⁰, potassium niobate (KNbO_3)⁹¹⁻⁹³, metal oxides⁹⁴⁻¹⁰¹, hexaborides^{102,103}, transition metal carbides and nitrides^{35,56,104-110}, etc. Unlike those metallic nanoparticles described in the previous section, facet tailoring and control of morphology for ceramic-based particles is practically more difficult, and its underlying mechanisms are more complicated due to the complexity in crystal structure, surface characteristics, bonding environment and experimental conditions. Nevertheless, similar kinetic and thermodynamic strategies used in the synthesis of shape-controlled metallic nanoparticles can be implemented to demonstrate the morphology control of ceramic particles.

Sodium chloride (NaCl) has been selected as the model system in many studies to investigate the growth behavior of *fcc* crystals, as it is naturally abundant and easy to be produced in-house. As a typical ionic *fcc* crystal, the ideal surfaces of $\{100\}$ and $\{110\}$ in NaCl are considered to be electrically neutral since both cations and anions are bonded throughout the $h00$ and $hh0$ lattice planes (Figure 1-16 b-c). While for the $\{111\}$ facets, they are electrostatically polar because only cations or anions are present in the $\{111\}$ lattice planes alternating along the $\langle 111 \rangle$ directions, even if the bulk crystal structure is centrosymmetric (Figure 1-16 d-e). This implies that the stability of $\{111\}$ facets is poor, and their presence can rarely be seen in the equilibrium morphology of NaCl crystals. Rather, cubic shapes will dominate.¹¹¹

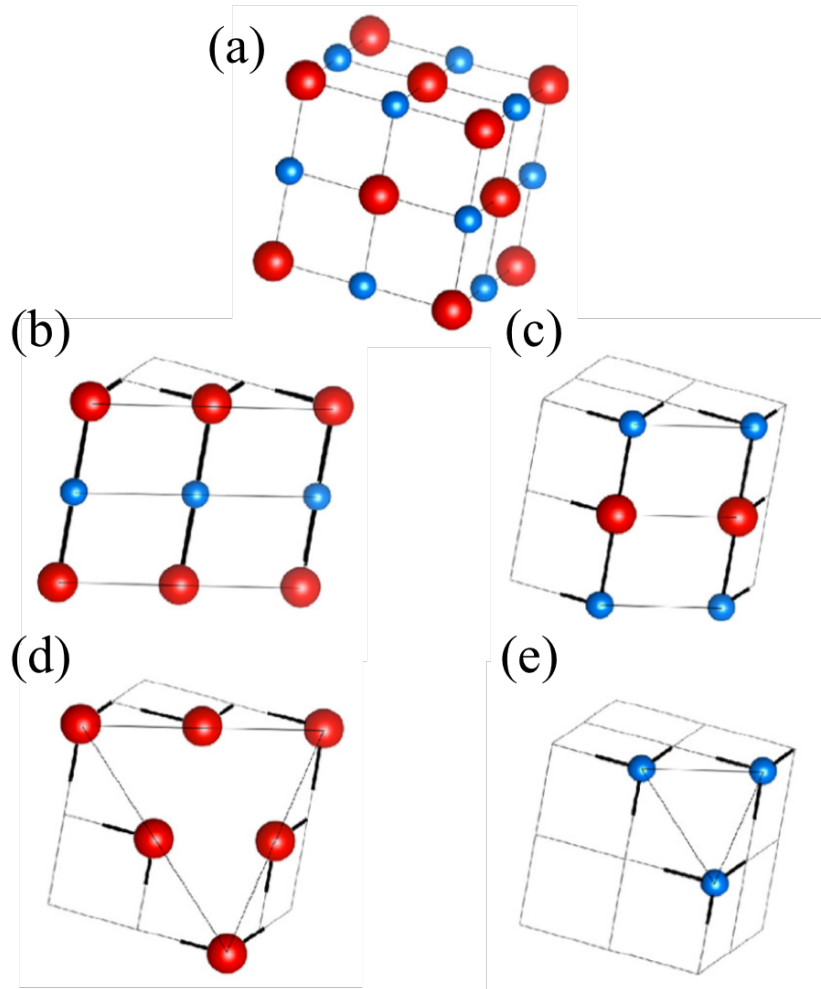


Figure 1-16. (a) Ideal surface structure of cubic NaCl crystal enclosed by $\{100\}$ facets. Cl^- ions in blue and Na^+ ions in red. (b-c) Surface structure of $\{110\}$ facets. (d-e) Surface structure of $\{111\}$ facets (reprinted and modified with permission from Ref. 111). (With color)

While the dominance of cubic shape serves as the main reason for natural halite to cake, people have been seeking for the so-called “habit modifier” in order to have more exposure of the $\{111\}$ facets in the final morphology, i.e., $\{100\} \rightarrow \{100\} + \{111\}$ enclosed particles, when grown from the evaporation of solutions. Several such habit modifiers have been discovered, including urea, formamide, cadmium chloride (CdCl_2), ferrocyanide ions, as well as polymeric additives.¹¹¹ The mechanisms of habit change during the growth of halite crystals from saturated solutions have also been extensively studied. By using surface X-ray diffraction, Redenović *et al.* were able to

reveal that the polar {111} surface is stabilized by formamide through the formation of an electrochemical double layer.¹¹² Further, they found that the appearance of {111} facets in alkali halide crystals grown from formamide solutions is closely related to their unit cell sizes.¹¹³ More recently, Townsend *et al.* from the same research group also discovered that the effectiveness of polymer species containing amide group, which induces the formation of {111} facets is 1 to 2 orders of magnitude stronger than their corresponding monomers. This owes to the enhanced bonding on the surface for polymer compare to monomer.¹¹⁴ An earlier study on NaCl crystals grown from CdCl₂-containing solutions claimed that the formation of an epitaxial layer of ordered CdCl₂ on the {111} facets of NaCl contributes to the stabilizing {111} facets.¹¹⁵ With various types of habit modifiers being reported in the past decades, the fundamental rules for stabilizing a crystallographic surfaces are essentially the following: (i) reducing their specific surface energies and (ii) decreasing their growth kinetics.

Besides sodium chloride, numerous recent studies have been conducted on controlling the particle morphology of many other technical ceramics. Grove *et al.* presented study cases on morphological changes of TiC and NbC caused by precursor carbon sources.^{35,56} Their TiC and NbC nanoparticles were synthesized using the arc discharge method, where pure metal rod (Ti and Nb) were used as electrodes for direct-current discharge and several hydrocarbons, including methane, ethylene and acetylene were selected as the carbon source. When a high-intensity direct-current was applied to the electrodes, metals, and carbon species were atomized by the arc discharge-generated plasma. Once the metal and carbon vapor is cooled, or their concentrations are high enough in the reaction chamber, the nucleation and growth process occurs. TiC or NbC particles were then collected in a bubbler containing acetonitrile. They found that the morphology of both TiC and NbC nanoparticles is largely affected by the carbon source, although differences

exist among two systems. TiC nanoparticles prefer a cubic morphology at low methane concentrations and a cuboctahedral morphology at high methane concentrations, as shown in Figure 1-17.

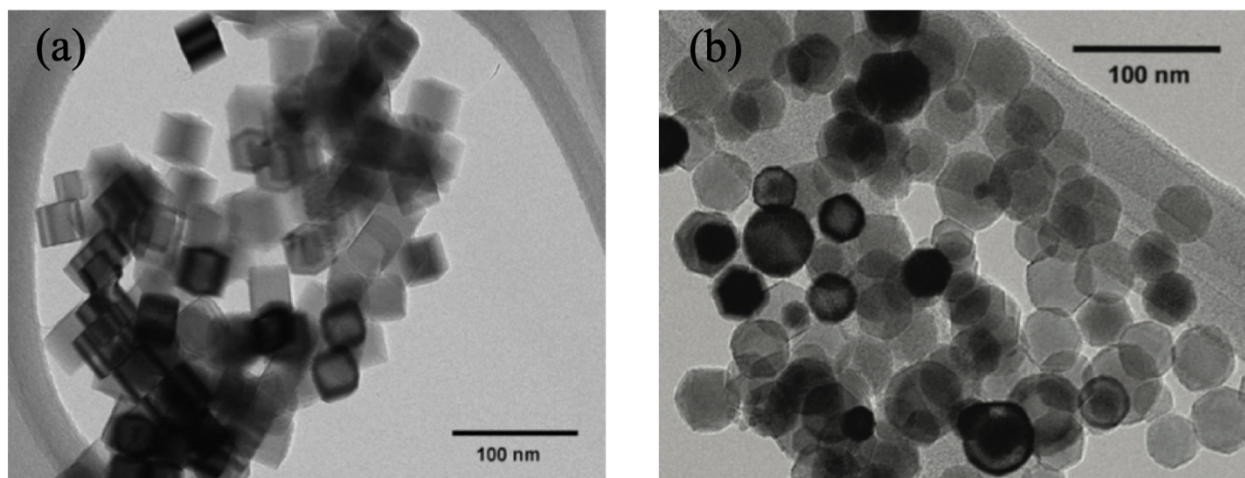


Figure 1-17. (a) TiC nanoparticles synthesized from arc discharge method with low methane concentrations showing cubic-dominated morphology. (b) At high methane concentration (60% in this case), the morphology of TiC nanoparticles favors cuboctahedron (reprinted and modified with permission from Ref. 35).

Based on Wulff's theorem and PBC theory, they attributed this morphological difference to excess carbon (from methane), which interacts with the kink sites along $\{111\}$ facets to capture their growth. For the NbC nanoparticles, the change in morphology is mainly controlled by the type of hydrocarbons, while the concentration of hydrocarbons does not show a significant impact. According to their results, the population of NbC nanoparticles synthesized with methane is dominated by cubes, whereas synthesizing with ethylene yielded a mixture of cubes and cuboctahedrons. In addition, acetylene resulted in cuboctahedrons only. Since the type and amount of hydrocarbon precursor are the only two variables, it is safe to say that they caused the morphological change by stabilizing $\{111\}$ facets during the growth of nanoparticles. However,

the fundamental mechanisms behind this behavior are still in the shadow and were not discussed in depth in these two publications by Grove *et al.*

A series of publications by Jin *et al.*^{107,109-110,116} provided another approach to the morphological evolution of stoichiometry-variable UHTC particles. The technique they employed to synthesize samples (including carbides, nitrides and diborides) is self-propagating high-temperature synthesis (SHS), in which commercial metal powders were mixed with carbon black, boron nitride (BN), and boron to produce carbides, nitrides, and diboride correspondingly. The raw powders were pressed into cylindrical compacts with the addition of powder aluminum, which serves as reaction media, and ignited by an arc in Ar atmosphere. The stoichiometry of samples was manipulated by varying the C/TM, BN/TM, and B/TM molar ratios in the reactants. They found that the ceramics with wide stoichiometric ranges all show a stoichiometry-induced morphology evolution. More specifically, the morphology evolution sequences are “octahedron → truncated octahedron → sphere-like → sphere” for both TMCs and TMNs, and “hexagonal prism → polyhedron → sphere-like” for TMDs, with the increasing stoichiometries. They claimed that the major mechanism for this morphology evolution is that the variation in stoichiometry significantly changes the bonding characteristics on the different crystallographic surfaces and the interfaces between the particles and the Al melt. Hence, the growth rates of different surfaces alter, eventually causing different morphological expressions. They also performed detailed analysis into the thermodynamic roughening behavior of the particles under high combustion temperature. They claimed that there is a critical temperature T_R above which some particle surfaces are roughened and rounded to induce the formation of sphere-like particles. Their study is comprehensive with respect to the stoichiometry-induced morphology changes, which is supported by both experimental observations and explanation of mechanisms. However, there is not much

guidance provided to control the morphology of nearly-stoichiometric UHTC crystalline particles, which are the most important ones for practical uses.

Besides the aforementioned non-oxide ceramics, perovskite structure oxides, due to their wide variety of applications, are among the most popular classes of ceramic materials being investigated to tailor their particle morphologies. Tungsten and molybdenum trioxide (WO_3 and MoO_3) are commonly studied transition metal oxides with perovskite structure owing to their excellent properties in catalysis, sensor, and electrochromic applications.¹¹⁷ Yao *et al.* presented their work on morphology evolution of WO_3 particles induced by Cr doping.¹¹⁸ They adopt an RF induction thermal plasma method to prepare Cr-doped WO_3 polyhedra, where Cr-loaded ammonium paratungstate tetrahydrate (Cr-APT) was subjected to thermal decomposition by Ar- O_2 plasma, and Cr-doped WO_3 polyhedra were collected at the bottom of the chamber. For producing monolithic WO_3 particles, APT without Cr was used. According to their results, only octahedron particles with $\{111\}$ facets exposed were obtained for monolithic WO_3 due to the fast growth of facets along the $\langle 100 \rangle$ directions (Figure 1-18(a)). When a certain amount of Cr is introduced (2.5 at.% Cr-doped WO_3 in this case), $\{100\}$ facets are exposed. When the Cr concentration was further increased to 10 at.%, cubic-shaped WO_3 particles are formed. (Figure 1-18(b-c)).

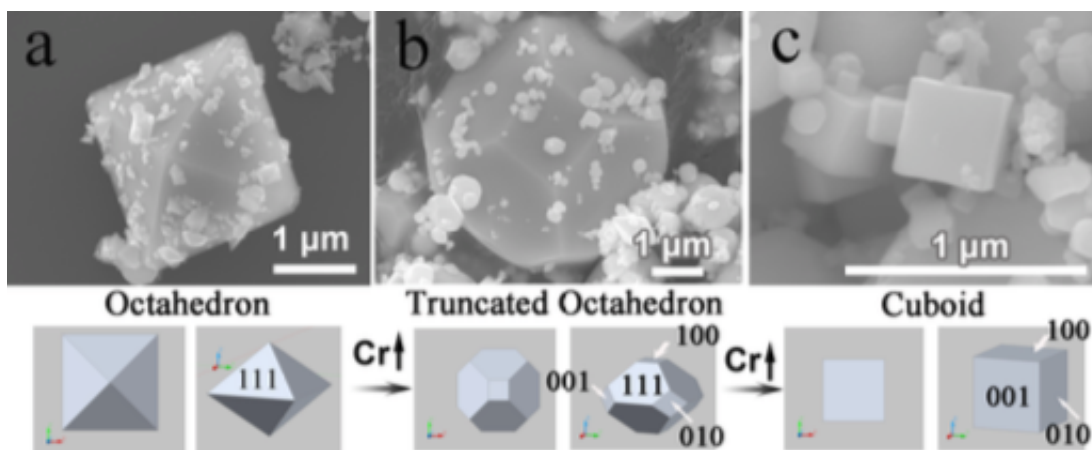


Figure 1-18. WO₃ particles with different morphologies caused by Cr-doping. (a) monolithic WO₃. (b) 2.5 at.% Cr-WO₃. (c) 10 at.% Cr-WO₃ (reprinted with permission from Ref. 117).

By using X-ray diffraction (XRD) and X-ray photoelectron spectroscopy (XPS), they were able to interpret the formation mechanisms as the effects of distortions introduced in the WO₃ matrix by Cr doping and a chromate layer on the crystal surface, which reduces the growth rate along the $\langle 100 \rangle$ directions. They also performed tests on the gas sensing capabilities of morphologically modified WO₃ polyhedra and revealed that 2.5 at.% Cr-WO₃ with truncated octahedron shape exhibits the highest sensing response. Their study elucidates in a detailed way that doping could be very effective in altering the crystal growth habit, which determines the final morphology, as well as the significance of the particle morphology towards the material properties. For MoO₃, the most common morphologies are nanorod, nanowire, nanofiber, nanotube, etc.¹¹⁷ The formation of three-dimensional polyhedra is seldom reported, and its discussion is therefore not going to be expanded here.

In recent years, various research projects related to molecule-sensing applications have been focused on metal oxide nanocubes. For example, Wang *et al.* obtained porous NiFe₂O₄ nanocubes for detecting low-concentration acetone through thermal annealing a metal-organic framework.¹⁴⁴ Li *et al.* reported In₂O₃ nanocubes for NO₂/H₂S detection prepared by a CTAB-

assisted solvothermal process.¹⁴⁵ Senapati and Nanda demonstrated MgO nanocubes for the detection of trinitrophenol (picric acid) by simply reacting and annealing the Mg metal ribbon inside a tube furnace in the air.¹⁴⁶ In fact, the studies on MgO nanocubes have been conducted for many years. Stankic *et al.* synthesized MgO nanocubes with sizes between 3 to 10 nm using chemical vapor deposition and subsequent annealing to probe its optical properties.¹⁴⁷ Takahashi succeeded in getting MgO nanocubes with 200 nm average size using a microwave oven.¹⁴⁸ Issa *et al.* produced sharp MgO nanocubes with sizes ranging from 20 to 300 nm by burning commercial magnesium chips in the air to study its microscopic mechanical behavior.¹⁴⁹ Nanocubes of quaternary oxide $\text{CaCu}_3\text{Ti}_4\text{O}_{12}$ possessing a perovskite-like structure were obtained by Maity *et al.* through a controlled oxidation reaction in molten salt.¹⁵⁰ This material has attractive properties in electrical energy storage applications, such as the supercapacitor. In an earlier work, Jang *et al.* demonstrated porous cobalt oxide (Co_3O_4) nanocubes for similar applications as the supercapacitor. They employed a hydrothermal synthesis approach using an autoclave.¹⁵¹ Figure 1-19 below shows some graphic examples from some of the references hereby mentioned. It should be noted that none of the studies described in this paragraph focuses heavily on the formation mechanisms of the nanocubes. Rather, they selectively utilized the thermodynamically stable cubic-shaped metal oxide particles as their research vehicles for different purposes.

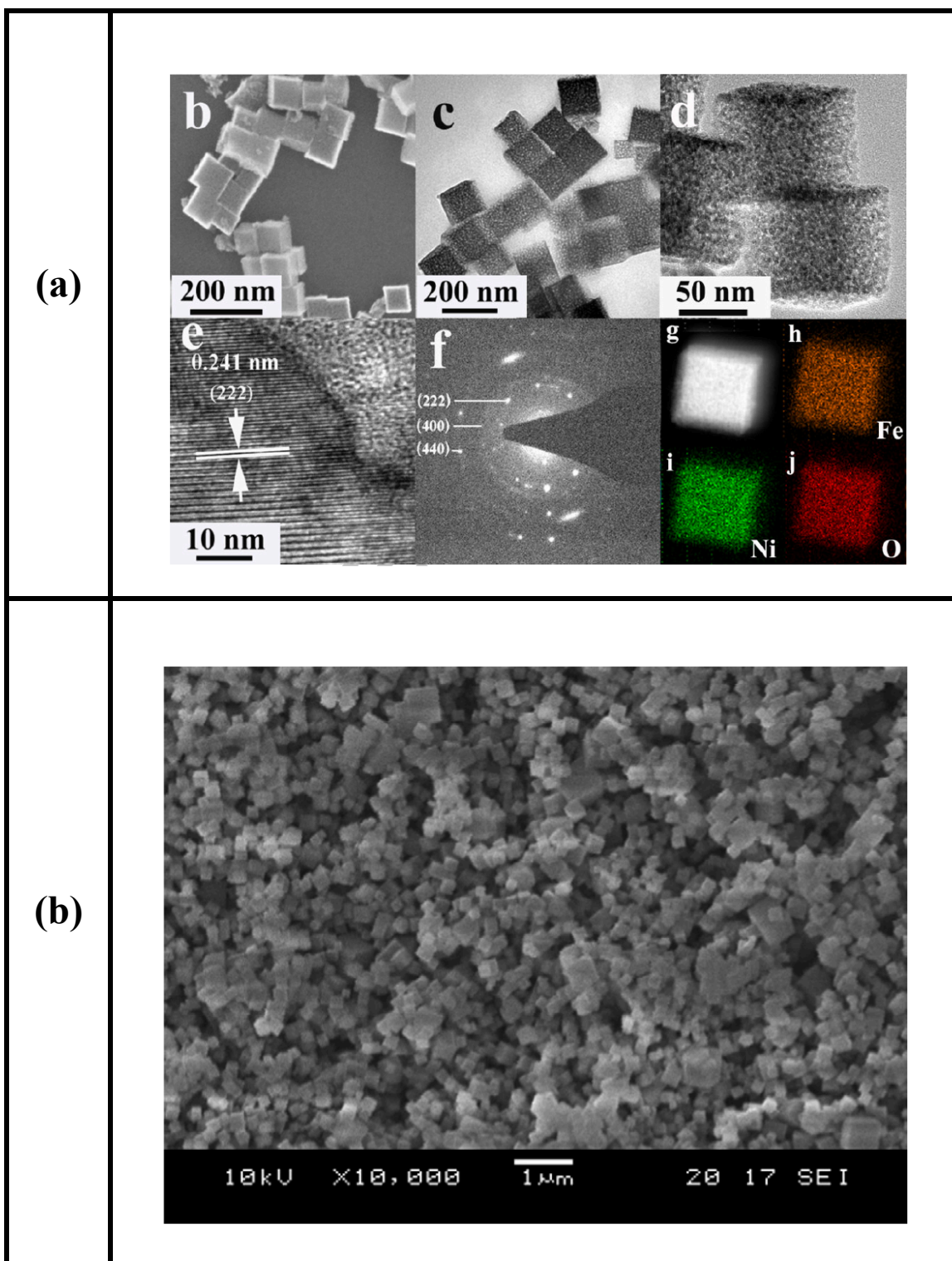


Figure 1-19. Microscopy graph examples of (a) NiFe_2O_4 porous nanocubes by Wang *et al.*; (b) MgO nanocubes by Takahashi; (c) MgO nanocubes by Issa *et al.*; (d) $\text{CaCu}_3\text{Ti}_4\text{O}_{12}$ nanocubes by Maity *et al.* (reprinted with permission from Ref. 144, 148, 149, 150).

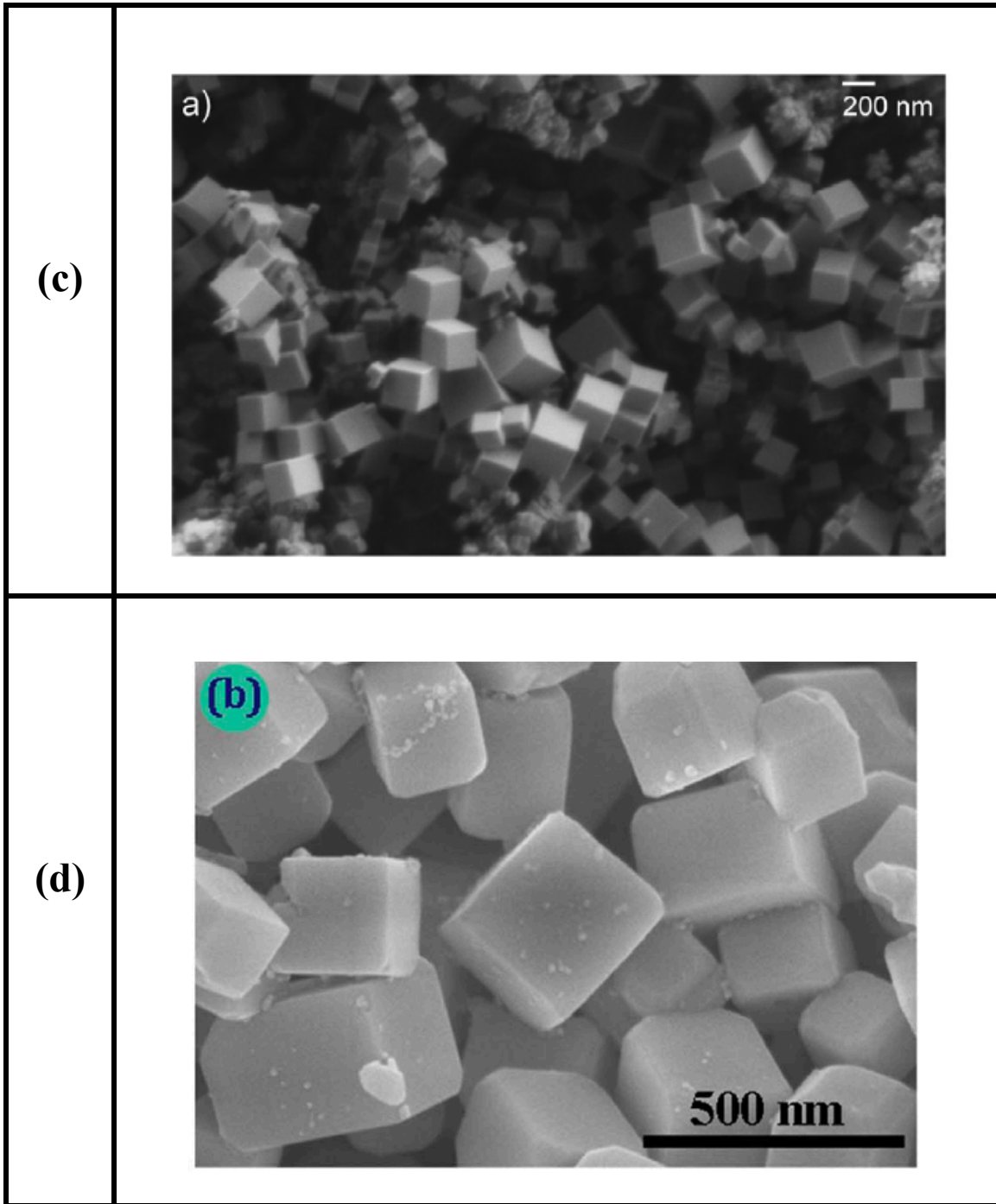


Figure 1-19. Microscopy graph examples of (a) NiFe_2O_4 porous nanocubes by Wang *et al.*; (b) MgO nanocubes by Takahashi; (c) MgO nanocubes by Issa *et al.*; (d) $\text{CaCu}_3\text{Ti}_4\text{O}_{12}$ nanocubes by Maity *et al.* (reprinted with permission from Ref. 144, 148, 149, 150). (continued)

Alkaline titanate (ATiO_3) is another family of perovskite oxides with important practical implication. Calcium titanate (CaTiO_3) is the mother mineral for perovskite prototype that has

been actively investigated due to its dielectric, catalytic and biocompatibility properties. It usually takes a rectangular prism shape when prepared hydrothermally. Crystal facets of CaTiO_3 can be tailored in poly-ethylene glycol (PEG) solutions as illustrated by Zhao *et al.*¹¹⁹ By varying the water content, temperature, reaction time and NaOH concentration, well-dispersed highly-faceted CaTiO_3 particles can be fabricated.

Barium titanate (BaTiO_3) is a well-known dielectric material widely found applications in multilayer ceramic capacitors (MLCCs), positive coefficient of resistance (PTCR) thermistors, high-performance nanocomposites, and electro-optic devices.¹²⁰⁻¹²⁴ Wada *et al.* first demonstrated the preparation of BaTiO_3 nanocubes by a solvothermal method,¹²⁰ where they used barium hydroxide ($\text{Ba}(\text{OH})_2$) and titanium dioxide (TiO_2) as the starting material. The type of solvent and the reaction temperature were shown to be the governing factors for the formation of BaTiO_3 nanocubes. According to their study, if a mixed solvent with 40 vol.% 2-methoxy ethanol and 60 vol.% ethanol is used, and the reaction temperature is over 200 °C, BaTiO_3 nanocubes with a size of 12 – 15 nm can be obtained (Figure 1-20). Sub-10 nm BaTiO_3 nanocubes have also been prepared using ethanol as the solvent and oleic acid (OLA) as the surfactant in a similar solvothermal method.¹²²

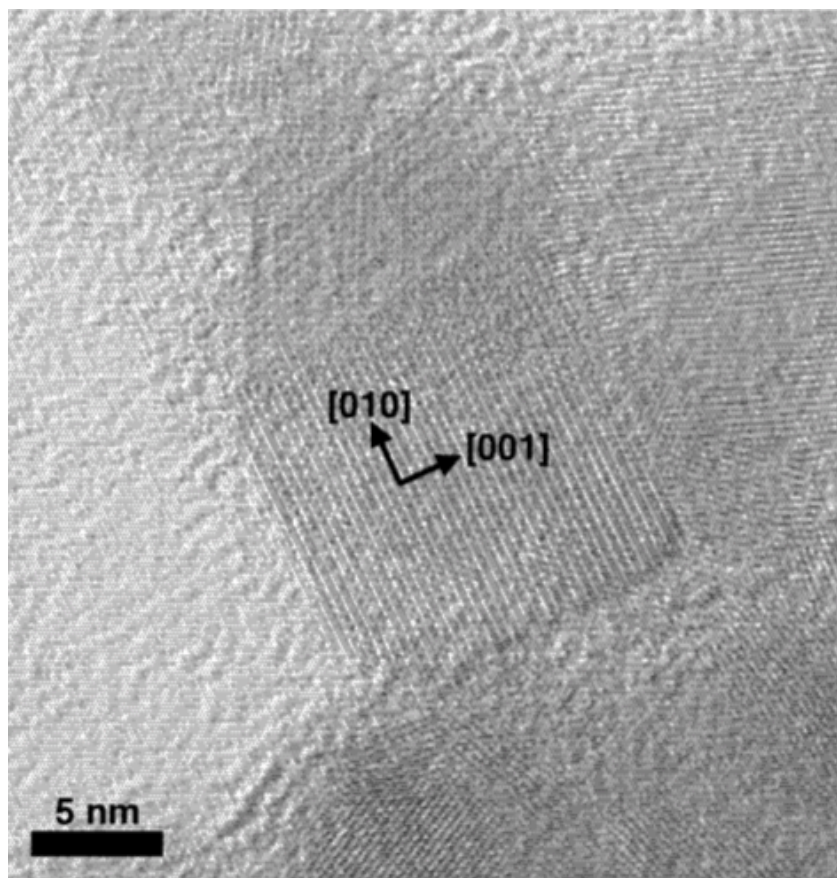


Figure 1-20. TEM micrograph of BaTiO₃ nanoparticles prepared at 240 °C for 18 hours using 40 vol.% 2-methoxy ethanol and 60 vol.% ethanol (reprinted with permission from Ref. 120).

Later, Ma *et al.* conducted a systematic study on the size of BaTiO₃ nanocubes depending on the precursor concentration and the molar ratio of the hydrothermal reaction system.¹²³ They demonstrated that with the concentration of precursors decreasing, in this case, Ba(OH)₂ and bis(ammonium lactate) titanium dihydroxide (TALH), the average size of BaTiO₃ nanocubes increases (Figure 1-21). The rate of nucleation is determined by the initial precursor concentrations, so is the number of nuclei. If a system is under high precursor concentrations, the duration for the reactant ions to reach supersaturation is short, leading to the rapid formation of nuclei then eventually, highly-populated small particles. Based on the same principle, low precursor concentrations result in fewer nuclei, which further develop into larger particles.

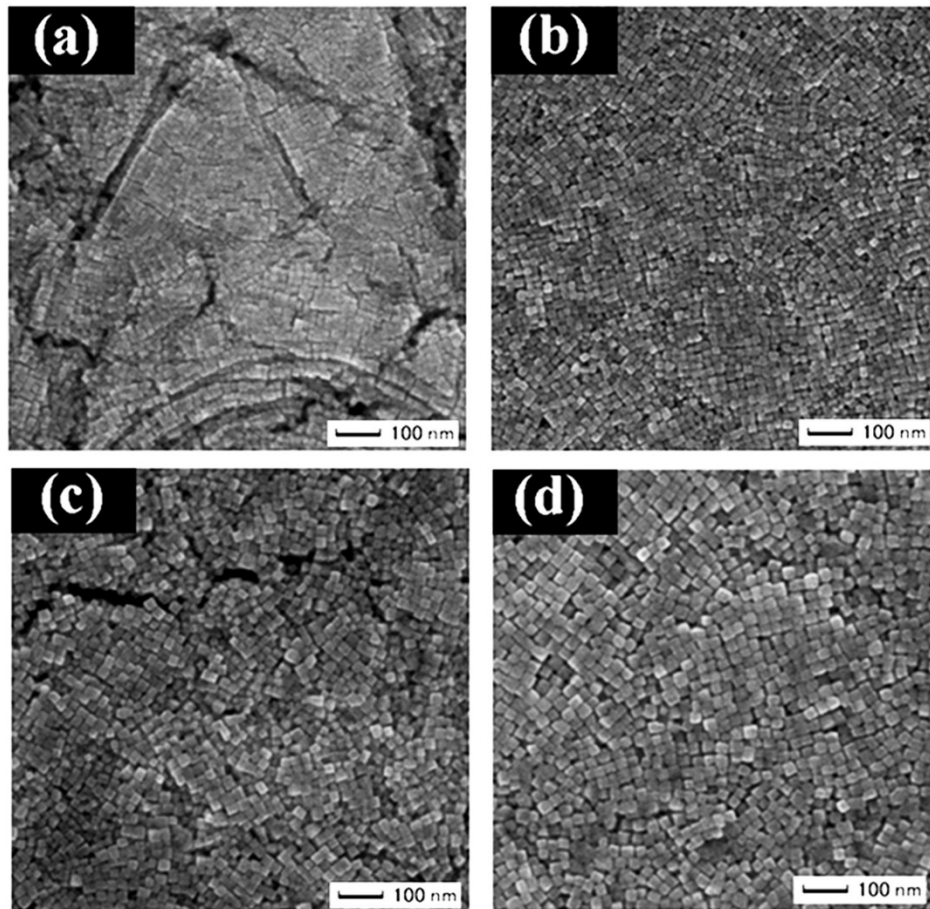


Figure 1-21. SEM micrographs of BaTiO₃ nanocubes synthesized using hydrothermal method with different precursor concentrations at 220 °C for 72 hours: (a) 0.1 M, (b) 0.05 M, (c) 0.03 M and (d) 0.025 M of Ba(OH)₂ and TALH (reprinted with permission from Ref. 123).

Besides precursor concentration, the formation of BaTiO₃ nanocubes is also strongly affected by the molar ratio between the reactant ions and the surfactants. In Ma *et al.*'s contribution, they revealed that OLA as a surfactant is critical for nanocube formation (Figure 1-22). When the molar ratio of Ba(OH)₂ : TALH : OLA was 1 : 1 : 6, cubic morphology of BaTiO₃ failed to be synthesized (Figure 1-15(a)). As the concentration of OLA increased to give a molar ratio of 1 : 1 : 18, well-dispersed nanocubes were formed (Figure 1-21(b)). This evidences that a high concentration of OLA molecules is essential for controlling the morphology of BaTiO₃ particles.

It is believed that during the crystal growth process, OLA molecules will selectively adsorb on the {100} facets through coordination with Ba metal ions, which drives the self-assembly process of nanocubes by the hydrophobic forces between the OLA molecules on adjacent BaTiO₃ nanocubes.¹²³ In addition, *tert*-butylamine as a co-surfactant, plays a positive role in the size of BaTiO₃ nanocubes. A high concentration of *tert*-butylamine in the precursor solution promotes the formation of larger-sized BaTiO₃ nanocubes by generating more OH⁻ ions in an aqueous environment to accelerate the growth of BaTiO₃ particles.¹²³

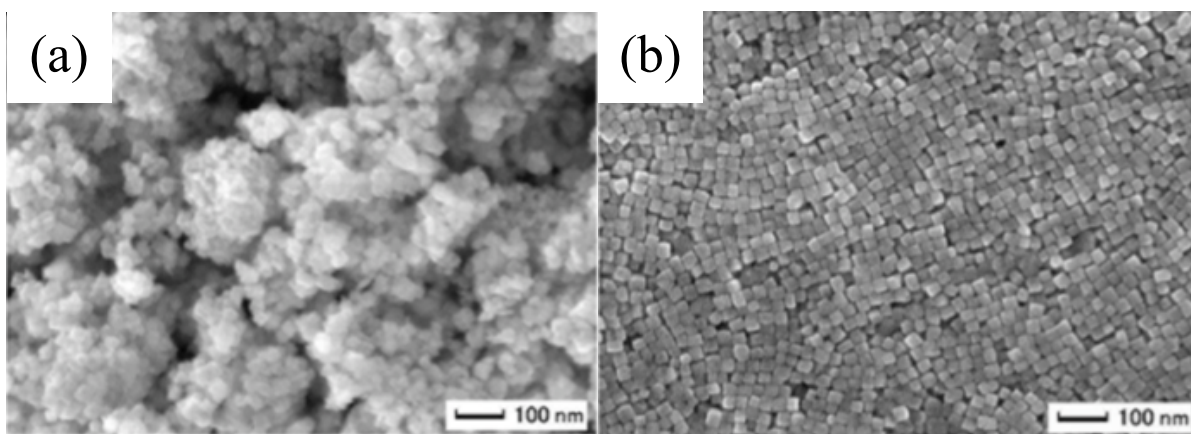


Figure 1-22. SEM micrographs of BaTiO₃ nanoparticles synthesized using hydrothermal method with different molar ratios (Ba(OH)₂ : TALH : OLA) at 220 °C for 72 hours: (a) 1 : 1 : 6 and (b) 1 : 1 : 18 (modified and reprinted with permission from Ref. 123).

Generalized growth mechanisms of BaTiO₃ nanocubes synthesized from the same hydrothermal process are well-established by Dang *et al.*¹²⁴ According to their analysis, the growth of BaTiO₃ nanocubes follows an *in-situ* mechanism, where BaTiO₃ nuclei are formed in Ti-based hydrous gel and transformed into a cubic morphology. Due to the adsorption of OLA on the metal-terminated surfaces, the as-grown nanocubes become hydrophobic in the aqueous solution and self-assembles into close-packed superlattices. Figure 1-23 provides a schematic illustration of such mechanisms.

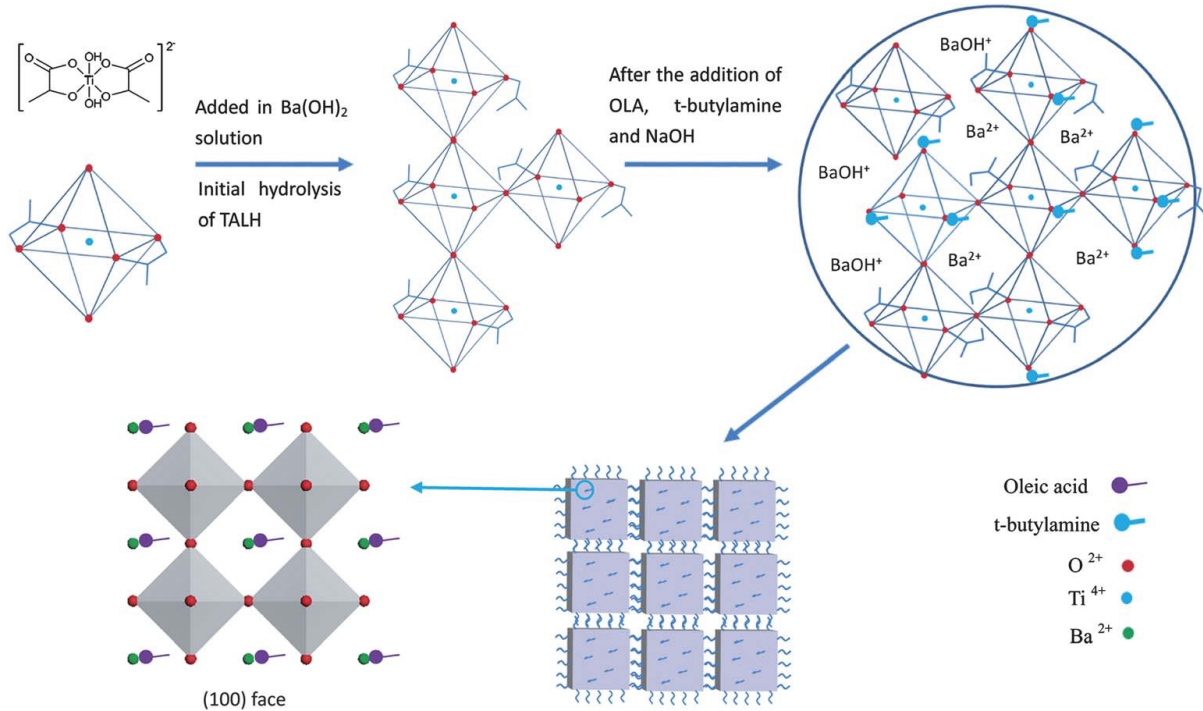


Figure 1-23. Schematic illustration of possible mechanisms (*in situ* transformation) for the development of BaTiO₃ nanocubes (reprinted with permission from Ref. 124).

In a more recent study by Sun *et al.*, detailed insights on the formation mechanisms of BaTiO₃ nanocubes were provided by a combination of experimental and computational efforts.¹²⁵ Their density functional theory (DFT) and molecular dynamics (MD) calculations indicated that hydrazine molecules adsorb preferably on the Ti position of the Ti-O terminated surface, while oleic acid molecules tend to adsorb on the Ba position of the Ba-O terminated surface. With the adsorption of hydrazine molecules, the formation of BaTiO₃ phase becomes easier based on a dissolution-precipitation process where Ba species break the Ti-O bond in a Ti-O-Ti cross-linked network formed by dissolved Ti monomers during the dehydration at a high concentration of NaOH. This further supported the experimental observations in Ma *et al.*'s article. For the formation of BaTiO₃ nanocubes, the {100} facets need to be stabilized in order for them to be

exposed in the final morphology. Because the density of Ba²⁺ ions is higher on {100} facets than other crystallographic planes, OLA molecules will therefore selectively adsorb on the {100} surfaces through intercalation with Ba²⁺ ions, stabilizing the surfaces accordingly.¹²⁵

Like BaTiO₃, the syntheses of strontium titanate (SrTiO₃) particles with well-defined shapes have also been demonstrated by a number of researchers. Nakashima *et al.* produced SrTiO₃ nanocubes with average size of 20 nm by the solvothermal method.¹²⁶ Toshima *et al.* used a self-propagating high-temperature synthesis (SHS) to obtain SrTiO₃ crystals with cubic, octahedral and multipod shapes. Souza *et al.* did a photoluminescence study on SrTiO₃ with cubic morphology fabricated by a microwave-assisted hydrothermal method.¹²⁸ However, these studies did not dig into the formation mechanisms in great detail. Calderone *et al.* reported the tailoring of size and morphology of SrTiO₃ particles by precipitation from aqueous gel suspension.¹²⁹ The size of SrTiO₃ particles can be tuned by varying the concentration of titanium precursor and the temperature. With the addition of citric acid, the morphology of SrTiO₃ particles was changed from cubic to spherical. By using high-resolution transmission electron microscopy (HRTEM), it was strongly evidenced that the observed SrTiO₃ particles were formed by the oriented aggregation of small nanocrystals (4 – 5 nm), and the particles produced in this fashion are defective as the dislocations and misalignment across the interfaces can be pictured (Figure 1-24). This formation mechanism reflects that the size and morphology of SrTiO₃ particles can be very precisely manipulated through changing the reaction conditions, including precursor concentration, temperature, and the presence of organic molecules. All these factors alter the directional aggregation process of nanocrystals.

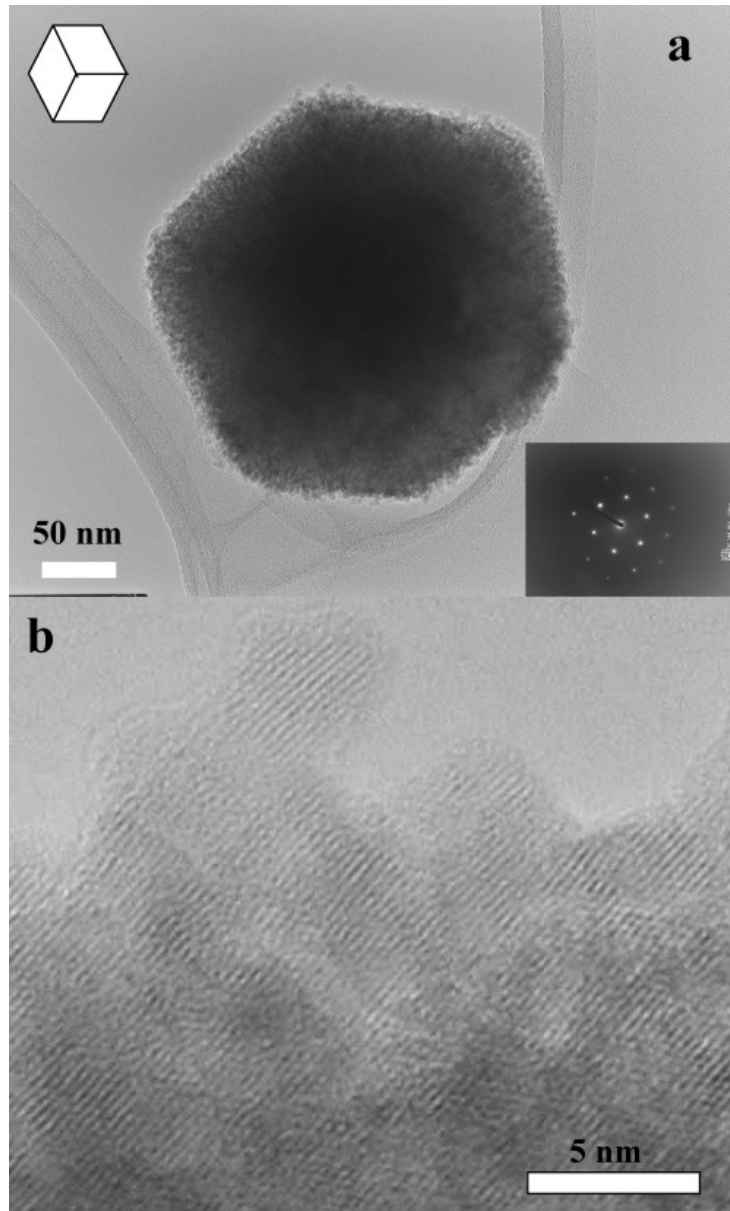


Figure 1-24. HRTEM micrographs of a cubic SrTiO_3 particle. (a) The particle shown is pictured along the body diagonal of a cube. The inset shows the electron diffraction pattern of the particle. (b) Magnified image of one edge showing dislocations and misalignments of nanocrystals across some interfaces (reprinted with permission from Ref. 129).

With the growth mechanisms of SrTiO_3 under hydrothermal conditions understood, the morphology of SrTiO_3 particles can be controlled by the concentration and the type of alcoholic surfactant, as demonstrated by Dong and Shi.¹³⁰ Their hydrothermally synthesized SrTiO_3 particles exhibit a decrease in size when the concentration of alcohols was increased. To determine

the governing mechanism for particle formation, they performed a comparative experiment by adding alcohols after the hydrolysis of titanium precursor is complete. It was found that no difference in size distribution between the particles produced by adding alcohols before and after the hydrolysis of the titanium precursor. This result supports that rather than the *in-situ* transformation of amorphous precursors to crystalline particles (refer to Figure 1-16), the growth of SrTiO₃ particles, in this case, follows a dissolution-recrystallization (precipitation) mechanism. Under this scheme, the increase in alcohol concentration improves the stability of TiO₂ hydrogel, which subsequently enhances the stability of newly formed SrTiO₃ nuclei, leading to smaller final particle sizes. Furthermore, they established a relationship between the particle morphology and the pK_a value of alcohol. With the pK_a value decreasing, the exposure of {110} facets is enriched, meaning that alcoholic molecules with lower pK_a values (i.e., “more acidic” alcohols) are more likely to attach to the {110} surfaces and stabilize it correspondingly (Figure 1-25).

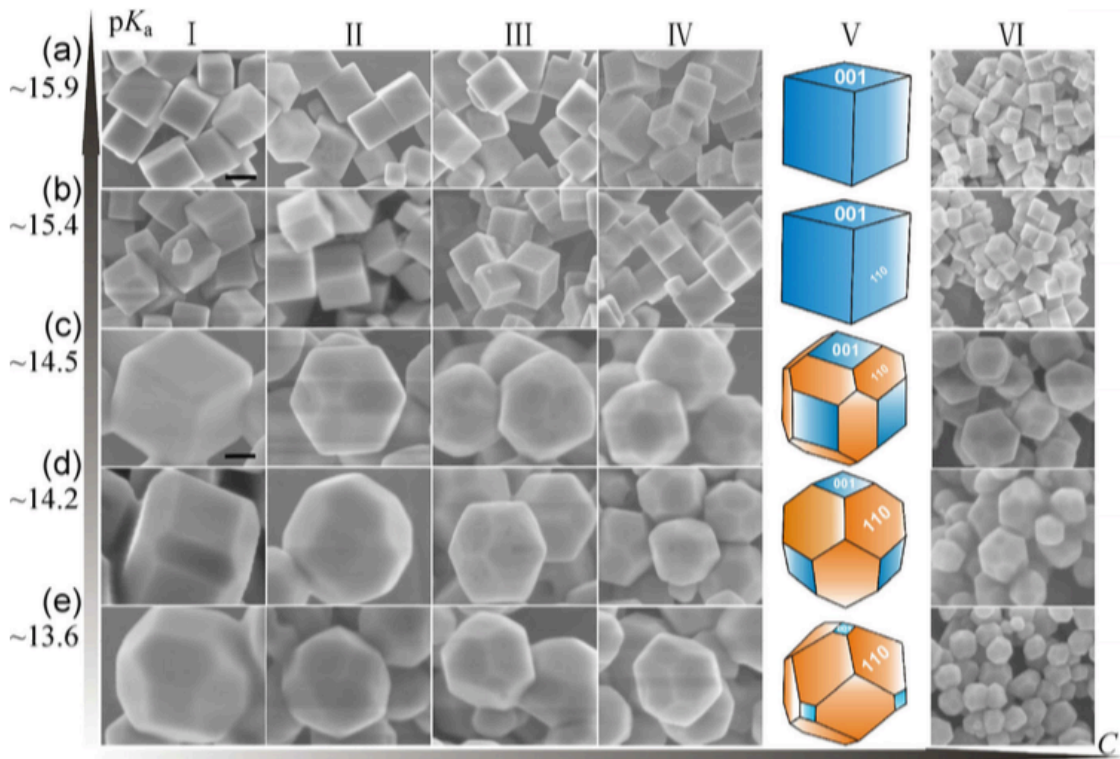


Figure 1-25. SEM micrographs of SrTiO₃ particles synthesized using alcohols with different pK_a values and concentrations. Decreasing pK_a value from top to bottom and increasing concentration from left to right (reprinted with permission from Ref. 130).

Perovskite niobates have also drawn significant research attention due to their excellent combination of ferroelectric, piezoelectric, and photocatalytic properties.¹³¹⁻¹³⁵ Wu and Xue demonstrated the preparation of NaNbO₃ microcubes using a solution-based ion exchange method.¹³³ The crystallization of NaNbO₃ particles was achieved by spontaneous ion exchange and recrystallization process, where the hydrothermally synthesized potassium niobate hollow sphere (KNHS) was used as the precursor. The metastable KNHS was then chemically activated in NaOH solution, forming NaNbO₃ microcrystals. Organic species, including ethylene glycol (EG), polyacrylamine (PA), and ethylenediamine (EN) were added separately into the system as surfactants for comparative study. With the presence of PA molecules, NaNbO₃ particles undergo a gradual morphology evolution from octahedron to cube (Figure 1-26). They believe that the

water-soluble PA molecules with multiple side functional groups promote the transportation of Nb-O species toward the growth interface by clustering the multimers in the alkaline solution. Hence, the dissolution of KNHS and the crystallization of NaNbO₃ are accelerated. In addition, PA molecules provide a surface-capping effect by selectively adsorb onto the {111} facets of NaNbO₃ particles, helping preserve its octahedral shape, although the particles transform to cubic shape over a prolonged reaction time (72 hours). Therefore, PA is considered to be dynamically beneficial in terms of opening the possibility of creating novel polyhedral shapes through precise control of its concentration as well as the reaction time. Other organic molecules investigated in their study also show effectiveness in controlling the particle morphology.

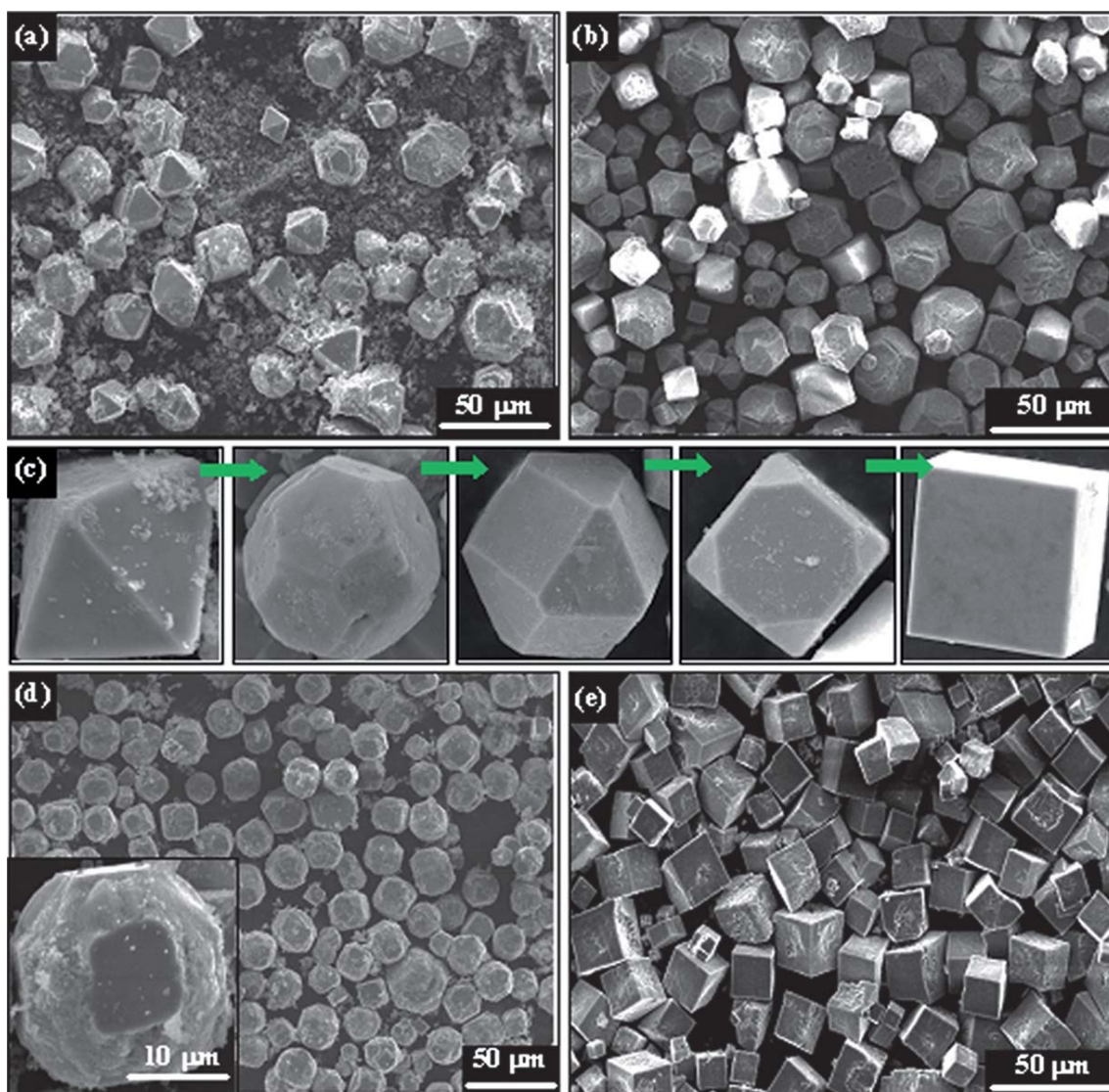


Figure 1-26. SEM micrographs of NaNbO_3 microcrystals synthesized from ion exchange reaction with different reaction conditions showing morphological evolution from octahedron to cube. KNHS = 0.12 g, H_2O = 20 mL, temperature = 180 °C, (a) PA = 0.2 g, NaOH = 1.0 M, 48 h. (b) PA = 0.2 g, NaOH = 1.0 M, 72 h. (d) PA = 0.1 g, NaOH = 2.0 M, 48 h. (e) PA = 0.1 g, NaOH = 2.0 M, 72 h (reprinted with permission from Ref. 133).

In addition to the niobates, alkaline tantalates, possessing excellent photocatalytic properties for water splitting applications, have also shown potential in tailoring their crystal facets to further enhance the photocatalytic performance, according to several studies.¹³⁶⁻¹³⁹ Hydrothermally obtained tantalate particles usually take cubic shape, indicating that the $\{100\}$

surfaces the most thermodynamically stable surface and have the slowest growth rate during crystallization. Chen *et al.* successfully tailored the morphology of submicron-sized NaTaO₃ particles from cubic to quasi-spherical by tuning the volumetric ratio between ethylene glycol and water, as well as the concentration of NaOH.¹³⁷ They synthesized NaTiO₃ particles by a solvothermal approach where tantalum (V) oxide hydrate (Ta₂O₅·*n*H₂O) and NaOH were dissolved in a composite solvent of water and EG and subsequently heated in an autoclave for the NaTiO₃ to precipitate out. The fundamentals of their morphological control strategy are established based on the Thomson-Gibbs equation, which infers that the surface energy of crystal facets is proportional to the supersaturation of crystal growth units during the growth process under a supersaturated condition.^{137,140} Therefore, the control of particle morphology can be achieved by varying the supersaturation level of the reacting species. In Chen *et al.*'s study, water acts as a “good” solvent for the growth of NaTaO₃ crystals, while EG is a “poor” solvent. By increasing the volumetric ratio of EG to water, high-energy surfaces that are generally not shown in pure water-based synthesis will be exposed due to the increase in supersaturation. As a result, NaTaO₃ particles undergo a morphology evolution from “cube → corner truncated cube → edge and corner truncated cube → sphere” with the increasing EG to water ratio (Figure 1-27).

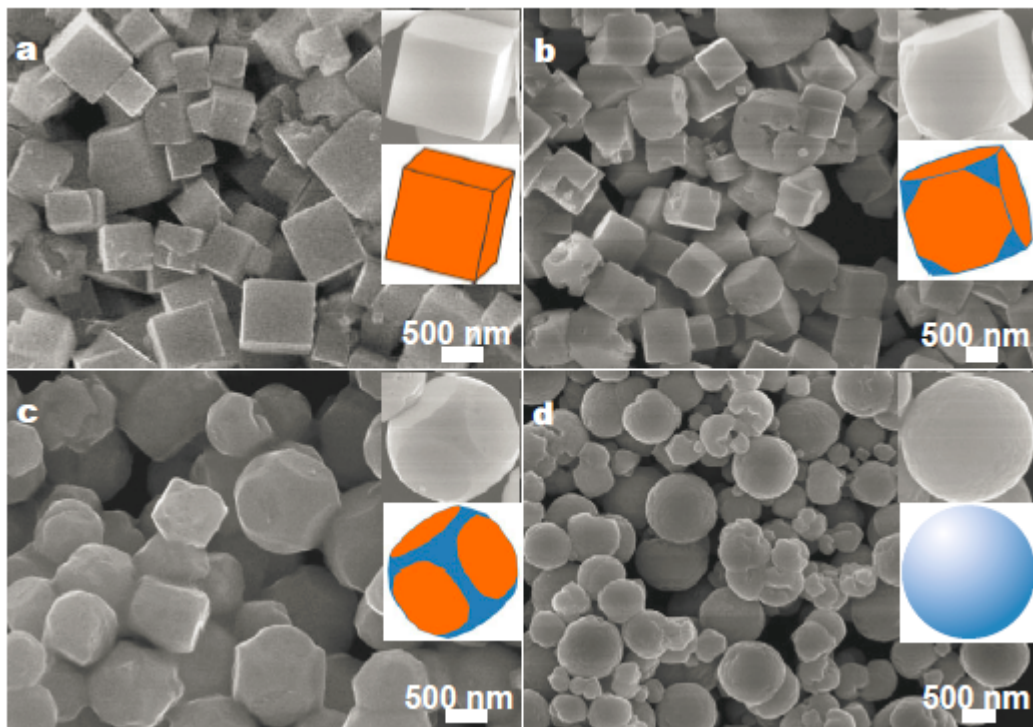


Figure 1-27. SEM micrographs of NaTaO_3 particles obtained with 10 mmol of NaOH and different volumetric ratios of EG to water: (a) 1/13. (b) 3/11. (c) 5/9. (d) 11/3 (reprinted with permission from Ref. 137).

Due to the lack of surface capping agent in their system, this morphology evolution depends solely on the EG to water ratio. The formation of unusually spherical NaTaO_3 particles clearly indicates that their crystal growth habit deviates from thermodynamic equilibrium conditions (i.e., the Wulff theorem described in the previous section). Therefore, in order to understand the formation mechanism, crystal growth kinetics need to be taken into consideration. During the growth process, two-dimensional nuclei attach to the broken bonds on the surfaces, forming the “building blocks” for the development of new surfaces. When the supersaturation is low, two-dimensional nuclei strongly favor attaching to the high-energy surfaces, where a large amount of broken bonds are present, giving them high growth rates. Low energy surfaces are therefore exposed. This condition is close to reach the thermodynamic equilibrium. In the case of

high supersaturation, the energy required for the nuclei to attach to different surfaces does not differ much, which leads to a similar growth rate among various facets, and eventually forms the spherical morphology.¹³⁷ This provides a solid support that kinetically-controlled crystal growth is able to create morphologies completely different from the thermodynamically stable shapes.

Moreover, particle morphology tailoring has also been demonstrated on various perovskite ferrites.^{141,142} The publication by Yuan *et al.* discussed the shape evolution and mechanisms of several ferrite systems synthesized by the hydrothermal method.¹⁴² The concentrations of KOH (mineralizer) and urea (surfactant) were identified as the controlling parameters for the shape evolution. For example, they graphically illustrated that PrFeO_3 crystals became truncated cubes when the urea content was increased from 1.2 g to 1.5 g (Figure 1-28(a-b)). The shape of LaFeO_3 particles changes from perfect cube to edge-truncated cube and subsequently elongated edge-truncated cube when the concentration of KOH was increased from 4.5 g to 5.5 g (Figure 1-29). These results show that the morphology evolution of perovskite ferrites originates from combined effects of KOH and urea. They concluded that NH_4^+ ions thermally decomposed from urea stabilize the $\{110\}$ facets during the growth of LaFeO_3 , while OH^- ions stabilize both $\{110\}$ and $\{002\}$ facets. NH_4^+ forms NH_3 molecules when OH^- is present, which has a similar size compared to the rare earth (RE) metal ions in ferrites. It may sit on the A-site of the lattice during the growth process, preventing continuous attachment of RE ions through the capping effect on the FeO_6 octahedron, and make the corresponding facet grow much slower than other un-capped facets (Figure 1-30).¹⁴¹ The morphology of such ferrite crystals can therefore be tailored by altering the KOH/urea ratio during synthesis. These studies give valuable insights into the facet engineering of crystals of similar types.

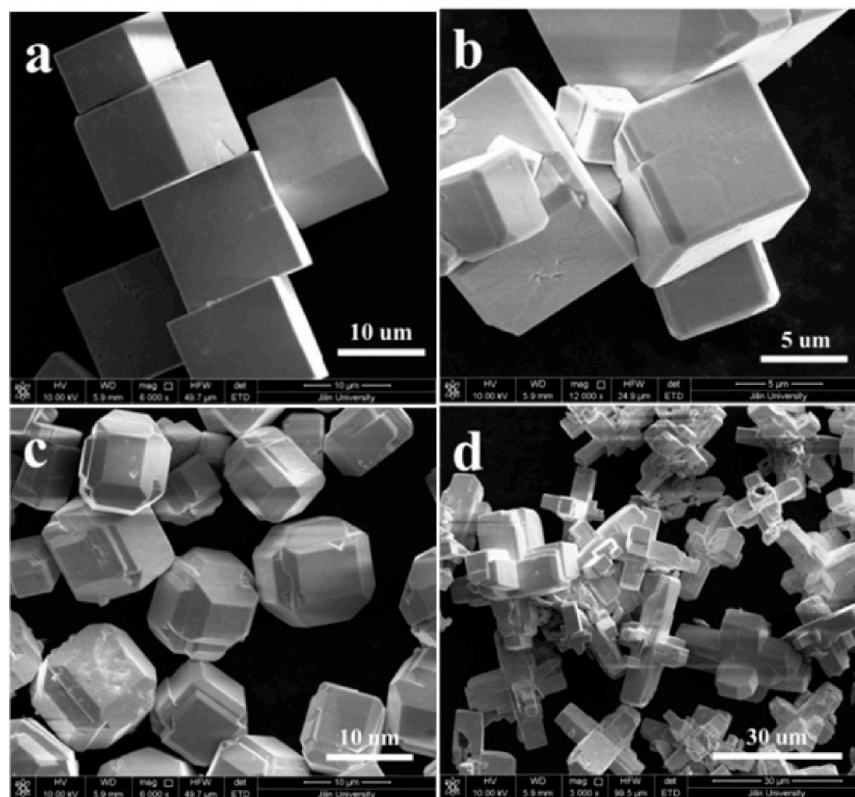


Figure 1-28. SEM micrographs of PrFeO₃ microcrystals grown under different urea concentration: (a) KOH/urea = 5.0 g/1.2 g, (b) KOH/urea = 5.0 g/1.5 g, (c) KOH/urea = 5.0 g/1.8 g, (d) KOH/urea = 5.0 g/2.0 g (reprinted with permission from Ref. 142).

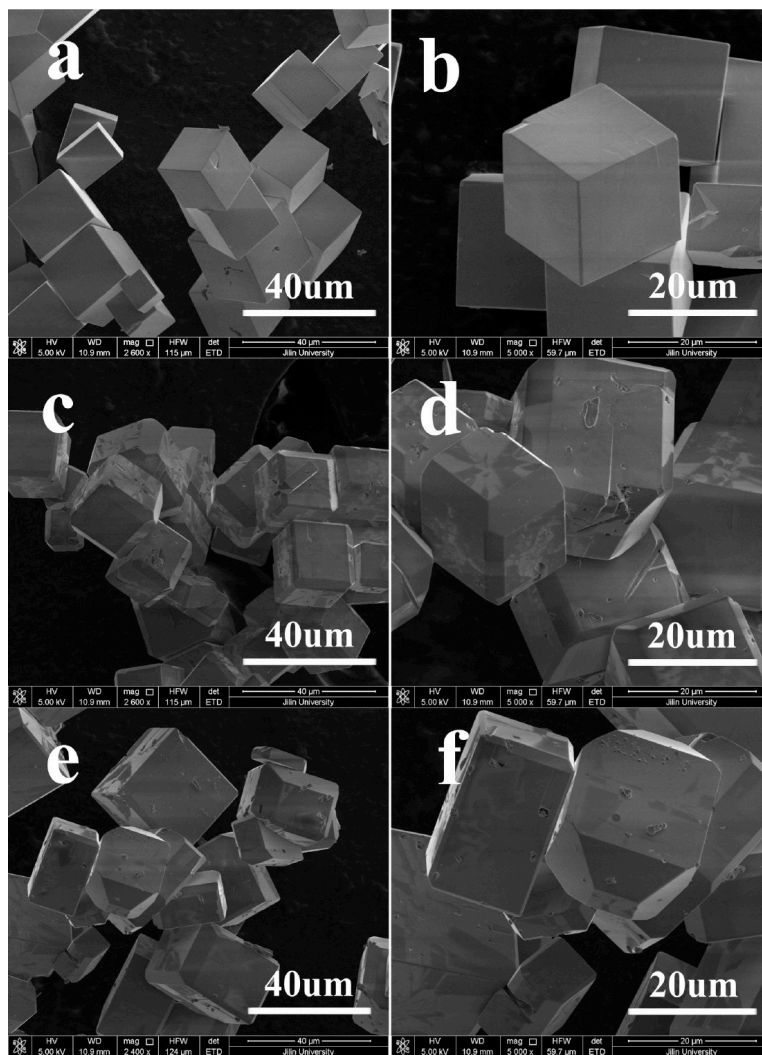


Figure 1-29. SEM micrographs of LaFeO_3 microcrystals grown with 1.5 g urea under different KOH concentrations: (a-b) 4.5 g, (c-d) 5.0 g, (e-f) 5.5 g (reprinted with permission from Ref. 142).

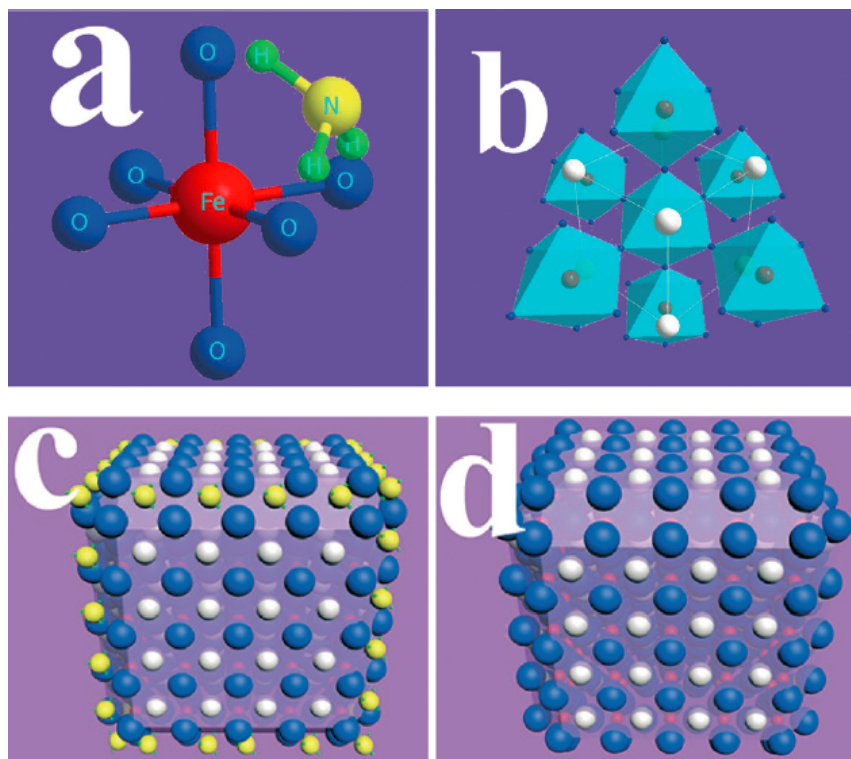


Figure 1-30. Schematic illustration of the surface capping effect of NH_3 molecules: (a) interaction between NH_3 molecule and FeO_6 octahedron, (b) relative positions of RE elements and FeO_6 octahedra in perovskite ferrite lattice, (c) attachment of NH_3 molecules to the $\{110\}$ facets of REFeO_3 and (d) resultant crystal facets of particles after growth, blue-O, yellow-N, green-H, white-Fe (reprinted with permission from Ref. 141). (With color)

In summary, facet tailoring and morphology control of functional ceramic materials can be achieved using various synthesis techniques, from low-temperature hydrothermal approach to high-temperature solid-state reactions. While thermodynamic aspects of systems (i.e., crystal structure, surface energy, reaction temperature, etc.) govern the particle shapes in equilibrium conditions, certain kinetic effects (i.e., surface capping, supersaturation, etc.) can cause dramatic changes in the growth behavior of crystals. As far as the current study is concerned, most of the previous work on the morphology control of ceramics has been focused on wet chemical processing techniques, with only a few examples demonstrating solid-state processes. With many open questions outstanding on the morphology control of particles under high-temperature/highly-

exothermic synthesizing conditions, there is plenty of room for the science and engineering community to make advancement on this topic.

1.4. Motivation of Study

The need for materials capable of withstanding extreme conditions, including hypersonic flights, rocket nozzles and scramjet components, highly corrosive and radioactive environments, etc., has been growing over the years. Both military and civil industries are seeking the next generation of refractory ceramic materials that enable better thermal protection, higher engine efficiency, and superior mechanical performances. As described in the earlier section, TaC is one such material that has a high potential to meet these demands. Therefore, understanding the scientific fundamentals for guiding its processing and engineering applications is critical.

Improving the mechanical properties of ceramics has always been the challenge and the goal of the materials community. In the case of UHTCs, their mechanical performance at elevated temperatures (e.g., creep resistance) becomes even more vital, as it determines their structural integrity over continuous high-temperature exposure and whether or not they become qualified candidates. Bulk mechanical properties are highly-relevant to the microstructures, while the microstructures correlate tightly to the initial particle characteristics, as well as the sintering steps of powders. TaC particles, due to their ultra-high melting temperature, are difficult to be sintered well using conventional sintering techniques. On one hand, an insufficient sintering temperature results in porous microstructures. Higher sintering temperature with prolonged dwelling time, however, leads to severe grain growth that is detrimental to the mechanical properties. Luckily, with the development of the spark plasma sintering technique (SPS, sometimes referred as “field-assisted sintering” or “current-assisted consolidation”), researchers are able to sinter fully-dense

UHTC bodies in a relatively short amount of time. A schematic drawing of the basic SPS configuration is shown below (Figure 1-31). In a typical sintering cycle by SPS, powder samples are pressurized between the dies (also serve as the electrodes), and a high flux of current (several kA) passes through the powders to consolidate them through Joule heating.

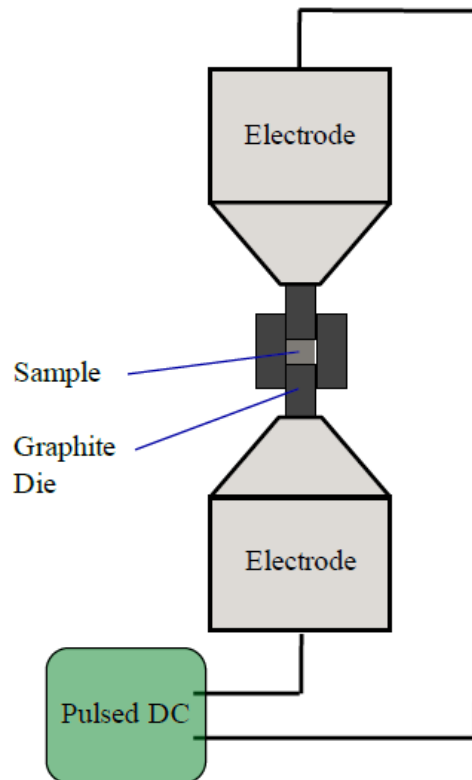


Figure 1-31. A schematic of typical SPS setup (reprinted with permission from Ref. 143).

The Joule heating induced by the pulsed direct current is essential for obtaining high sintering rates that suppress the grain growth and finally enhance the mechanical properties of the sintered body. While most of the previous research has been focused on reducing the size of grains to improve the tensile strength and fracture toughness, not much attention has been paid to the grain shape, which contributes largely to the creep behavior of ceramics. Moreover, it was found

that the grain growth is more active during the creep of bulk alumina sintered by SPS than by the conventional hot pressing.¹⁴³ That is to say, smaller grain size produced by SPS potentially accelerates diffusion-based creep. This further raises the importance of suppressing creep by hindering grain boundary sliding and dislocation movement via grain shape engineering. Therefore, as the most direct way of controlling the grain shape, particle morphology modification of the starting powder is a promising route to explore. Besides, it is also interesting to study the sintering behavior under SPS upon successful facet control of particles. As illustrated in Figure 1-32, the current pathways across the particles are expected to be very different by comparing round-shaped and highly-faceted particles.

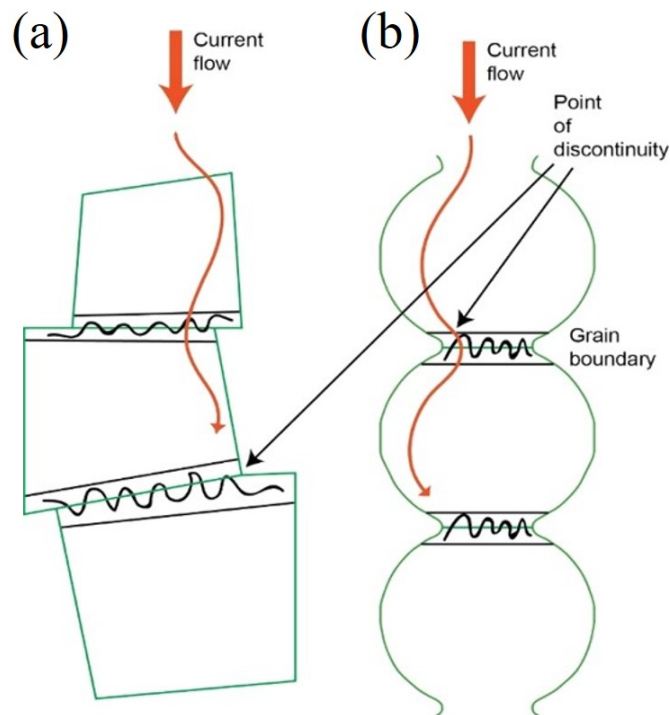


Figure 1-32. A proposed comparison of the current pathways during SPS in powders with different particle morphologies: (a) highly faceted particles, point of discontinuity at corners/edges, (b) round-shaped particles, point of discontinuity at necks/grain boundaries.

Very few works in the materials science community have been reported on how the particle morphology affects the sintering behavior. The works done by Yamamoto *et al.* and Dan *et al.* based on CeO₂ set a good starting point. Yamamoto *et al.* prepared Gd³⁺-doped CeO₂ (GDC) nanocubes exposed with highly active {001} facets by an organic-ligand-assisted hydrothermal method, in which the organic ligands selectively adsorbed on particular crystallographic plane. They observed that the nanocube NiO-GDC can be well-sintered at 200 °C lower temperature compared to the conventional NiO-GDC composite with the more stable {111} facets.¹⁵² Dan *et al.*'s work represents a more systematic study on the sintering behaviors of CeO₂ nanocubes versus conventional nanoparticles. Their results showed that the densification temperature for CeO₂ nanocubes with (100) planes exposed at the surfaces was lowered by 200 °C, which is in agreement with Yamamoto *et al.* They took a further step to calculate the surface energies and found that the (100) planes have much higher surface energy (0.455 eV Å⁻²) than the (111) plane (0.084 eV Å⁻²), which is the most critical factor they attributed for the sinterability improvement.¹⁵³ Figure 1-33 summarizes the major results from Dan *et al.* Both studies refresh the importance of the starting powder morphology towards the sintering results for such functional ceramics.

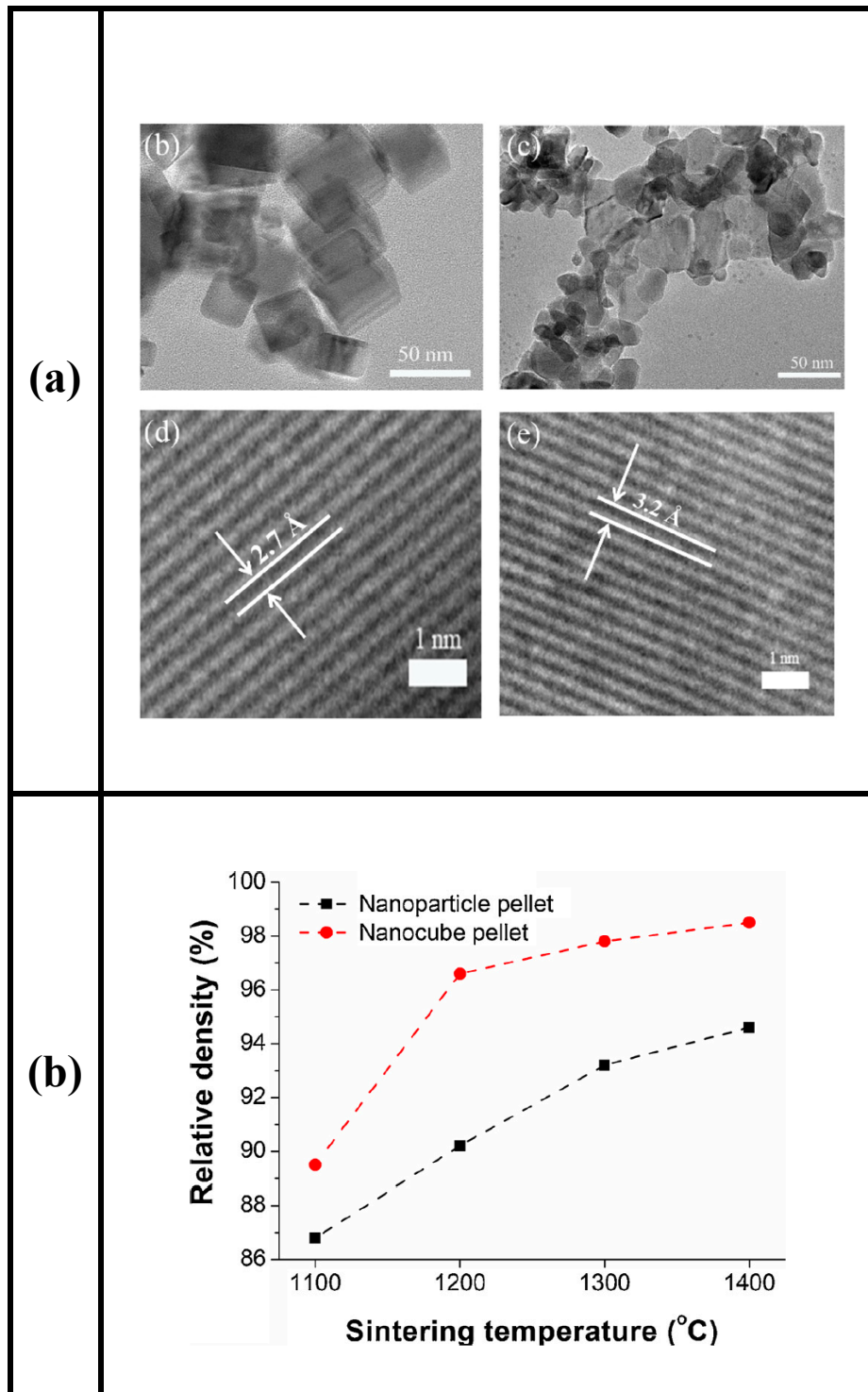


Figure 1-33. (a) TEM micrographs for the CeO₂ nanocubes (inset b and d) and conventional nanoparticles (inset c and e); (b) The relative density of CeO₂ ceramics sintered from nanocubes and conventional nanoparticles at different sintering temperatures (reprinted with permission from Ref. 153).

Recall from the literature review, most of the morphology-controlled syntheses and formation mechanisms discussed so far are based on solution-based techniques. There is still a large gap in understanding the morphology control of particles derived from fast, non-aqueous-based techniques. Questions such as “Are we able to control the morphology of particles in high-temperature solid-state synthesis?”, “What are the mechanisms behind altering the growth habit of UHTC nanoparticles?”, and “Are there any general guidelines that can be proposed to perform morphologically controlled syntheses of all types of UHTC particles?” remain in the shadow. While these questions are within the broad scope that a series of related studies aim to answer, other aspects such as catalytic and plasmonic properties have already been proven to be highly surface-dependent, as discussed in the literature review sections, elucidating the power of morphology.

In short, the current phase of the research hereby is considered a fundamental study of the growth behavior of UHTC nanoparticles. The alternation of particle morphology by dopant incorporation is experimentally explored. The mechanisms that govern the morphology alternation are proposed. Overall, this study is driven by the ultimate goal of enhancing the high-temperature mechanical performance of the sintered UHTC materials by precisely controlling the particle morphology.

1.5. References

1. G. Pulci, M. Tului, J. Tirillò, F. Marra, S. Lionetti, and T. Valente, “High Temperature Mechanical Behavior of UHTC Coatings for Thermal Protection of Re-Entry Vehicles,” *J. Therm. Spray Technol.*, **20** [1-2] 139-44 (2011).
2. J. Cotton, “Ultra-High-Temperature Ceramics,” *Adv. Mater. Processes*, **168** [6] 26-8 (2010).

3. J.B. Berkowitz-Mattuck, "High-Temperature Oxidation, IV. Zirconium and Hafnium Carbides," *J. Electrochem Soc.*, **114** [10] 1030-33 (1967).
4. W.C. Tripp and H.C. Graham, "Thermogravimetric Study of the Oxidation of ZrB_2 in the Temperature Range of 800° to 1500°C," *J. Electrochem. Soc.*, **118** [7] 1195-9 (1971).
5. L. Kaufman and H. Nesor, "Stability Characterization of Refractory Materials Under High Velocity Atmospheric Flight Conditions," Part III, Volume III: Experimental Results of High Velocity Hot Gas/Cold Wall Tests, Report AFML-TR-69-84, ManLabs, Inc., Cambridge, MA, February 1970.
6. E.V. Clougherty, R.J. Hill, W. H. Rhodes, E.T. Peters, "Research and Development of Refractory Oxidation-Resistant Diborides," Part II, Volume II: Processing and Characterization, Report AFML-TR-68-190, ManLabs, Inc., Cambridge, MA, January 1970.
7. L. Kaufman and H. Nesor, "Stability Characterization of Refractory Materials Under High Velocity Atmospheric Flight Conditions," Part II, Volume I: Facilities and Techniques Employed for Characterization of Candidate Materials, Report AFML-TR-69-84, ManLabs, Inc., Cambridge, MA, December 1969.
8. L. Kaufman and H. Nesor, "Stability Characterization of Refractory Materials Under High Velocity Atmospheric Flight Conditions," Part III, Volume I: Experimental Results of Low Velocity Cold Gas/Hot Wall Tests, Report AFML-TR-69-84, ManLabs, Inc., Cambridge, MA, December 1969.
9. E.V. Clougherty, K.E. Wilkes, and R.P. Tye, "Research and Development of Refractory Oxidation-Resistant Diborides," Part II, Volume V: Thermal, Physical, Electrical and Optical Properties, Report AFML-TR-68-190, ManLabs, Inc., Cambridge, MA, November 1969.
10. E.V. Clougherty, R.L. Pober, L. Kaufman, "Synthesis of Oxidation Resistant Metal Diboride Composites," *Trans. Met. Soc.*, **242**, 1077-82 (1968).
11. J. Salute, J. Bull, D. Rasky, and D. Keese, "SHARP-B2: Flight Test Objectives, Project Implementation and Initial Results," AIAA Paper 2001-1580, January 2001.
12. P. Kolodziej, J. Bull, J. Salute, and D.L. Keese, "First Flight Demonstration of a Sharp Ultra-High Temperature Ceramic Nostip," NASA TM 112215, December 1997.

13. J. Bull, P. Kolodziej, J. Salute, and D. Keese, "Design, Instrumentation and Preflight Testing of a Sharp Ultra-High Temperature Ceramic Nostetip," NASA TM-1998-112229, October 1998.
14. J.D. Bull, D.J. Rasky, and C.C. Karika, "Stability Characterization of Diboride Composites Under High Velocity Atmospheric Flight Conditions," *24th International SAMPE Technical Conference*, pp. T1092-1106, 1992.
15. R. Monti, M.D.S. Fumo, and R. Savino, "Thermal Shielding of a Re-Entry Vehicle by UHTC materials," *J. Thermophys. Heat Transfer*, **20** [3] 500-06 (2006).
16. N. Richet, P. Lespade, P. Goursat, and E. Laborde, "Oxidation Resistance of HfB₂-SiC Coatings for Protection of Carbon Fiber Based Composites," *Key Eng. Mater.*, **264-268** [TTP] 1047-50 (2004).
17. F. Monteverde and L. Scatteia, "Resistance to Thermal Shock and to Oxidation of Metal Diborides-SiC Ceramics for Aerospace Application," *J. Am. Ceram. Soc.*, **90** [4] 1130-8 (2007).
18. Y. Wang, W. Liu, L. Cheng, and L. Zhang, "Preparation and Properties of 2D C/ZrB₂-SiC Ultra High Temperature Ceramic Composites," *Mater. Sci. Eng. A*, **524** [1-2] 129-33 (2009).
19. F. Monteverde and R. Savino, "Stability of Ultra-High-Temperature ZrB₂-SiC Ceramics Under Simulated Atmospheric Re-Entry Conditions," *J. Eur. Ceram. Soc.*, **27** [16] 4797-805 (2007).
20. W.G. Fahrenholtz, G.E. Hilmas, I.G. Talmy, and J.A. Zaykoski, "Refractory Diborides of Zirconium and Hafnium," *J. Am. Ceram. Soc.*, **90** [5] 1347-64 (2007).
21. D.M. Van Wie, D.G. Drewry Jr., D.E. King, C.M. Hudson, "They Hypersonic Environment: Required Operating Conditions and Design Challenges," *J. Mater. Sci.*, **39** [19] 5915-24 (2004).
22. T.A. Jackson, D.R. Eklund, and A.J. Fink, "High Speed Propulsion: Performance Advantage of Advanced Materials," *J. Mater. Sci.*, **39** [19] 5905-13 (2004).
23. H.F. Jackson, D.D. Jayaseelan, W.E. Lee, M.J. Reece, F. Inam, D. Manara, C.P. Casoni, F. De Bruycker, and K. Bobridis, "Laser Melting of Spark Plasma-Sintered Zirconium Carbide: Thermophysical Properties of a Generation IV Very High-Temperature Reactor Material," *Int. J. Appl. Ceram. Technol.*, **7** [3] 316-26 (2010).

24. E.T. Curran, "Scramjet Engines: The First Forty Years," *J. Propul. Power*, **17** [6] 1138-48 (2001).
25. D.D. Jayaseelan, H. Jackson, E. Eakins, P. Brown, W.E. Lee, "Laser Modified Microstructures in ZrB₂, ZrB₂/SiC and ZrC," *J. Eur. Ceram. Soc.*, **30** [11] 2279-2288 (2010).
26. R.A. Morris, Characterization of the Microstructural Formations and Phase Transformation Pathways in Tantalum Carbides, Ph.D. Dissertation, The University of Alabama (2010).
27. K. Hackett, S. Verhoef, R.A. Cutler, and D.K. Shetty, "Phase Constitution and Mechanical Properties of Carbides in the Ta-C System," *J. Am. Ceram. Soc.*, **92** [10] 2404-7 (2009).
28. A.L. Bowman, "The Variation of Lattice Parameter with Carbon Content of Tantalum Carbide," *J. Phys. Chem.*, **65** [9] 1596-8 (1965).
29. A.I. Gusev, A.S. Kurlov, and V.N. Lipatnikov, "Atomic and Vacancy Ordering in Carbide ζ -Ta₄C_{3-x} (0.28 ≤ x ≤ 0.4) and Phase Equilibria in the Ta-C System," *J. Solid State Chem.*, **180** [11] 3234-46 (2007).
30. D.L. Price, J.M. Wills, and B.R. Cooper, "Linear-Muffin-Tin-Orbital Calculation of TaC(001) Surface Relaxation," *Phys. Rev. B*, **48** [20] 15301-10 (1993).
31. C. Fan, L. Sun, Z. Wei, M. Ma, R. Liu, S. Zeng, and W. Wang, "Valence Electronic Structure of Tantalum Carbide and Nitride," *Sci. China, Ser. G*, **50** [6] 737-41 (2007).
32. A. Vojvodic and C. Ruberto, "Trends in Bulk Electron-Structural Features of Rocksalt Early Transition-Metal Carbides," *J. Phys.: Condens. Matter*, **22** [37] 375001-10 (2010).
33. J.H. Adair and E. Suvaci, "Morphological Control of Particles," *Curr. Opin. Colloid Interface Sci.*, **5** [1-2] 160-7 (2000).
34. D.E. Grove, U. Gupta, and A.W. Castleman Jr., "Effect of Carbon Concentration on Changing the Morphology of Titanium Carbide Nanoparticles from Cubic to Cuboctahedron," *ACS Nano*, **4** [1] 49-54 (2010).
35. P.B. Merrill and S.S. Perry, "Adsorption of Water on TiC(100): Evidence for Complex Reaction and Desorption Pathways," *J. Phys. Chem. B*, **102** [39] 7606-12 (1998).

36. S.V. Didziulis, P. Frantz, S.S. Perry, O. Elbjeirami, S. Imaduddin, and P.B. Merrill, "Substrate-Dependent Reactivity of Water on Metal Carbide Surface," *J. Phys. Chem. B*, **103** [50] 11129-40 (1999).
37. P. Frantz, S.V. Didziulis, L.C. Fernandez-Torres, R.L. Guenard, and S.S. Perry, "Reaction of Methanol with TiC and VC (100) Surfaces," *J. Phys. Chem. B*, **106** [25] 6456-64 (2002).
38. L.C. Fernandez-Torres, S.S. Perry, S.V. Didziulis and P. Frantz, "The Interaction of Ammonia with Transition Metal Carbide Surfaces," *Surf. Sci.* **511** [1-3] 121-32 (2002).
39. R.L. Guenard, L.C. Fernandez-Torres, B. Kim, S.S. Perry, P. Frantz and S.V. Didziulis, "Selective Surface Reactions of Single Crystal Metal Carbides: Alkene Production from Short Chain Alcohols on Titanium Carbide and Vanadium Carbide," *Surf. Sci.* **515** [1] 103-16 (2002).
40. T. Nishinga, *Handbook of Crystal Growth*; Ch. 2. Elsevier, 2015.
41. T. Nishinga, *Handbook of Crystal Growth*; Ch. 4. Elsevier, 2015.
42. M. Yoshimura and K. Byrappa, "Hydothermal Processing of Materials, Past, Present and Future," *J. Mat. Sci.*, **43** [7] 2085-103 (2008).
43. G. Wulff, "Zur Frage der Geschwindigkeit des Wachstums und der Auflösung der Krystallflagen," *Zeits. F. Kristallog.* **34** [5-6] 449-530 (1901).
44. I. Sunagawa, "Growth and Morphology of Crystals," *Forma*, **14** [1-2] 147-66 (1999).
45. Y. Xia, Y. Xiong, B. Lim, and S.E. Skrabalak, "Shape-Controlled Synthesis of Metal Nanocrystals, Simple Chemistry Meets Complex Physics?" *Angew Chem. Int. Ed. Engl.*, **48** [1] 60-103 (2009).
46. A. Jawahar, S. Radha, and S. Vadivelan, "Connectivity-Guaranteed Hybrid Topology Management Scheme for Improving the Operational Lifetime of 3-Dimensional Wireless Sensor Networks," *Int. J. Distrib. Sens. N.*, **6** [1] 1-11 (2010).
47. P. Hartman and W.G. Perdok, "On the Relations between Structure and Morphology of Crystals. I," *Acta Cryst.*, **8** [1] 49-52 (1955).

48. J.A. McLean, K.A. Stumpo, and D.H. Russell, "Size-Selected (2-10 nm) Gold Nanoparticles for Matrix Assisted Laser Desorption Ionization of Peptides," *J. Am. Chem. Soc.*, **127** [15] 5304-5 (2005).
49. X. Li, A.E. Kuznetsov, H. Zhang, A.I. Boldyrev, L. Wang, "Observation of All-Metal Aromatic Molecules," *Science*, **291** [5505] 859-61 (2001).
50. J.D. Aiken III, R.G. Finke, "A Review of Modern Transition-Metal Nanoclusters: Their Synthesis, Characterization, and Applications in Catalysis," *J. Mol. Catal. A*, **145** [1-2] 1-44 (1999).
51. P.F. Ho and K.M. Chi, "Size-controlled Synthesis of Pd Nanoparticles from β -diketonato Complexes of Palladium," *Nanotechnology*, **15** [8] 1059-64 (2004).
52. Y. Xiong, A.R. Siekkinen, J. Wang, Y. Yin, M.J. Kim, and Y. Xia, "Synthesis of Silver Nanoplates at High Yields by Slowing Down the Polyol Reduction of Silver Nitrate with Polyacrylamide," *J. Mater. Chem.*, **17** [25] 2600-2 (2007).
53. Y. Xiong, I. Washio, J. Chen, H. Cai, Z.Y. Li, and Y. Xia, "Poly(vinyl pyrrolidone): A Dual Functional Reductant and Stabilizer for the Facile Synthesis of Noble Metal Nanoplates in Aqueous Solutions," *Langmuir*, **22** [20] 8563-70 (2006).
54. Y. Xiong, J.M. McLellan, J. Chen, Y. Yin, Z.Y. Li, and Y. Xia, "Kinetically Controlled Synthesis of Triangular and Hexagonal Nanoplates of Palladium and Their SPR/SERS Properties," *J. Am. Chem. Soc.*, **127** [48] 17118-27 (2005).
55. D.E. Grove, U. Gupta, and A.W. Castleman Jr., "Effect of Hydrocarbon on the Morphology of Synthesized Niobium Carbide Nanoparticles," *Langmuir*, **26** [21] 16517-21 (2010).
56. Z.L. Wang, "Transmission Electron Microscopy of Shape-Controlled Nanocrystals and Their Assemblies," *J. Phys. Chem. B*, **104** [6] 1153-75 (2000).
57. T.S. Ahmadi, Z.L. Wang, T.C. Green, A. Henglein, and M.A. El-Sayed, "Shape-Controlled Synthesis of Colloidal Platinum Nanoparticles," *Science*, **272** [5270] 1924-5 (1996).
58. R.S. Geonmonond, A.G.M. Da Silva, and P.H.C. Camargo, "Controlled Synthesis of Noble Metal Nanomaterials: Motivation, Principles, and Opportunities in Nanocatalysts," *An. Acad. Bras. Cienc.*, **90** [1] 719-44 (2018).
59. M.A. El-Sayed, "Some Interesting Properties of Metals Confined in Time and Nanometer Space of Different Shapes," *Acc. Chem. Res.*, **34** [4] 257-64 (2001).

60. I.O. Sosa, C. Noguez, and R.G. Barrera, "Optical Properties of Metal Nanoparticles with Arbitrary Shapes," *J. Phys. Chem. B*, **107** [26] 6269-75 (2003).
61. M. Valden, X. Lai, and W. Goodman, "Onset of Catalytic Activity of Gold Clusters on Titania with the Appearance of Nonmetallic Properties," *Science*, **281** [5383] 1647-50 (1998).
62. R. Narayanan and M.A. El-Sayed, "Catalysis with Transition metal Nanoparticles in Colloidal Solution: Nanoparticle Shape Dependence and Stability," *J. Phys. Chem. B*, **109** [26] 12663-76 (2005).
63. Y. Xiong, J. Chen, B. Wiley, and Y. Xia, "Understanding the Role of Oxidative Etching in the Polyol Synthesis of Pd Nanoparticles, with Uniform Shape and Size," *J. Am. Chem. Soc.*, **127** [20] 7332-3 (2005).
64. M. Jin, H. Zhang, Z. Xie, and Y. Xia, "Palladium Nanocrystals Enclosed by {100} and {111} Facets in Controlled Properties and Their Catalytic Activities for Formic Acid Oxidation," *Energy Environ. Sci.*, **5** [4] 6352-7 (2012).
65. Y. Sun and Y. Xia, "Shape-Controlled Synthesis of Gold and Silver Nanoparticles," *Science*, **298** [5601] 2176-9 (2002).
66. Y. Xiong, J. Chen, B. Wiley, Y. Xia, Y. Yin, and Z-Y. Li, "Size-Dependence of Surface Plasmon Resonance and Oxidation for Pd Nanocubes Synthesized via a Seed Etching Process," *Nano Lett.*, **5** [7] 1237-42 (2005).
67. Y. Xiong, H. Cai, B.J. Wiley, J. Wang, M.J. Kim, and Y. Xia, "Synthesis and Mechanistic Study of Palladium Nanobars and Nanorods," *J. Am. Chem. Soc.*, **129** [12] 3665-75 (2007).
68. Y. Xia, P. Yang, Y. Sun, Y. Wu, B. Mayers, B. Gates, Y. Yin, F. Kim, and H. Yan, "One-Dimensional Nanostructures: Synthesis, Characterization, and Applications," *Adv. Mater.*, **15** [5] 353-89 (2003).
69. X. Peng, L. Manna, W. Yang, J. Wickham, E. Scher, A. Kadavanich, and A.P. Alivisatos, "Shape Control of CdSe Nanocrystals," *Nature*, **404** 59-61 (2000).
70. J.L. Elechiguerra, J. Reyes-Gasga, and M.J. Yacaman, "The Role of Twinning in Shape Evolution of Anisotropic Noble Metal Nanostructures," *J. Mater. Chem.*, **16** [40] 3906-19 (2006).

71. B. Kim, Y. Xiong, and Y. Xia, "A Water-Based Synthesis of Octahedral, Decahedral, and Icosahedral Pd Nanocrystals," *Angew Chem. Int. Ed.*, **46** [48] 9279-82 (2007).
72. C. Li, K.L. Shuford, Q.-H. Park, W. Cai, Y. Li, E.J. Lee, and S.O. Cho, "High-Yield Synthesis of Single-Crystalline Gold Nano-Octahedra," *Angew Chem. Int. Ed.*, **46** [18] 3264-8 (2007).
73. F. Kim, S. Connor, H. Song, T. Kuykendall, and P. Yang, "Platonic Gold Nanocrystals," *Angew Chem. Int. Ed.*, **43** [28] 3673-7 (2004).
74. D. Seo, J.C. Park, and H. Song, "Polyhedral Gold Nanocrystals with O_h Symmetry: From Octahedra to Cubes," *J. Am. Chem. Soc.*, **128** [46] 14863-70 (2006).
75. S. Kundu, S. Panigrahi, S. Praharaj, S. Basu, S.K. Ghosh, A. Pal, and T. Pal, "Anisotropic Growth of Gold Clusters to Gold Nanocubes under UV Irradiation," *Nanotechnology*, **18** [7] 075712 (2007).
76. J.-E. Park, Y. Lee, and J.-M. Nam, "Precisely Shaped, Uniformly formed Gold Nanocubes with Ultrahigh Reproducibility in Single-Particle Scattering and Surface Enhanced Raman Scattering," *Nano Lett.* **18** [10] 6475-82 (2018).
77. K.M. Bratlie, H. Lee, K. Komvopoulos, P. Yang, and G.A. Somorjai, "Platinum Nanoparticle Shape Effects on Benzene Hydrogenation Selectivity," *Nano Lett.*, **7** [10] 3097-3101 (2007).
78. H. Lee, S.E. Habas, S. Kweskin, D. Butcher, G.A. Somorjai, and P. Yang, "Morphological Control of Catalytically Active Platinum Nanocrystals," *Angew Chem. Int. Ed.*, **45** [46] 7824-8 (2006).
79. Y.-W. Lee, S.-B. Han, D.-Y. Kim, and K.-W. Park, "Monodispersed Platinum Nanocubes for Enhanced Electrocatalytic Properties in Alcohol Electrooxidation," *Chem. Comm.*, **47** [22] 6296-8 (2011).
80. J. Chen, J. Mao, J. Zhao, M. Ren, and M. Wei, "Surfactant-Free Platinum Nanocubes with Greatly Enhanced Activity towards Methanol/Ethanol Electrooxidation," *RSC Adv.*, **4** [55] 28832-5 (2014).
81. M. Borah and D. Mohanta, "Composite-Hydroxide-Mediated Formation of Barium Titanate Nanocubes and Their Optical Emission Responses," *Chin. J. Phys.*, **53** [1] 020804 (2015).

82. Q. Liu, Z. Yan, G. Sun, and W. Zheng, "Solvothermal Preparation and Characterization of Barium Titanate Nanocubes," *Chem. Lett.*, **36** [3] 458-9 (2007).
83. Q. Ma and K. Kato, "Crystallographic Fusion Behavior and Interface Evolution of Mono-layer BaTiO₃ Nanocube Arrangement," *Cryst. Eng. Comm.* **18** [9] 1543-49 (2016).
84. K. Mimura and K. Kato, "Fabrication and Characterization of Barium Titanate Nanocube Ordered Assemblies on Micro-patterned Substrates," *J. Ceram. Soc. Jpn.*, **123** [7] 579-82 (2015).
85. S. Qin, D. Liu, H. Liu, and Z. Zuo, "Size-Dependent Selective Etching Mechanism: Cavity Formation on Barium Titanate Nanocubes," *J. Phys. Chem. C*, **122** [44] 17171-4 (2008).
86. S.S. Parizi, A. Mellinger, and G. Caruntu, "Ferroelectric Barium Titanate Nanocubes as Capacitive Building Blocks for Energy Storage Applications," *ACS Appl. Mater. Inter.*, **6** [20] 17506-17 (2014).
87. B. Sarkar, K. Chakrabarti, K. Das, and S.K. De, "Optical and Ferroelectric Properties of Ruthenium-doped BaTiO₃ Nanocubes," *J. Phys. D: Appl. Phys.*, **45** [50] 505304 (2012).
88. S. Wada, A. Nozawa, M. Ohno, H. Kakemoto, T. Tsurumi, Y. Kameshima, and Y. Ohba, "Preparation of Barium Titanate Nanocube Particles by Solvothermal Method and Their Characterization," *J. Mater. Sci.*, **44** [19] 5161-6 (2009).
89. G. Sreedhar, A. Sivanantham, T. Baskaran, R. Rajapandian, S. Vengatesan, L.J. Berchmans, and S.G. Babu, "A Role of Lithiated Sarcosine TFSI on the Formation of Single Crystalline SrTiO₃ Nanocubes via Hydrothermal Method," *Mater. Lett.*, **133** 127-31 (2014).
90. K. Nakashima, S. Ueno, and S. Wada, "Solvothermal Synthesis of KNbO₃ Nanocubes Using Various Organic Solvents," *J. Ceram. Soc. Jpn.*, **122** [7] 547-51 (2014).
91. K. Nakashima, S. Ueno, and S. Wada, "Microwave Synthesis of KNbO₃ Nanocubes," *J. Ceram. Soc. Jpn.*, **123** [5] 363-6 (2015).
92. Y. Yoneda, S. Kohara, K. Nakashima, H. Nagata, and S. Wada, "Local Structure Analysis of KNbO₃ Nanocubes by Solvothermal Synthesis," *Jpn. J. Appl. Phys.*, **54** [10S] 10NC01 (2015).

93. J. Feng and H.C. Zeng, "Size-Controlled Growth of Co_3O_4 Nanocubes," *Chem. Mater.*, **15** [14] 2829-35 (2003).
94. K. Kato, F. Deng, K. Mimura, Y. Kinemuchi, H. Imai, S. Wada, M. Osada, H. Haneda, and M. Kuwabara, "Nano-sized Cube-shaped Single Crystalline Oxides and Their Potentials; Composition, Assembly and Functions," *Adv. Powder Technol.*, **25** [5] 1401-14 (2014).
95. T. Taniguchi, K. Katsumata, S. Omata, K. Okada, and N. Matsushita, "Tuning Growth Modes of Ceria-Based Nanocubes by a Hydrothermal Method," *Cryst. Growth Des.*, **11** [9] 3754-60 (2011).
96. H.L. Wu, R. Sato, A. Yamaguchi, M. Kimura, M. Haruta, H. Kurata, and T. Teranishi, "Formation of Pseudomorphic Nanocages from Cu_2O Nanocrystals through Anion Exchange Reactions," *Science*, **351** [6279] 1306-10 (2016).
97. Z. Yang, Z. Zhang, K. Liu, Q. Yuan, and B. Dong, "Controllable Assembly of SnO_2 Nanocubes onto TiO_2 Electrospun Nanofibers toward Humidity Sensing Applications," *J. Mater. Chem. C*, **3** [26] 6701-8 (2015).
98. J. Zhang, S. Ohara, M. Umetsu, T. Naka, Y. Hatakeyama, and T. Adschiri, "Colloidal Ceria Nanocrystals: A Tailor-Made Crystal Morphology in Supercritical Water," *Adv. Mater.*, **19** [2] 203-6 (2007).
99. T. Xu, X. Zhou, Z. Jiang, Q. Kuang, Z. Xie, and L. Zheng, "Syntheses of Nano/Submicrostructured Metal Oxides with All Polar Surfaces Exposed via a Molten Salt Route," *Cryst. Growth Des.*, **9** [1] 192-96 (2008).
100. Z.L. Wang and X. Feng, "Polyhedral Shapes of CeO_2 Nanoparticles," *J. Phys. Chem. B*, **107** [49] 13563-6 (2003).
101. P. Li, C. Li, J. Nie, J. Ouyang, X. Liu, "Growth and Design of LaB_6 Microcrystals by Aluminum Melt Reaction Method," *Cryst. Eng. Comm.*, **15** [2] 411-20 (2013).
102. R. Ramachandran and T.T. Salguero, "Nanostructuring of Strontium Hexaboride via Lithiation," *Inorg. Chem.*, **57** [1] 4-7 (2018).
103. R. Fu, K. Chen, S. Agathopoulos, and J.M.F. Ferreira, "Factors Which Affect the Morphology of AlN Particles Made by Self-propagating High-temperature Synthesis (SHS)," *J. Cryst. Growth.*, **296** [1] 97-103 (2006).

104. G. Liu, K. Chen, H. Zhou, J. Tian, C. Pereira, and J.M.F. Ferreira, "Fast Shape Evolution of TiN Microcrystals in Combustion Synthesis," *Cryst. Growth Des.*, **6** [10] 2404-11 (2006).
105. J. Nie, Y. Wu, P. Li, H. Li, and X. Liu, "Morphological Evolution of TiC from Octahedron to Cube Induced by Elemental Nickel," *Cryst. Eng. Comm.*, **14** [6] 2213-21 (2012).
106. D. Zhou, S. Jin, Y. Li, F. Qiu, F. Deng, J. Wang, and Q. Jiang, "Effect of Stoichiometry on the Surface Energies of {100} and {111} and the Crystal Shape of TiC_x and TiN_x," *Cryst. Eng. Comm.*, **15** [4] 643-9 (2013).
107. M. Song, B. Huang, Y. Huo, S. Zhang, M. Zhang, Q. Hu, and J. Li, "Growth of TiC Octahedron Obtained by Self-propagating Reaction," *J. Cryst. Growth.*, **311** [2] 378-82 (2009).
108. S. Jin, P. Shen, Q. Lin, L. Zhan, and Q. Jiang, "Growth Mechanism of TiC_x during Self-propagating High-temperature Synthesis in An Al-Ti-C System," *Cryst. Growth Des.*, **10** [4] 1590-7 (2010).
109. S. Jin, P. Shen, D. Zhou, and Q. Jiang, "Self-propagating High-temperature Synthesis of Nano-TiC_x particles with Different Shapes by Using Carbon Nano-tube as C Source," *Nanoscale Res. Lett.*, **6** [1] 515 (2011).
110. D. Aquilano, F. Otálora, L. Pastero, J.M. García-Ruiz, "Three Study Cases of Growth Morphology in Minerals: Halite, Calcite and Gypsum", *Prog. Cryst. Growth Ch.*, **62** [2] 227-51 (2016).
111. N. Radenović, D. Kaminski, W. van Enkevort, S. Graswinckel, I. Shah, M. in 't Veld, R. Algra, and E. Vlieg, "Stability of the Polar {111} NaCl Crystal Face," *J. Chem. Phys.*, **124** [16] 164706 (2006).
112. N. Radenović, W. van Enkevort, and E. Vlieg, "Formamide Adsorption and Habit Changes of Alkali Halide Crystals Grown from Solutions," *J. Cryst. Growth*, **263** [1-4] 544-51 (2004).
113. E.R. Townsend, W.J.P. van Enchevort, J.A.M. Meijer, and E. Vlieg, "Polymer versus Monomer Action on the Growth and Habit Modification of Sodium Chloride Crystals," *Cryst. Growth Des.*, **15** [11] 5375-81 (2015).
114. R. Boistelle and B. Simon, "Épitaxies de CdCl₂, 2NaCl, 3H₂O sur les faces (100), (110) et (111) des cristaux de chlorure de sodium," *J. Cryst. Growth*, **26** [1] 140-6 (1974).

115. S. Jin, P. Shen, D. Zhou, and Q. Jiang, "A Common Regularity of Stoichiometry-Induced Morphology Evolution of Transition Metal Carbides, Nitrides, and Diborides during Self-Propagating High-Temperature Synthesis," *Cryst. Growth Des.*, **12** [6] 2814-24 (2012).
116. K. Huang, L. Yuan, and S. Feng, "Crystal Facet Tailoring Arts in Perovskite Oxides," *Inorg. Chem. Front.*, **2** [11] 965-81 (2015).
117. M. Yao, Q. Li, G. Hou, C. Lu, B. Cheng, K. Wu, G. Xu, F. Yuan, F. Ding, and Y. Chen, "Dopant-Controlled Morphology Evolution of WO₃ Polyhedra Synthesized by RF Thermal Plasma and Their Sensing Properties," *ACS Appl. Mater. Inter.*, **7** [4] 2856-66 (2015).
118. H. Zhao, Y Duan, and X. Sun, "Synthesis and Chatacterization of CaTiO₃ Particles with Controlled Shape and Size," *New J. Chem.*, **37** [4] 986-91 (2013).
119. Z. Sun, L. Zhang, F. Dang, Y. Liu, Z. Fei, Q. Shao, H. Lin, J. Guo, L. Xiang, N. Yerra, and Z. Guo, "Experimental and Simulation-Based Understanding of Morphology Controlled Barium Titanate Nanoparticles under Co-adsorption of Surfactants," *Cryst. Eng. Comm.*, **19** [24] 3288-98 (2017).
120. S. Wada, M. Ohno, T. Hoshima, Y. Kameshima, Y. Ohba, H. Kakemoto, and T. Tsurumi, "Prepration of Barium Titanate Nanocube Particles by Solvothermal Method and Their Characterization," *2007 Sixteenth IEEE Symposium on the Application of Ferroelectrics*, 531-4 (2007).
121. J. Zhou and Z. Yang, "Solvothermal Growth of Sub-10 nm Monodispersed BaTiO₃ Nanocubes," *Cryst. Eng. Comm.*, **15** [44] 8912-4 (2013).
122. Q. Ma, K. Mimura, and K. Kato, "Diversity in Size of Barium Titanate Nanocubes Synthesized by a Hydrothermal Method Using An Aqueous Ti Compound," *Cryst. Eng. Comm.*, **16** [36] 8398-405 (2014).
123. F. Dang, K. Mimura, K. Kato, H. Imai, S. Wada, H. Haneda and M. Kuwabara, "In situ Growth BaTiO₃ Nanocubes and Their Superlattice from An Aqueous Process," *Nanoscale*, **4** [4] 1344-9 (2012).
124. Z. Sun, L. Zhang, F. Dang, Y. Liu, Z. Fei, Q. Shao, H. Lin, J. Guo, L. Xiang, N. Yerra, and Z. Guo, "Experimental and Simulation-Based Understanding of Morphology Controlled Barium Titanate Nanoparticles under Co-adsorption of Surfactants," *Cryst. Eng. Comm.*, **19** [24] 3288-98 (2017).

125. K. Nakashima, M. Kera, I. Fujii, and S. Wada, "A New Approach for the Preparation of SrTiO₃ Nanocubes," *Ceram. Int.*, **39** [3] 3231-4 (2013).
126. T. Toshima, H. Ishikawa, S. Tanda, and T. Akiyama, "Multipod Crystals of Perovskite SrTiO₃," *Cryst. Growth Des.*, **8** [7] 2066-9 (2008).
127. A.E. Souza, G.T.A. Santos, B.C. Barra, W.D. Macedo, Jr, S.R. Teixeira, C.M. Santos, A.M.O.R. Senos, L. Amaral, and E. Longo, "Photoluminescence of SrTiO₃: Influence of Particle Size and Morphology," *Cryst. Growth Des.*, **12** [11] 5671-9 (2012).
128. V.R. Calderone, A. Testino, M.T. Buscaglia, M. Bassoli, C. Bottino, M. Viviani, V. Buscaglia, and P. Nanni, "Size and Shape Control of SrTiO₃ Particles Grown by Epitaxial Self-Assembly," *Chem. Mater.*, **18** [6] 1627-33 (2006).
129. L. Dong, H. Shi, K. Cheng, Q. Wang, W. Weng, and W. Han, "Shape-Controlled Growth of SrTiO₃ Polyhedral Submicro/Nanocrystals," *Nano Res.*, **7** [9] 1311-8 (2014).
130. C. Yan, L. Nikolova, A. Dadvand, C. Harnagea, A. Sarkissian, D.F. Perepichka, D. Xue, and F. Rosei, "Multiple NaNbO₃/Nb₂O₅ Heterostructure Nanotubes, A New Class of Ferroelectric/Semiconductor Nanomaterials," *Adv. Mater.*, **22** [15] 1741-5 (2010).
131. Y. Saito, H. Takao, T. Tani, T. Nonoyama, K. Takatori, T. Homma, T. Nagaya, and M. Nakamura, "Lead-Free Piezoceramics," *Nature*, **432** 84-7 (2004).
132. J. Wu and D. Xue, "Crystallization of NaNbO₃ Microcubes by A Solution-Phase Ion Exchange Route," *Cryst. Eng. Comm.*, **13** [11] 3773-81 (2011).
133. Q. Ding, Y. Yuan, X. Xiong, R. Li, H. Huang, Z. Li, T. Yu, Z. Zou, and S. Yang, "Enhanced Photocatalytic Water Splitting Properties of KNbO₃ Nanowires Synthesized through Hydrothermal Method," *J. Phys. Chem. C*, **112** [48] 18846-8 (2008).
134. K. Saito and A. Kudo, "Niobium-Complex-Based Syntheses of Sodium Niobate Nanowires Possessing Superior Photocatalytic Properties," *Inorg. Chem.*, **49** [5] 2017-9 (2010).
135. Y. He, Y. Zhu, and N. Wu, "Synthesis of Nanosized NaTaO₃ in Low Temperature and Its Photocatalytic Performance," *J. Solid State Chem.*, **177** [11] 3868-72 (2004).

136. W. Chen, Q. Kuang, and Z. Xie, "Morphology Evolution of NaTaO₃ Submicrometer Single-Crystals: from Cubes to Quasi-Spheres," *Sci. China Mater.*, **58** [4] 281-8 (2015).
137. X. Li and J. Zang, "Facile Hydrothermal Synthesis of Sodium Tantalate (NaTaO₃) Nanocubes and High Photocatalytic Properties," *J. Phys. Chem. C*, **113** [45] 19411-8 (2009).
138. J. Shi, G. Liu, N. Wang, and C. Li, "Microwave-Assisted Hydrothermal Synthesis of Perovskite NaTaO₃ Nanocrystals and Their Photocatalytic Properties," *J. Mater. Chem.*, **22** [36] 18808-13 (2012).
139. H. Lin, Z. Lei, Z. Jiang, C. Hou, D. Liu, M. Xu, Z. Tian, and Z. Xie, "Supersaturation-Dependent Surface Structure Evolution: From Ionic, Molecular to Metallic Micro/Nanocrystals," *J. Am. Chem. Soc.*, **135** [25] 9311-4 (2013).
140. C. Hou, W. Feng, L. Yuan, K. Huang, and S. Feng, "Crystal Facet Control of LaFeO₃, LaCrO₃ and La_{0.75}Sr_{0.25}MnO₃," *Cryst. Eng. Comm.*, **16** [14] 2874-7 (2014).
141. L. Yuan, K. Huang, S. Wang, C. Hou, X. Wu, B. Zou, and S. Feng, "Crystal Shape Tailoring in Perovskite Structure Rare-Earth Ferrites REFeO₃ (RE = La, Pr, Sm, Dy, Er, and Y) and Shape-Dependent Magnetic Properties of YFeO₃," *Cryst. Growth Des.*, **16** [11] 6522-30 (2016).
142. J.T. Cahill, *A Study on the Phase Stability and Diffusion Behavior of Alkaline-Earth Hexaborides*; Ph.D. Dissertation. University of California, San Diego, (2016).
143. E. Karamian, A. Bataille, and A. Monshi, "Comparison of Creep Behaviour in Alumina Based Ceramics Densified by SPS and HP," *Mater. Ceram.*, **63** [2] 251-5 (2011).
144. X.-F. Wang, W. Ma, F. Jiang, E.-S. Cao, K.-M. Sun, L. Cheng, and X.-Z. Song, "Prussian Blue Analog Derived Porous NiFe₂O₄ Nanocubes for Low-Concentration Acetone Sensing at Low Working Temperature," *Chem. Eng. J.*, **338** 504-12 (2018).
145. Z. Li, S. Yan, M. Sun, H. Li, Z. Wu, J. Wang, W. Shen, and Y.Q. Fu, "Significantly Enhanced Temperature-Dependent Selectivity for NO₂ and H₂S Detection Based on In₂O₃ Nano-Cubes Prepared by CTAB Assisted Solvothermal Process," *J. Alloys Compd.*, **816** 152518 (2020).

146. S. Senapati and K.K. Nanda, "MgO Nanocubes as Self-Calibrating Optical Probes for Efficient Ratiometric Detection of Picric Acid in the Solid State," *ACS Sustainable Chem. Eng.*, **6** [11] 13719-29 (2018).
147. S. Stankic, M. Muller, O. Diwald, M. Sterrer, E. Knozinger, and J. Bernardi, "Size-Dependent Optical Properties of MgO Nanocubes," *Angew. Chem. Int. Ed.*, **44** 4917-20 (2005).
148. N. Takahashi, "Simple and Rapid Synthesis of MgO with Nano-Cube Shape by Means of a Domestic Microwave Oven," *Solid State. Sci.*, **9** 722-4 (2007).
149. I. Issa, J. Amodeo, J. Rethore, L. Joly-Pottuz, J. Morthomas, M. Perez, J. Chevalier, and K. Masenelli-Varlot, "In Situ Investigation of MgO Nanocube Deformation at Room Temperature," *Acta. Mater.*, **86** 295-304 (2015).
150. S. Maity, M. Samanta, A. Sen, and K.K. Chattopadhyay, "Investigation of Electrochemical Performance of Ceramic Oxide $\text{CaCu}_3\text{Ti}_4\text{O}_{12}$ Nanostructures," *J. Solid State Chem.*, **269** 600-7 (2019).
151. G.-S. Jang, S. Ameen, A. Shaheer Akhtar, and H.-S. Shin, "Cobalt Oxide Nanocubes as Electrode Material for the Performance Evaluation of Electrochemical Supercapacitor," *Ceram. Int.*, **44** [1] 588-95 (2018).
152. K. Yamamoto, T. Hashishin, M. Matsuda, N. Qiu, Z. Tan, and S. Ohara, "High-Performance Ni Nanocomposite Anode Fabricated from Gd-Doped Ceria Nanocubes for Low-Temperature Solid-Oxide Fuel Cells," *Nano Energy*, **6** 103-8 (2014).
153. X. Dan, C. Wang, X. Xu, X. Cheng, M. Fronzi, L. Bi, and X.S. Zhao, "Improving the Sinterability of CeO_2 by Using Plane-Selective Nanocubes," *J. Eur. Ceram. Soc.*, **39** [14] 4429-34 (2019).

Chapter 2

Experimental Procedure

2.1. Experimental Design

Due to the exploratory nature of this work, experiments were designed in such a way that a variety of material systems were proposed and tested in the first place in order to narrow down to the best dopant candidates for controlling the morphology of TaC nanoparticles. Dopants that have been screened in the current study are highlighted in the Periodic Table below (Figure 2-1).

Figure 2-1 shows the Periodic Table of Elements. The elements highlighted in the table are: Ti (Yellow), Nb (Red), Hf (Red), Zr (Red), Y (Red), Ta (Red), Fe (Green), Co (Green), Ni (Green). The legend indicates the format for element information: Atomic Number, Name, Symbol, and Atomic Weight.

Figure 2-1. The Periodic Table highlighting the elements been screened as the dopants for morphology modification of TaC nanoparticles. Red: dopants showing no effect; Green: dopants showing effectiveness; Yellow: dopant showing effectiveness when co-doped with Ni. (With color)

After the rough screening, those dopant elements showing certain effectiveness in the morphology modification of TaC nanoparticles (i.e., induce facet development of particles) were further evaluated in detail by varying their concentrations. Table 2-1 lists the samples being investigated with their corresponding dopant type and concentrations, including the initial concentration during precursor powder mixing and the final concentration remaining in the

products. To ensure the repeatability of experiments and statistical reliability, the synthesis of each sample was repeated at least two times.

Table 2-1. List of major TaC-based samples investigated in this study.

Dopant Type	Sample ID	Initial Dopant Conc. (at.%)	Final Dopant Conc. (at.%)	Detailed Analysis?
None	TaC-1	0	0	No
	TaC-2*	0	0	Baseline
Zr	Zr-1	10	N/A	No
	Zr-2	15	N/A	No
Hf	Hf-1	10	N/A	No
	Hf-2	15	N/A	No
Nb	Nb-1	10	4.4	No
	Nb-2	15	7.8	No
	Nb-3	20	14.3	No
Ti	Ti-1	10	8.1	No
	Ti-2	15	15.4	No
Y	Y-1	10	0.6	Yes
	Y-2	15	1.0	Yes
	Y-3	20	1.3	Yes
	Y-4	25	1.6	Yes
	Y-5	30	2.3	Yes
Ni	Ni-1	5	0.9	Yes
	Ni-2	10	1.4	Yes
	Ni-3	15	1.7	Yes
	Ni-4	20	2.5	Yes
	Ni-5	25	4.1	Yes
	Ni-6	30	5.7	Yes
Co	Co-1	5	0.9	Yes
	Co-2	10	1.6	Yes
	Co-3	15	1.9	Yes
	Co-4	20	2.3	Yes
	Co-5	25	2.6	Yes
	Co-6	30	3.4	Yes
Fe	Fe-1	3	0.5	Yes
	Fe-2	5	1.2	Yes
	Fe-3	10	2.1	Yes
	Fe-4	15	2.7	Yes
	Fe-5	20	4.0	Yes
	Fe-6	25	4.2	Yes

Table 2-1. List of major TaC-based samples investigated in this study. (continued)

Dopant Type	Sample ID	Initial Dopant Conc. (at.%)	Final Dopant Conc. (at.%)	Detailed Analysis?
Fe	Fe-7	30	4.8	Yes
Ni-Ti**	NiTi-1	3	2.2	Yes
	NiTi-2	5	4.1	Yes
	NiTi-3	10	8.0	Yes
	NiTi-4	15	12.4	Yes
	NiTi-5	20	16.4	Yes
	NiTi-6	25	18.5	Yes

* TaC-2 is undoped TaC sample with reaction diluent added during combustion.

** Dopant concentration is based on Ti with fixed amount of Ni.

2.2. Synthesis of Carbide Particles

The synthesis of TaC particles is based on a modified solvothermal method developed by Kelly *et al.*^{1,2} Tantalum (V) chloride (TaCl₅, 99.8%, anhydrate, Sigma-Aldrich, No. 14614) and carbon black (>99.9%, power, Alfa Aesar, No. 39724) were used as the metal and carbon sources. Lithium granules (Li, 99%, Sigma-Aldrich, No. 499811) were employed as the non-aqueous solvent and reductant, according to the following reaction:



The amount of each component was calculated based on a 3-gram theoretical yield of TaC, while two times of excess carbon and lithium were used to ensure phase purity. For different dopant systems, metallic nickel (Ni, 99.9% metals basis, powder, Alfa Aesar, No. A17943), iron (Fe, >99.9% metals basis, powder, Sigma-Aldrich, No. 267953), cobalt (Co, >99.9% metals basis, powder, Sigma-Aldrich, No. 697745), titanium (Ti, 99.5%, metals basis, powder, Alfa Aesar, No. 43102), niobium (Nb, 99.9%, metals basis, Alfa Aesar, No. 11548), and yttrium (Y, 99.6%, powder, Alfa Aesar, No. 44147) were added as a part of the precursor powders. Their amounts were varied

based on different atomic ratios between the dopant and the host, as tabulated in Table 2-1. It should be noted that the actual dopant concentration in the product is generally much lower than the amount of precursor added due to limited dopant solubility and the homogeneity of solid-state reactions. To avoid the thermodynamic roughening of particles, the maximum flame temperature during reaction must be lowered. Therefore, 30 wt.% of pure TaC powders (99.5%, Alfa Aesar) were added as the reaction diluent. The precursors, excluding Li granules, were weighted and thoroughly ground manually with mortar and pestle in an argon-protected glovebox for at least 15 minutes to create a homogeneous mixture. Sufficient amounts of Li granules were then added into the quartz test tube containing the precursor mixture. The test tube was rolled to ensure that the surfaces of the Li granules were fully covered with precursor powders and temporarily sealed with a Parafilm® before being transferred out of the glovebox for preheating and ignition. To initialize the reaction, a volumetric external heating apparatus was custom-made using a stainless-steel hollow cylinder wrapped with a dual-element high-temperature heating tape. The setup was preheated to ~400 °C in order for the reaction to occur. This also helps improve the phase purity of the reaction product by avoiding degradation of the precursors by prolonged pre-ignition period. To minimize oxidation during the reaction, the test tube was flushed with ultra-high purity argon gas 5 times before being inserted into the heating cylinder. The tube was then capped by a rubber stopper and connected to a vacuum pump for outgassing. The reaction self-ignited once the powder mixture was heated to a critical temperature that was high enough to melt the Li granules. Due to the highly exothermic nature of the formation of TaC, the reaction was able to sustain itself until most of the reacting species were consumed. The duration of reaction was less than 40 seconds. Figure 2-2(a) is a schematic of the solvothermal reaction mechanism, while Figure 2-2(b) provides the time-lapse photographs during the actual reaction. Note that the reaction shown

in Figure 2-2(b) was done in a high-temperature silicone bath instead of the stainless-steel heating apparatus. This is for visualized illustration purpose only. The system was then air-cooled to room temperature. The post-reaction products were rinsed using deionized water to dissolve excess lithium, followed by two wash cycles using hydrochloric acid (HCl, 25 vol%). Within each acid wash cycle, 15 minutes of magnetic stirring and 30 minutes of ultrasonication were included for the thoroughness of washing and particle deagglomeration. Acid-washed powders were cleaned one more time using deionized water and finally rinsed with ethanol. The resulting powders were collected for analysis after 24 hours of drying in the air (Figure 2-3).

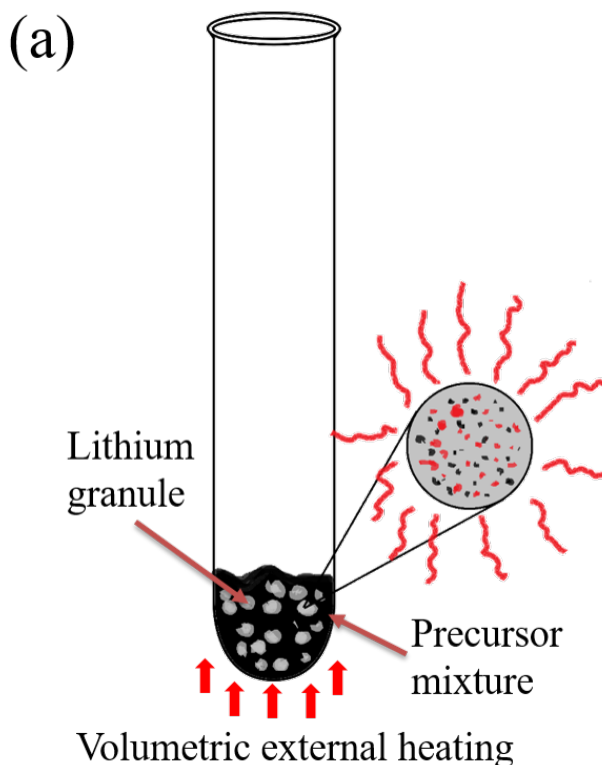
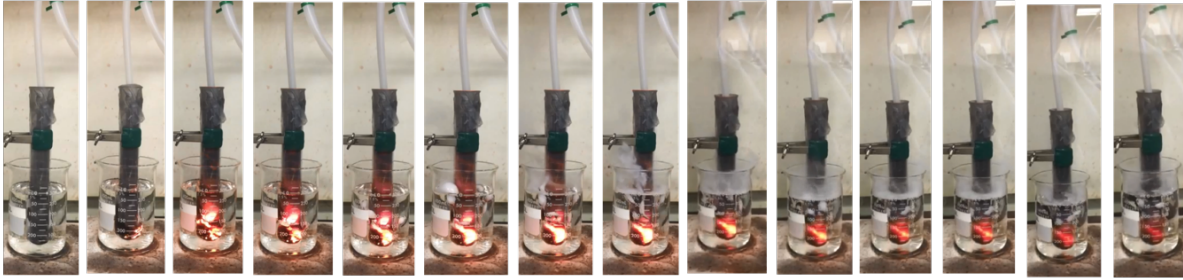


Figure 2-2. Illustration of TaC-forming reaction. (a) Schematics of the solvothermal reaction. Ta and C atoms bond in molten lithium to form TaC in a highly-exothermic way. (b) Time-lapse photographs of the actual reaction. Note that for demonstration purpose the reaction shown in the photo took place in a heated silicone oil. All other reactions for the fabrication of samples took place in a heated stainless-steel cylinder, as described above.

(b)



Reaction time: 30~40s \longrightarrow Max. flame temp $> 2000^{\circ}\text{C}$

Figure 2-2. Illustration of TaC-forming reaction. (a) Schematics of the solvothermal reaction. Ta and C atoms bond in molten lithium to form TaC in a highly-exothermic way. (b) Time-lapse photographs of the actual reaction. Note that for demonstration purpose the reaction shown in the photo took place in a heated silicone oil. All other reactions for the fabrication of samples took place in a heated stainless-steel cylinder, as described above. (continued)

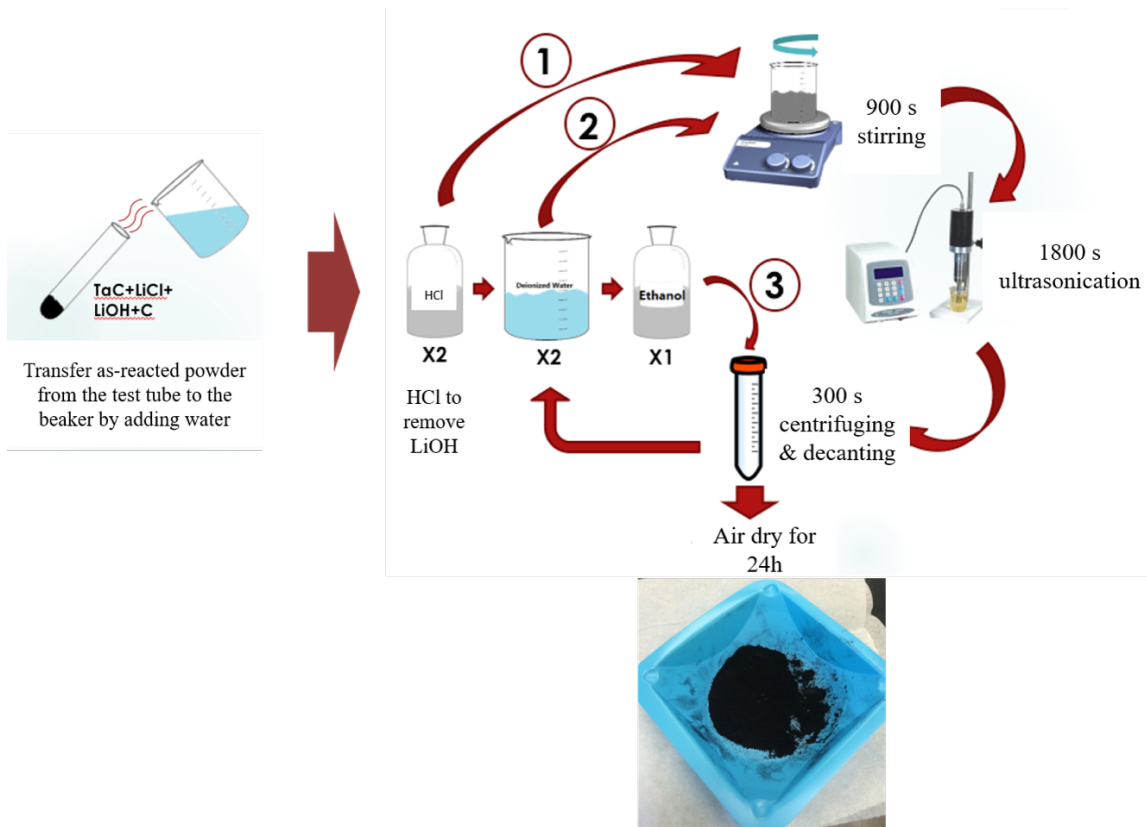


Figure 2-3. Detailed powder washing procedures with a photograph of actual TaC sample produced.

The techniques depicted here can be universally applied to synthesize other ultra-high temperature TMCs, including ZrC, NbC, HfC, VC, etc., although synthesis/washing parameters may vary.

2.3. Analytical Techniques

The phase purity of samples was analyzed by X-ray diffraction (XRD, Bruker D2 Phaser, Germany) using Cu-K α radiation. The general morphology of particles was imaged by field-emission scanning electron microscopy (Apreo SEM, ThermoFisher Scientific, Hillsboro, OR, USA). For each SEM characterization, a small amount of synthesized powder sample was dispersed in deionized water and ultrasonicated for 15 minutes. A few drops of the slurry were drip onto a silicon substrate, and subsequently dried in the air prior to imaging. Elemental composition characterization was performed by energy dispersive spectroscopy (EDS) embedded in the Apreo SEM and X-ray photoelectron spectroscopy on a custom designed system (SPECS Surface Nano Analysis GmbH, Berlin, Germany) equipped with a PHOIBOS 150 WAL analyzer with DDL-2 detector and a FOCUS 500/600 ellipsoidal monochromatic X-ray source with a dual anode of Al and Ag. The elemental surface compositions are calculated by deconvolution of individual peak on survey spectra using CasaXPS software. To statistically describe the morphological modification, particles were evaluated based on multiple SEM images taken at three different SEM sessions for each sample. At least 300 particles were counted and justified after each microscopy imaging session, which totals at least 900 particles for each sample. This ensures the randomness of measurement, as well as statistically significant sampling. For each dopant precursor concentration, two individual batches of powder were synthesized and characterized using identical procedures to confirm the repeatability of the results.

This chapter, in part, has been accepted for publication titled “Morphology Control of Tantalum Carbide Nanoparticles through Dopant Additions” in the Journal of Physical Chemistry C, 2021, where the dissertation author was the primary investigator and the co-first author of this paper. The paper is co-authored by R. Tran (co-first author), S. Lee, A. Bandera, M. Herrera, X.-G. Li, S.P. Ong, and O.A. Graeve.

2.4. References

1. J.P. Kelly and O.A. Graeve, “Statistical Experimental Design Approach for the Solvothermal Synthesis of Nanostructured Tantalum Carbide Powders,” *J. Am. Ceram. Soc.*, **94** [6] 1706-15 (2011).
2. J.P. Kelly, R. Kanakala, and O.A. Graeve, “A Solvothermal Approach for the Preparation of Nanostructured Carbide and Boride Ultra-High-Temperature Ceramics,” *J. Am. Ceram. Soc.*, **93** [10] 3035-8 (2010).

Chapter 3

Dopant-Dependent Morphology Selectivity of Tantalum Carbide Particles

3.1. Brief Introduction

TaC is an ultra-high temperature transition metal carbide (UHT-TMCs) with its properties holding great engineering relevance under harsh environments. Its high melting temperature (~ 4100 K) and exceptional hardness are attributed to its predominant Ta-C covalent bonds within its rock-salt structure.¹⁻³ Practical applications of TaC at high temperatures is limited due to the degradation of mechanical properties caused by porosity, and other microstructural defects, as well as problems connected to oxidation and creep deformation. Improvement of properties begins with control of powder size and shape. For example, the work by Kim *et al.* reported the formation of dense bodies via the sintering of TaC nanoparticles can largely eliminate the porosity.⁴ This is due to the increase in its surface area-to-volume ratio as the powder becomes finer, allowing closer packing of particles, and thus near theoretical density and grain growth prevention. It is possible to increase the amount of close-packing by using cubic particles instead of the rounded morphology observed by Kim *et al.*, thereby bringing its density even closer to the theoretical values. Researchers have also looked into improving the sinterability of ceramic powders by using cubic-shaped nanoparticles.⁵ In the work done by Dan *et al.*, the sintering temperature of CeO₂ ceramic was substantially reduced to 1200 °C when ceria nanocubes were used as the raw powder, compared to 1400 °C for the conventional nanopowder. They attributed the improved sinterability to the exposure of {100} planes, which possess higher surface energy than the more typical {111} planes and cause faster grain growth of nanocubes.

Several studies have also explored nanoparticle morphology control to exploit the high surface area-to-volume ratio in other applications such as catalysis and chemical sensing, whereby

specific facets, such as those with steps and kinks, will better facilitate chemical reactions than others.⁶⁻⁸ As such, there have been a good number of experimental and computational studies exploring morphology modification. A few experimental efforts have explored shape change in carbides with cubic crystal structure as a function of carbon stoichiometry or characteristics of carbon precursor molecules, which influenced the relative growth rate of the dominant {111} and {100} facets.⁹⁻¹¹ In addition, previous studies using density functional theory (DFT) explored molecular adsorption of H₂O on ZrC to obtain cubes and octahedrons and carbon adsorption on Ru to produce nanorods.^{12,13} Strain effects had also been explored as parameters for morphological modifications on Cu and Ni particles, with the increasing strain shown to increase the coverage of facets containing step sites.¹⁴

Recently, doping has been suggested as a possible driving forces to form nanocubes in ceramic materials. For transition metal dopants, the interactions between the *d*-orbitals of dopants and the anionic *p*-orbitals of the non-metallic elements in ceramics are thought to promote adsorption on the {100} facets, especially for metallic dopants with high carbon solubility.^{8,9} With this in mind, the morphology transition of particles from octahedrons to cuboids with an increasing dopant concentration was successfully demonstrated for Cr-doped WO₃ and Ni-doped TiC.^{7,8} However, the fundamental principles behind dopant-induced morphological selectivity and control remains largely in the shadow.

TaC nanoparticles can be successfully synthesized via a modified solvothermal method,²⁰ however, it still lacks means to control its particle shape and obtain highly-faceted/cubic morphologies. Following the success of previous studies, it is presented hereby, for the first time, a combined experimental and computational effort that demonstrates and explains the shape selectivity and morphology evolution of TaC particles using different dopants. A self-sustaining

high-temperature reaction based on the non-aqueous solvothermal method is used to synthesize doped TaC particles of different polyhedron shapes. SEM images and XRD patterns were used to identify the content and shape of the particles synthesized, while XPS and EDS results are coupled with DFT calculations to explore the underlying principles behind dopant shape selectivity and morphology evolution. Through a thorough analysis, it is shown that morphology modification results from a combination of dopant segregation towards the surface in the $\{111\}$ facets, the sub-surface segregation in the $\{100\}$ facets, and dopant interaction with surface carbon through $p-d$ orbital hybridization. These mechanisms will lower the surface energy, which will suppress the crystal growth and facilitate the formation of polyhedrons. Doping with Fe and Y, and Ni-Ti co-doping results in cubes and cuboctahedrons, while Co and Ni doping selectively forms faceted polyhedrons. This study seeks to provide critical insights into controlling and optimizing the yield of ceramic nanoparticle powders of desired shapes such as cubes and cuboctahedrons, which have exceptional potential in tuning the desired properties of ceramic materials. It should be also noted that the understanding of such solid-state dopant-induced morphology selectivity is still shallow due to the highly exploratory nature of the study. More material systems need to be both experimentally and computationally probed to establish broader knowledge foundation in the scientific communities. This chapter will focus on describing the logics behind the dopant choices, as well as the detailed results and analysis of the interplay between the dopants and TaC particle morphologies.

3.2. Rationale of Dopant and Precursor Selection

To alter the shape of synthetic nanoparticles, a number of knobs can be tuned, including the stoichiometry, local bonding environment, surface characteristics, synthesis media, etc. Chapter 1 can be referred for a detailed explanation regarding the mechanisms for controlling the

morphology of nanoparticles. To isolate the effects of the reaction environment and carbide stoichiometry, a number of synthesis cycles were performed based on the undoped TaC samples. The corresponding results will be elaborated in later sections. For the doped TaC samples, yttrium was chosen to be the first dopant candidate due to relatively large difference in the ionic radii between Y^{3+} (104 Å) and Ta^{4+} (82 Å). The hypothesis is that with larger dopant ions incorporated into TaC lattices, the local bonding environment between tantalum and carbon atoms changes to some extent, leading to a deviated crystal growth behavior, which eventually tailors the particle morphology.

The question then becomes: what is the most suitable reaction precursor to deliver yttrium to the TaC matrix without substantial formation of secondary phases? Yttrium salts, including yttrium nitrate [$Y(NO_3)_3$, hexahydrate, Sigma Aldrich, 237957] and yttrium chloride (YCl_3 , anhydrous, Sigma Aldrich, 451363) were initially attempted to be the yttrium source. However, it turned out that the use of yttrium salts led to significant oxidation and sub-stoichiometric TaC_{1-x} phases after the high-temperature reactions. Figures 3-1 to 3-3 show the XRD patterns for the Y-doped TaC samples with 15 at% calculated amount of yttrium addition. It can be clearly observed from the patterns that noticeable amounts of tantalum oxides and sub-stoichiometric TaC_{1-x} phases were present in the final products.

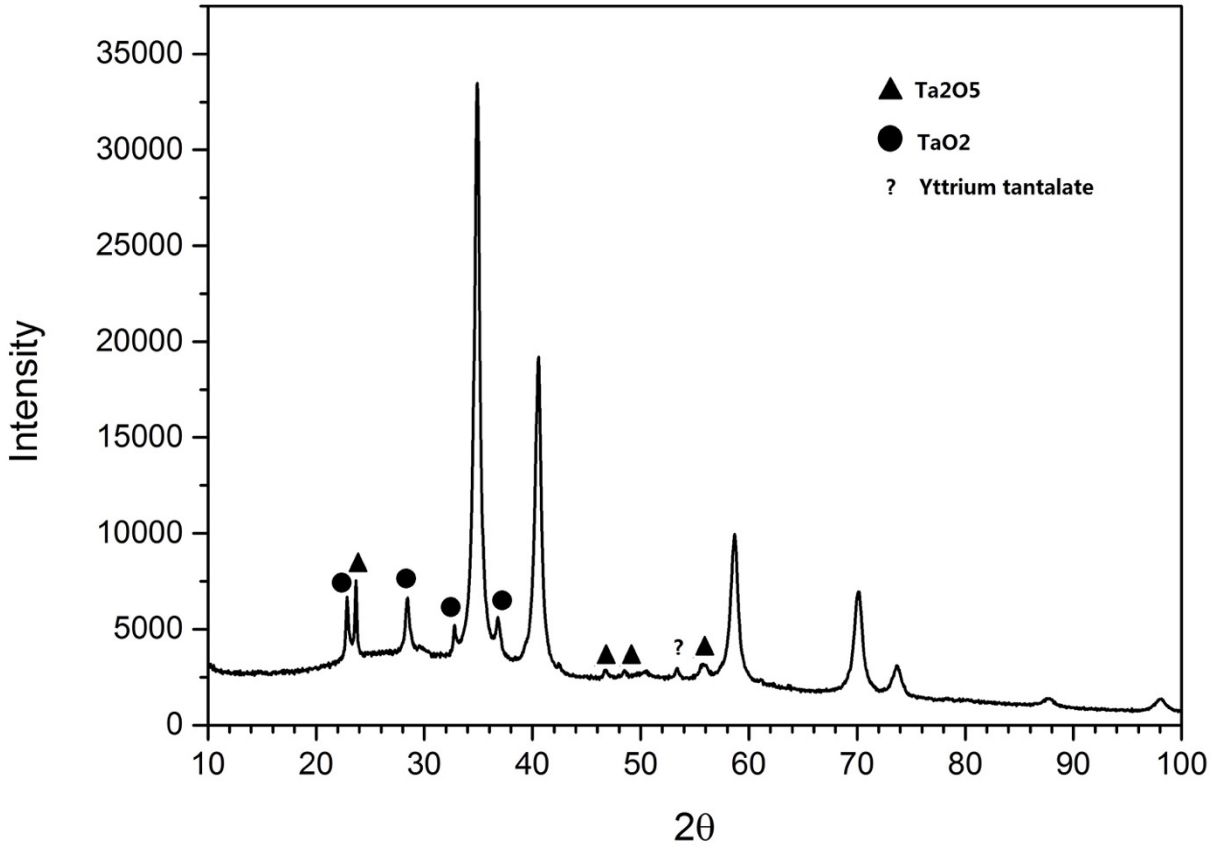


Figure 3-1. X-ray diffraction pattern of Y-doped TaC sample with 15 at% calculated Y amount using yttrium nitrate as the precursor.

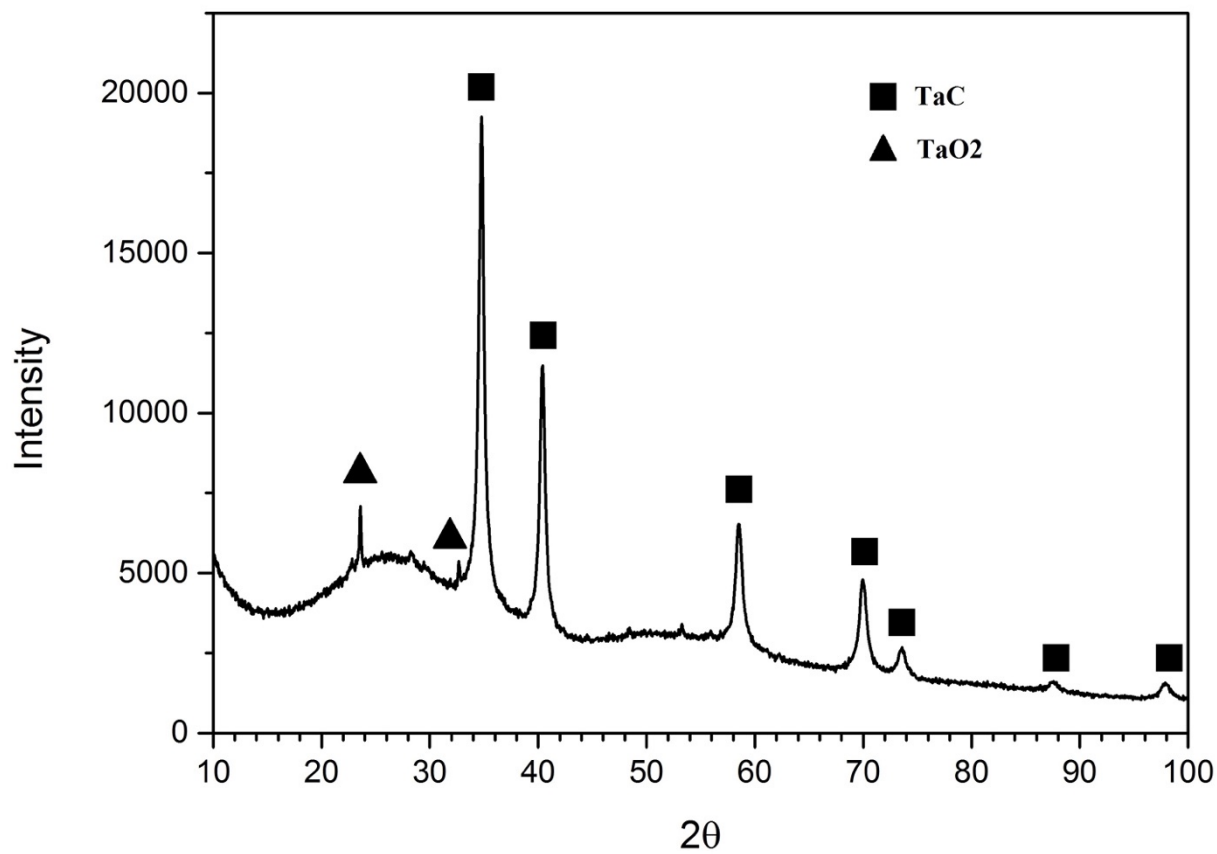


Figure 3-2. X-ray diffraction pattern of Y-doped TaC sample with 15 at% calculated Y amount using yttrium chloride as the precursor. Note the hump at the lower diffraction angles signals the presence of amorphous oxide phases.

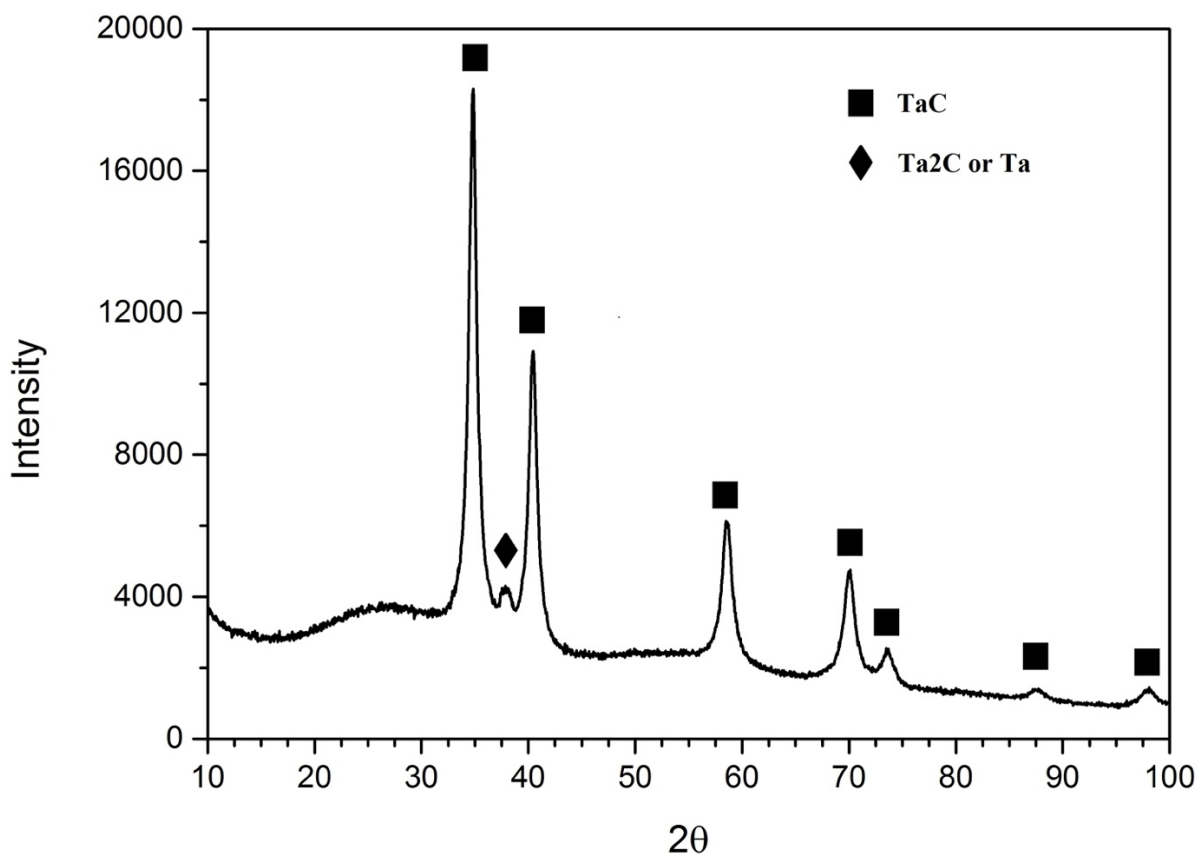


Figure 3-3. X-ray diffraction pattern of Y-doped TaC sample with 15 at% calculated Y amount using yttrium chloride as the precursor synthesized through improved reaction setups.

Maintaining the phase purity of near-stoichiometric TaC powders is critical for avoiding confusion during particle identification under electron microscope. Tantalum oxides and sub-stoichiometric TaC_{1-x} phases are difficult to be removed through the powder washing steps, as they hardly dissolve in water or acids. To address this issue, metallic yttrium powder was employed to substitute yttrium salts as the precursor based on the expectation that it is less chemically reactive at high temperature compared to yttrium salts. As a result, lesser amount of impurity phases were detected by XRD (Figure 3-4). Nevertheless, it will be described in the following sections that doping with Y still faces challenges in defining the facets of TaC particles.

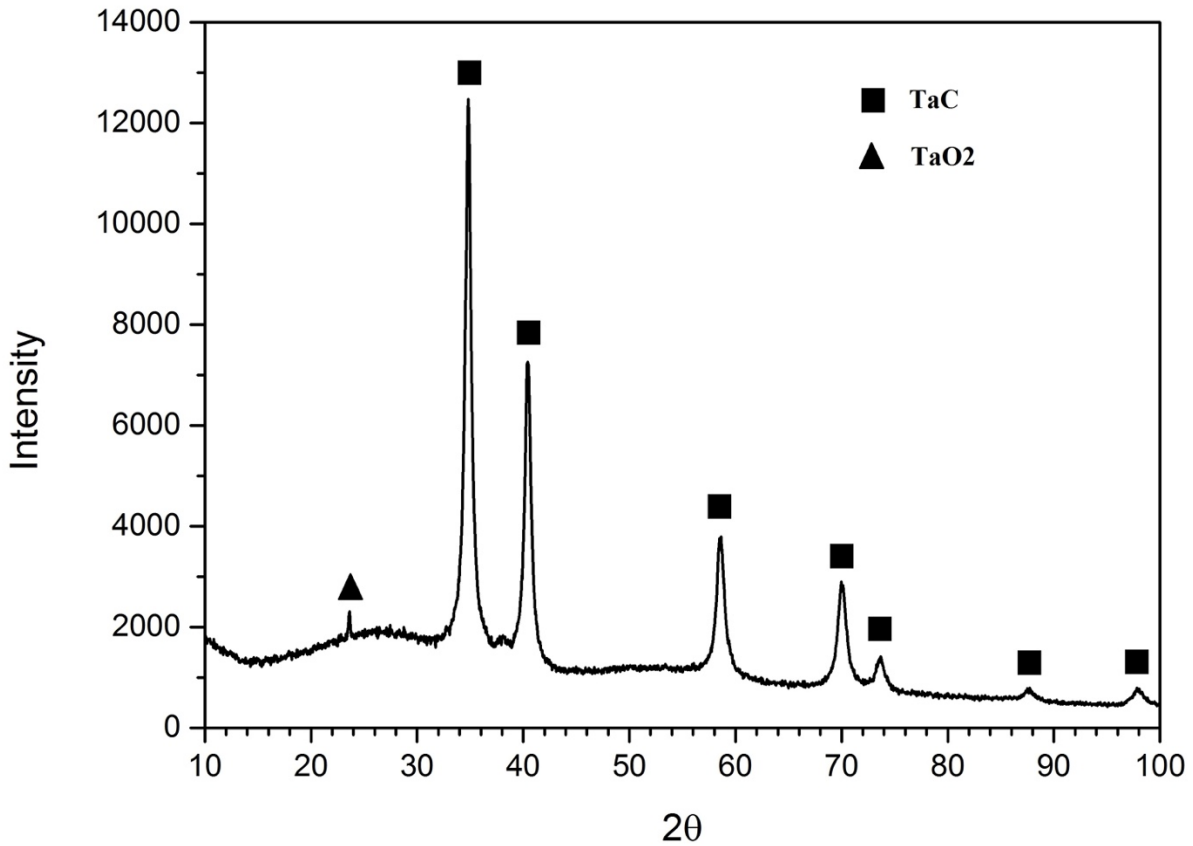


Figure 3-4. X-ray diffraction pattern of Y-doped TaC sample with 15 at% calculated Y amount using metallic yttrium as the precursor synthesized through improved reaction setups.

Following the positive results obtained from metallic yttrium powder on improving the phase purity, most of the other doping elements being investigated in the later stage of the study were introduced to the TaC matrices using their metal-form precursors.

Unlike choosing Y as the dopant, which is based on the consideration of the difference in ionic radii, the exploration of other dopants, including Nb, Hf, and Zr, originated from the fact that they are closely located with Ta on the Periodic Table. Their carbides, NbC, HfC and ZrC, all form complete solid solutions with TaC as they share the *fcc* crystal structure. Therefore, these dopants were expected to enter the TaC lattice and substitute the Ta sites effectively. Moreover, the phase purity issue was expected to be better contained through the formation of solid solution.

As such, if the morphology of the resulting particles turned out to be noticeably changed from the undoped samples, the dopants could be almost immediately attributed to cause the morphology modification, thus providing a strong support for the principles of this project. Aligning well with the expectation, the XRD patterns for TaC doped with various amount of Nb displays high phase purity (Figure 3-5).

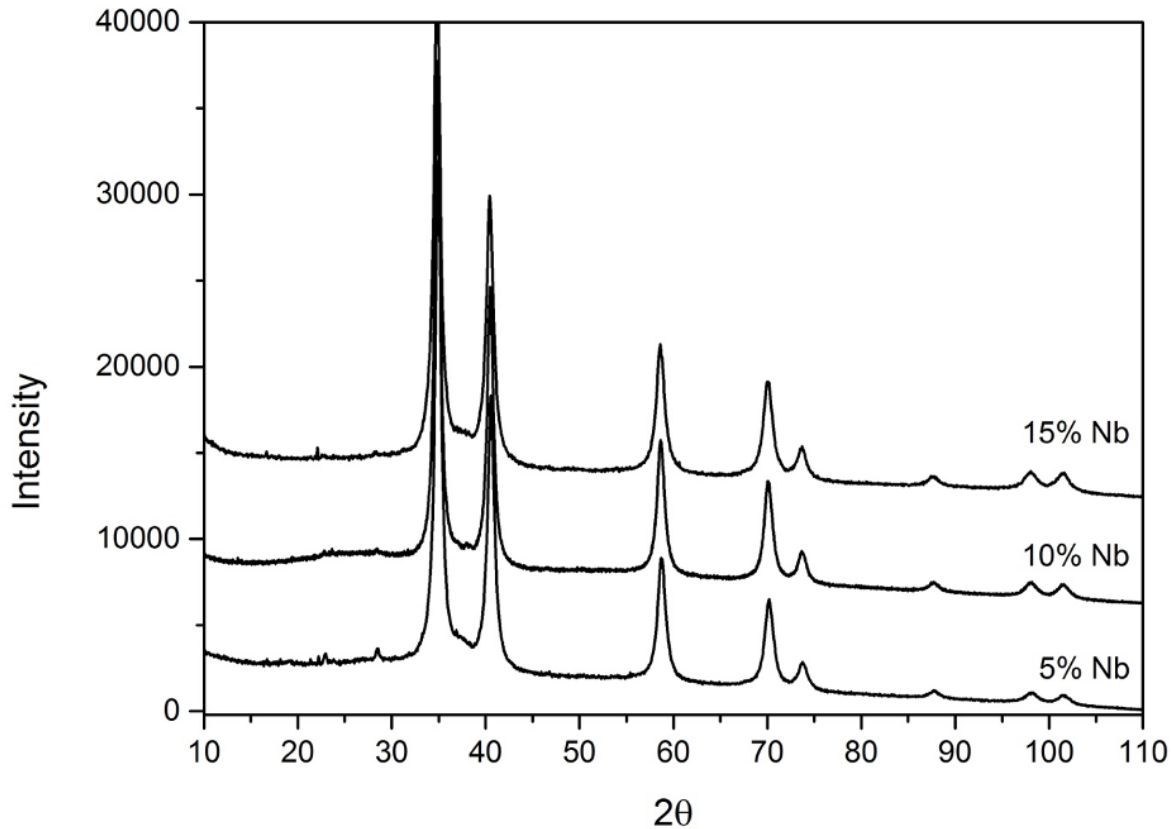


Figure 3-5. X-ray diffraction patterns of Nb-doped TaC samples with different Nb amount using metallic Nb as the precursor synthesized through improved reaction setups.

The Zr doping, however, induced a noticeable amount of tantalum oxidation similar to the Y doping (Figure 3-6). The underlying reason can be explained that the addition of Zr, which has a +4 valence, potentially introduced a significant number of vacancies in the matrices where Ta⁵⁺ ions dominate due to charge compensation. As a result, oxygen diffusion was promoted to facilitate the formation of tantalum oxides during the high-temperature reaction processes. The

Hf doping did not show oxidation as severe as the Zr doping, but low-angle oxidation humps and sub-stoichiometric carbides were seen under XRD (Figure 3-7).

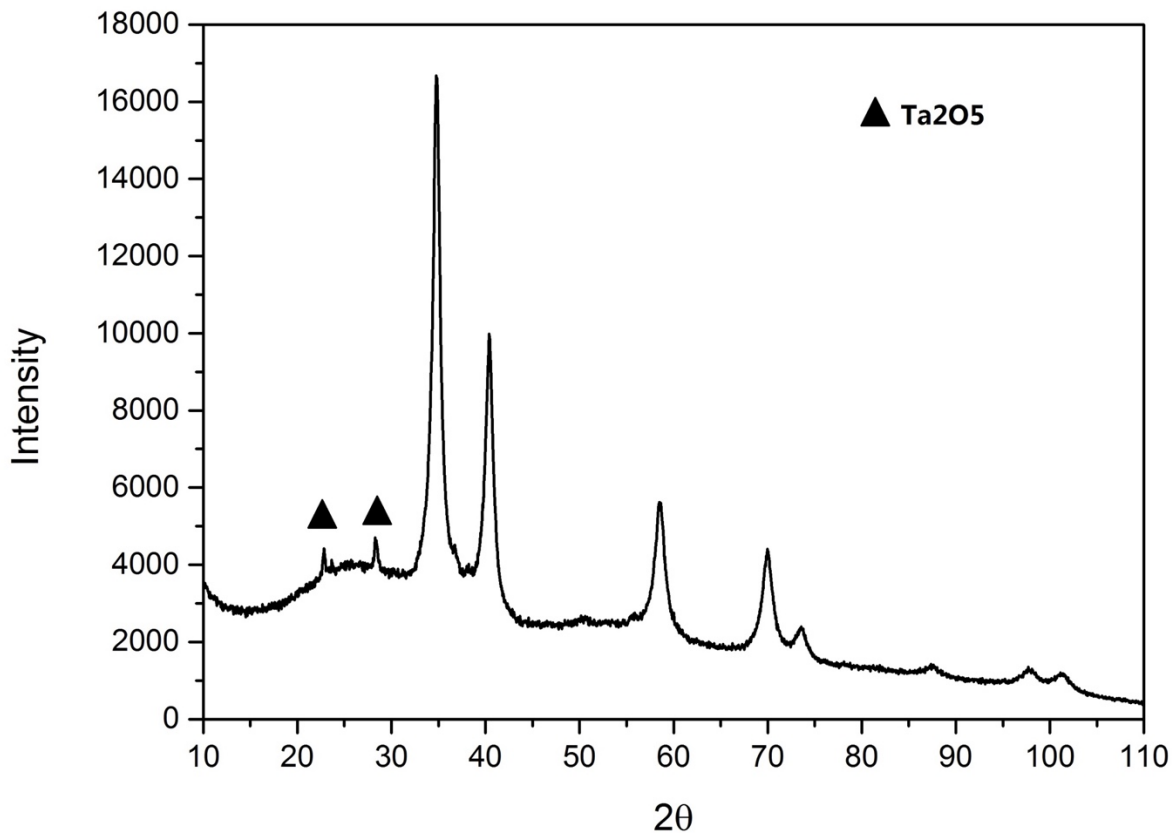


Figure 3-6. X-ray diffraction pattern of Zr-doped TaC sample with 15 at% calculated Zr amount using metallic Zr as the precursor synthesized through improved reaction setups.

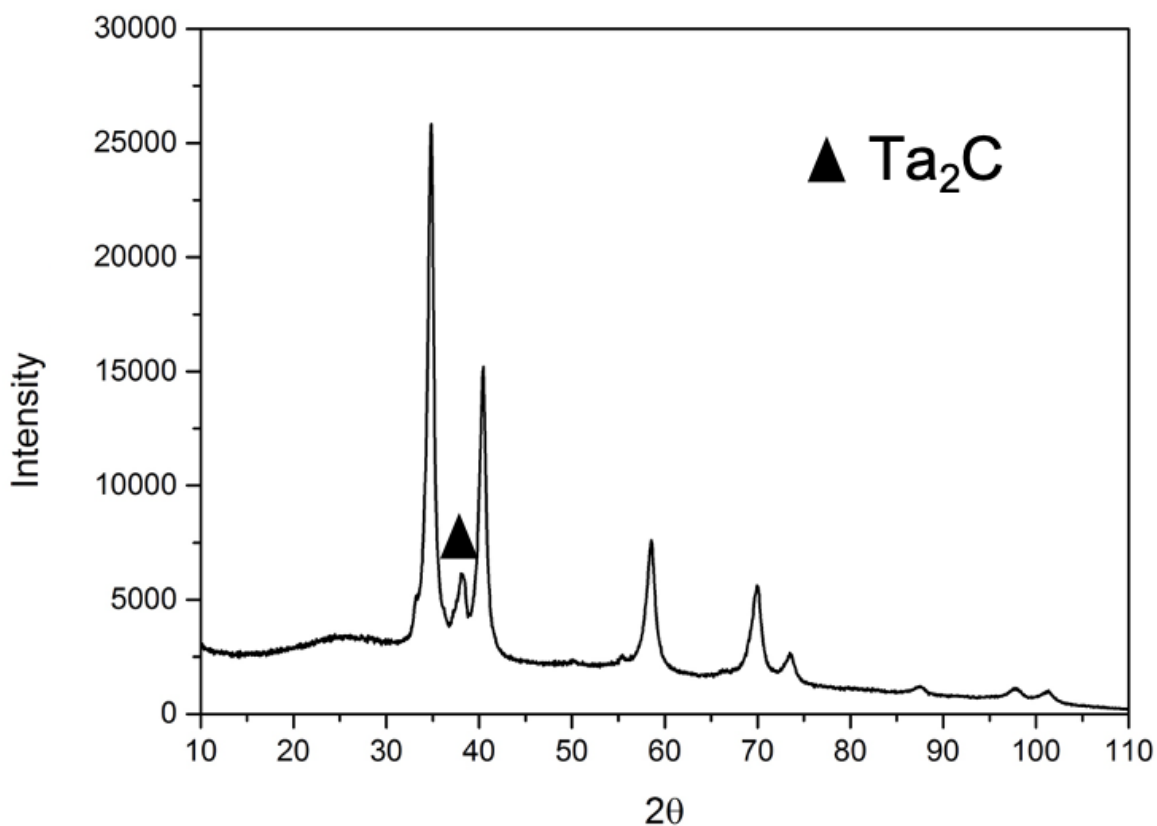


Figure 3-7. X-ray diffraction pattern of Hf-doped TaC sample with 15 at% calculated Hf amount using metallic Hf as the precursor synthesized through improved reaction setups.

In the next phase of experiments, ferromagnetic transition elements including Fe, Ni, and Co were selected as the dopants in hope that they would have strong interaction with the surface C atoms of TaC particles via *p-d* electron orbital hybridization. As described in the report by Nie *et al.*, the morphology of TiC particles switched from octahedron to truncated cubes when grown in Ni melt (Figure 3-8). They provided a theory with good validity that Ni selectively adheres to the {100} facets via strong covalent bonding between Ni-3*d* and C-2*p* orbitals. Then, the binding energy of the {100} facets is reduced and its corresponding growth rate is lowered, leading to its exposure in the final particle morphology.⁸

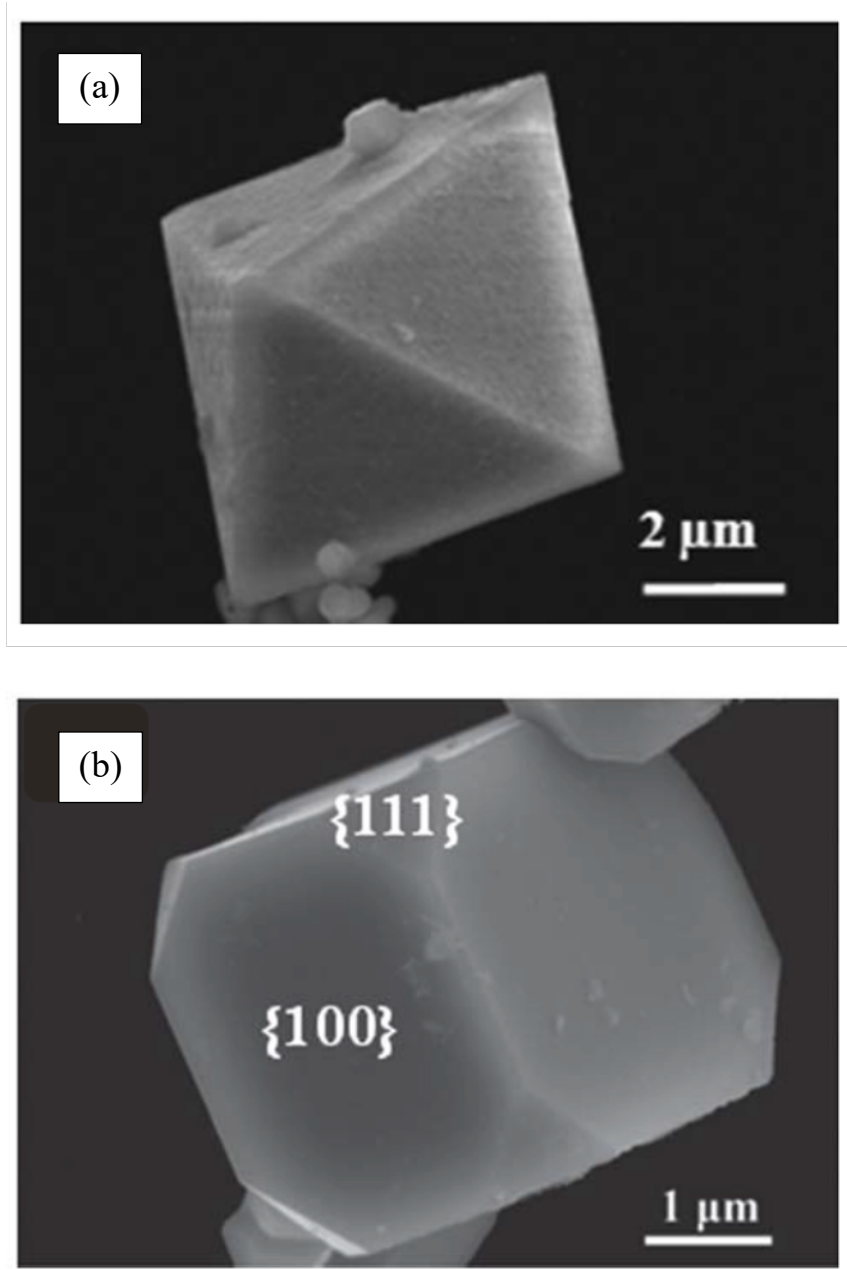


Figure 3-8. Typical morphology of TiC particles synthesized from (a) non-Ni containing melts and (b) Ni-containing melts (reprinted with permission from Ref. 8).

Inspired by this theory, and based on the fact that TiC and TaC have both structural and chemical similarity, doping by Fe, Ni, and Co was explored, although there are still certain differences in the synthesizing methodologies between the present study and Nie *et al.*'s. The results obtained from this series were the most promising compared to other dopants previously

depicted. Figure 3-9, 3-10, and 3-11 illustrate the XRD patterns for typical Ni-, Co-, and Fe-doped TaC produced. It can be clearly seen that the phase purity and the overall crystallinity (the elimination of amorphous humps) were substantially improved. It also hints that Ni, Co, and Fe can be more effectively incorporated into the TaC lattice without introducing many secondary phases.

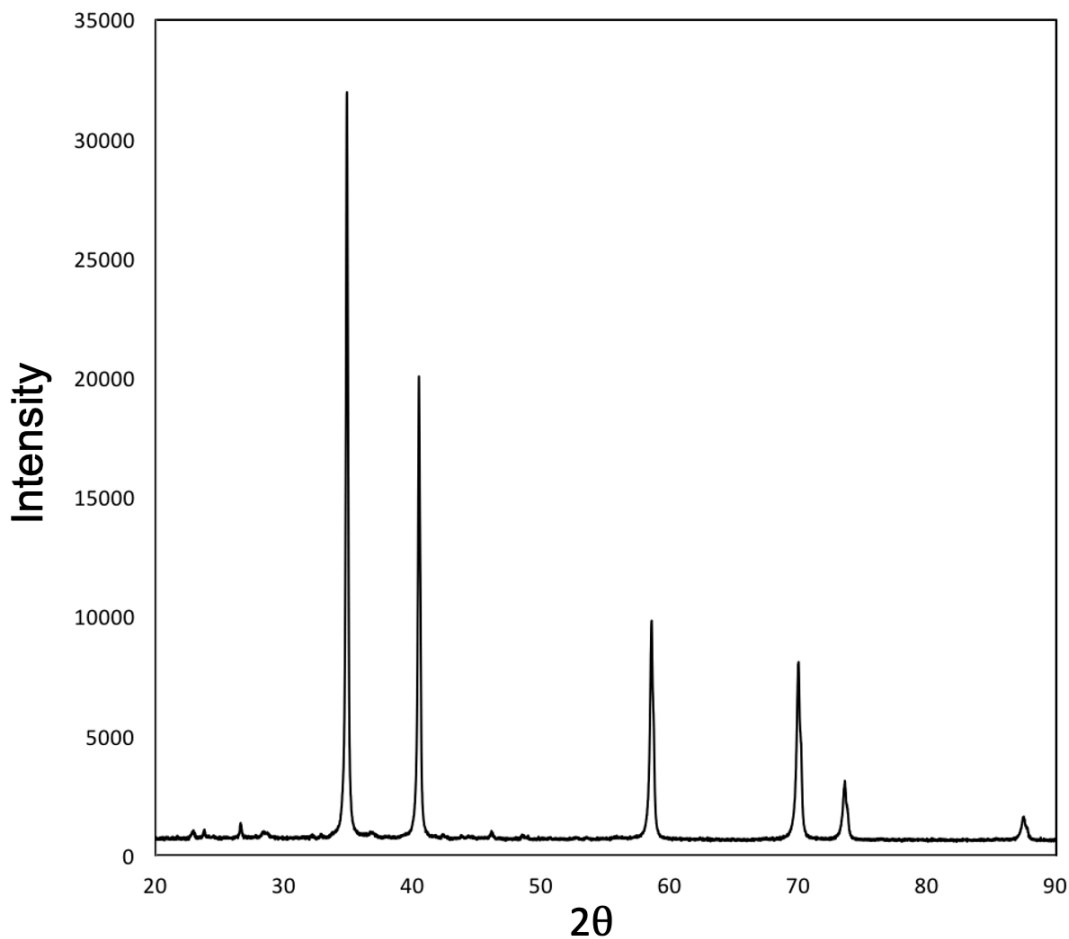


Figure 3-9. X-ray diffraction pattern of Ni-doped TaC sample with 15 at% calculated Ni amount using metallic Ni as the precursor synthesized through improved reaction setups.

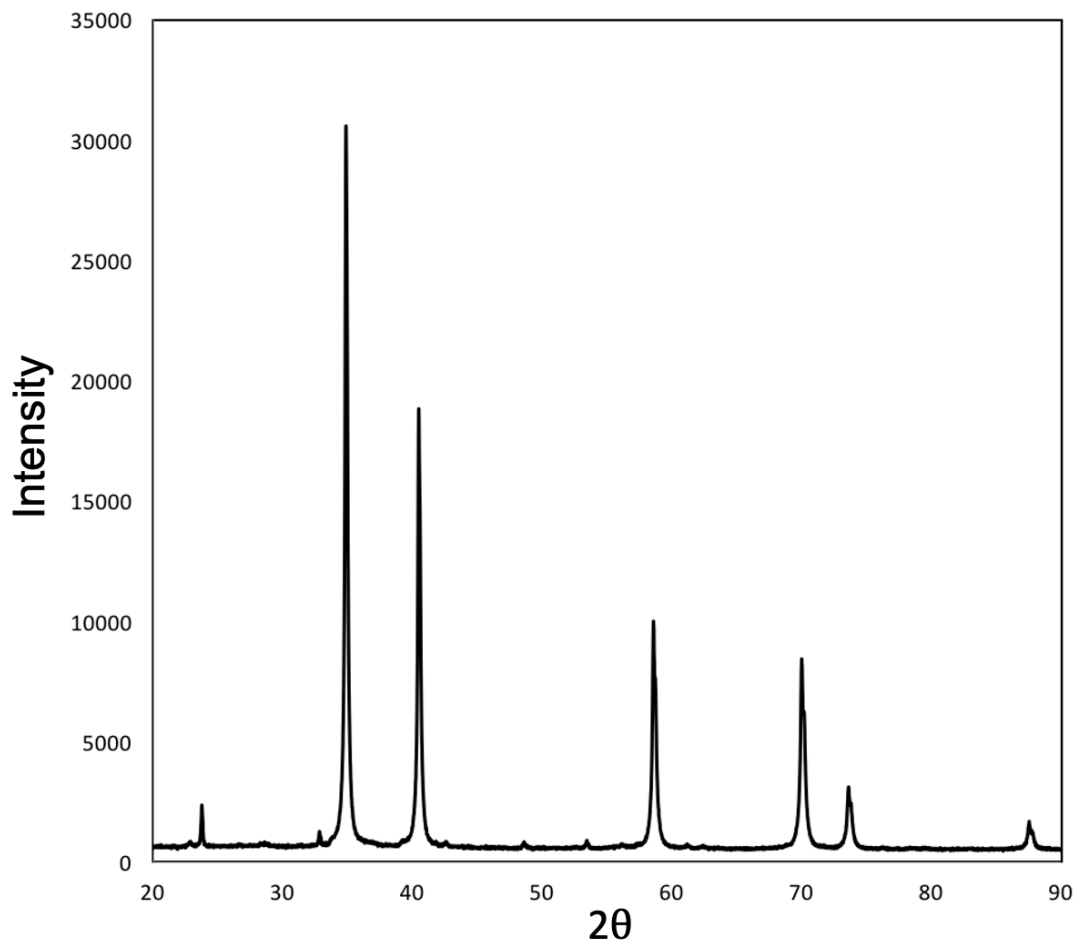


Figure 3-10. X-ray diffraction pattern of Co-doped TaC sample with 15 at% calculated Co amount using metallic Co as the precursor synthesized through improved reaction setups.

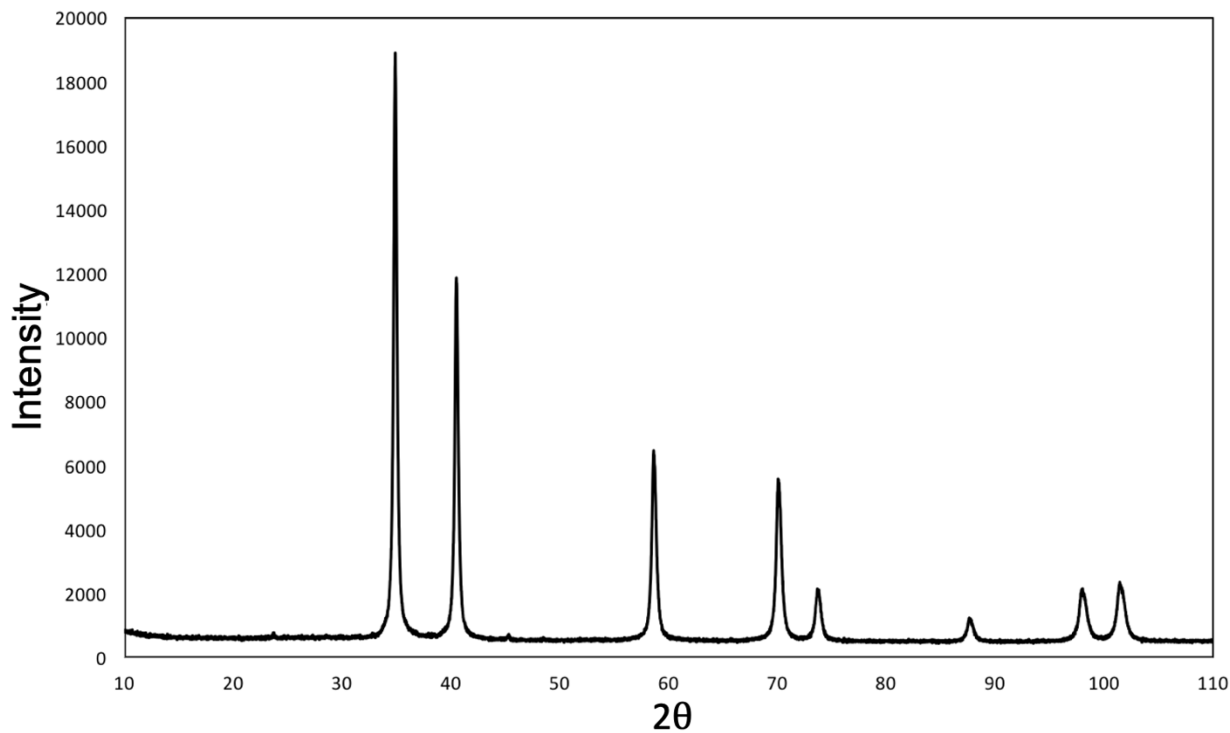


Figure 3-11. X-ray diffraction pattern of Fe-doped TaC sample with 15 at% calculated Fe amount using metallic Fe as the precursor synthesized through improved reaction setups.

So far, a variety of material systems based on doping with a single element have been discussed. To further elucidate the dopant-induced morphology selectivity, dual-element doping was also attempted using Ni and Ti as the co-dopants. Being demonstrated in the subsequent sections, Ni was proven to be an effective morphology modifier to produce highly-faceted cuboctahedron TaC particles. As mentioned in Chapter 1, TaC exhibits a mixed bonding environment combining covalent Ta-C, ionic Ta-C, and metallic Ta-Ta bonds. One hypothesis is that increasing the ionicity of TaC will weaken the highly directional Ta-C covalent bonds in the (100) directions, hence stabilize the {100} faces during crystal growth. It was found by calculation that the ionicity of transition metal carbides decreases from left to right across the Groups.¹⁵ Therefore, if some Ta sites in TaC were substituted by co-doping with Ti, the overall ionicity of $Ta_{1-x}Ti_xC$ superlattice is expected to increase, making the probability of obtaining cubic-shaped

particles higher. The overall phase purity of Ni-Ti co-doped TaC samples is surprisingly great. Figure 3-12 gives an example of a typical XRD pattern seen on the co-doped samples free of secondary phases.

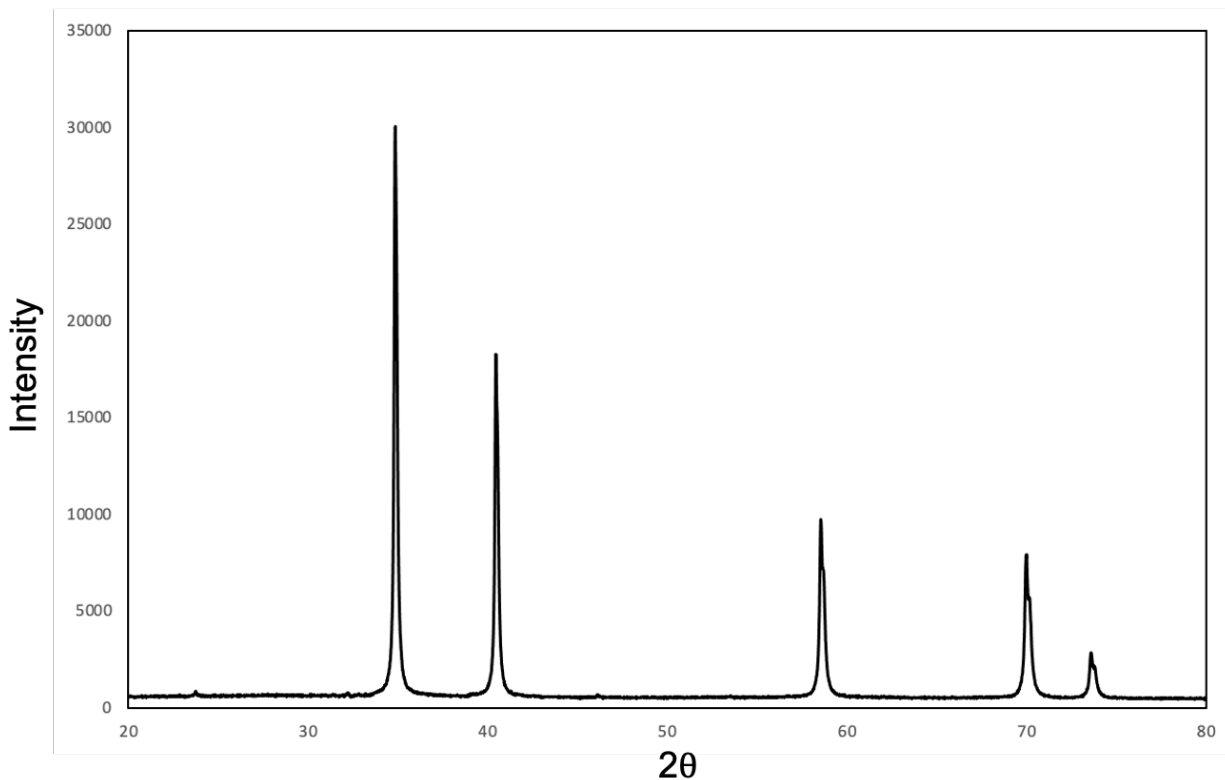


Figure 3-12. X-ray diffraction pattern of Ni-Ti co-doped TaC sample with 20 at% calculated Ni amount and 5 at% calculated Ti amount using metallic Ni and Ti as the precursors synthesized through improved reaction setups.

In summary, the selection of dopants follows the governing principles of crystal growth on the microscopic level. Metallic precursors of dopants were chosen based on macroscopic observation of the reaction outcomes.

3.3. Detailed Results and Discussion

3.3.1. Undoped TaC

Phase-pure TaC particles with no doping were synthesized using excess carbon black as the raw material. Figure 3-13 gives the XRD pattern of a typical undoped sample (TaC-1) showing monolithic TaC phase with high crystallinity. The lattice parameter obtained from Rietveld refinement is $4.4543 \pm 0.00003 \text{ \AA}$, which is slightly non-stoichiometric when compared to the published value of $4.4570 \pm 0.00010 \text{ \AA}$.^{16,17} This is within the expectation since non-stoichiometry is one of the characteristics of synthetic transition-metal carbides. Here, the stoichiometry is high enough to be considered as a model system of tantalum mono-carbide.

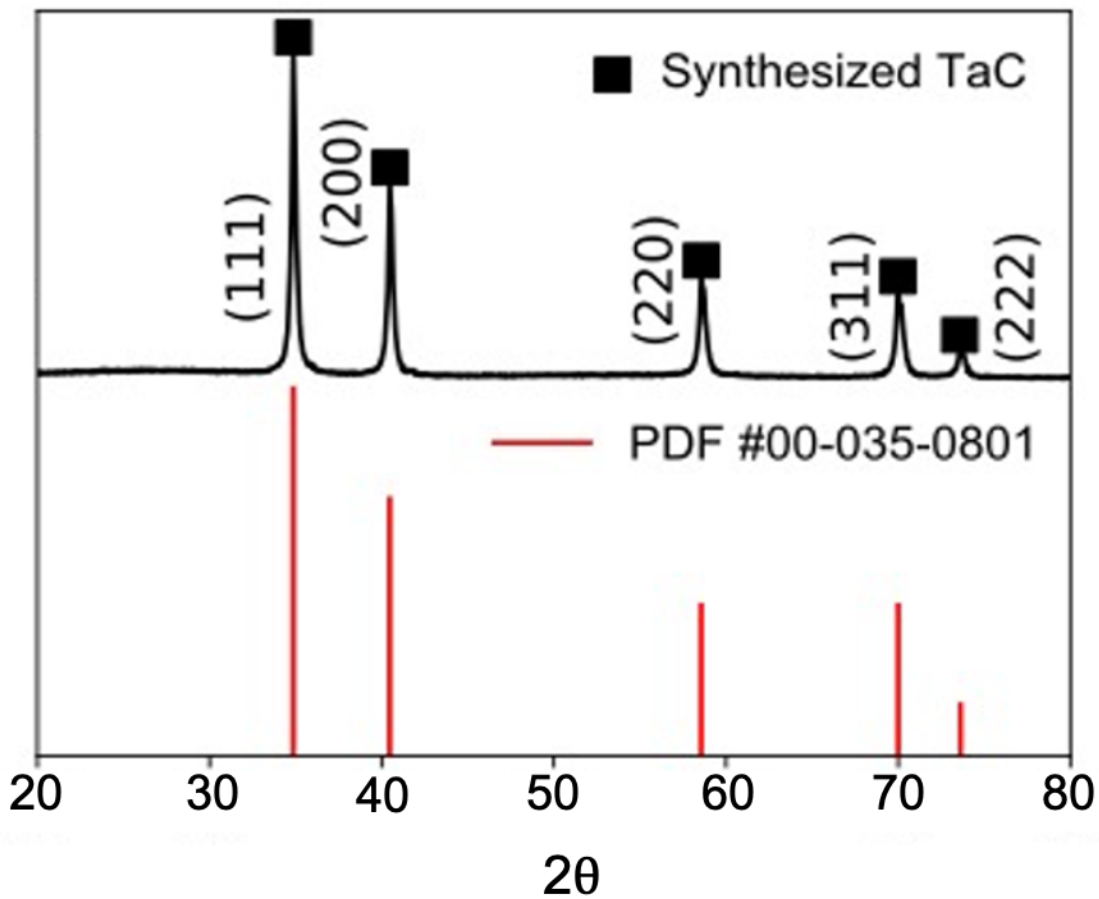


Figure 3-13. X-ray diffraction pattern of undoped TaC sample synthesized with improved reaction setups.

Figure 3-14 shows the SEM micrographs of the corresponding undoped TaC sample. The particle size is less than 100 nm. It can be clearly observed from different magnifications that most of the particles are irregularly shaped, meaning that no well-defined facets were developed during the growth process.

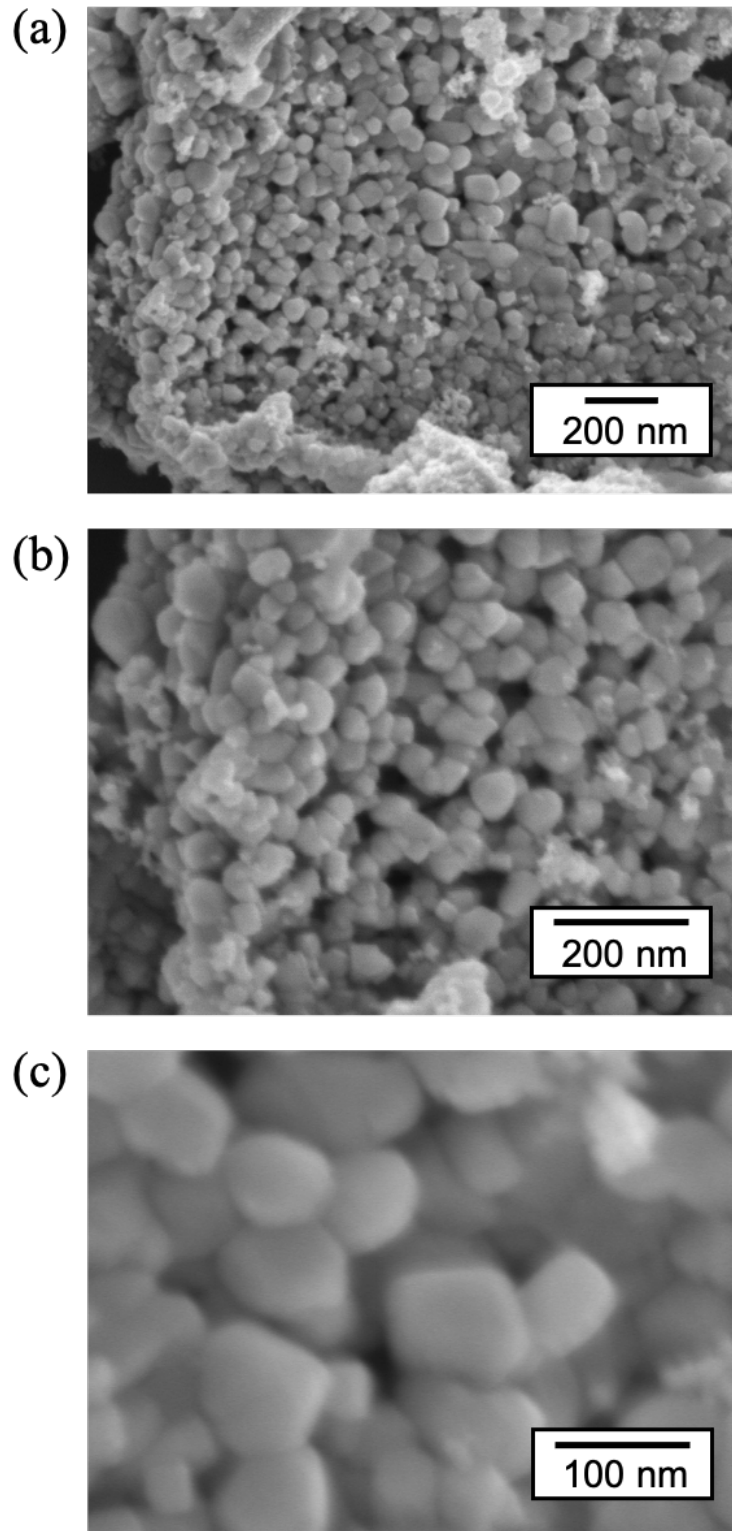


Figure 3-14. Scanning electron micrographs of undoped TaC sample imaged at different magnifications (TaC-1).

To explain why the undoped TaC particles showed no facets, the thermodynamic roughening mechanisms described by several researchers is considered to be applicable in this case. The final morphology of particles is a reflection of the competition among different crystallographic surfaces on their growth rates, which is a function of their corresponding surface energies (γ).¹⁸ Faster growth of a particular crystal surface results in quicker extinction of that surface, leaving the slower growing surfaces as the enclosing surfaces for the final crystal. For the equilibrium crystal shapes (ECS) of cubic materials, decreasing the growth rate ratio ($R = \gamma_{111}/\gamma_{100}$) will lead to more cuboctahedron geometries, while increasing the ratio results in more cubic geometries. This can be graphically illustrated using the Wulff construction (Figure 3-15). A value of R below 0.58 results in octahedrons, values between 0.58 and 1.73 results in cuboctahedrons, the values greater than 1.73 results in cubes. The classical broken bond model for surface energy dictates that surfaces with a larger areal density of broken bonds are more unstable (γ increases). The areal density of broken bonds for TaC surfaces are 0.199 and 0.345 for the $\{100\}$ and $\{111\}$ facets respectively. As such, the $\{100\}$ facet is expected to be the more stable than the $\{111\}$ facet.

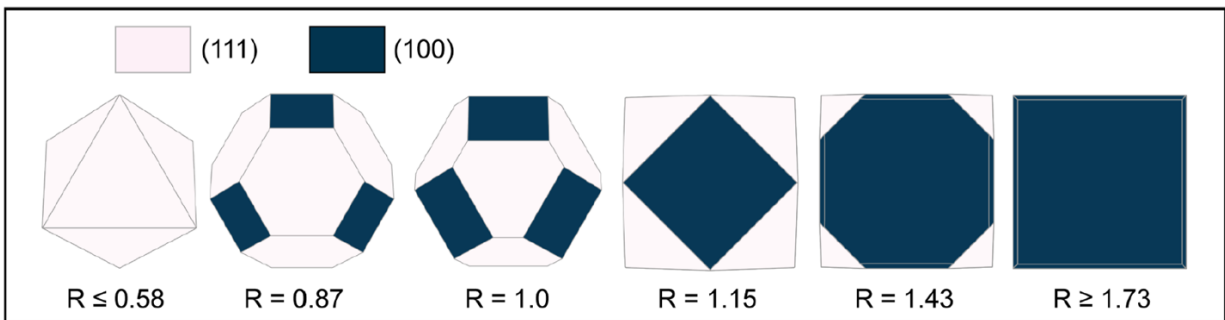


Figure 3-15. An illustration of various particles morphologies corresponding to the surface energy ratio ($R = \gamma_{111}/\gamma_{100}$).

Burton *et al.* proposed that facets with a high growth rate will go through thermodynamic roughening, whereby the crystal morphology transitions from its ECS to a round/irregular shape due to free energy minimization at elevated temperatures.¹⁹ More recently, Jin *et al.* also reported similar thermodynamic roughening behavior of TMCs at elevated reaction temperatures.⁹ In the current study, it is likely that the growth rate of {100} facets has surpassed the temperature threshold for the thermodynamic roughening due to the extremely high synthesis temperatures (>2000 K), according to the observation that the inner wall of the quartz test tube was partially melted after each synthesis. To further verify the validity of this explanation, another set of undoped TaC samples were synthesized with 30 wt% of commercial TaC powders (99.5%, Alfa Aesar, 12144) added as the diluent to reduce the flame temperature of the reaction. The particle morphology of commercial TaC powders was characterized by SEM to avoid confusion when imaging the in-house synthesized particles. Figure 3-16 reveals that commercial TaC particles are distinctive by both their size and morphology compared to the synthesized TaC particles.

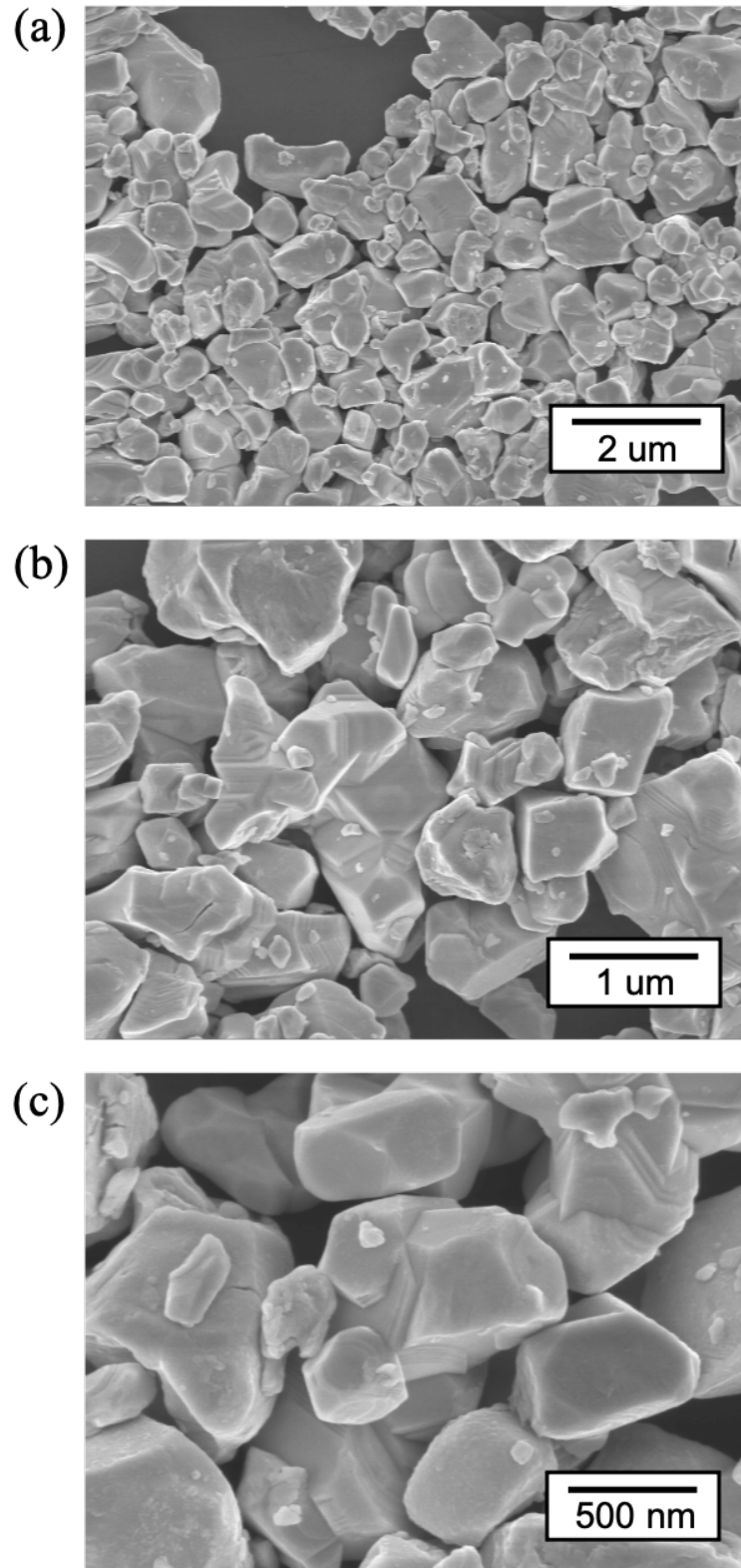


Figure 3-16. Scanning electron micrographs of commercial TaC powders imaged at different magnifications.

A noticeable difference on the morphology of undoped TaC synthesized with and without reaction diluent was observed, as shown in Figure 3-17 below. Particles with some defined facets can be found under SEM, although the population of such particles is not large (~10% out of total counts). Despite the inability to measure the maximum flame temperature during the reaction, the effect of the reaction diluent imposed on the final morphology provided experimental evidence that thermodynamic roughening could in fact be one of the reasons for the morphological irregularity of undoped TaC particles.

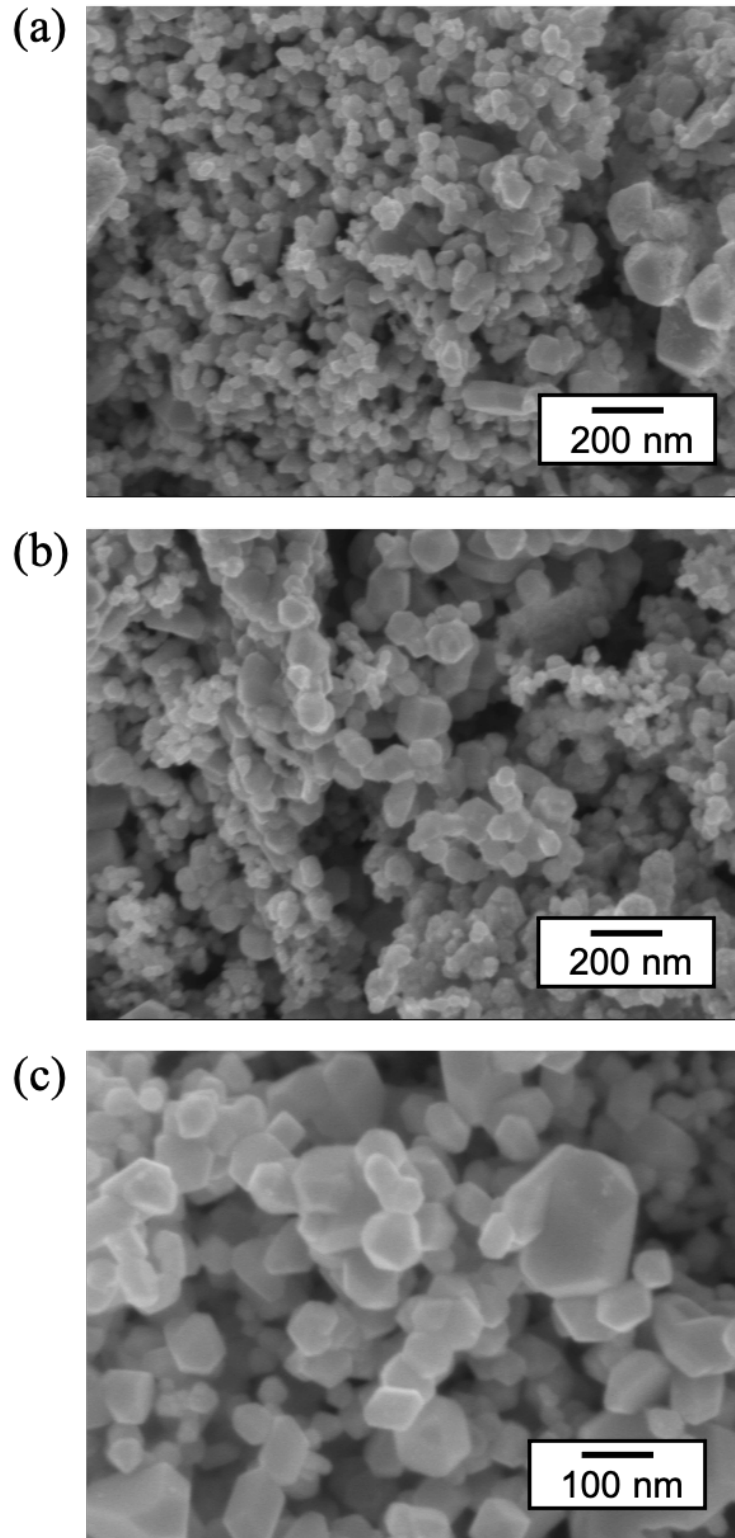


Figure 3-17. Scanning electron micrographs of undoped TaC sample synthesized with the addition of 30 wt% commercial TaC powder as the reaction diluent imaged at different magnifications (TaC-2).

Experimental approaches can provide evidence. But they are not enough to illuminate the interplays among the carbon stoichiometry, the surface energy, and the final particle morphology. Therefore, to better understand why the growth of the undoped TaC particles does not end up being highly-faceted, computational methods based on the Density Functional Theory (DFT) were coherently introduced through the collaboration with Dr. Richard Tran and Prof. Shyue Ping Ong of the Materials Virtual Lab in the Department of NanoEngineering, UC San Diego.²¹ All DFT calculations were performed using the Vienna Ab initio Simulation Package (VASP) within the projector augmented wave (PAW) approach.²²⁻²⁵ The exchange-correlation effects were modeled using the Perdew-Berke-Ernzerhof (PBE) generalized gradient approximation (GGA) functional, and all calculations were spin-polarized with a plane wave cutoff of 400 eV.²⁶ The pseudopotentials used are similar to those used in the Materials Project.²⁷ The energies and atomic forces of all calculations were converged within 10^{-4} eV and $0.02 \text{ eV}\text{\AA}^{-1}$ respectively. Γ -centered k -point meshes of $\frac{50}{a} \times \frac{50}{b} \times \frac{50}{c}$ and $\frac{50}{a} \times \frac{50}{b} \times 1$ were used for the oriented unit cell and slab calculations respectively with non-integer values rounded up to the nearest integer.²⁸

The surface energies used to determine the relative stability of all slab systems were calculated using the surface grand potential which is given by:

$$\gamma = \frac{1}{2A} [E^{slab+X} - \sum_i N_i \mu_i] \quad \text{Eq. 5}$$

where E^{slab} is the total energy of the slab (X is a dopant) with i unique species, μ_i is the chemical potential of a specie i and N_i is the total number of i atoms in the slab, A is the surface area and the factor of 2 accounts for the slab model containing two symmetrically equivalent surfaces.²² Since there are several possible terminations for the TaC (111) facet, only the most stable terminations were investigated on their interaction with the dopants. Furthermore, when γ has been determined for several facets, it can be used to construct the Wulff shape.

To better understand the lack of facets for the undoped TaC samples, the surface energy is plotted against the chemical potential of carbon ($\Delta\mu_C$) based on the following relationship in Figure 3-18:

$$\gamma(\mu_i) = \frac{1}{2A} [E^{slab} - \sum_i N_i \mu_i] \quad \text{Eq. 6}$$

The plot includes the facets with Miller indices of (111), (110), (100), and the (111)*fcc* Ta surface. Here, the chemical potential of carbon represents the carbon content at the surface. γ is defined as the difference between the total energy of the slab used to model the surface (E^{slab}) and the summation of chemical potentials ($\sum_i N_i \mu_i$) normalized by the surface area ($2A$). For the stoichiometric slabs, such as (110) and (100), $\sum_i N_i \mu_i$ adds up to the total bulk energy, making γ_{100} and γ_{110} constant relative to $\Delta\mu_C$. The derivation can be expanded in detail as the follows.

In general, the surface energies of undoped TaC can be obtained from the expression:

$$\gamma(\Delta\mu_C) = \frac{E^{slab} - N_{Ta} g_{TaC}^{bulk}}{2A} + \Gamma_C (\Delta\mu_C + E_C^{graphite}) \quad \text{Eq. 7}$$

where $\gamma(\Delta\mu_C)$ is the surface energy as a function of the carbon chemical potential, $\Delta\mu_C$, relative to the energy of graphite per atom ($E_C^{graphite}$), g_{TaC}^{bulk} is the Gibbs free energy of bulk TaC per formula unit, A is the cross-sectional area, E^{slab} is the total DFT energy of the slab, $\Gamma_C = \frac{1}{2A} (N_{Ta} - N_C)$ is the number of excess or deficient C atoms per surface area, which is negative for excess C and positive for deficient C, and N_{Ta} and N_C is the number of Ta and C atoms in the slab, respectively. For a stoichiometric system, $\Gamma_C = 0$, and the surface energy becomes a constant value given by:

$$\gamma = \frac{1}{2A} [E^{slab} - N_{Ta} g_{TaC}^{bulk}] \quad \text{Eq. 8}$$

By rearranging Eq. 6 and Eq. 8, and assuming the surface phase is in equilibrium with the bulk, the chemical potential for all species in the undoped system is connected via Gibbs free energy by:

$$g_{TaC}^{bulk} = \sum_i N_i \mu_i = \mu_{Ta} + \mu_C \quad \text{Eq. 10}$$

For the non-stoichiometric (111) surface slab terminated by Ta atoms, the carbon deficiency relative to the bulk TaC results in a positive linear relationship between γ_{111} and $\Delta\mu_C$ (see Eq. 7). At high $\Delta\mu_C$, the (100) facet is the most stable surface due to the smaller number of broken bonds compared to the (111) facet. At lower $\Delta\mu_C$, however, the Ta-terminated (111) surface is increasingly stabilized as it behaves more like the stable (111) surface in an *fcc* metal.³⁰ This is in-line with the Rietveld refinement results mentioned above that the undoped TaC samples have some carbon deficiency. Moreover, when the calculated work functions of the Ta (111) (4.70 eV) and TaC (111) (4.62 eV) surfaces are so close, while that of the TaC (100) surface (3.61 eV) is significantly lower. This allows more cuboctahedron geometries as the stabilization of the (111) facet pushes its growth rate below the roughening threshold, but not the formation of cubes.

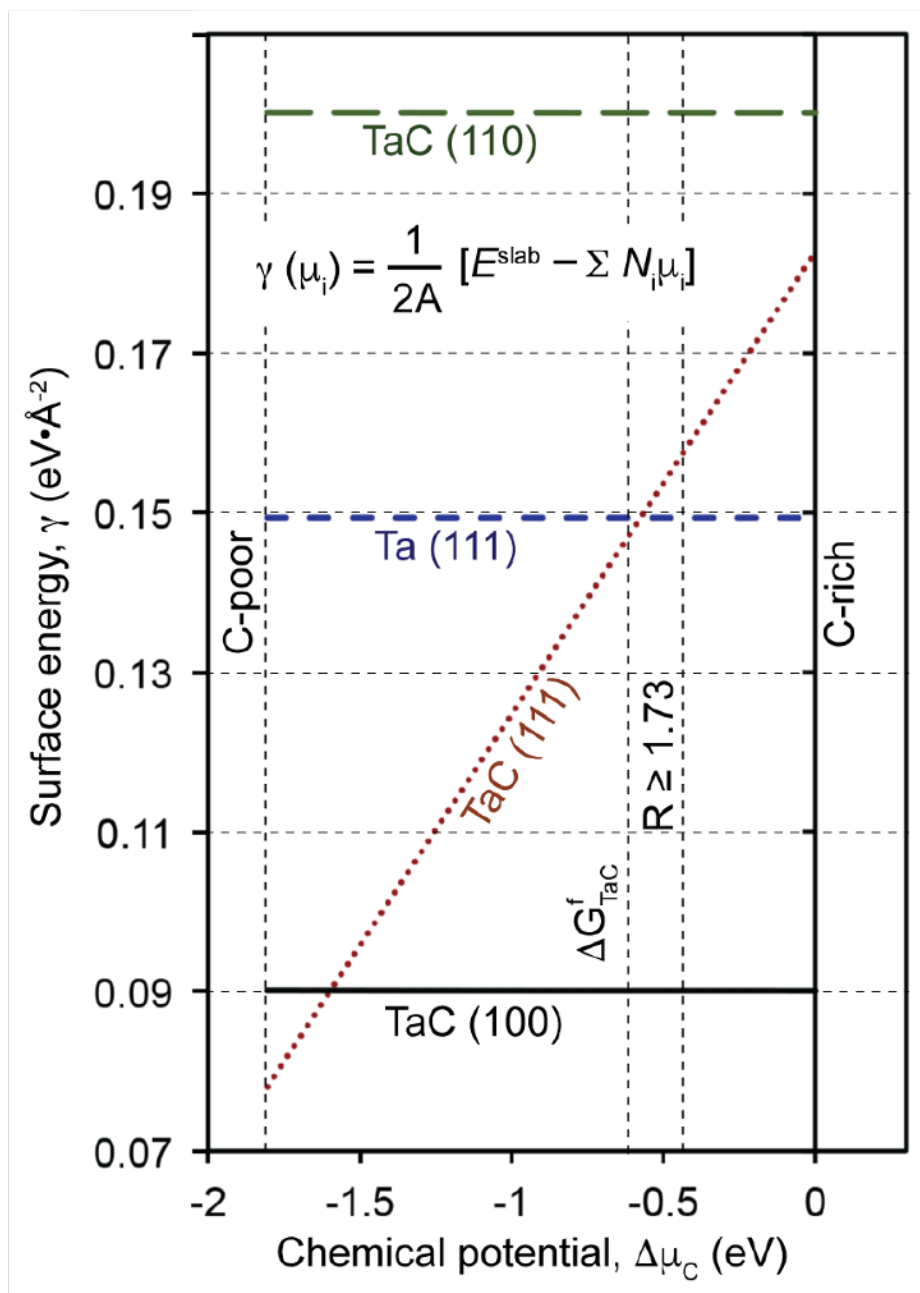


Figure 3-18. Plot of surface energies for the TaC (100), (111), (110), and the face-centered cubic Ta (111) slabs as a function of the chemical potential of carbon ($\Delta\mu_C$).

So far, the mechanisms behind the shape-irregularity of the undoped TaC particles are elaborated by combining both experimental and computational efforts. To reiterate the purpose of this study, which is to produce highly-faceted TaC nanoparticles and disclose the underlying

mechanisms for the morphology selectivity, the following sections will describe how different dopants affect the morphology of TaC nanoparticles.

3.3.2. Y-Doped TaC

As depicted in Section 3.2., Y was the first dopant being incorporated in TaC through this study. Due to precursor and reaction setup optimizations, along with other uncertainties associated with the early stage of experiments, mixed results were obtained. For the trials done with yttrium salt precursors, the particle morphologies under SEM showed no defined facets (Figure 3-19). Some even developed into uncommon shapes, making it hard to justify that they were derived from TaC crystals [Figure 3-19 (g)]. Although the main crystalline phase is still TaC, according to the XRD patterns in Figures 3-1 to 3-3, there is a good chance that the particles imaged by SEM contain many undesired phases, such as the tantalum oxides and sub-stoichiometric carbides. Hence, the confusion in particle identification caused by impurities triggered the dismissal of yttrium salts to be used as the precursors.

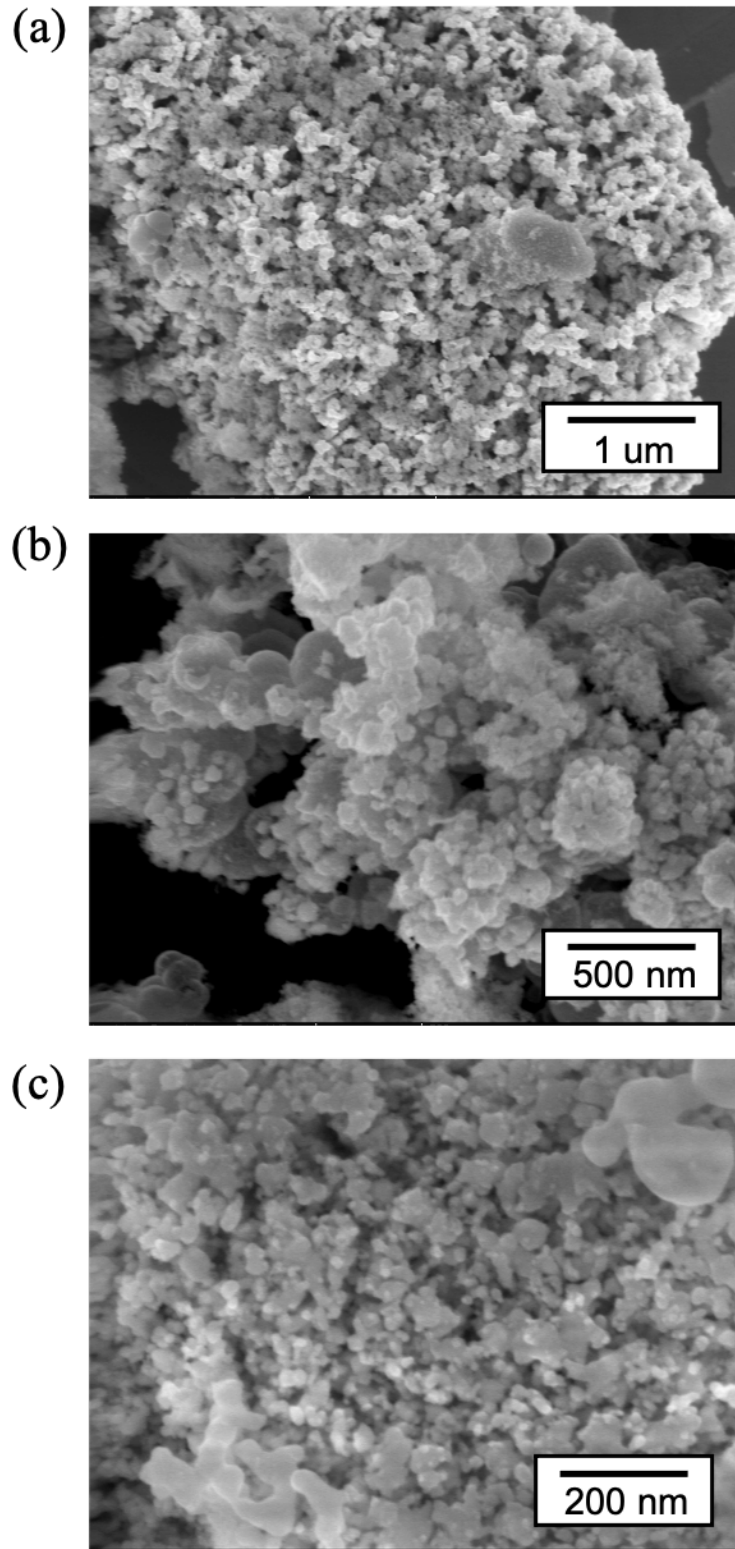


Figure 3-19. Scanning electron micrographs at different magnifications of Y-doped TaC sample with 15 at% calculated Y amount using yttrium nitrate (a)-(c) and yttrium chloride (d)-(g) as the precursors.

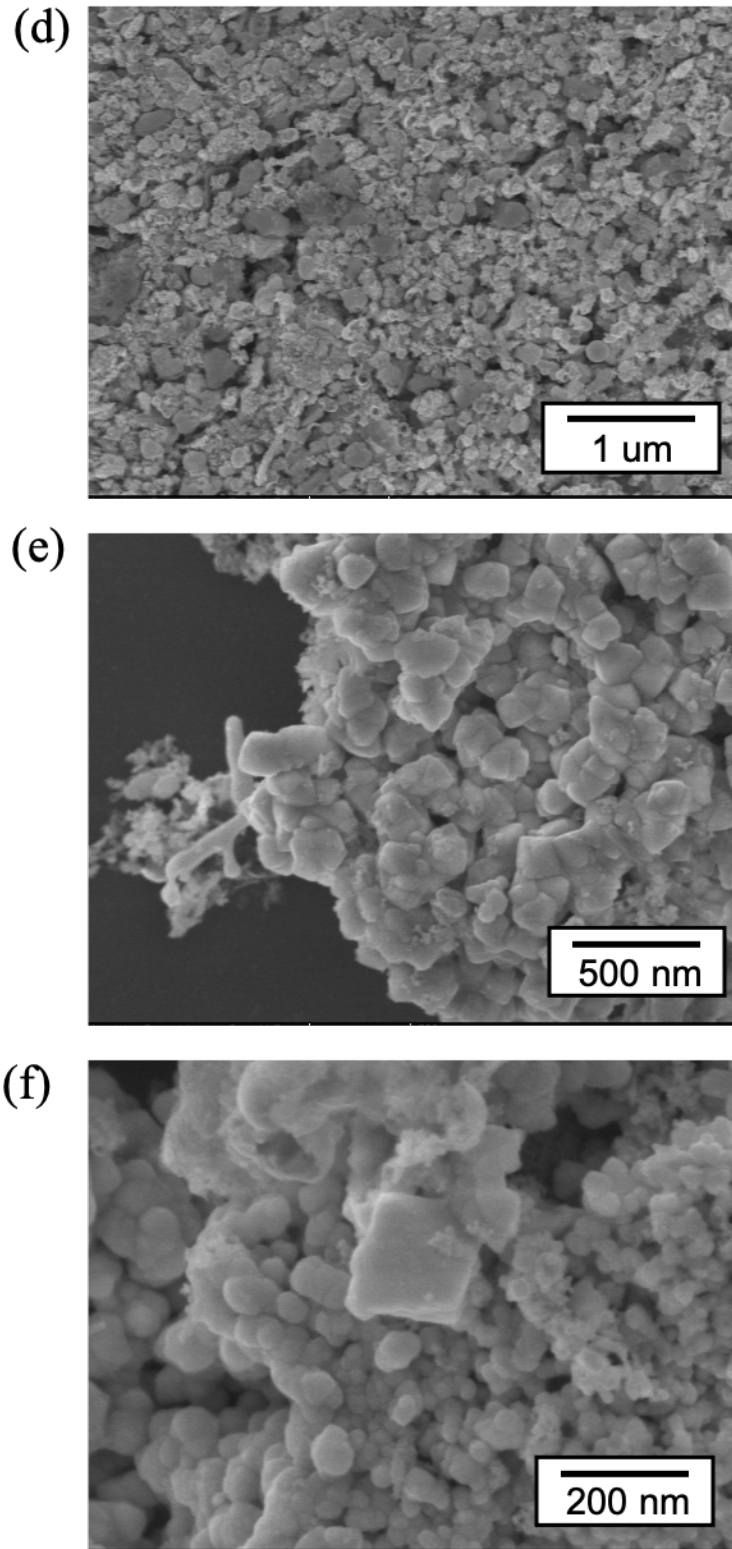


Figure 3-19. Scanning electron micrographs at different magnifications of Y-doped TaC sample with 15 at% calculated Y amount using yttrium nitrate (a)-(c) and yttrium chloride (d)-(g) as the precursors. (continued)

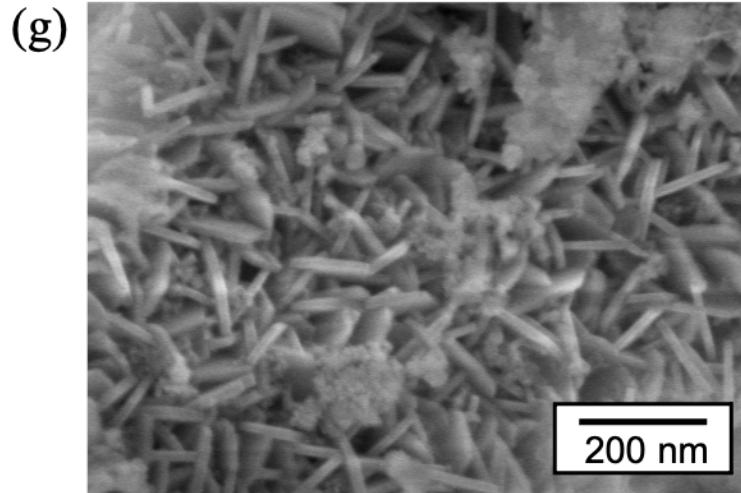


Figure 3-19. Scanning electron micrographs at different magnifications of Y-doped TaC sample with 15 at% calculated Y amount using yttrium nitrate (a)-(c) and yttrium chloride (d)-(g) as the precursors. (continued)

Figure 3-20 presents the morphology of TaC particles with a series of Y doping using Y metal powder as the precursor. The phase purity of sample Y-1 to Y-5 is indicated by the XRD patterns in Figure 3-21.

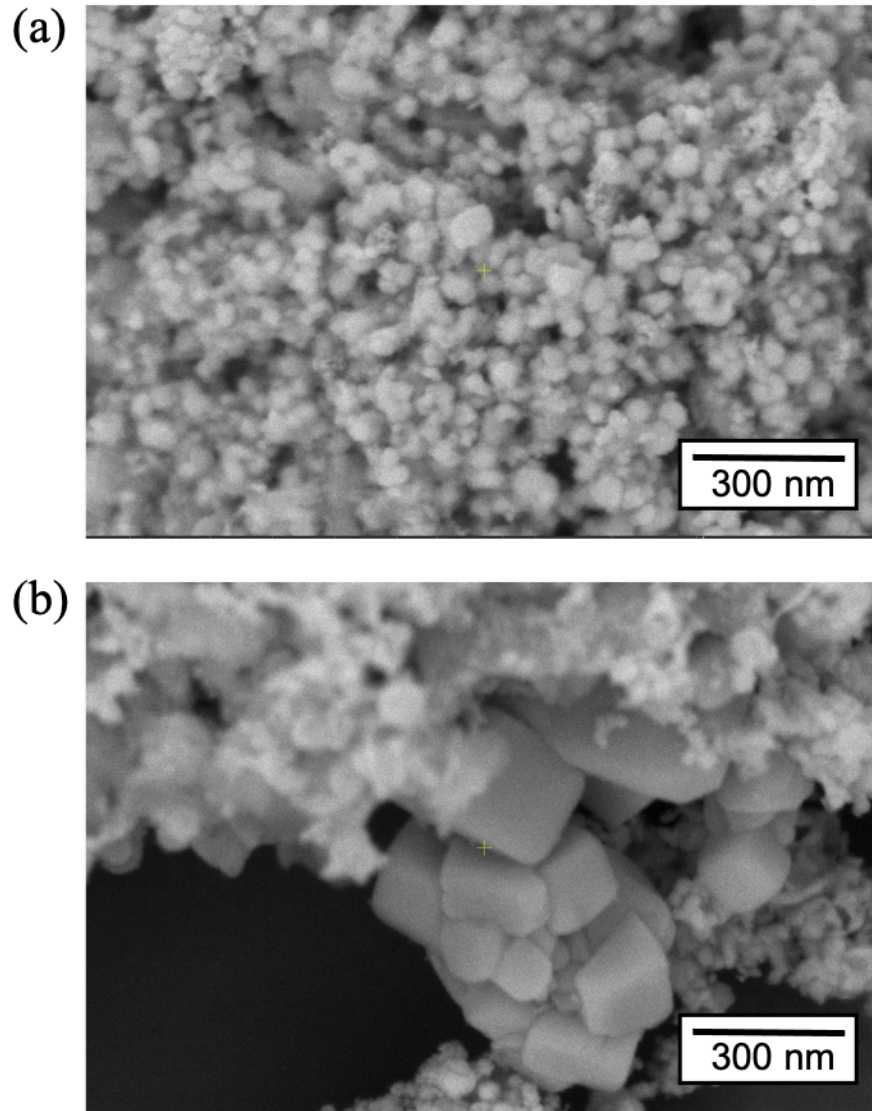


Figure 3-20. Scanning electron micrographs of Y-doped TaC samples with different doping levels using metallic Y as the precursor: (a) and (b) 10 at% calculated Y amount (Y-1); (c) to (e) 15 at% calculated Y amount (Y-2); (f) to (h) 20 at% calculated Y amount (Y-3); (i) and (j) 25 at% calculated Y amount (Y-4); (k) and (l) 30 at% calculated Y amount (Y-5).

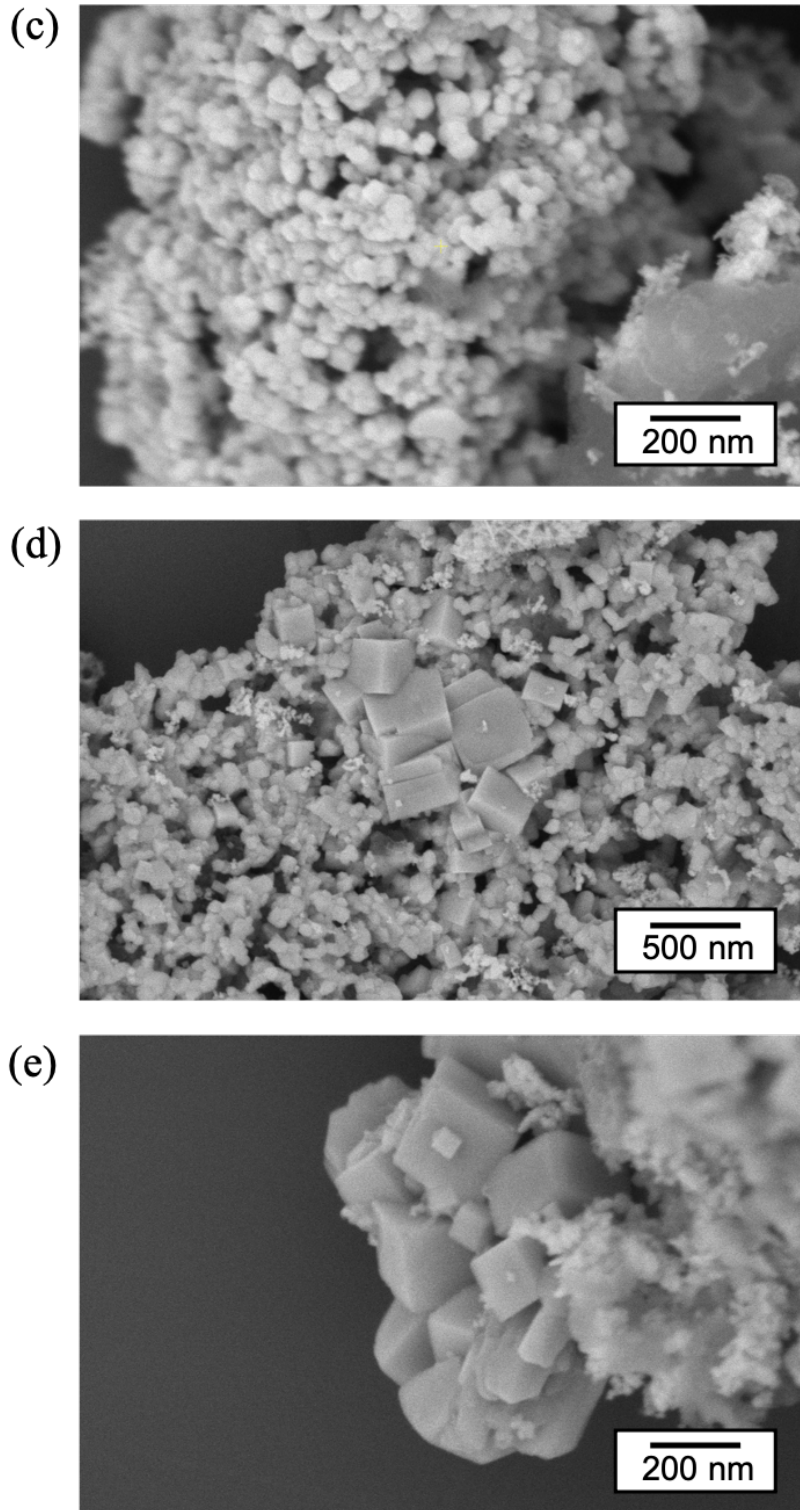


Figure 3-20. Scanning electron micrographs of Y-doped TaC samples with different doping levels using metallic Y as the precursor: (a) and (b) 10 at% calculated Y amount (Y-1); (c) to (e) 15 at% calculated Y amount (Y-2); (f) to (h) 20 at% calculated Y amount (Y-3); (i) and (j) 25 at% calculated Y amount (Y-4); (k) and (l) 30 at% calculated Y amount (Y-5). (continued)

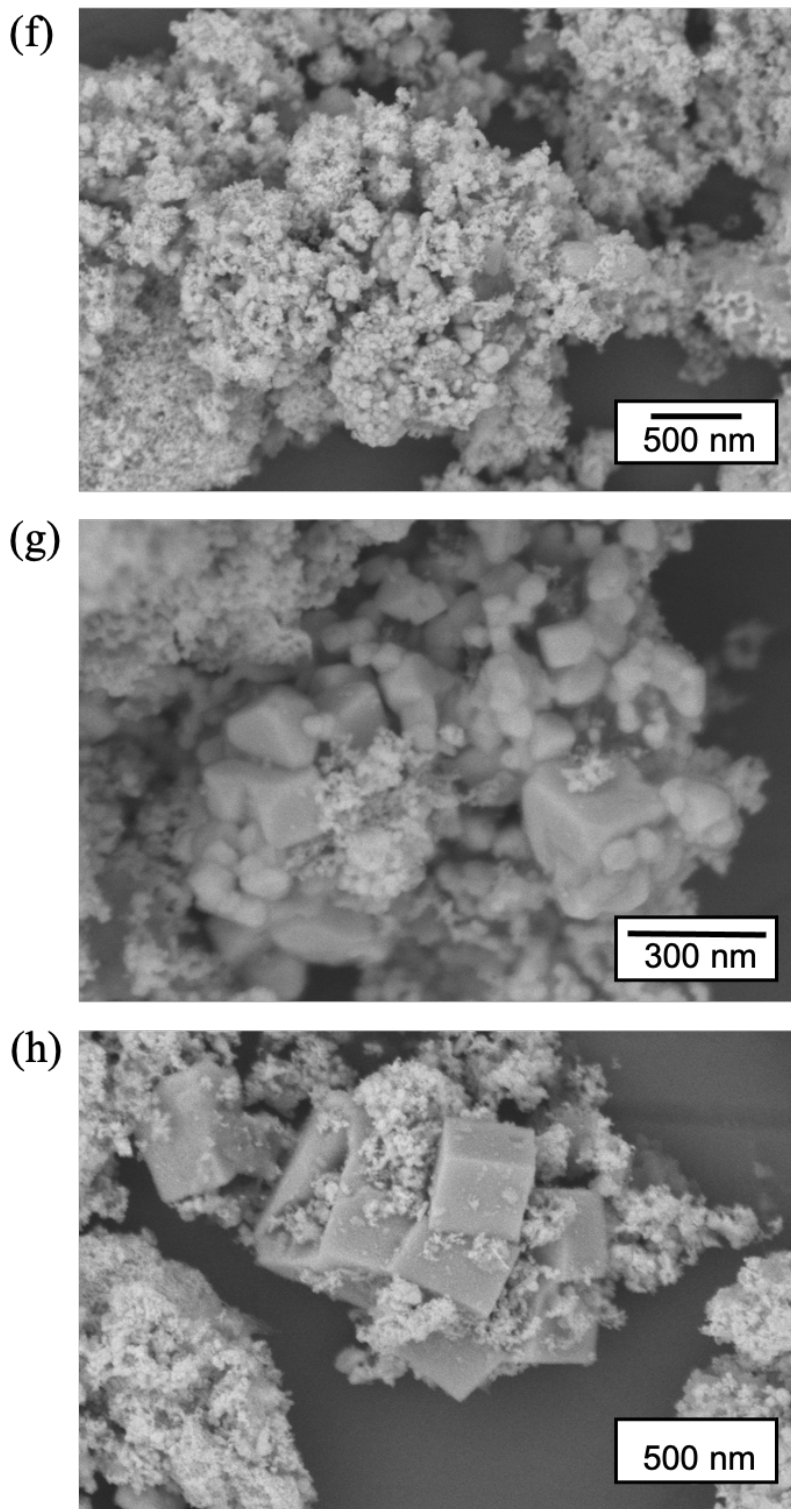


Figure 3-20. Scanning electron micrographs of Y-doped TaC samples with different doping levels using metallic Y as the precursor: (a) and (b) 10 at% calculated Y amount (Y-1); (c) to (e) 15 at% calculated Y amount (Y-2); (f) to (h) 20 at% calculated Y amount (Y-3); (i) and (j) 25 at% calculated Y amount (Y-4); (k) and (l) 30 at% calculated Y amount (Y-5). (continued)

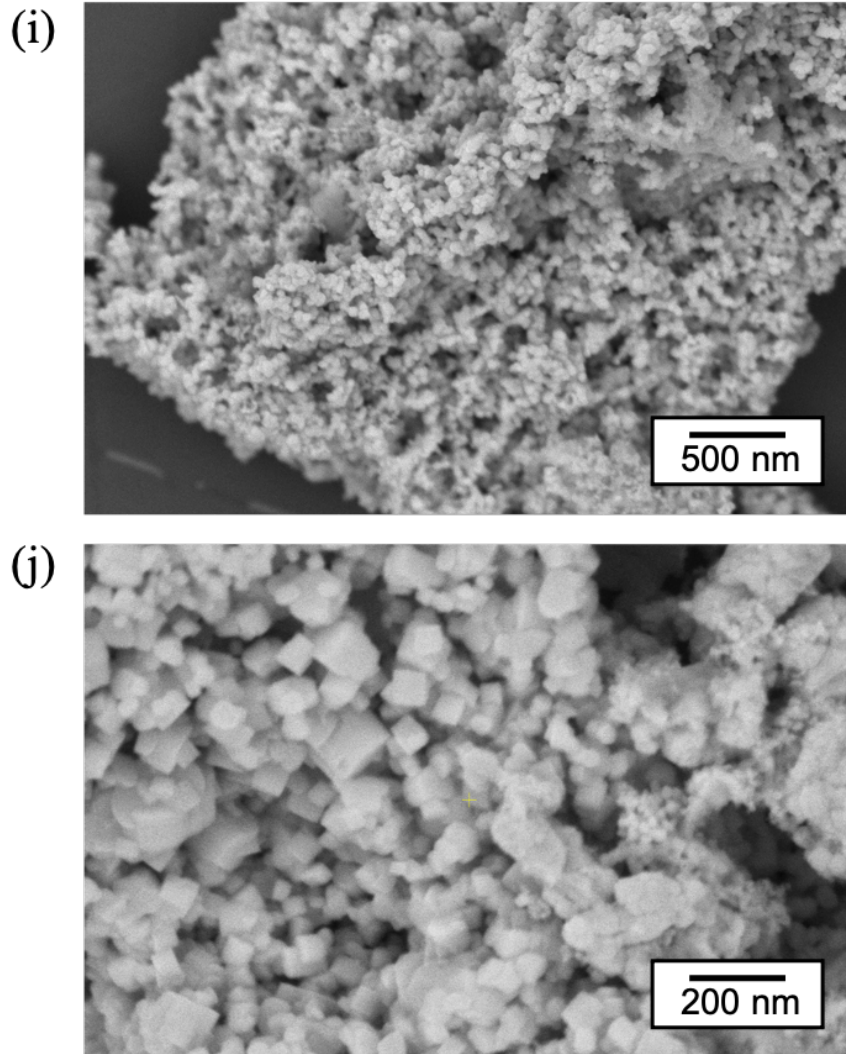


Figure 3-20. Scanning electron micrographs of Y-doped TaC samples with different doping levels using metallic Y as the precursor: (a) and (b) 10 at% calculated Y amount (Y-1); (c) to (e) 15 at% calculated Y amount (Y-2); (f) to (h) 20 at% calculated Y amount (Y-3); (i) and (j) 25 at% calculated Y amount (Y-4); (k) and (l) 30 at% calculated Y amount (Y-5). (continued)

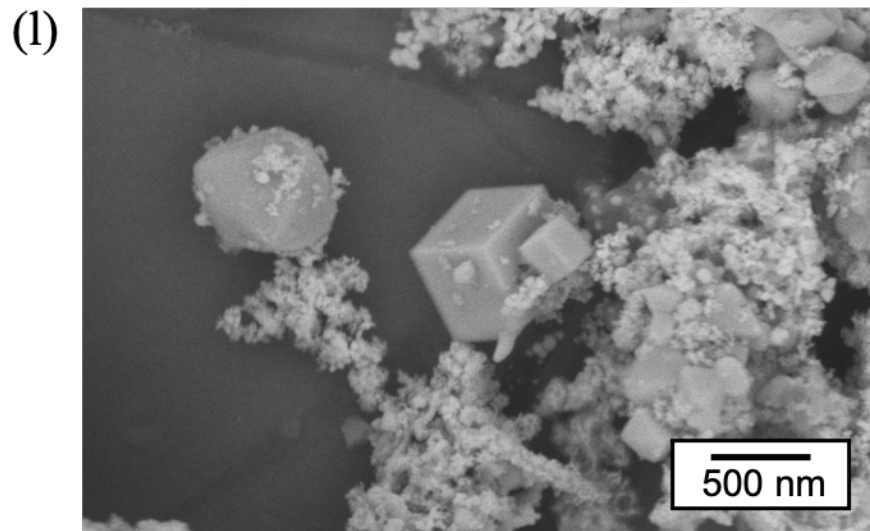
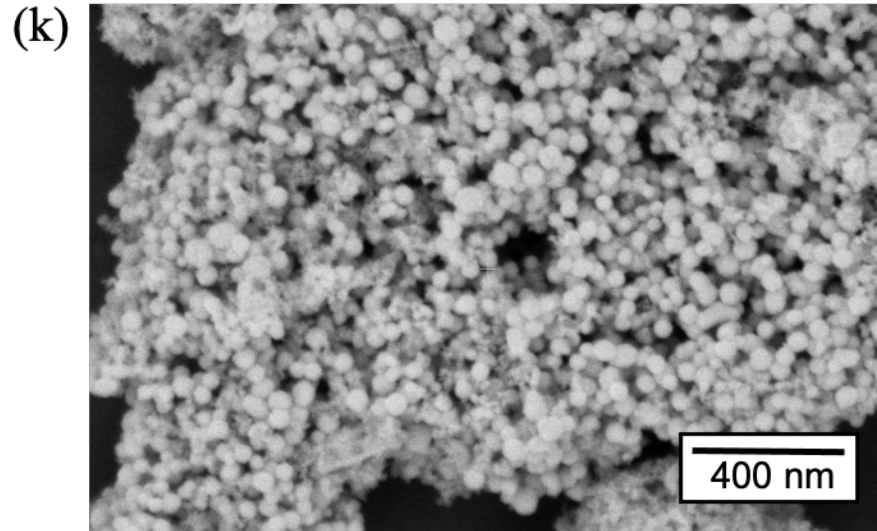


Figure 3-20. Scanning electron micrographs of Y-doped TaC samples with different doping levels using metallic Y as the precursor: (a) and (b) 10 at% calculated Y amount (Y-1); (c) to (e) 15 at% calculated Y amount (Y-2); (f) to (h) 20 at% calculated Y amount (Y-3); (i) and (j) 25 at% calculated Y amount (Y-4); (k) and (l) 30 at% calculated Y amount (Y-5). (continued)

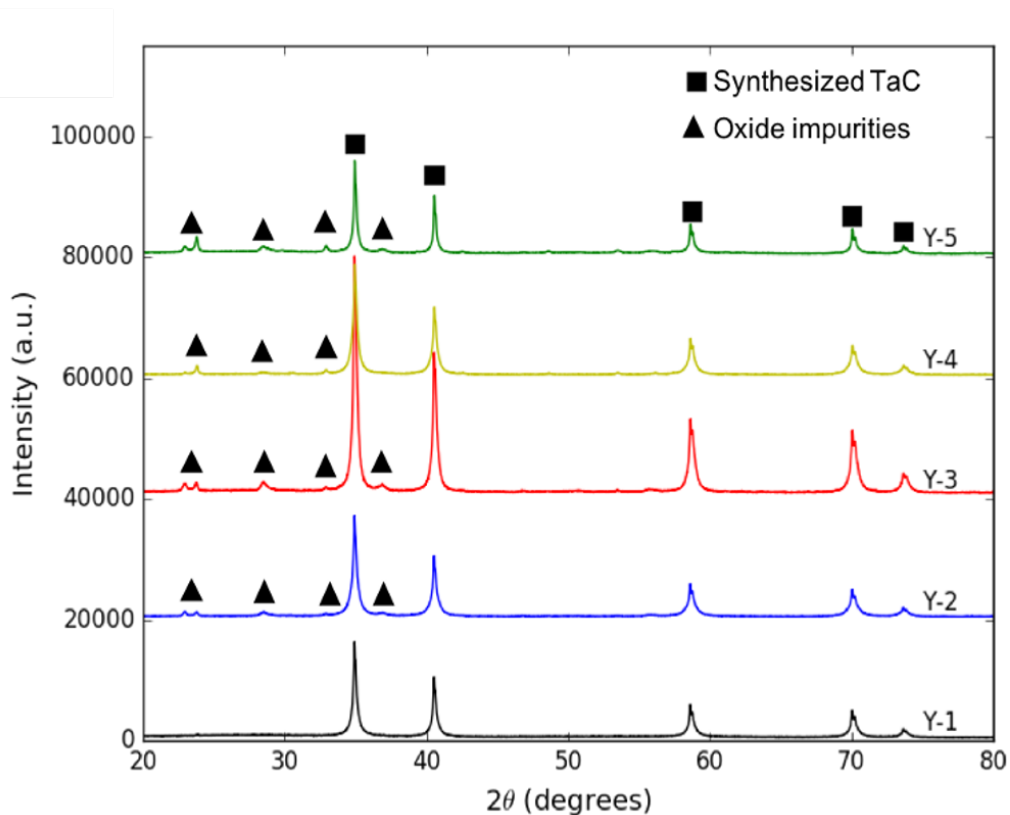


Figure 3-21. X-ray diffraction patterns of Y-doped TaC samples with different doping levels using metallic Y as the precursor.

Although there are still some secondary phases detected by the XRD, the overall phase purity has improved to a great extent compared to the previous trials where the dopant precursor was yttrium salts. The SEM micrographs indicate that most of the particles preserve well-defined shapes, including spheres and highly-faceted cubic particles. Moreover, it is observed that cubic particles generally have larger sizes, while their percent population is much smaller than the spherical counterparts. Figure 3-22 statistically summarizes the abundance of TaC particle morphologies in the Y-doping series by manually counting and assessing at least 900 particles. It was confirmed that non-faceted particles are still the dominating morphology. No other polyhedron-typed faceting was found in all Y-doped systems. Further, no clear trend of the

morphological abundance against the Y concentration can be drawn, suggesting that the presence of particle faceting is not a strong function of the dopant concentration in this case. One possible explanation to this phenomenon is that the actual Y concentration in each sample detected by the EDS technique on SEM only ranges from 0.6 to 2.3 at%, as shown in Table 2-1, evidencing that a significant portion of elemental Y was lost over the course of either the reaction or the powder washing procedures. However, even higher Y concentrations were not attempted due to the concern of severe oxidation.

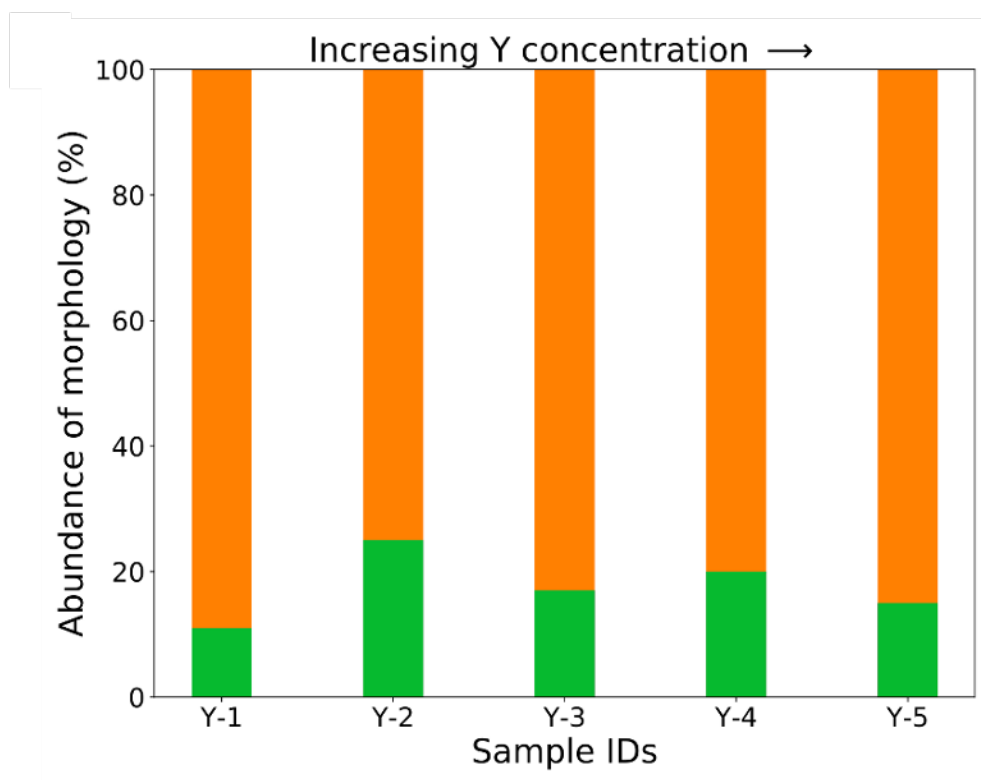


Figure 3-22. Statistical abundance of particle morphology for Y-doped TaC samples with different doping levels using metallic Y as the precursor. Color legends: Orange – non-faceted particles; Green – cubic/truncated cubic particles.

It is intriguing that cubic particles are the only form of faceting observed in the Y-TaC system, despite its relatively small population. The understanding of this part will be deepened and expanded in the later paragraphs based on the insights from DFT modeling.

3.3.3. Nb/Zr/Hf-Doped TaC

Figures 3-23 to 3-25 provide the general morphology of TaC particles with Nb, Zr, and Hf doping respectively. None of these systems shows signs of particle faceting. Therefore, these dopants can be categorized as “ineffective morphology modifier” having no impact on the growth of TaC particles. The Nb-TaC system also served as the contrast to those “effective morphology modifier” in the DFT simulation study to unveil the mechanisms of the dopant-induced morphology change. One noticeable difference on the Nb-TaC system compared to the Y-TaC, as well as the Ni-, Co-, and Fe-TaC systems is that the actual concentration of Nb detected by EDS (ranges from 4.4 to 14.3 at%) is much higher than other dopant elements hereby mentioned. This is likely caused by the high bulk solubility of Nb in TaC, as NbC and TaC are mutually soluble in each other.

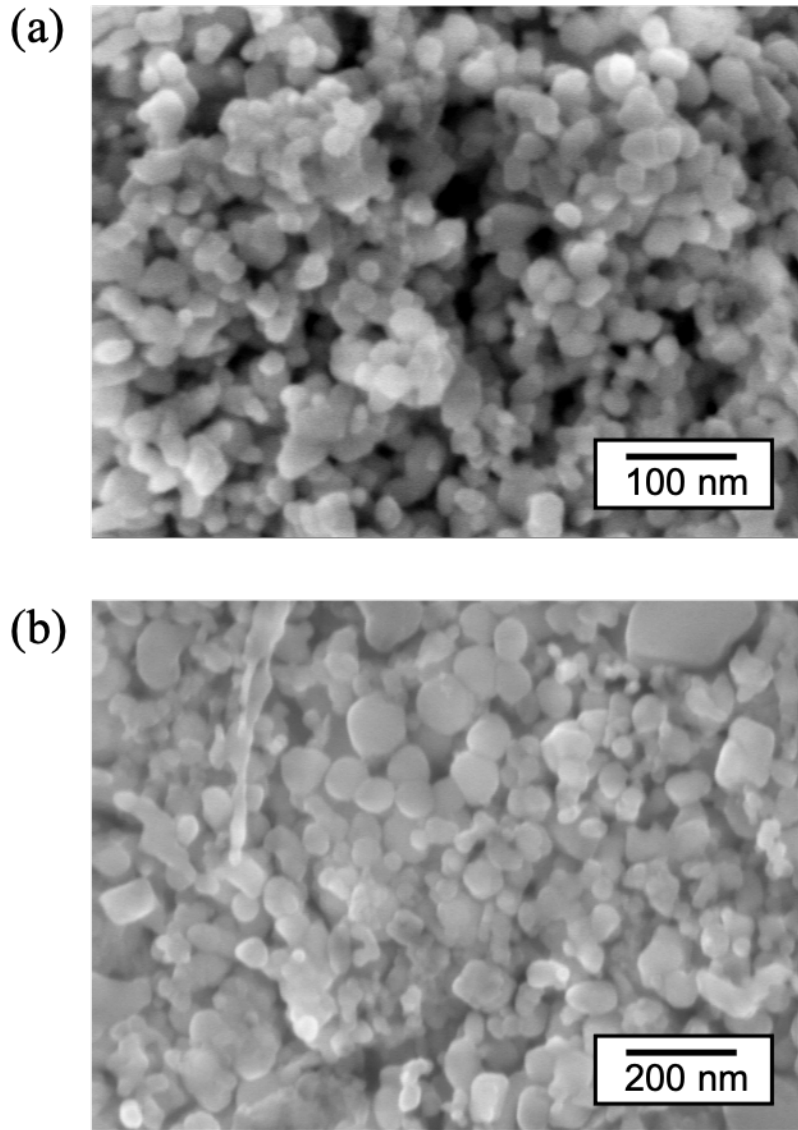


Figure 3-23. Scanning electron micrographs of Nb-doped TaC samples with different doping levels using metallic Nb as the precursor: (a) and (b) 10 at% calculated Nb amount (Nb-1); (c) and (d) 15 at% calculated Nb amount (Nb-2); (e) and (f) 20 at% calculated Nb amount (Nb-3).

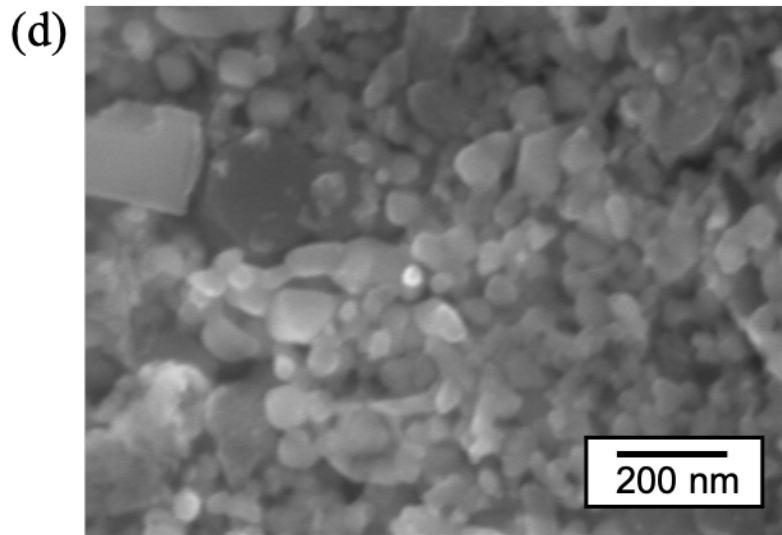
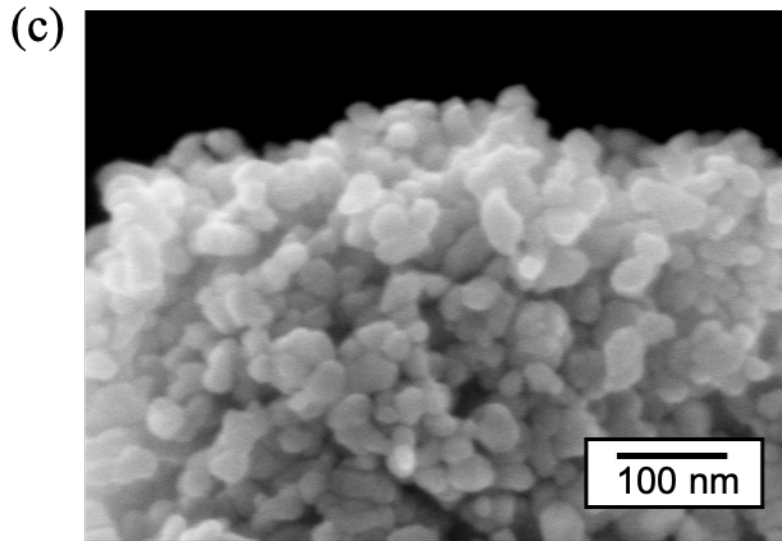


Figure 3-23. Scanning electron micrographs of Nb-doped TaC samples with different doping levels using metallic Nb as the precursor: (a) and (b) 10 at% calculated Nb amount (Nb-1); (c) and (d) 15 at% calculated Nb amount (Nb-2); (e) and (f) 20 at% calculated Nb amount (Nb-3). (continued)

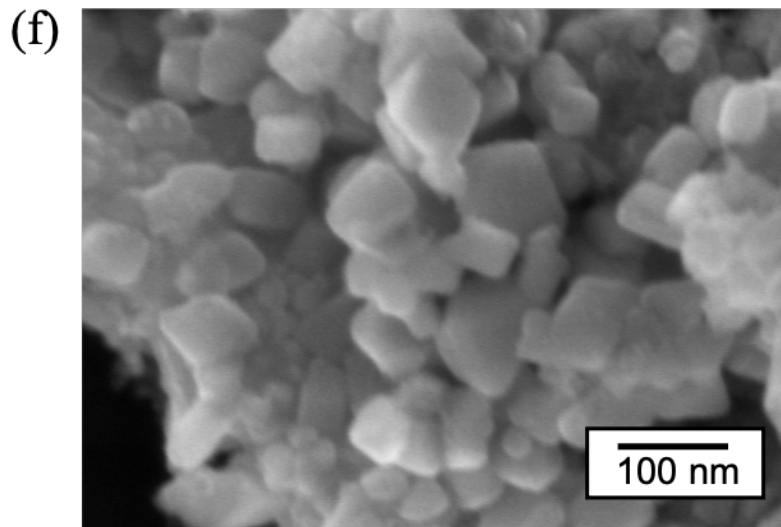
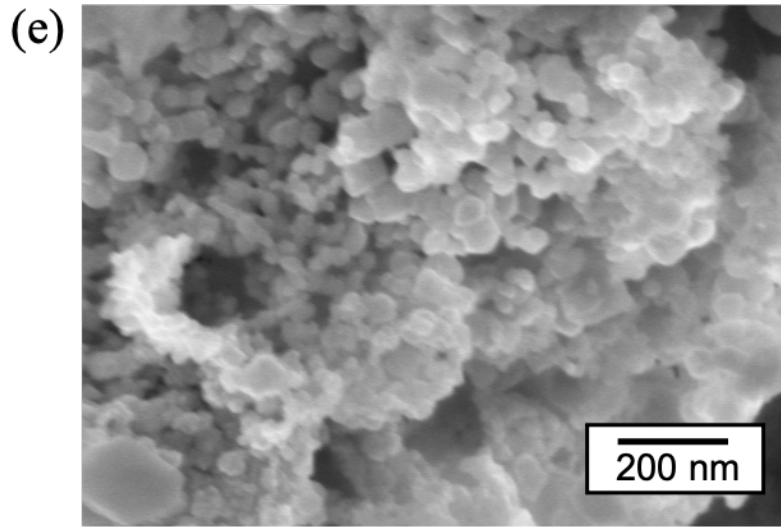


Figure 3-23. Scanning electron micrographs of Nb-doped TaC samples with different doping levels using metallic Nb as the precursor: (a) and (b) 10 at% calculated Nb amount (Nb-1); (c) and (d) 15 at% calculated Nb amount (Nb-2); (e) and (f) 20 at% calculated Nb amount (Nb-3). (continued)

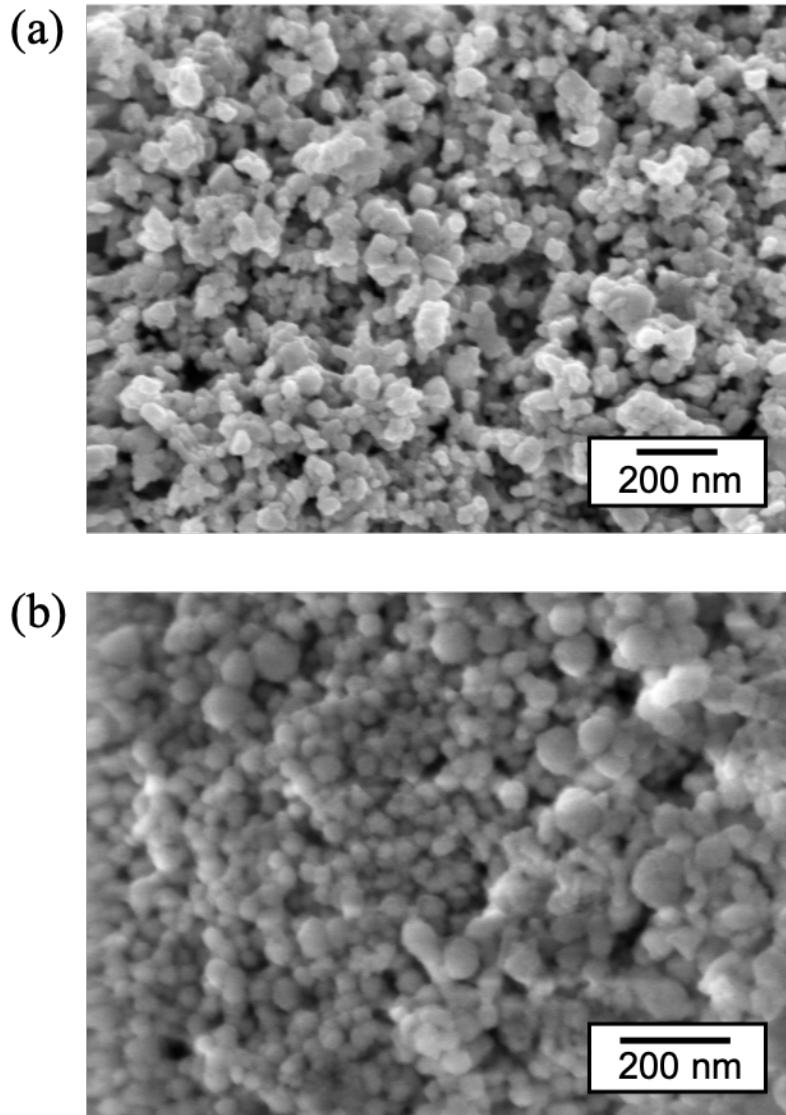


Figure 3-24. Scanning electron micrographs of Zr-doped TaC samples with different doping levels using metallic Zr as the precursor: (a) and (b) 10 at% calculated Zr amount (Zr-1); (c) and (d) 15 at% calculated Zr amount (Zr-2).

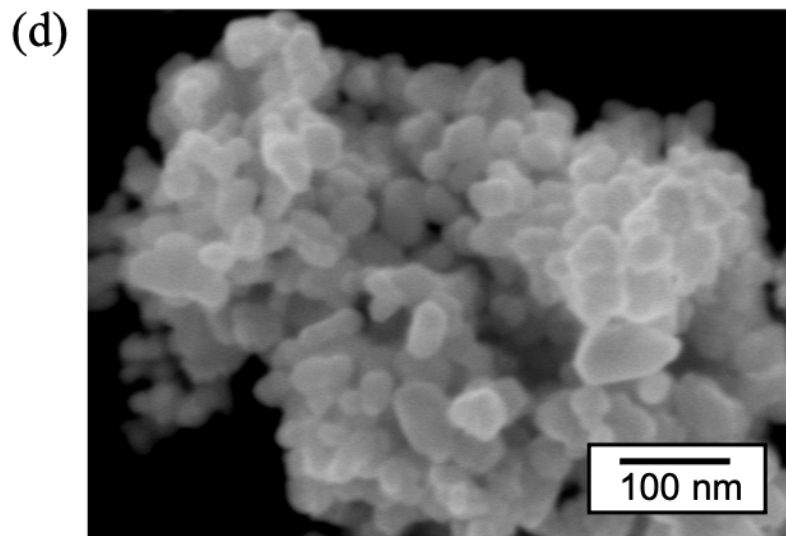
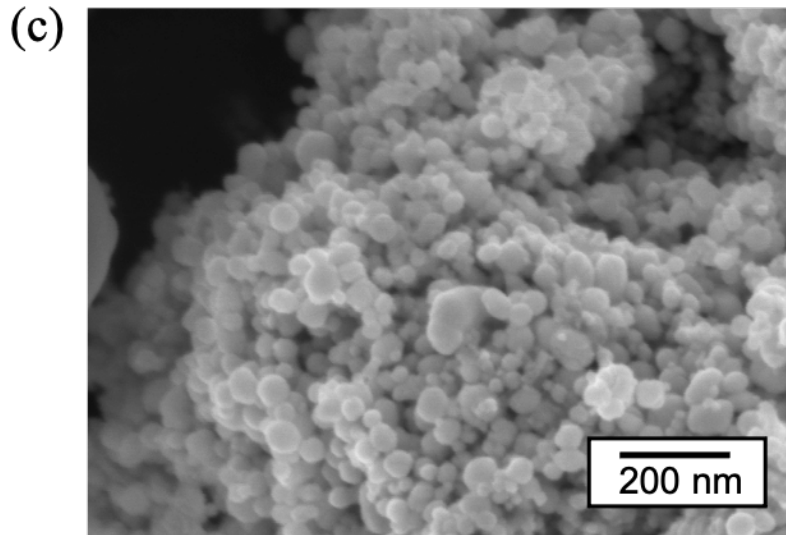


Figure 3-24. Scanning electron micrographs of Zr-doped TaC samples with different doping levels using metallic Zr as the precursor: (a) and (b) 10 at% calculated Zr amount (Zr-1); (c) and (d) 15 at% calculated Zr amount (Zr-2). (continued)

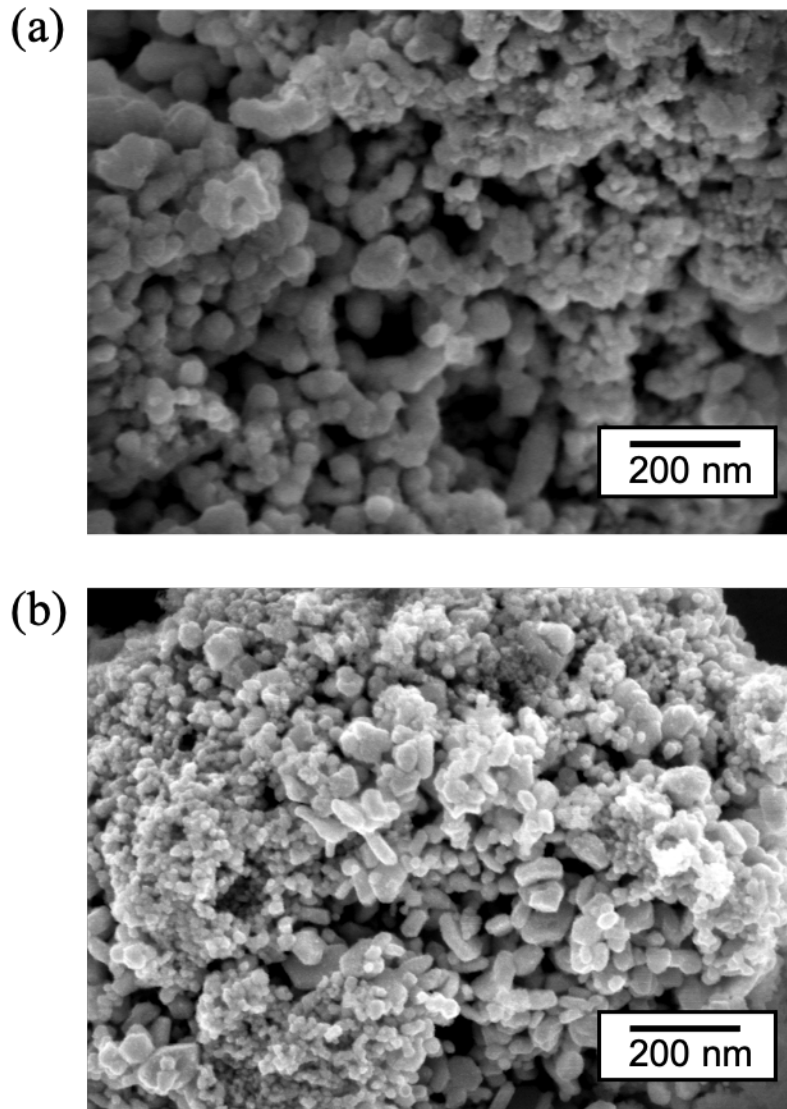


Figure 3-25. Scanning electron micrographs of Hf-doped TaC samples with different doping levels using metallic Hf as the precursor: (a) and (b) 10 at% calculated Hf amount (Hf-1); (c) and (d) 15 at% calculated Hf amount (Hf-2).

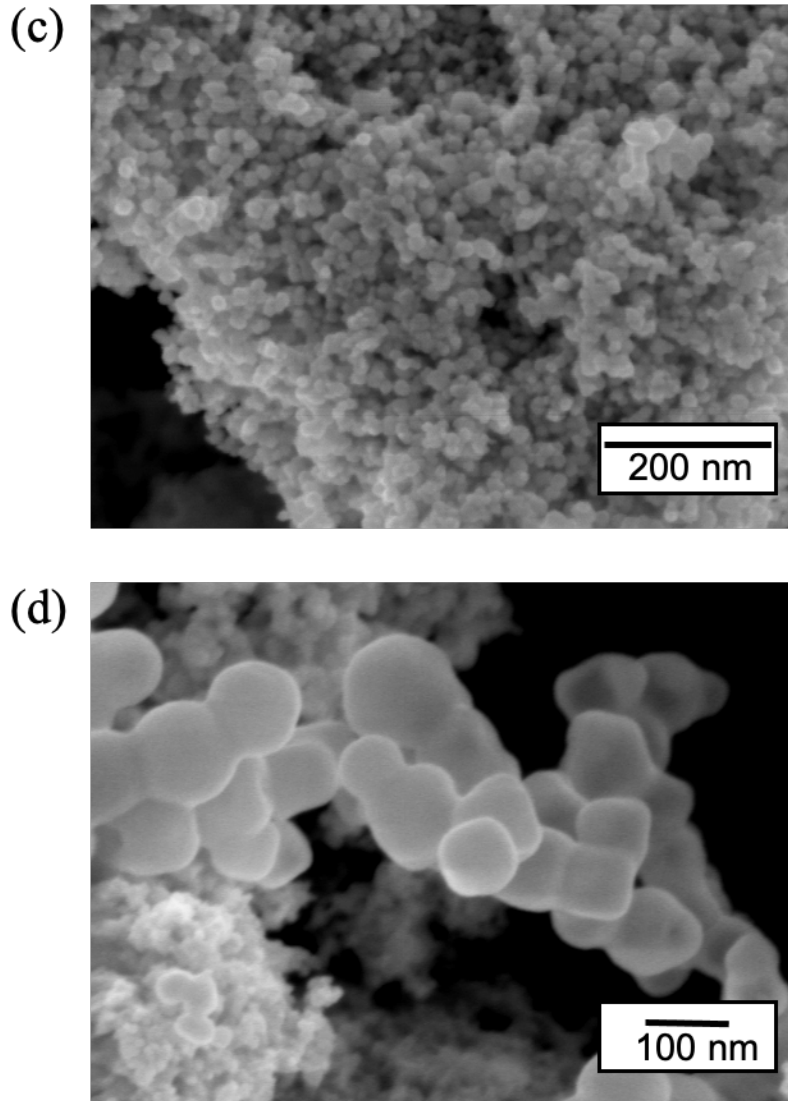


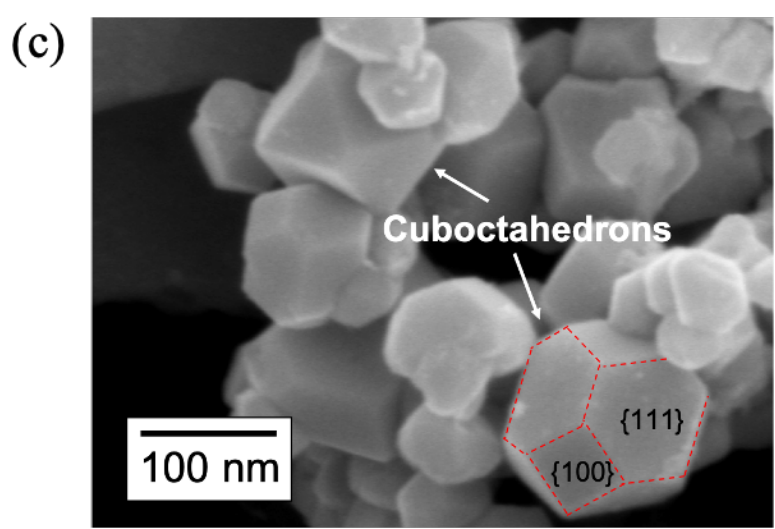
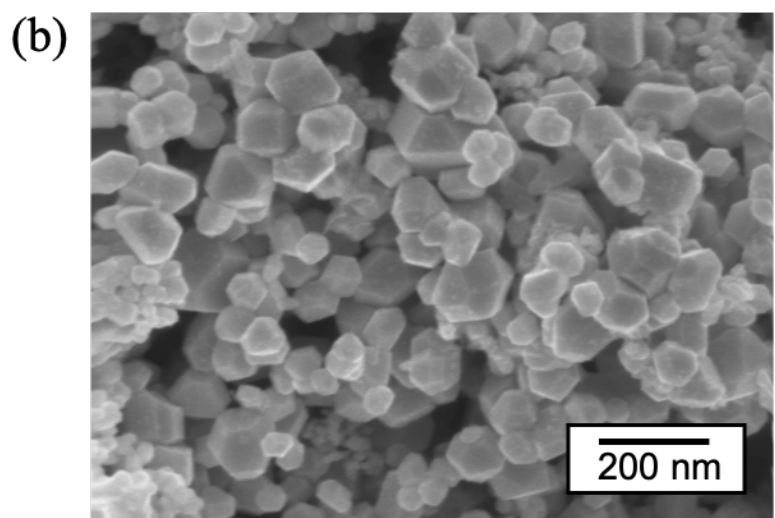
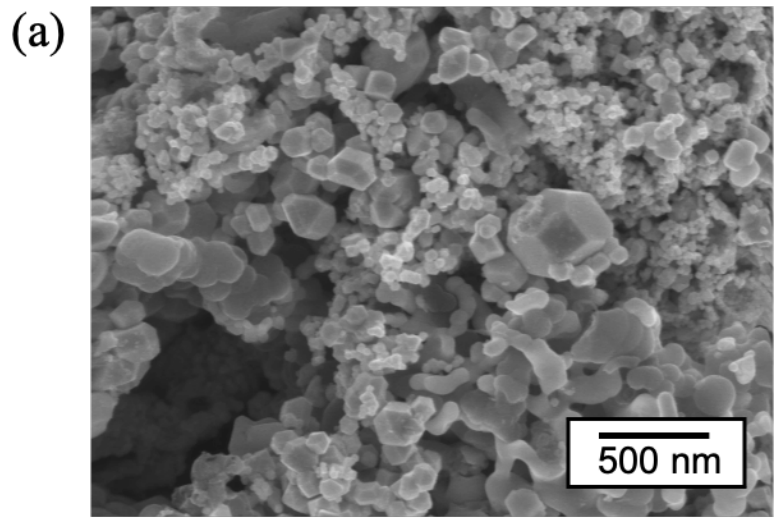
Figure 3-25. Scanning electron micrographs of Hf-doped TaC samples with different doping levels using metallic Hf as the precursor: (a) and (b) 10 at% calculated Hf amount (Hf-1); (c) and (d) 15 at% calculated Hf amount (Hf-2). (continued)

3.3.4. Ni-Doped TaC

Ni was the first dopant in this study to massively induce the faceting of TaC particles, as proven by the SEM micrographs in Figure 3-26. The XRD patterns for the Ni-doped TaC samples (Ni-1 to Ni-6) show high phase purity with minimal amount of secondary phases (Figure 3-27). According to the SEM images, clear crystallographic surfaces along with sharp edges and corners

are exposed in the majority of particles, forming cuboctahedrons. Although the area of different crystallographic surfaces varies particle by particle, cubes or truncated cubes are rarely seen. Sample Ni-4 was counted to own the highest percent population of cuboctahedron particles close to 80% out of all the particles assessed (Figure 3-28). As the final particle morphology is fundamentally determined by the surface energies of each crystallographic planes, it is certain that the incorporation of Ni has influenced the relative growth rate of surfaces by changing their surface energies. Similar to the Y-TaC system, Ni has low bulk solubility in TaC as indicated by the elemental quantification data through EDS in Table 2-1.

Figure 3-26. Scanning electron micrographs of Ni-doped TaC samples with different doping levels using metallic Ni as the precursor: (a)-(c) 5 at% calculated Ni amount (Ni-1), with (c) showing particularly the typical cuboctahedron morphology; (d) and (e) 10 at% calculated Ni amount (Ni-2); (f) and (g) 15 at% calculated Ni amount (Ni-3); (h)-(j) 20 at% calculated Ni amount (Ni-4); (k) and (l) 25 at% calculated Ni amount (Ni-5); (m) and (n) 30 at% calculated Ni amount (Ni-6).



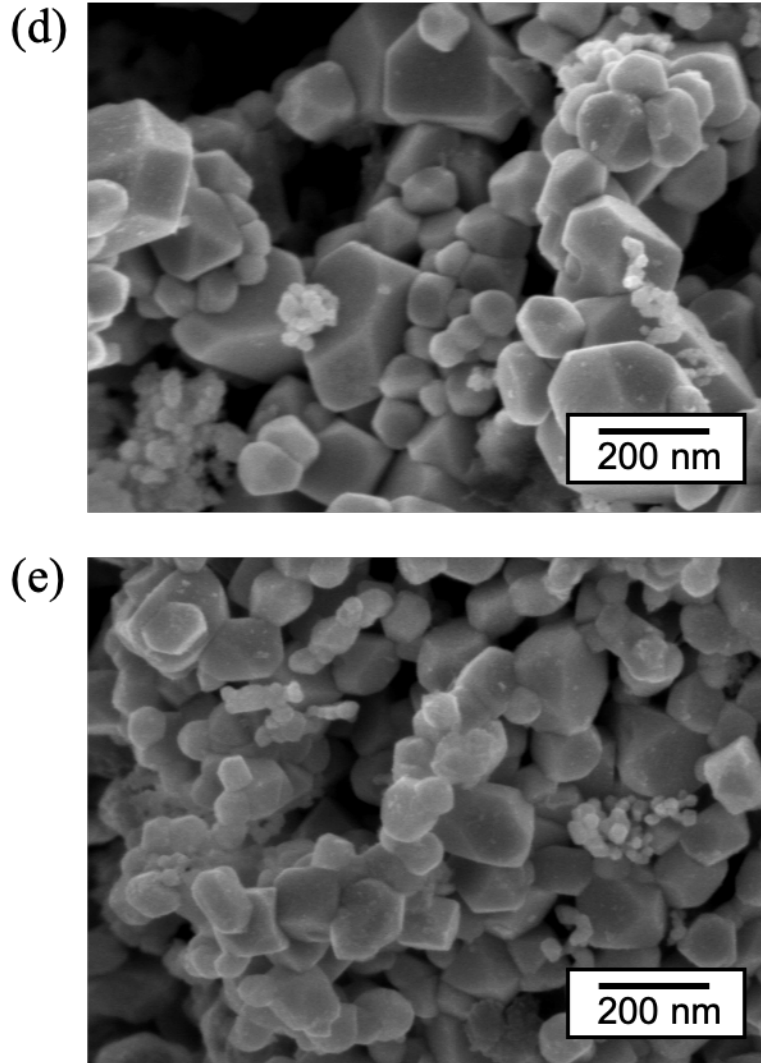


Figure 3-26. Scanning electron micrographs of Ni-doped TaC samples with different doping levels using metallic Ni as the precursor: (a)-(c) 5 at% calculated Ni amount (Ni-1), with (c) showing particularly the typical cubo-octahedron morphology; (d) and (e) 10 at% calculated Ni amount (Ni-2); (f) and (g) 15 at% calculated Ni amount (Ni-3); (h)-(j) 20 at% calculated Ni amount (Ni-4); (k) and (l) 25 at% calculated Ni amount (Ni-5); (m) and (n) 30 at% calculated Ni amount (Ni-6). (continued)

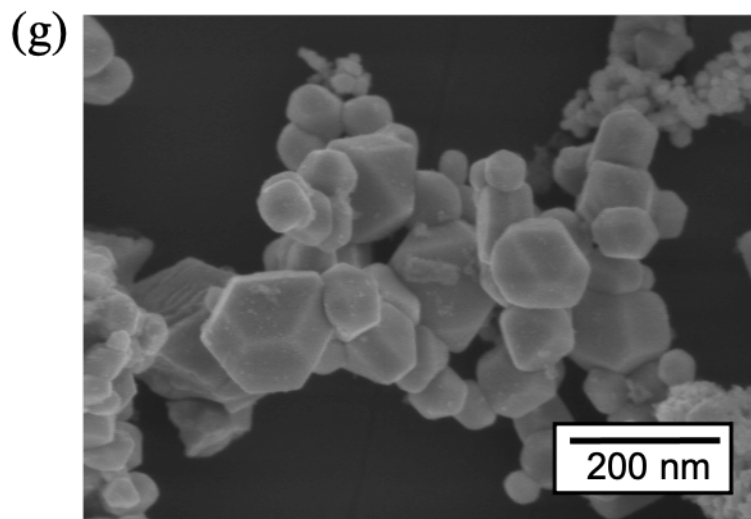
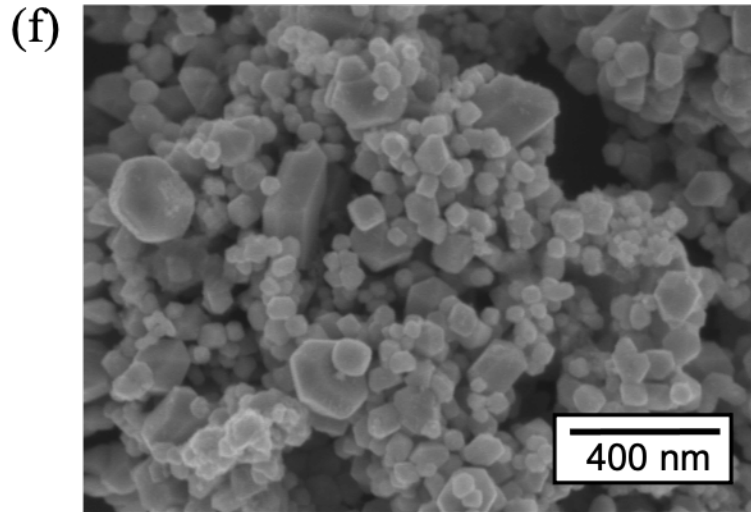
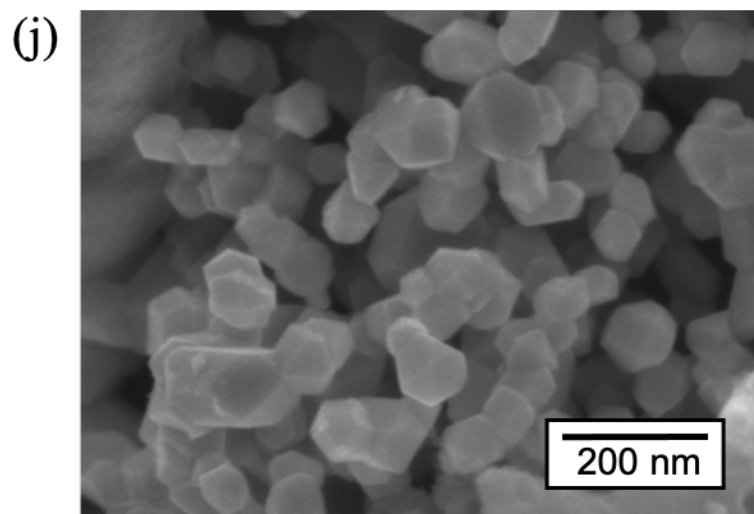
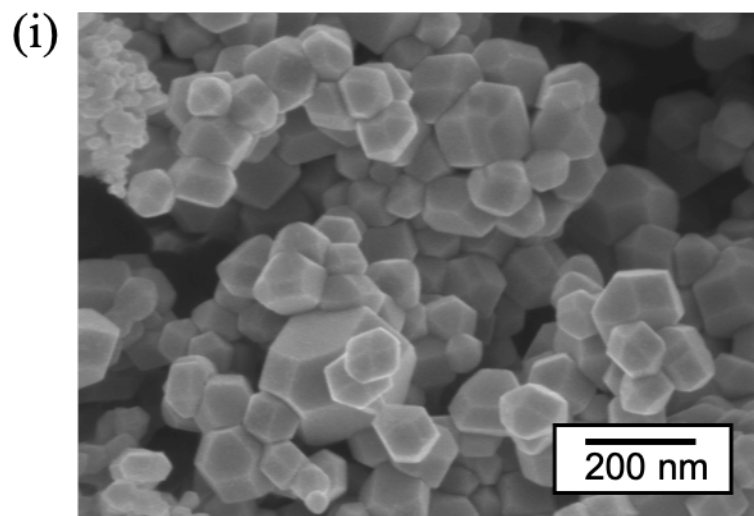
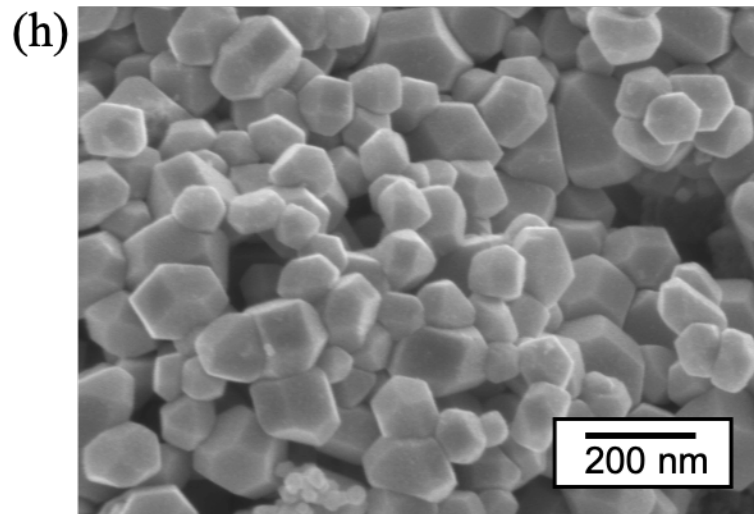


Figure 3-26. Scanning electron micrographs of Ni-doped TaC samples with different doping levels using metallic Ni as the precursor: (a)-(c) 5 at% calculated Ni amount (Ni-1), with (c) showing particularly the typical cuboctahedron morphology; (d) and (e) 10 at% calculated Ni amount (Ni-2); (f) and (g) 15 at% calculated Ni amount (Ni-3); (h)-(j) 20 at% calculated Ni amount (Ni-4); (k) and (l) 25 at% calculated Ni amount (Ni-5); (m) and (n) 30 at% calculated Ni amount (Ni-6). (continued)

Figure 3-26. Scanning electron micrographs of Ni-doped TaC samples with different doping levels using metallic Ni as the precursor: (a)-(c) 5 at% calculated Ni amount (Ni-1), with (c) showing particularly the typical cuboctahedron morphology; (d) and (e) 10 at% calculated Ni amount (Ni-2); (f) and (g) 15 at% calculated Ni amount (Ni-3); (h)-(j) 20 at% calculated Ni amount (Ni-4); (k) and (l) 25 at% calculated Ni amount (Ni-5); (m) and (n) 30 at% calculated Ni amount (Ni-6). (continued)



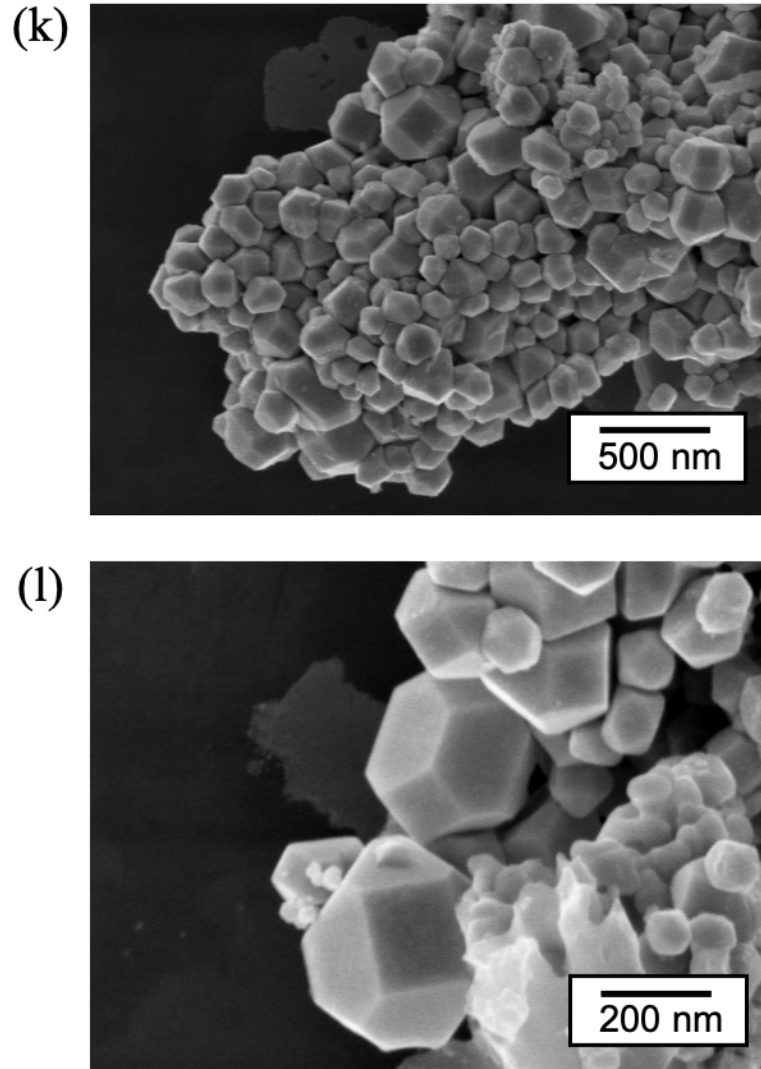


Figure 3-26. Scanning electron micrographs of Ni-doped TaC samples with different doping levels using metallic Ni as the precursor: (a)-(c) 5 at% calculated Ni amount (Ni-1), with (c) showing particularly the typical cubo-octahedron morphology; (d) and (e) 10 at% calculated Ni amount (Ni-2); (f) and (g) 15 at% calculated Ni amount (Ni-3); (h)-(j) 20 at% calculated Ni amount (Ni-4); (k) and (l) 25 at% calculated Ni amount (Ni-5); (m) and (n) 30 at% calculated Ni amount (Ni-6). (continued)

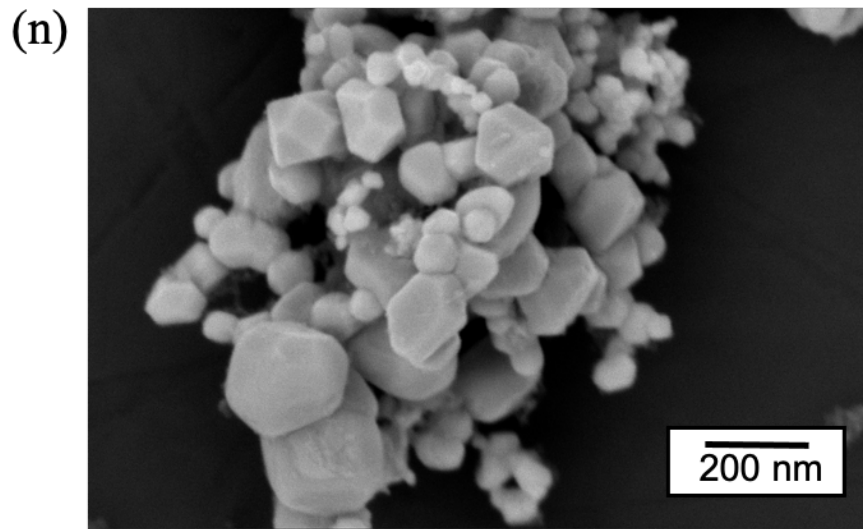
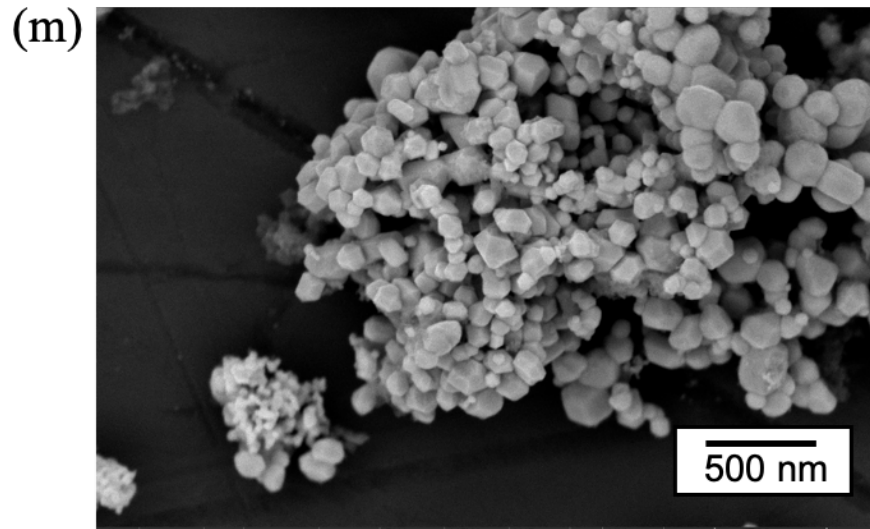


Figure 3-26. Scanning electron micrographs of Ni-doped TaC samples with different doping levels using metallic Ni as the precursor: (a)-(c) 5 at% calculated Ni amount (Ni-1), with (c) showing particularly the typical cubo-octahedron morphology; (d) and (e) 10 at% calculated Ni amount (Ni-2); (f) and (g) 15 at% calculated Ni amount (Ni-3); (h)-(j) 20 at% calculated Ni amount (Ni-4); (k) and (l) 25 at% calculated Ni amount (Ni-5); (m) and (n) 30 at% calculated Ni amount (Ni-6). (continued)

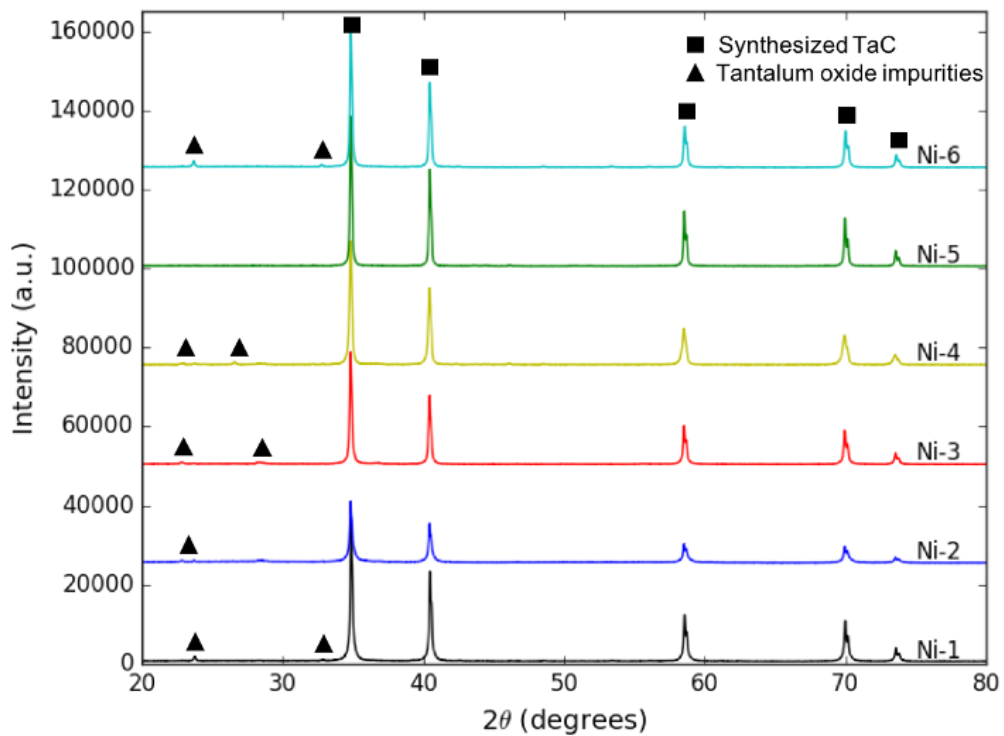


Figure 3-27. X-ray diffraction patterns of Ni-doped TaC samples with different doping levels using metallic Ni as the precursor.

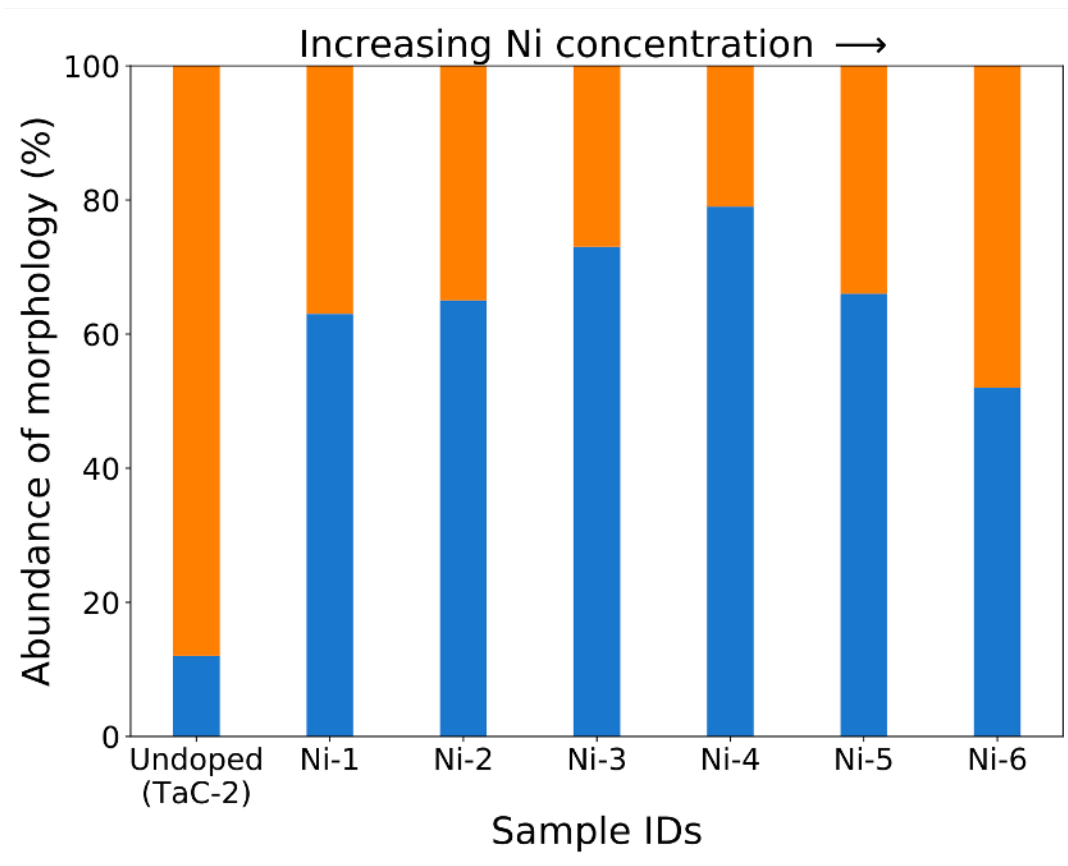


Figure 3-28. Statistical abundance of particle morphology for Ni-doped TaC samples with different doping levels using metallic Ni as the precursor in comparison with the undoped TaC sample. Color legends: Orange – non-faceted particles; Blue – cuboctahedron particles.

To further evaluate the effectiveness of Ni for modifying the morphology, Ni-doped ZrC samples was also synthesized and briefly characterized in addition to the Ni-TaC system. Figure 3-29 below presents that the morphology of ZrC particles evolved from facet-less shapes to cuboctahedrons after incorporating Ni.

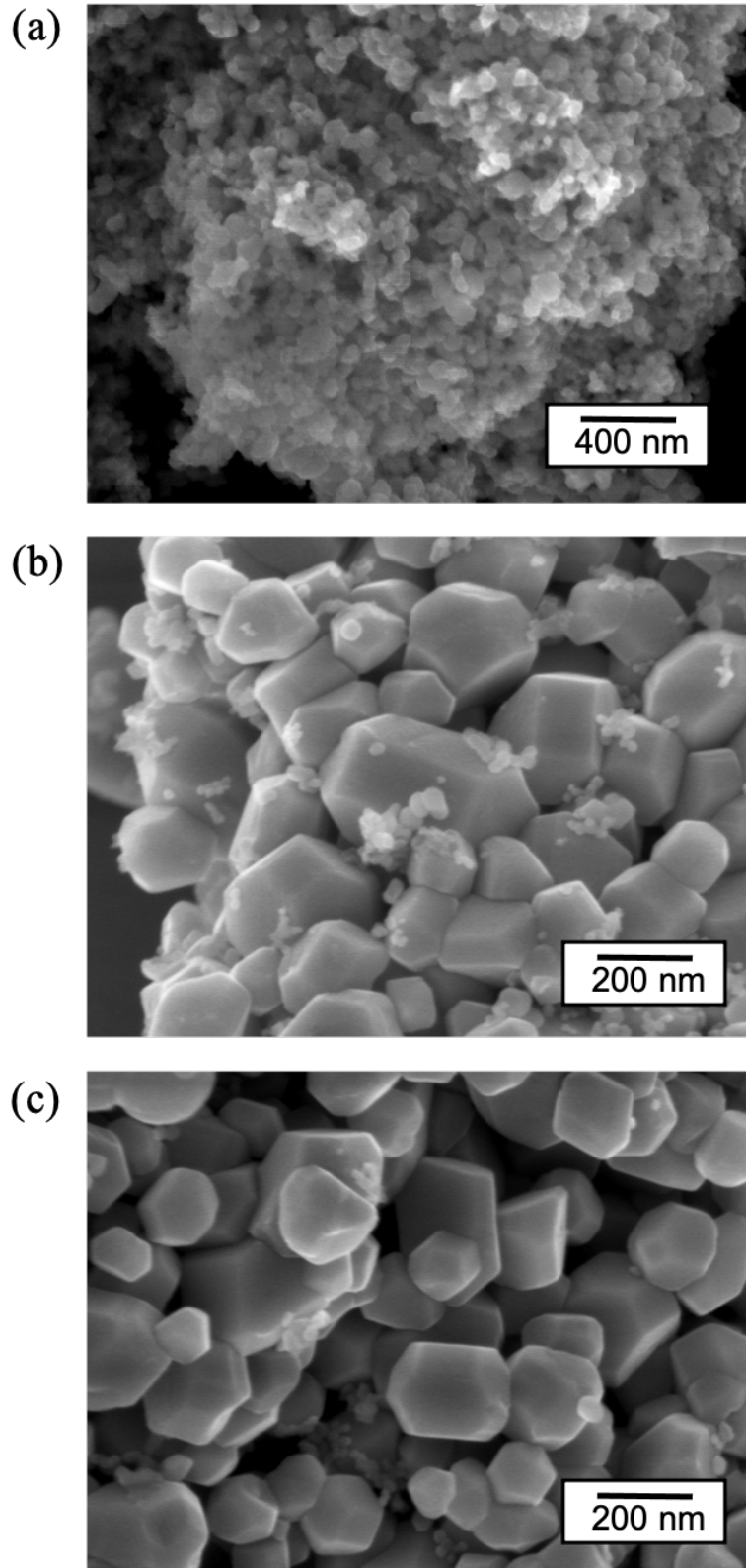


Figure 3-29. Scanning electron micrographs of (a) undoped ZrC sample, (b) Ni-doped ZrC sample with 10 at% calculated amount of Ni, and (c) 15 at% calculated amount of Ni.

3.3.5. Co-Doped TaC

SEM images below revealed that Co doping behaves similar to Ni on the type of morphology it induced, namely, the cuboctahedrons (Figure 3-30). It also yielded excellent phase purity of the products (Figure 3-31). However, the overall percent population of cuboctahedron particles is less than that of Ni-doped samples with its highest abundance being close to 60% on sample Co-3, as summarized by the statistical abundance chart in Figure 3-32.

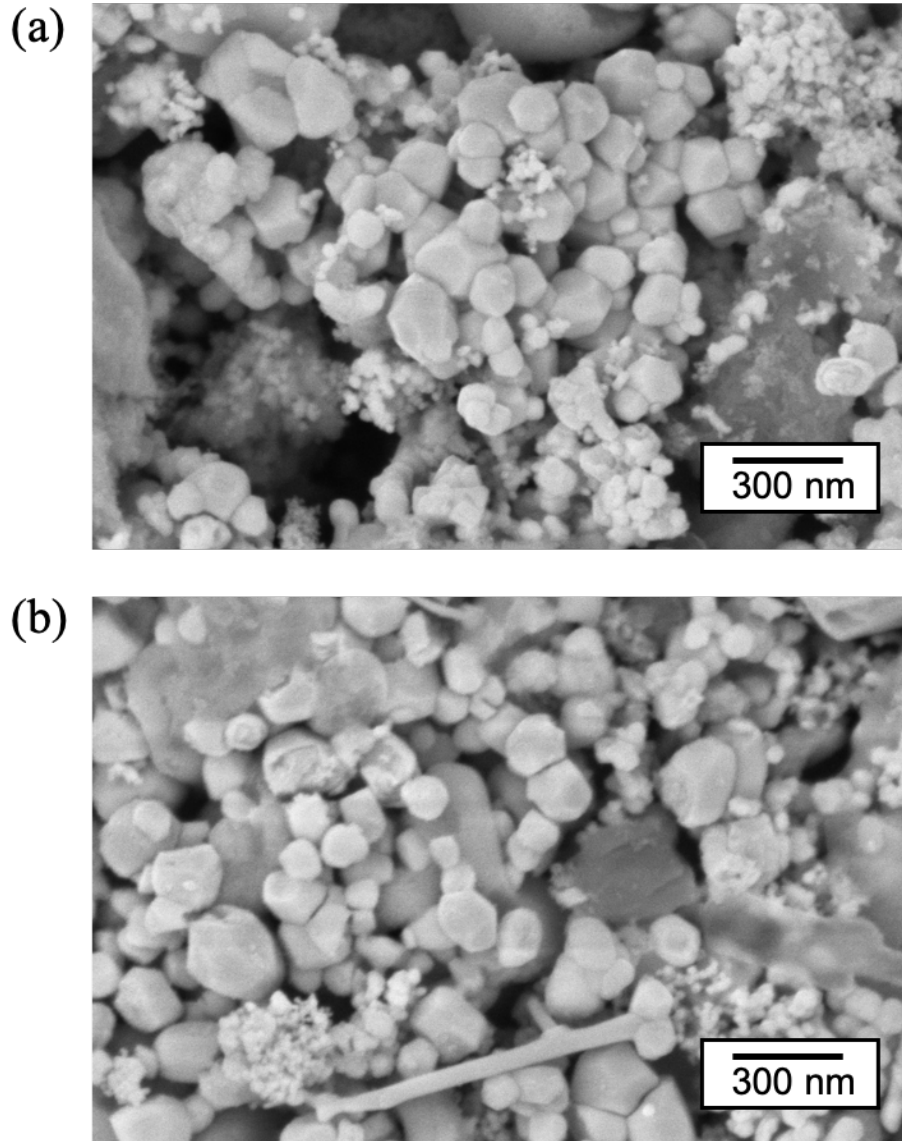


Figure 3-30. Scanning electron micrographs of Co-doped TaC samples with different doping levels using metallic Co as the precursor: (a) and (b) 5 at% calculated Co amount (Co-1); (c) and (d) 10 at% calculated Co amount (Co-2); (e) and (f) 15 at% calculated Co amount (Co-3); (g) and (h) 20 at% calculated Co amount (Co-4); (i) and (j) 25 at% calculated Co amount (Co-5); (k) and (l) 30 at% calculated Co amount (Co-6).

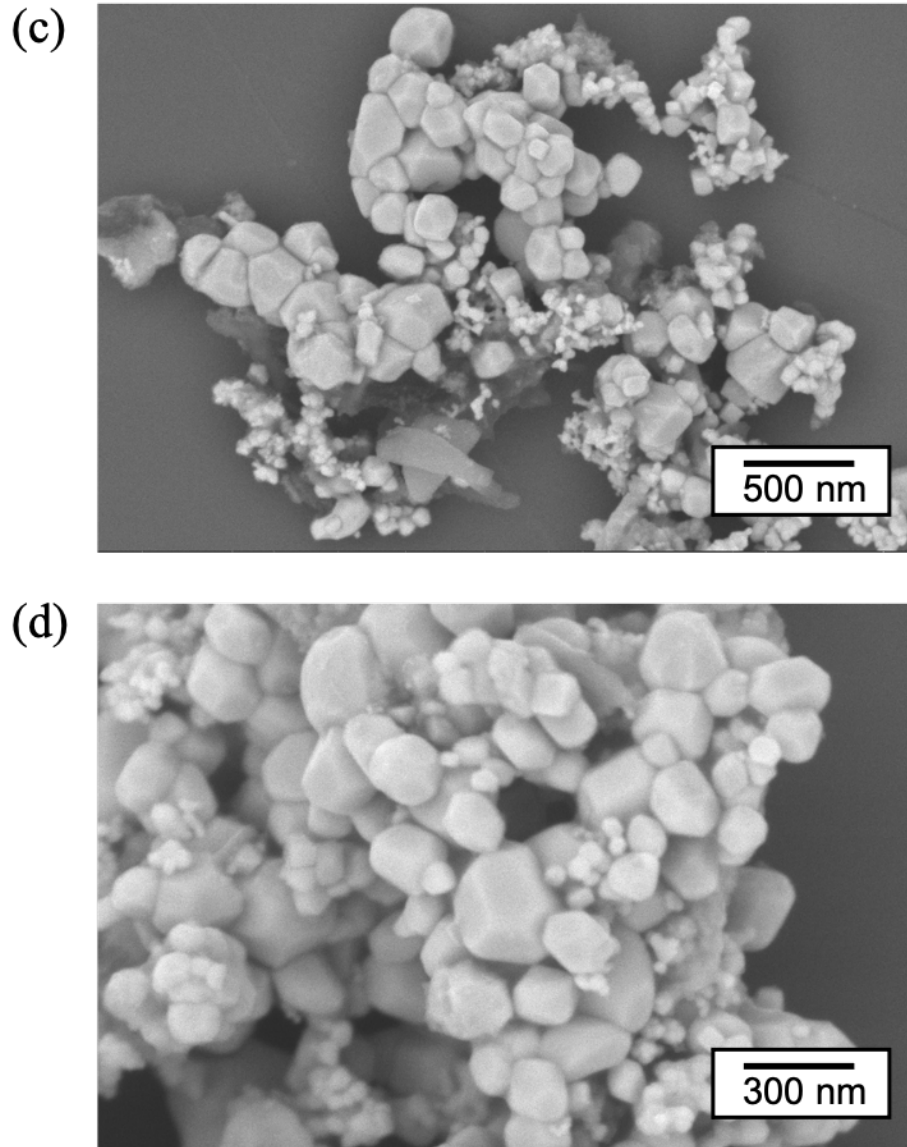


Figure 3-30. Scanning electron micrographs of Co-doped TaC samples with different doping levels using metallic Co as the precursor: (a) and (b) 5 at% calculated Co amount (Co-1); (c) and (d) 10 at% calculated Co amount (Co-2); (e) and (f) 15 at% calculated Co amount (Co-3); (g) and (h) 20 at% calculated Co amount (Co-4); (i) and (j) 25 at% calculated Co amount (Co-5); (k) and (l) 30 at% calculated Co amount (Co-6). (continued)

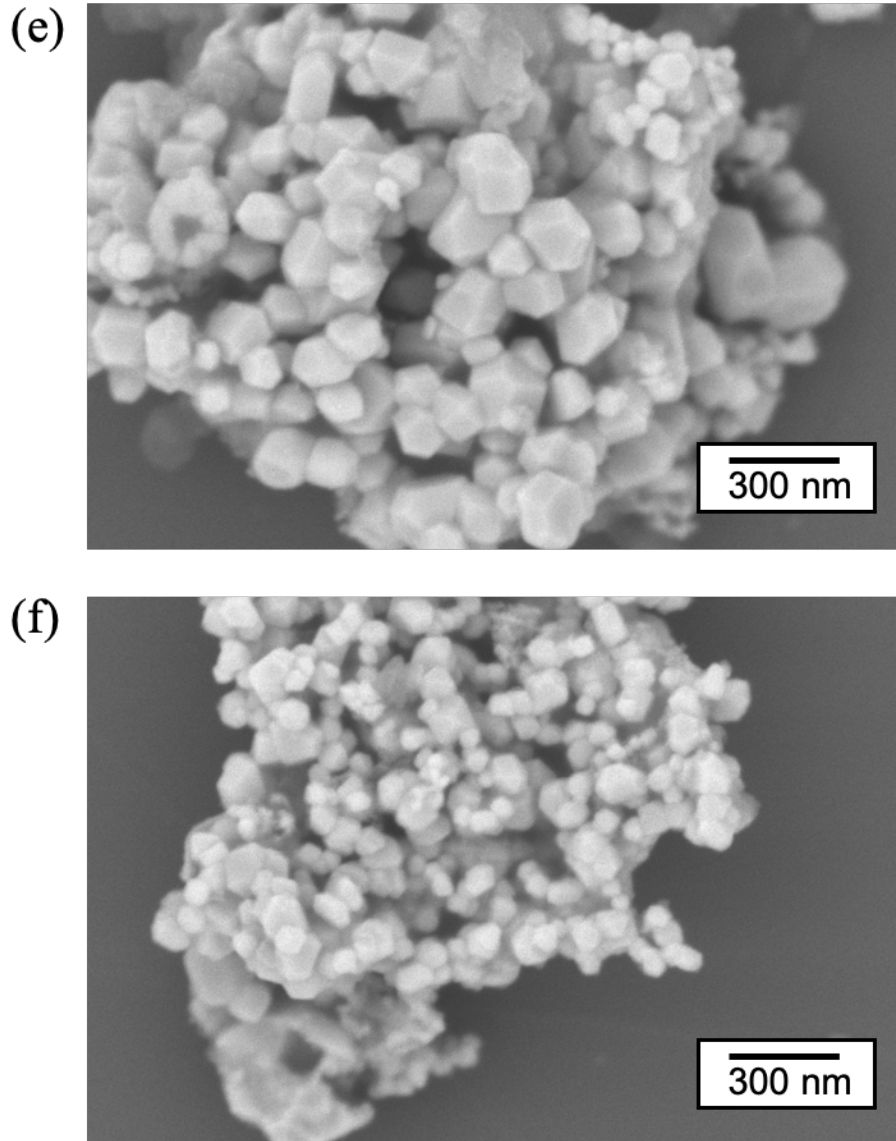


Figure 3-30. Scanning electron micrographs of Co-doped TaC samples with different doping levels using metallic Co as the precursor: (a) and (b) 5 at% calculated Co amount (Co-1); (c) and (d) 10 at% calculated Co amount (Co-2); (e) and (f) 15 at% calculated Co amount (Co-3); (g) and (h) 20 at% calculated Co amount (Co-4); (i) and (j) 25 at% calculated Co amount (Co-5); (k) and (l) 30 at% calculated Co amount (Co-6). (continued)

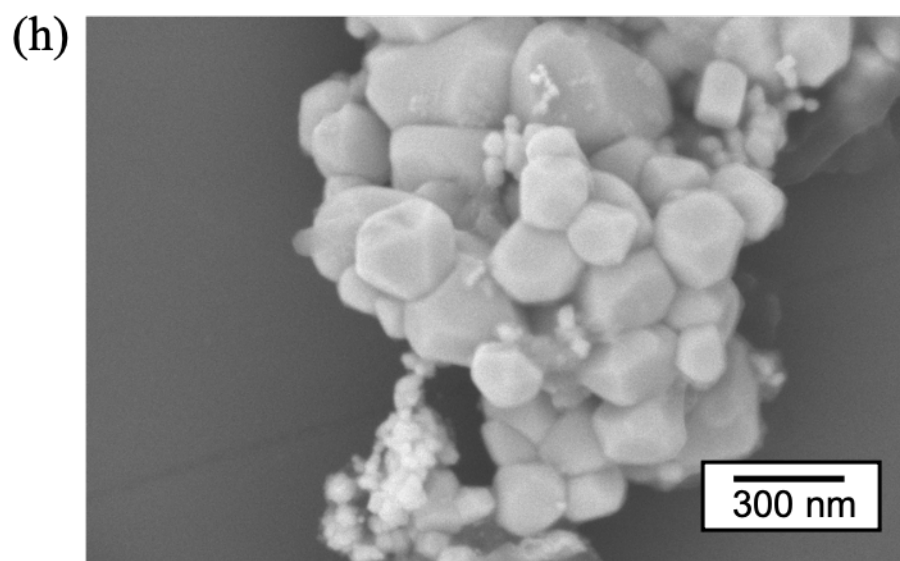
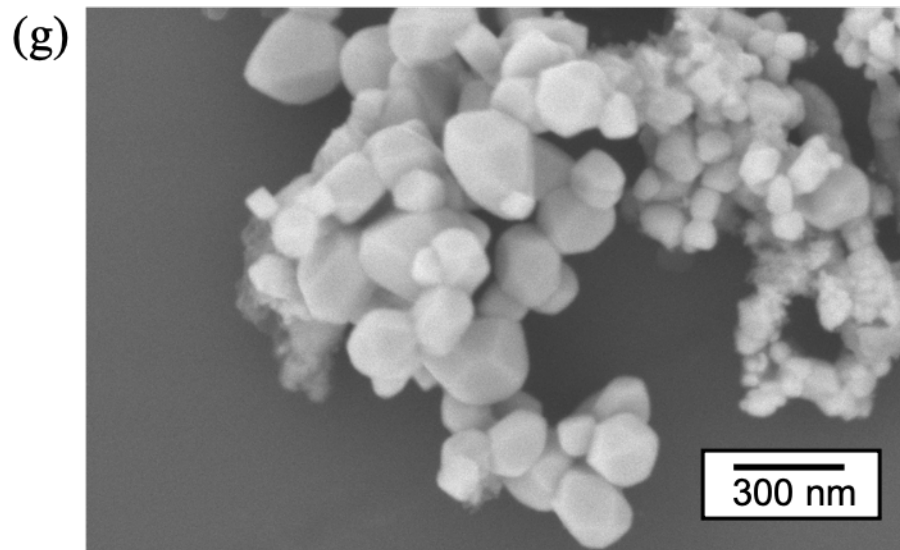


Figure 3-30. Scanning electron micrographs of Co-doped TaC samples with different doping levels using metallic Co as the precursor: (a) and (b) 5 at% calculated Co amount (Co-1); (c) and (d) 10 at% calculated Co amount (Co-2); (e) and (f) 15 at% calculated Co amount (Co-3); (g) and (h) 20 at% calculated Co amount (Co-4); (i) and (j) 25 at% calculated Co amount (Co-5); (k) and (l) 30 at% calculated Co amount (Co-6). (continued)

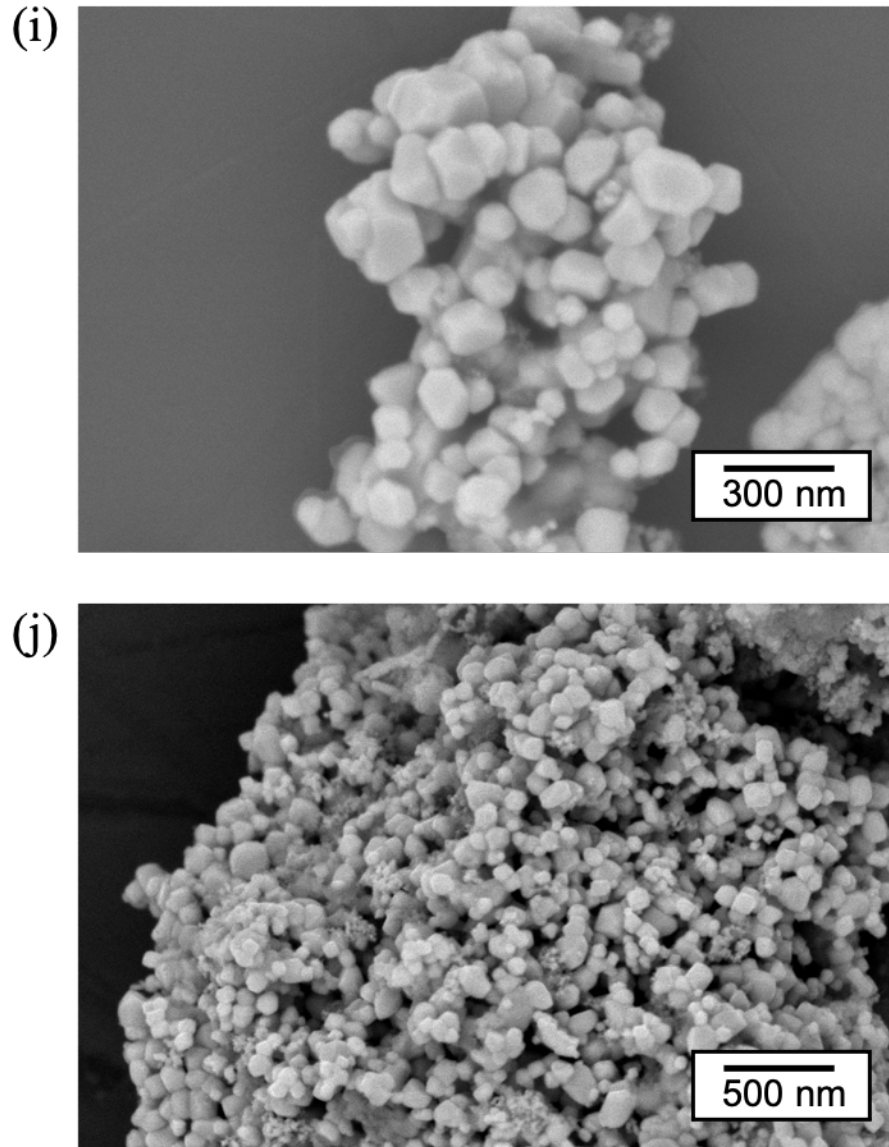


Figure 3-30. Scanning electron micrographs of Co-doped TaC samples with different doping levels using metallic Co as the precursor: (a) and (b) 5 at% calculated Co amount (Co-1); (c) and (d) 10 at% calculated Co amount (Co-2); (e) and (f) 15 at% calculated Co amount (Co-3); (g) and (h) 20 at% calculated Co amount (Co-4); (i) and (j) 25 at% calculated Co amount (Co-5); (k) and (l) 30 at% calculated Co amount (Co-6). (continued)

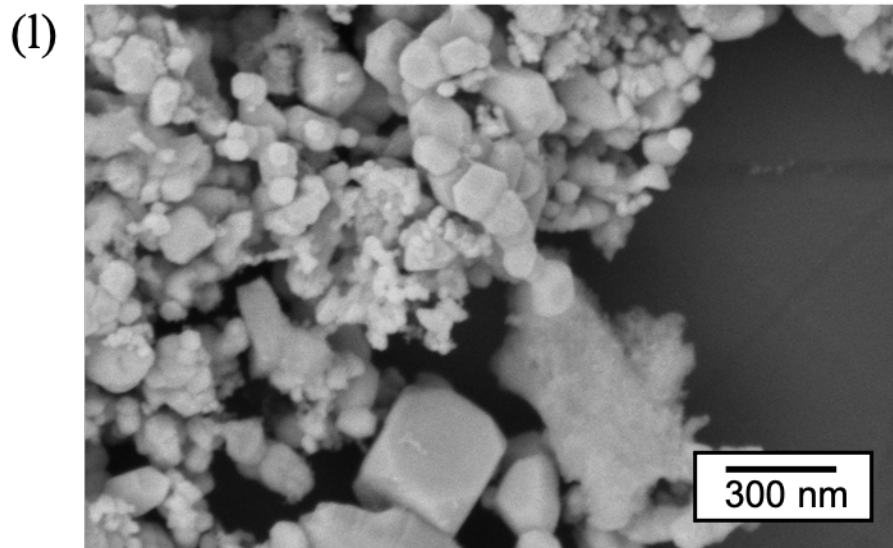
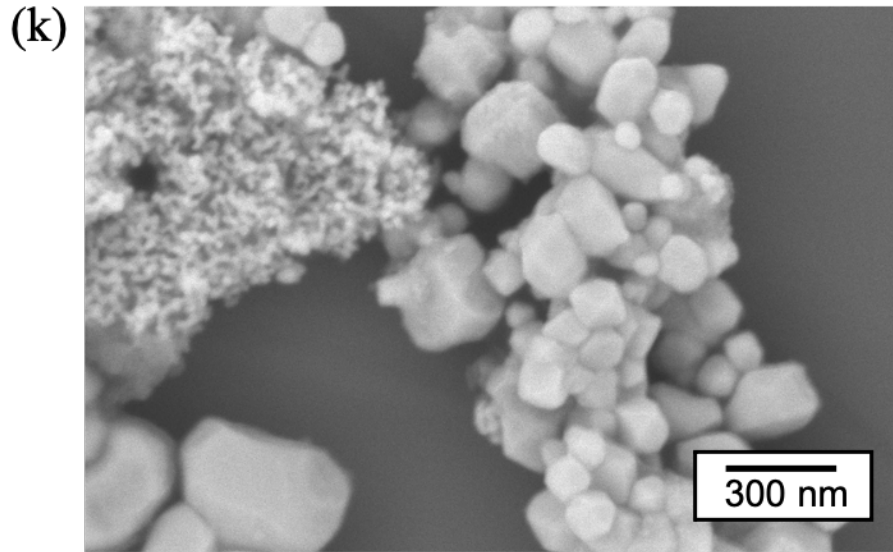


Figure 3-30. Scanning electron micrographs of Co-doped TaC samples with different doping levels using metallic Co as the precursor: (a) and (b) 5 at% calculated Co amount (Co-1); (c) and (d) 10 at% calculated Co amount (Co-2); (e) and (f) 15 at% calculated Co amount (Co-3); (g) and (h) 20 at% calculated Co amount (Co-4); (i) and (j) 25 at% calculated Co amount (Co-5); (k) and (l) 30 at% calculated Co amount (Co-6). (continued)

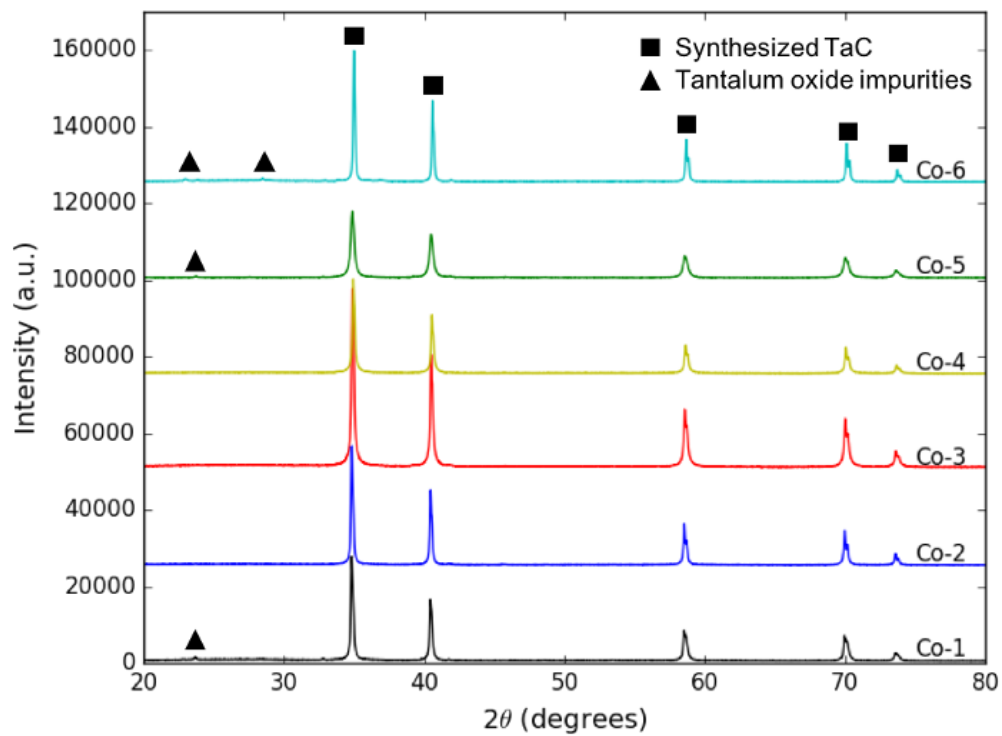


Figure 3-31. X-ray diffraction patterns of Co-doped TaC samples with different doping levels using metallic Co as the precursor.

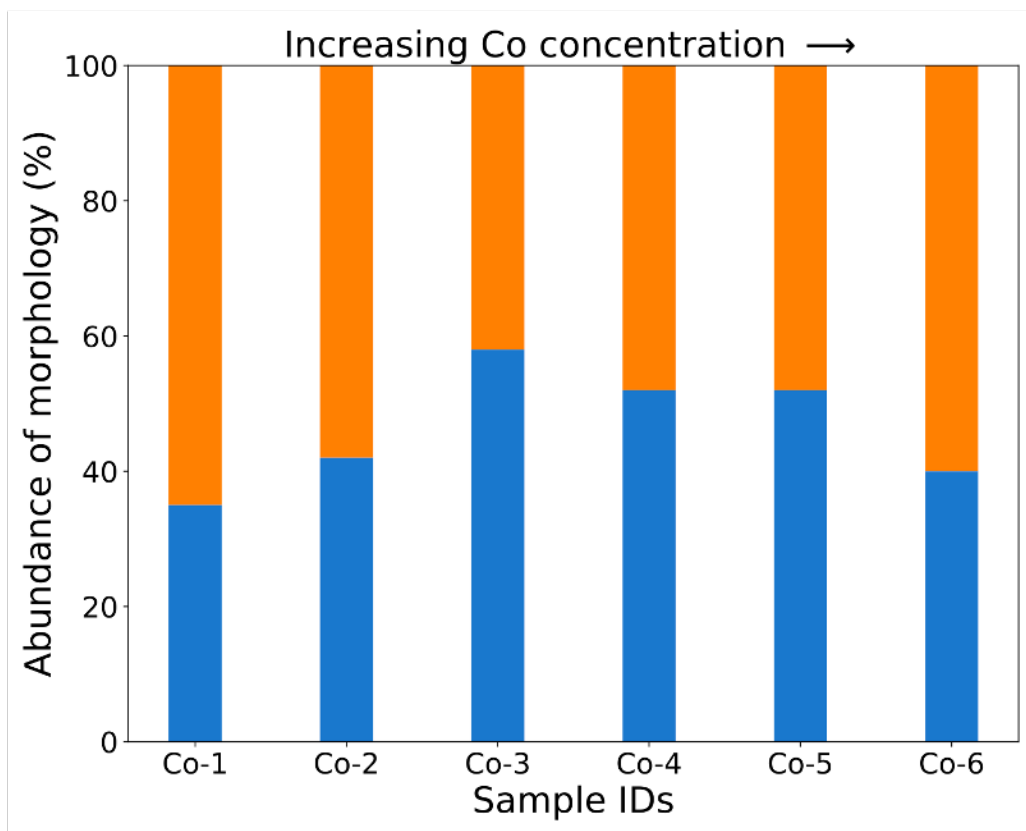


Figure 3-32. Statistical abundance of particle morphology for Co-doped TaC samples with different doping levels using metallic Co as the precursor. Color legends: Orange – non-faceted particles; Blue – cuboctahedron particles.

3.3.6. Fe-Doped TaC

Following the success of generating highly-faceted TaC particles by doping with Ni and Co, Fe was expected to resemble the effectiveness in alternating the morphology. In fact, the Fe-TaC system demonstrated another level of particle faceting by creating a significant number of cubes and truncated cubes, meaning that the $\{100\}$ surfaces of TaC were prominently stabilized during crystal growth. The general morphologies of Fe-doped TaC samples are illustrated in Figure 3-33. Excellent phase purity is maintained through all samples as confirmed by the XRD patterns (Figure 3-34). Statistical abundance chart in Figure 3-35 summarizes that the percentage of cubes/truncated cubes reached about 50% of the total counted particles in sample Fe-3 and Fe-

4. It should be noted that the octahedron particles still covered about 30% of the population, contributing to the total percentage of faceted particles.

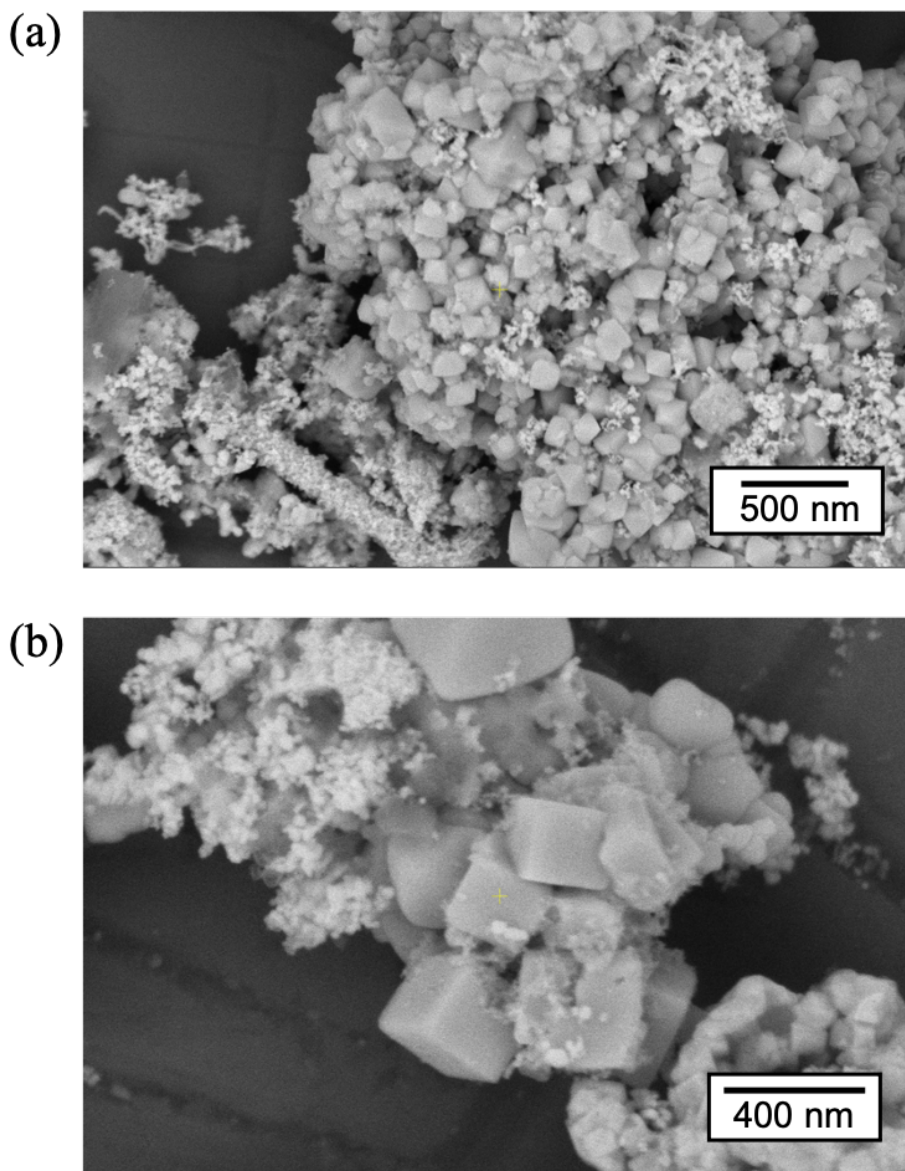


Figure 3-33. Scanning electron micrographs of Fe-doped TaC samples showing both cuboctahedron and cubic particles with different doping levels using metallic Fe as the precursor: (a) and (b) 3 at% calculated Co amount (Fe-1); (c) and (d) 5 at% calculated Fe amount (Fe-2); (e)-(g) 10 at% calculated Fe amount (Fe-3) showing the co-existence of two types of faceted particles; (h) and (j) 15 at% calculated Fe amount (Fe-4); (j) and (k) 20 at% calculated Fe amount (Fe-5); (l) and (m) 25 at% calculated Fe amount (Fe-6); (n) and (o) 30 at% calculated Fe amount (Fe-7).

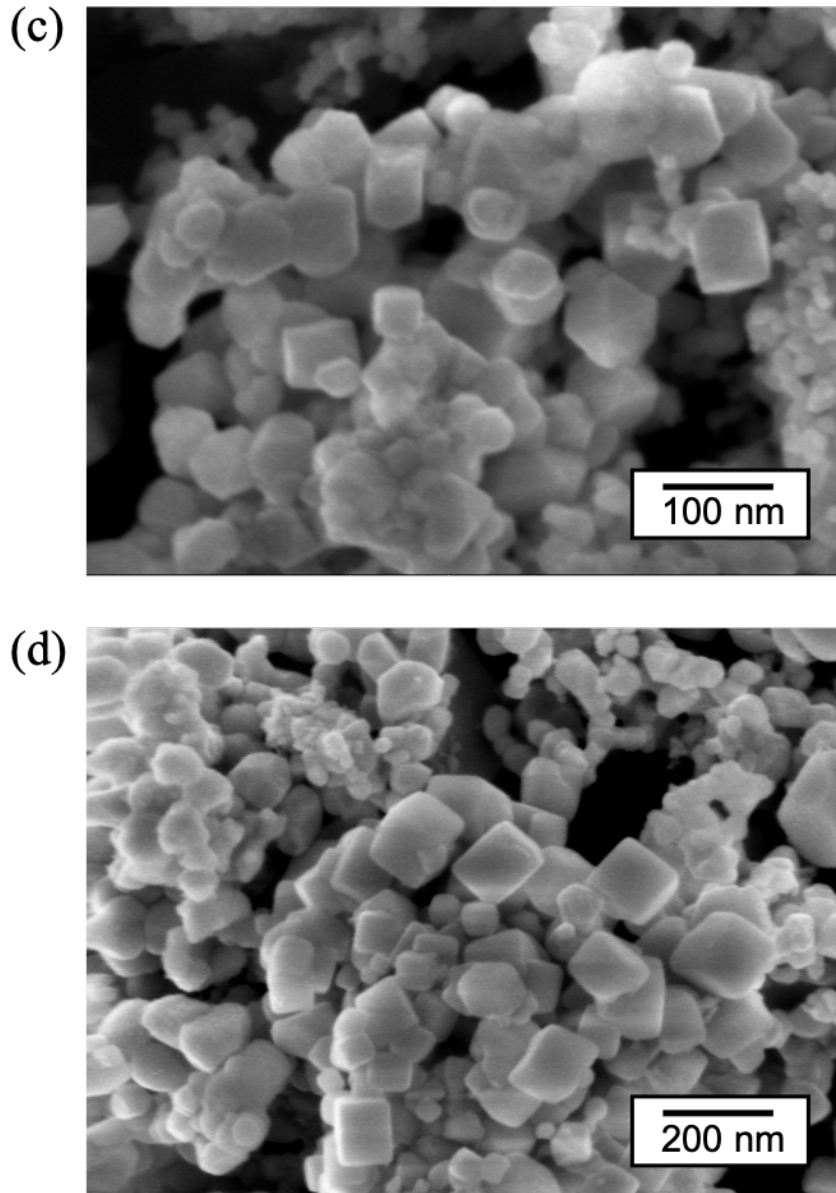
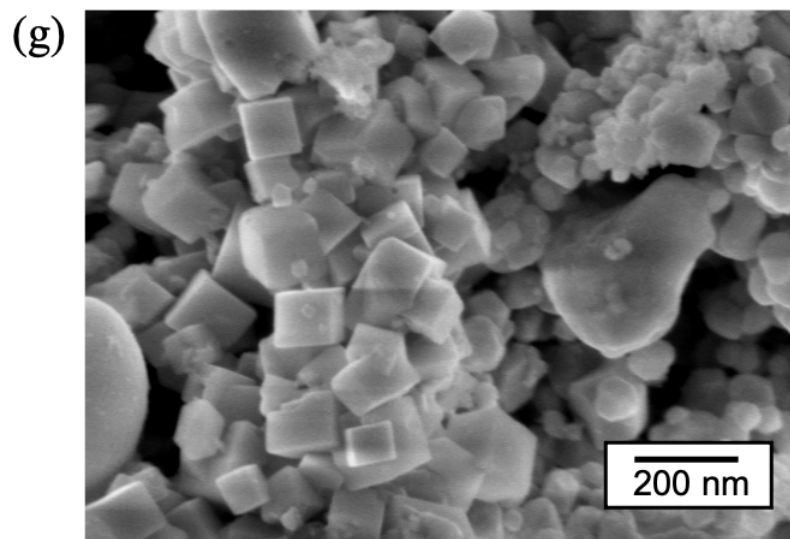
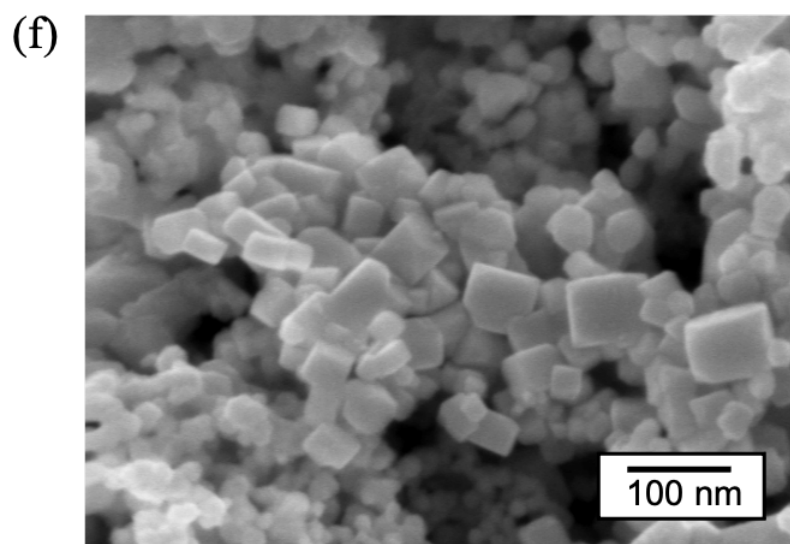
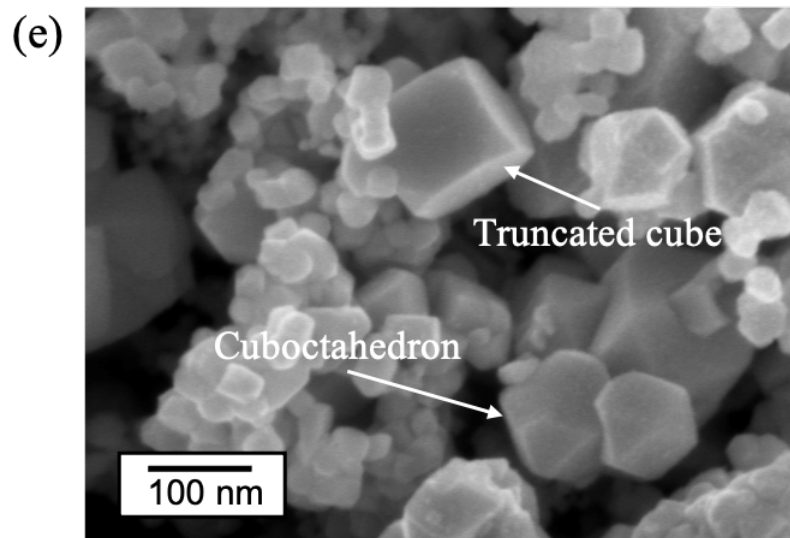


Figure 3-33. Scanning electron micrographs of Fe-doped TaC samples showing both cuboctahedron and cubic particles with different doping levels using metallic Fe as the precursor: (a) and (b) 3 at% calculated Co amount (Fe-1); (c) and (d) 5 at% calculated Fe amount (Fe-2); (e)-(g) 10 at% calculated Fe amount (Fe-3) showing the co-existence of two types of faceted particles; (h) and (j) 15 at% calculated Fe amount (Fe-4); (j) and (k) 20 at% calculated Fe amount (Fe-5); (l) and (m) 25 at% calculated Fe amount (Fe-6); (n) and (o) 30 at% calculated Fe amount (Fe-7). (continued)

Figure 3-33. Scanning electron micrographs of Fe-doped TaC samples showing both cuboctahedron and cubic particles with different doping levels using metallic Fe as the precursor: (a) and (b) 3 at% calculated Co amount (Fe-1); (c) and (d) 5 at% calculated Fe amount (Fe-2); (e)-(g) 10 at% calculated Fe amount (Fe-3) showing the co-existence of two types of faceted particles; (h) and (j) 15 at% calculated Fe amount (Fe-4); (i) and (k) 20 at% calculated Fe amount (Fe-5); (l) and (m) 25 at% calculated Fe amount (Fe-6); (n) and (o) 30 at% calculated Fe amount (Fe-7). (continued)



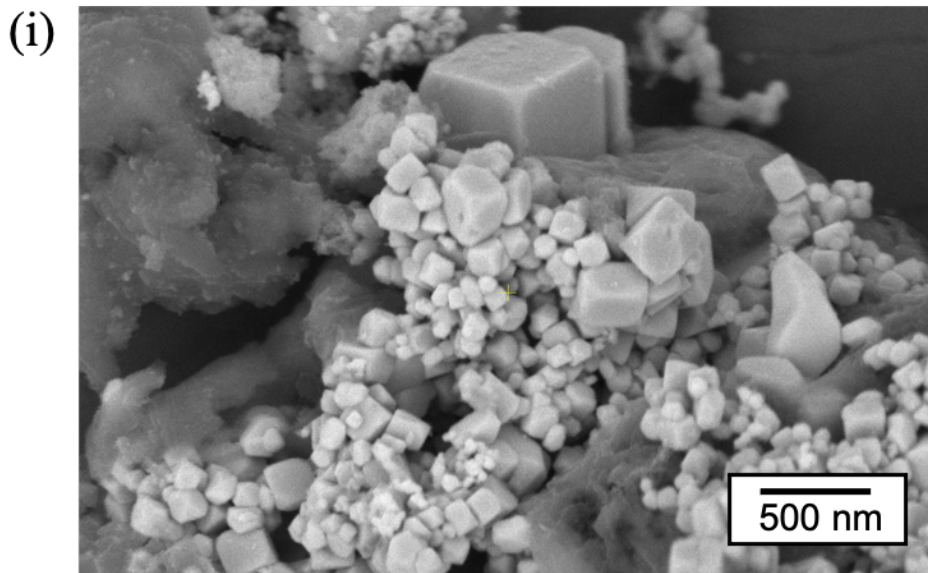
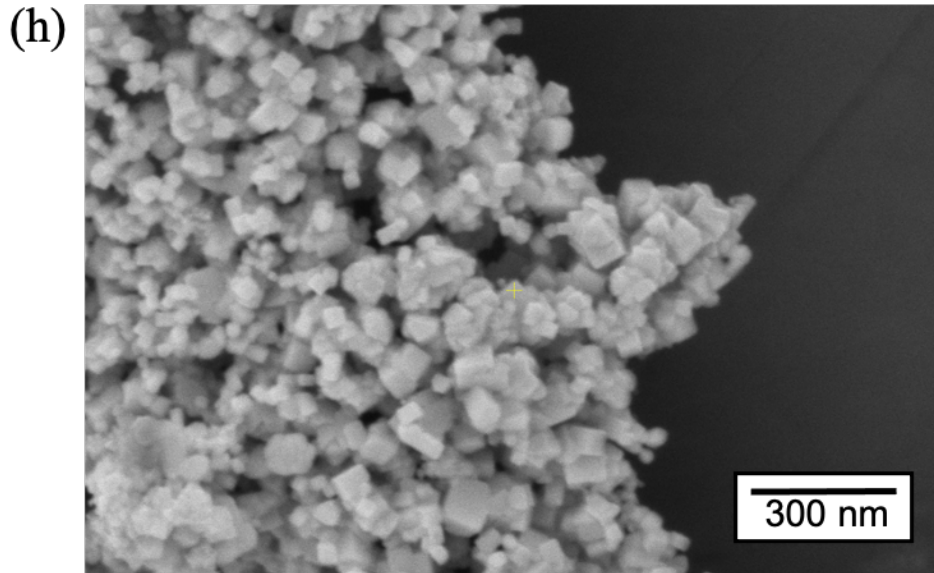


Figure 3-33. Scanning electron micrographs of Fe-doped TaC samples showing both cuboctahedron and cubic particles with different doping levels using metallic Fe as the precursor: (a) and (b) 3 at% calculated Co amount (Fe-1); (c) and (d) 5 at% calculated Fe amount (Fe-2); (e)-(g) 10 at% calculated Fe amount (Fe-3) showing the co-existence of two types of faceted particles; (h) and (i) 15 at% calculated Fe amount (Fe-4); (j) and (k) 20 at% calculated Fe amount (Fe-5); (l) and (m) 25 at% calculated Fe amount (Fe-6); (n) and (o) 30 at% calculated Fe amount (Fe-7). (continued)

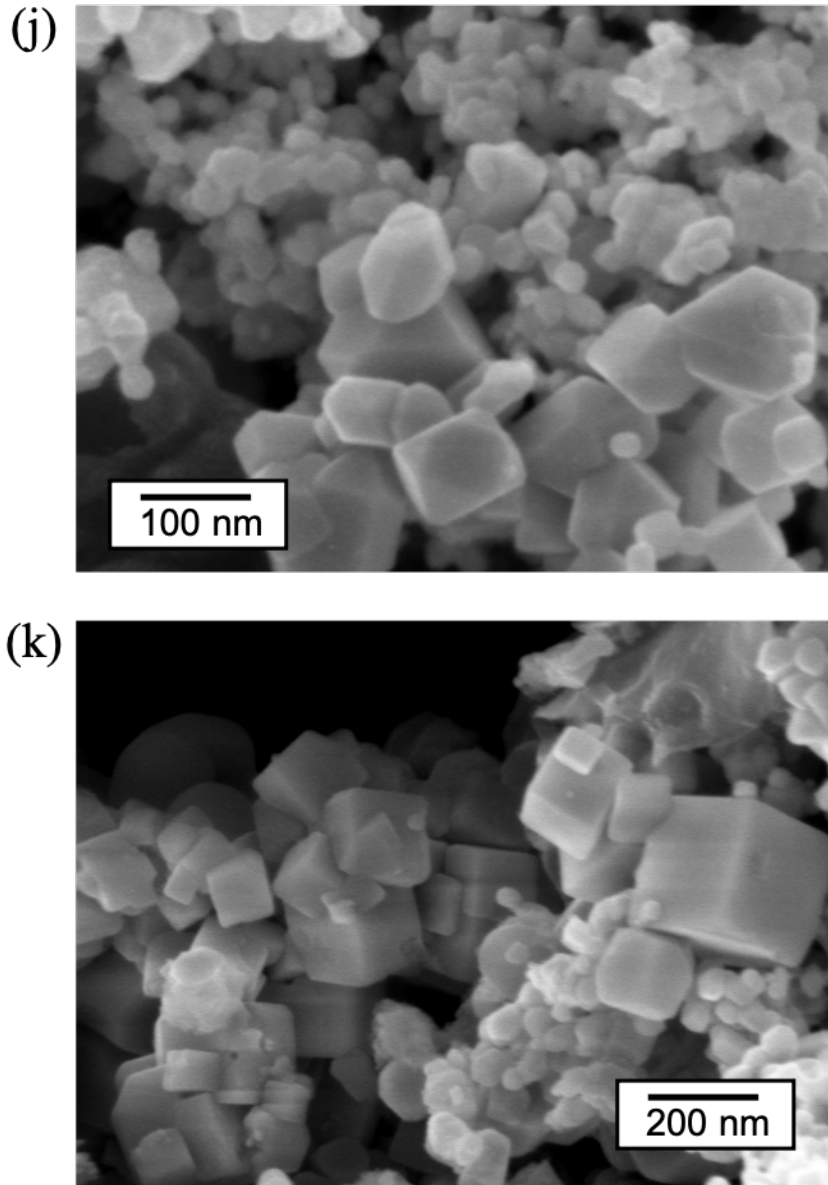


Figure 3-33. Scanning electron micrographs of Fe-doped TaC samples showing both cuboctahedron and cubic particles with different doping levels using metallic Fe as the precursor: (a) and (b) 3 at% calculated Co amount (Fe-1); (c) and (d) 5 at% calculated Fe amount (Fe-2); (e)-(g) 10 at% calculated Fe amount (Fe-3) showing the co-existence of two types of faceted particles; (h) and (j) 15 at% calculated Fe amount (Fe-4); (j) and (k) 20 at% calculated Fe amount (Fe-5); (l) and (m) 25 at% calculated Fe amount (Fe-6); (n) and (o) 30 at% calculated Fe amount (Fe-7). (continued)

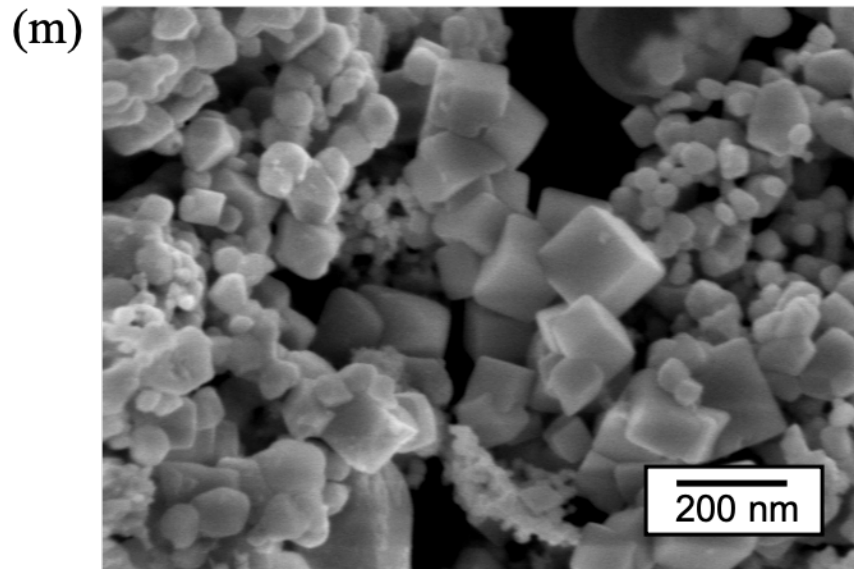
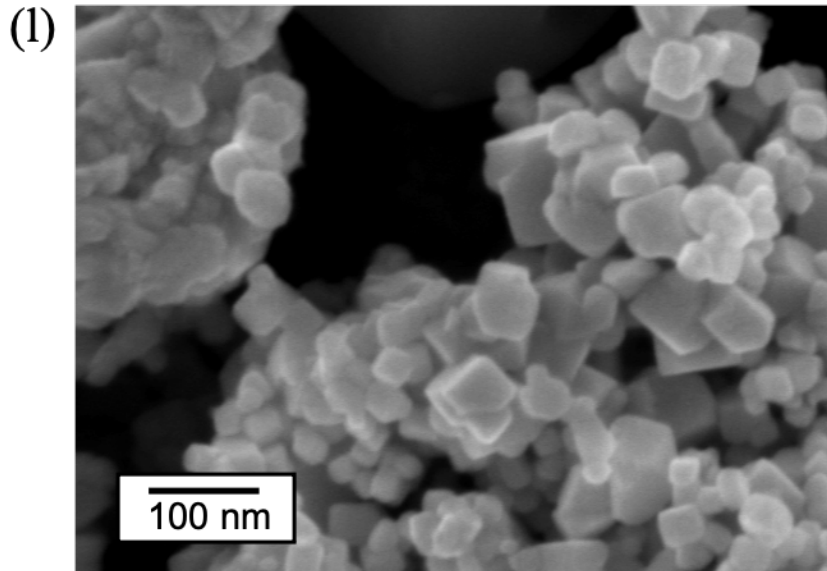


Figure 3-33. Scanning electron micrographs of Fe-doped TaC samples showing both cuboctahedron and cubic particles with different doping levels using metallic Fe as the precursor: (a) and (b) 3 at% calculated Co amount (Fe-1); (c) and (d) 5 at% calculated Fe amount (Fe-2); (e)-(g) 10 at% calculated Fe amount (Fe-3) showing the co-existence of two types of faceted particles; (h) and (j) 15 at% calculated Fe amount (Fe-4); (j) and (k) 20 at% calculated Fe amount (Fe-5); (l) and (m) 25 at% calculated Fe amount (Fe-6); (n) and (o) 30 at% calculated Fe amount (Fe-7). (continued)

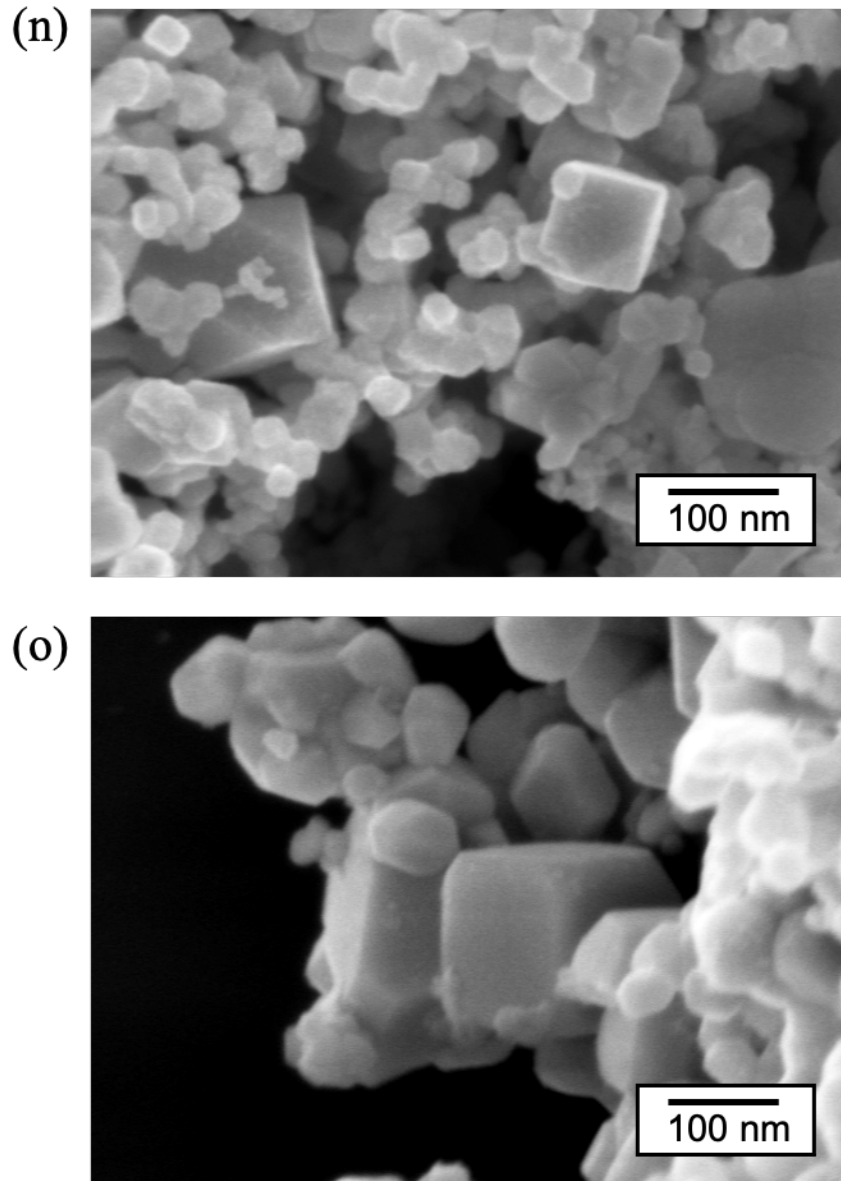


Figure 3-33. Scanning electron micrographs of Fe-doped TaC samples showing both cuboctahedron and cubic particles with different doping levels using metallic Fe as the precursor: (a) and (b) 3 at% calculated Co amount (Fe-1); (c) and (d) 5 at% calculated Fe amount (Fe-2); (e)-(g) 10 at% calculated Fe amount (Fe-3) showing the co-existence of two types of faceted particles; (h) and (j) 15 at% calculated Fe amount (Fe-4); (j) and (k) 20 at% calculated Fe amount (Fe-5); (l) and (m) 25 at% calculated Fe amount (Fe-6); (n) and (o) 30 at% calculated Fe amount (Fe-7). (continued)

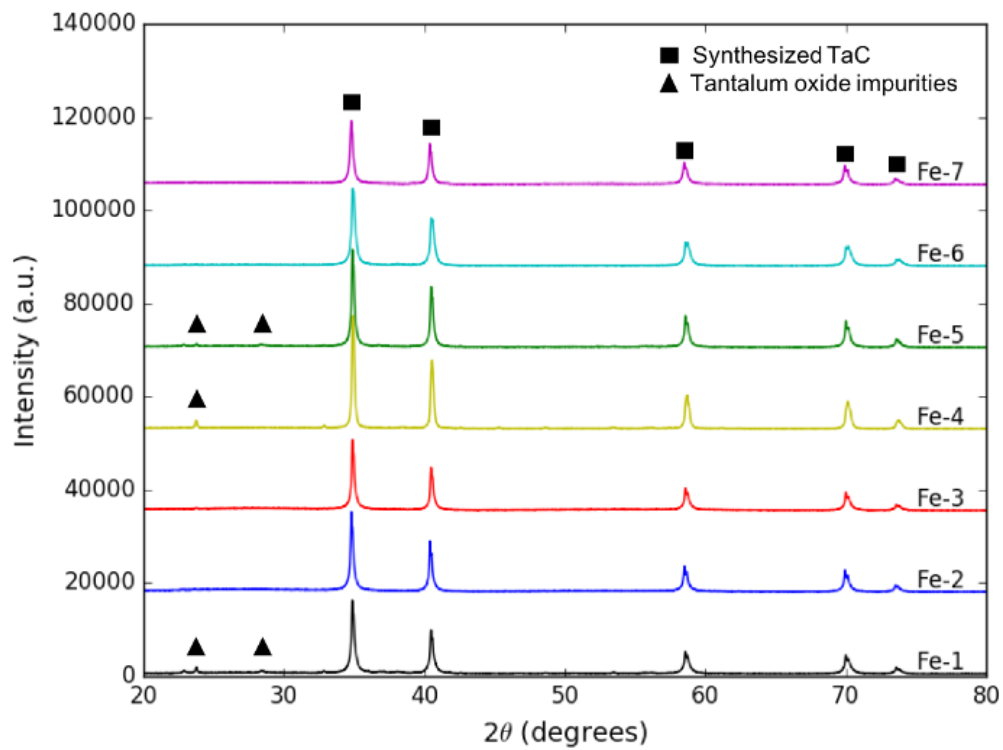


Figure 3-34. X-ray diffraction patterns of Fe-doped TaC samples with different doping levels using metallic Fe as the precursor.

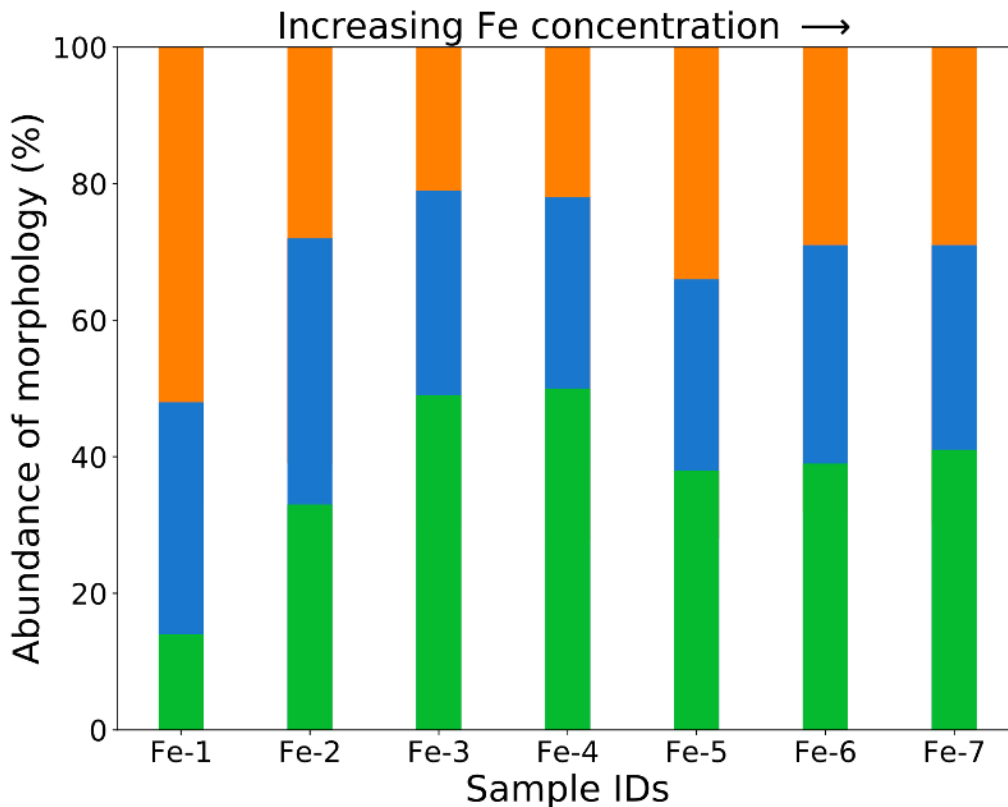


Figure 3-35. Statistical abundance of particle morphology for Fe-doped TaC samples with different doping levels using metallic Fe as the precursor. Color legends: Orange – non-faceted particles; Blue – cuboctahedron particles; Green – cubic/truncated cubic particles.

3.3.7. Ni-Ti Co-Doped TaC

Recall from Section 3.2 that the addition of Ti as the co-dopant aims to stabilize the growth of $\{100\}$ surfaces by increasing the ionicity of the TaC lattices. It can be observed from the SEM images in Figure 3-36 below that there is a pronounced population of cubic TaC particles enclosed by $\{100\}$ facets in all Ni-Ti co-doped samples, which is also reflected in the statistical abundance chart (Figure 3-38). The morphology distribution is comparable with the Fe-TaC system. All samples with co-doping possess a negligible amount of secondary phases, as shown by the XRD patterns in Figure 3-37. Owing to the high solubility of Ti in TaC, the actual Ti concentrations in the final powders were much closer to the calculated precursor concentrations, with the Ni amount

intentionally kept constant (Table 2-1). Although this result provides strong experimental evidence to support the hypothesis, it is still of great challenge to reveal the most fundamental mechanisms responsible for the changes in the growth habits of TaC particles by hands-on experiments alone.

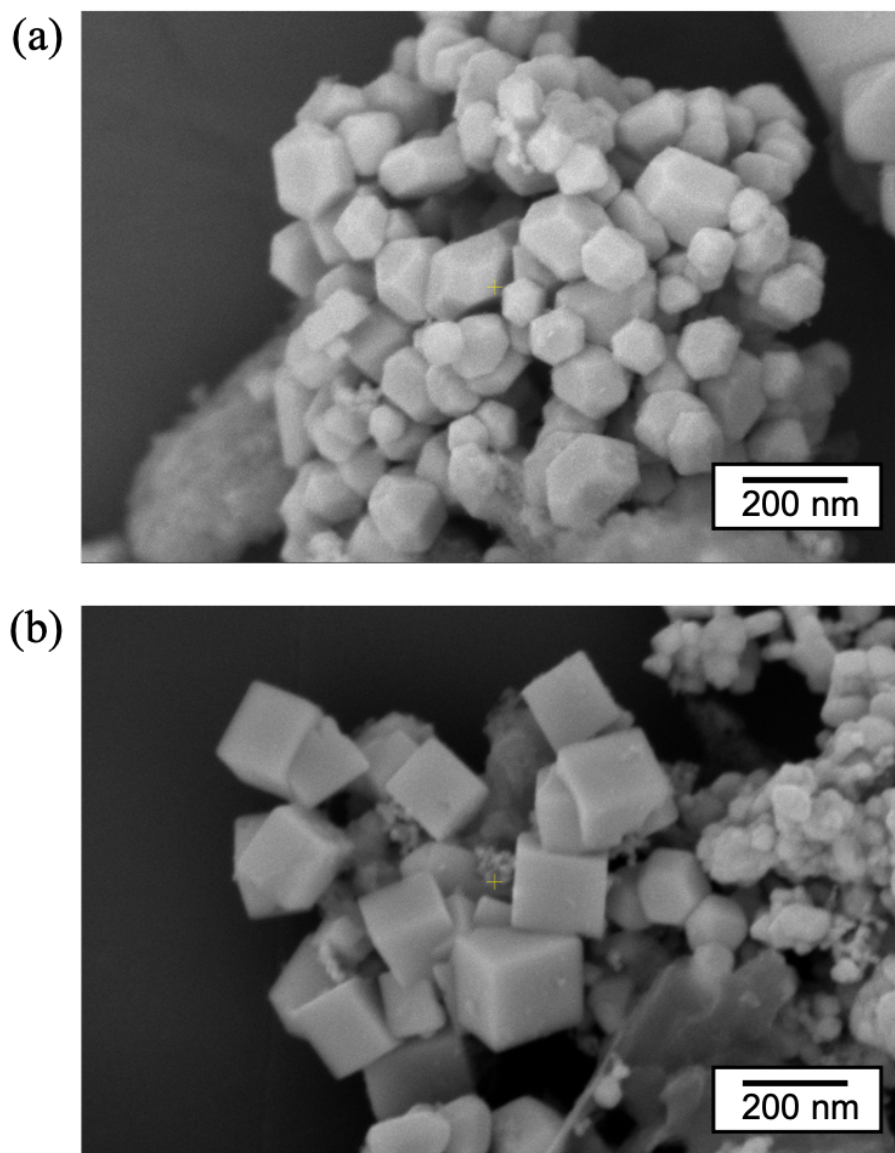


Figure 3-36. Scanning electron micrographs of Ni-Ti co-doped TaC samples showing both cuboctahedron and cubic particles with fixed amount of Ni (20 at% calculated) and different Ti doping levels using metallic Ni and Ti as the precursors: (a) and (b) 3 at% calculated Ti amount (NiTi-1); (c) and (d) 5 at% calculated Ti amount (NiTi-2); (e)-(g) 10 at% calculated Ti amount (NiTi-3); (h)-(j) 15 at% calculated Ti amount (NiTi-4); (k)-(m) 15 at% calculated Ti amount (NiTi-5); (n)-(p) 20 at% calculated Ti amount (NiTi-6).

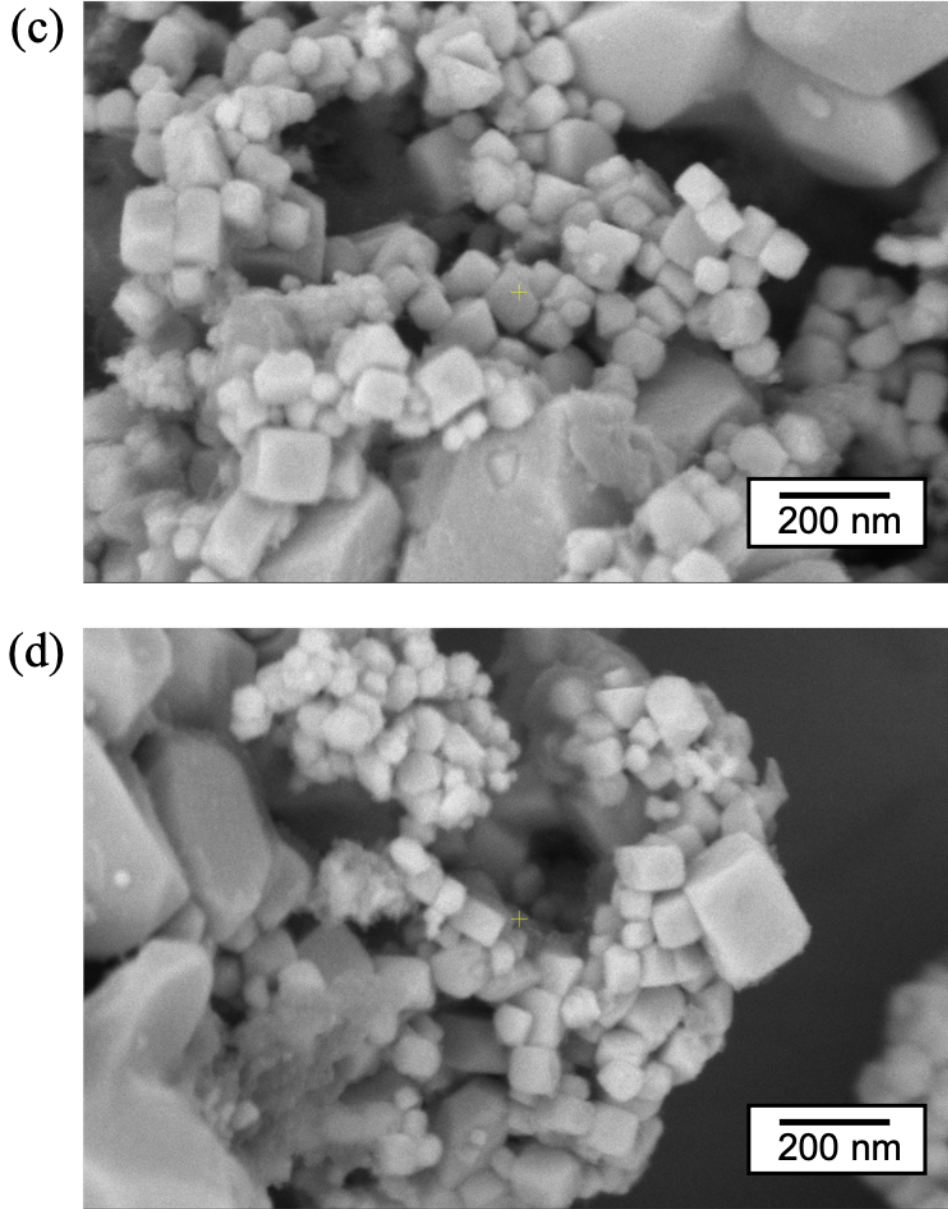


Figure 3-36. Scanning electron micrographs of Ni-Ti co-doped TaC samples showing both cuboctahedron and cubic particles with fixed amount of Ni (20 at% calculated) and different Ti doping levels using metallic Ni and Ti as the precursors: (a) and (b) 3 at% calculated Ti amount (NiTi-1); (c) and (d) 5 at% calculated Ti amount (NiTi-2); (e)-(g) 10 at% calculated Ti amount (NiTi-3); (h)-(j) 15 at% calculated Ti amount (NiTi-4); (k)-(m) 15 at% calculated Ti amount (NiTi-5); (n)-(p) 20 at% calculated Ti amount (NiTi-6). (continued)

Figure 3-36. Scanning electron micrographs of Ni-Ti co-doped TaC samples showing both cuboctahedron and cubic particles with fixed amount of Ni (20 at% calculated) and different Ti doping levels using metallic Ni and Ti as the precursors: (a) and (b) 3 at% calculated Ti amount (NiTi-1); (c) and (d) 5 at% calculated Ti amount (NiTi-2); (e)-(g) 10 at% calculated Ti amount (NiTi-3); (h)-(j) 15 at% calculated Ti amount (NiTi-4); (k)-(m) 15 at% calculated Ti amount (NiTi-5); (n)-(p) 20 at% calculated Ti amount (NiTi-6). (continued)

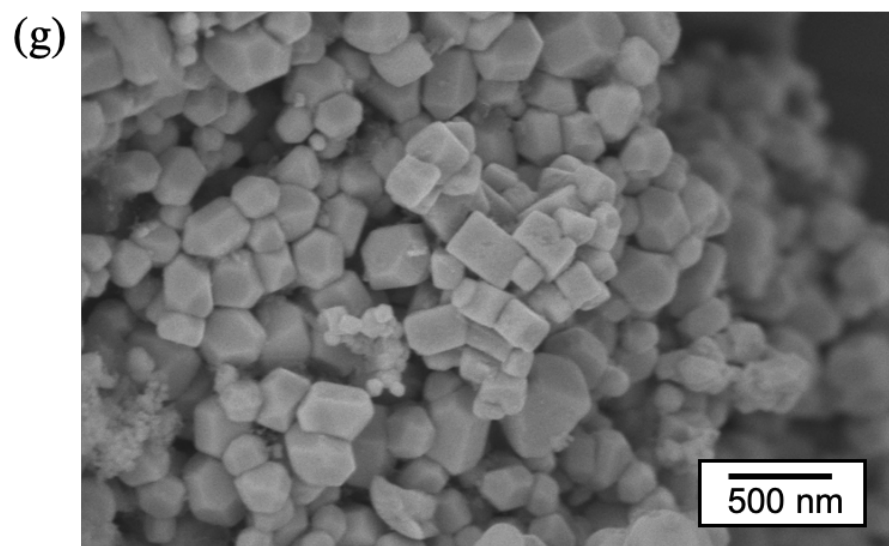
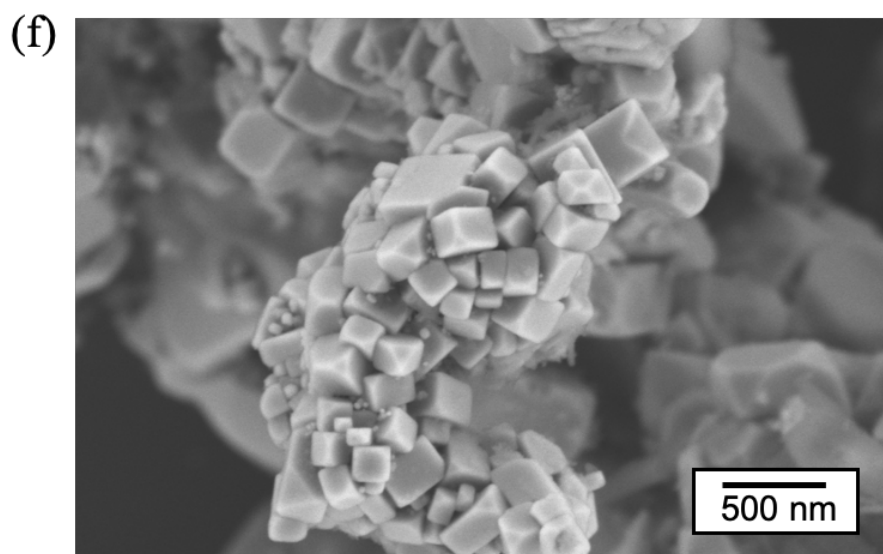
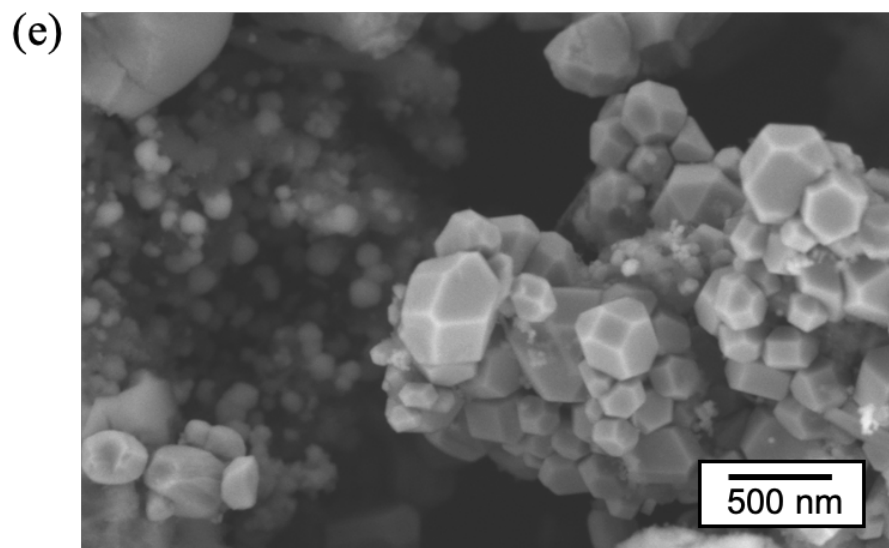


Figure 3-36. Scanning electron micrographs of Ni-Ti co-doped TaC samples showing both cuboctahedron and cubic particles with fixed amount of Ni (20 at% calculated) and different Ti doping levels using metallic Ni and Ti as the precursors: (a) and (b) 3 at% calculated Ti amount (NiTi-1); (c) and (d) 5 at% calculated Ti amount (NiTi-2); (e)-(g) 10 at% calculated Ti amount (NiTi-3); (h)-(j) 15 at% calculated Ti amount (NiTi-4); (k)-(m) 15 at% calculated Ti amount (NiTi-5); (n)-(p) 20 at% calculated Ti amount (NiTi-6). (continued)

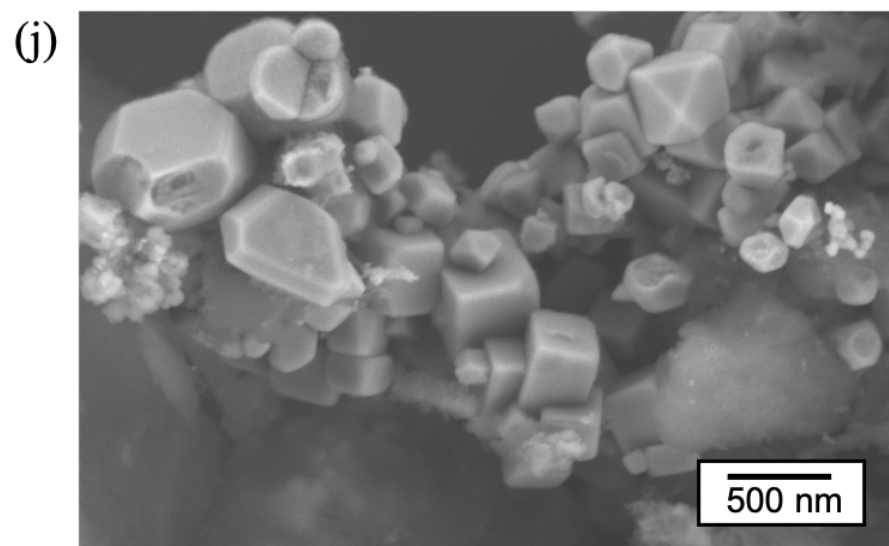
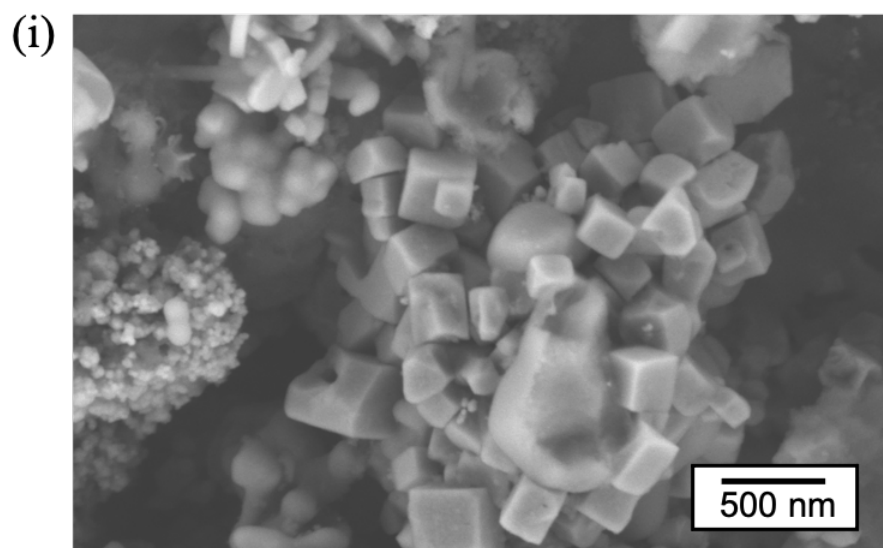
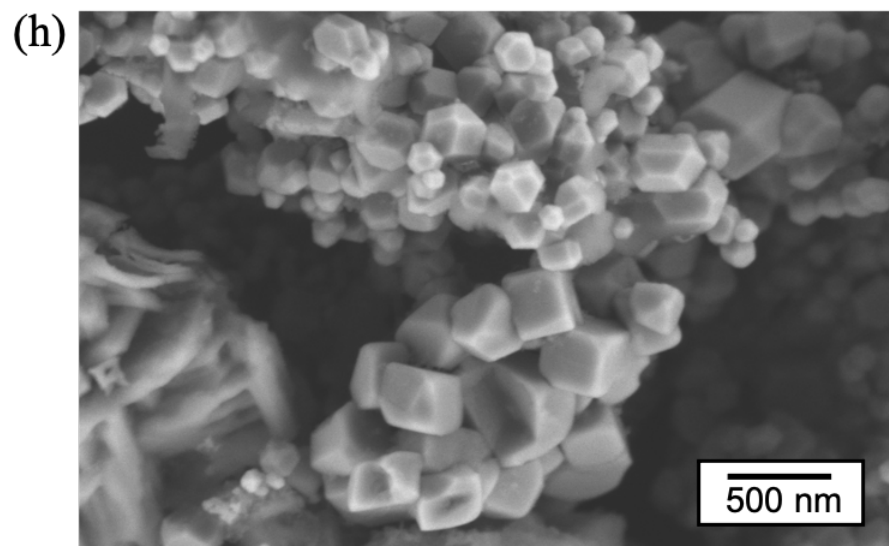
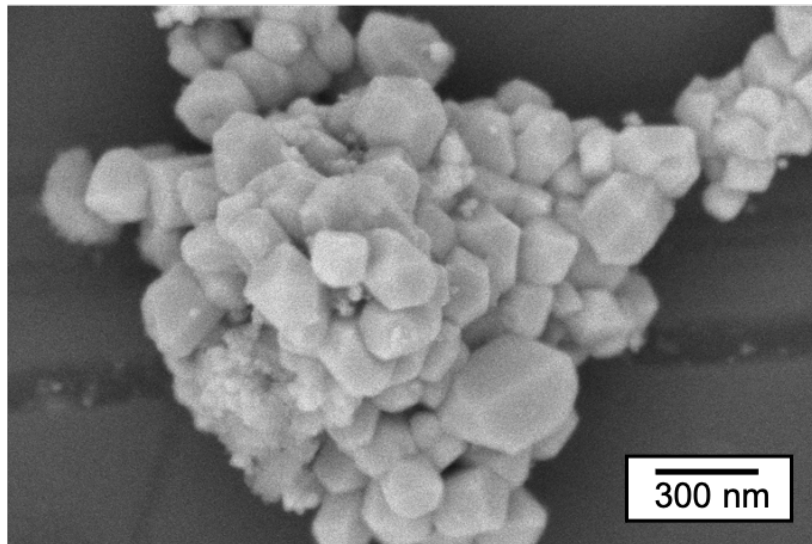
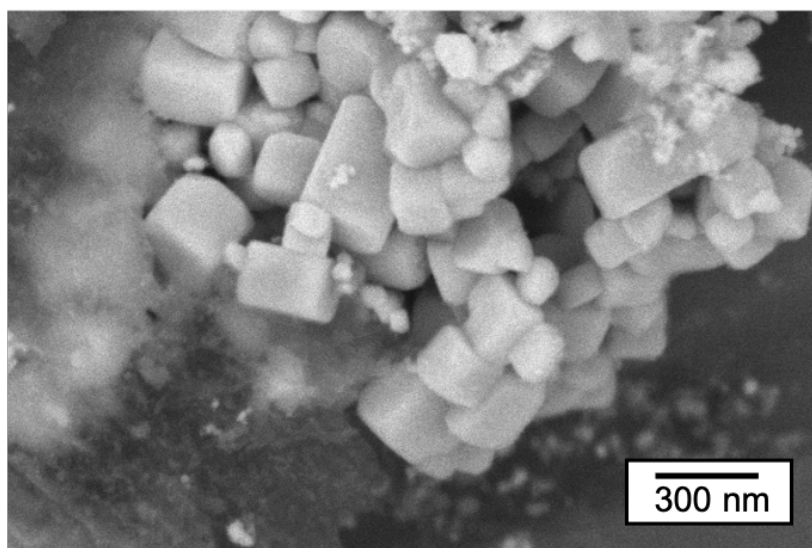


Figure 3-36. Scanning electron micrographs of Ni-Ti co-doped TaC samples showing both cuboctahedron and cubic particles with fixed amount of Ni (20 at% calculated) and different Ti doping levels using metallic Ni and Ti as the precursors: (a) and (b) 3 at% calculated Ti amount (NiTi-1); (c) and (d) 5 at% calculated Ti amount (NiTi-2); (e)-(g) 10 at% calculated Ti amount (NiTi-3); (h)-(j) 15 at% calculated Ti amount (NiTi-4); (k)-(m) 15 at% calculated Ti amount (NiTi-5); (n)-(p) 20 at% calculated Ti amount (NiTi-6). (continued)

(k)



(l)



(m)

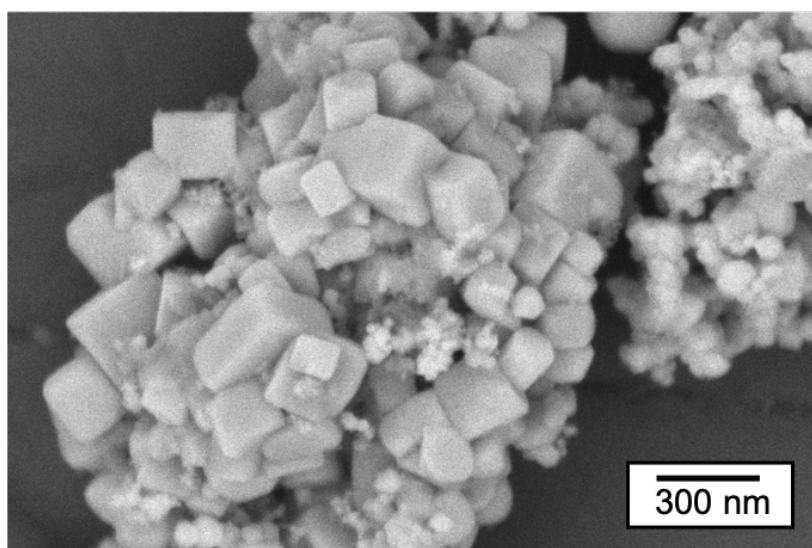
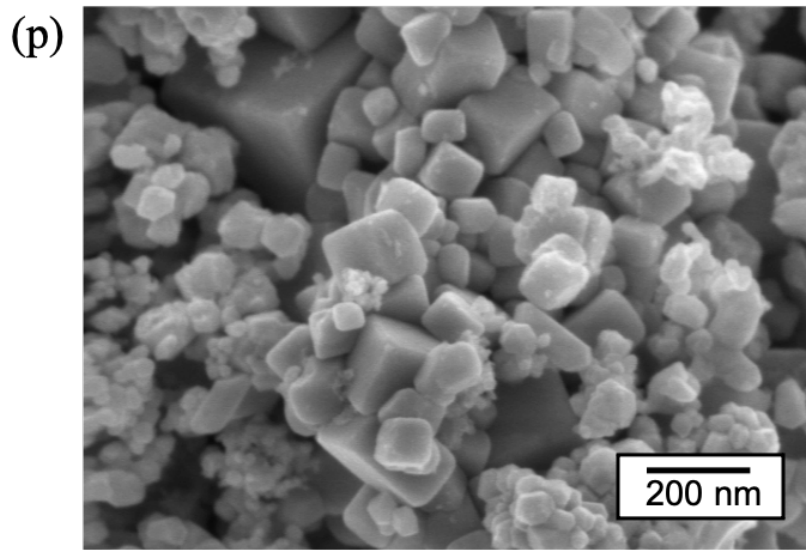
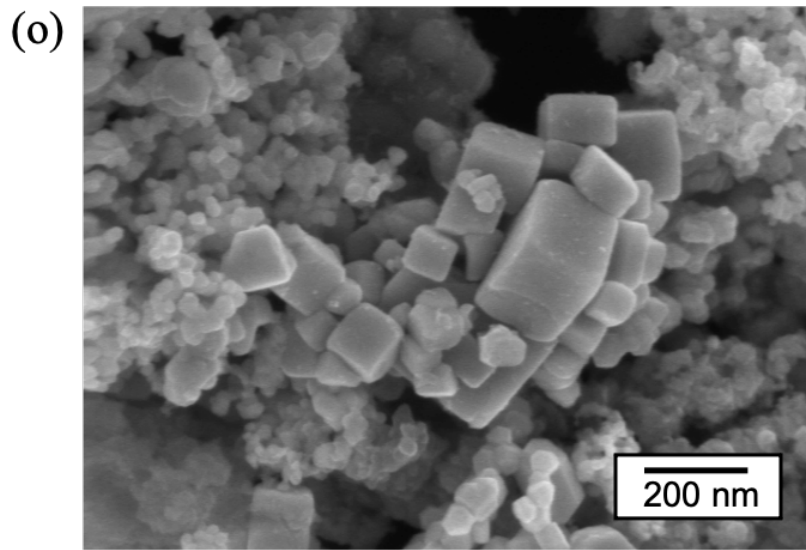
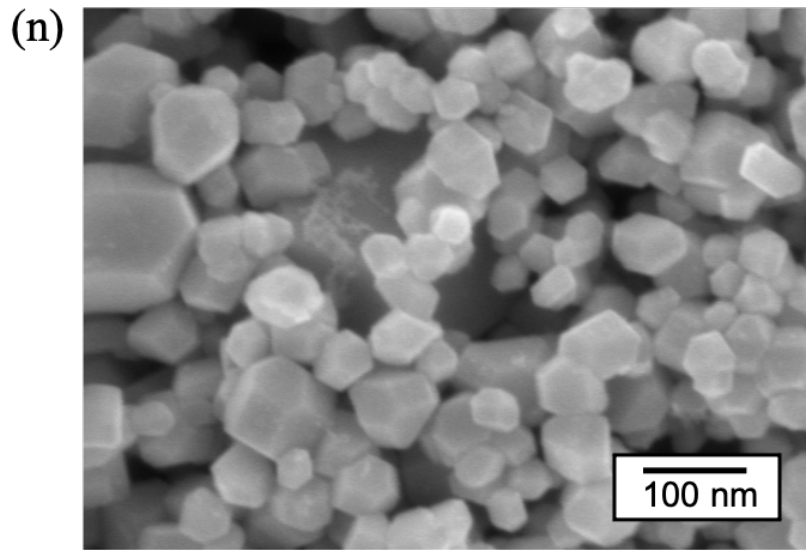


Figure 3-36. Scanning electron micrographs of Ni-Ti co-doped TaC samples showing both cuboctahedron and cubic particles with fixed amount of Ni (20 at% calculated) and different Ti doping levels using metallic Ni and Ti as the precursors: (a) and (b) 3 at% calculated Ti amount (NiTi-1); (c) and (d) 5 at% calculated Ti amount (NiTi-2); (e)-(g) 10 at% calculated Ti amount (NiTi-3); (h)-(j) 15 at% calculated Ti amount (NiTi-4); (k)-(m) 15 at% calculated Ti amount (NiTi-5); (n)-(p) 20 at% calculated Ti amount (NiTi-6). (continued)



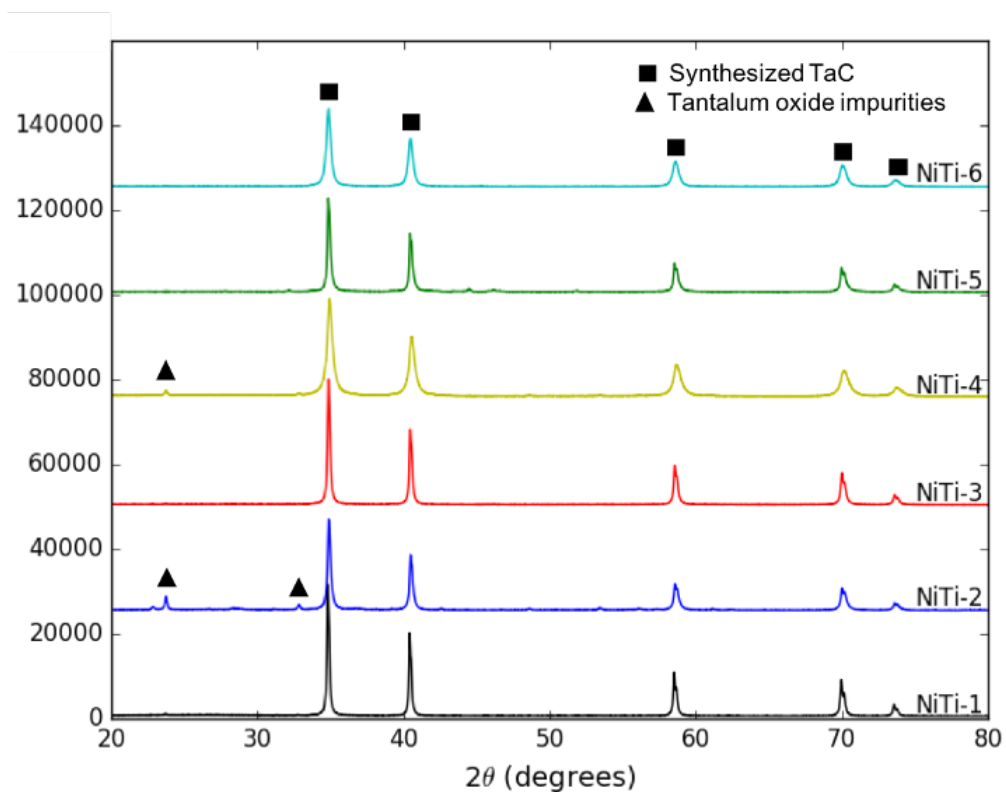


Figure 3-37. X-ray diffraction patterns of Ni-Ti co-doped TaC samples with fixed Ni amount (20 at% calculated) and different Ti doping levels using metallic Ni and Ti as the precursors.

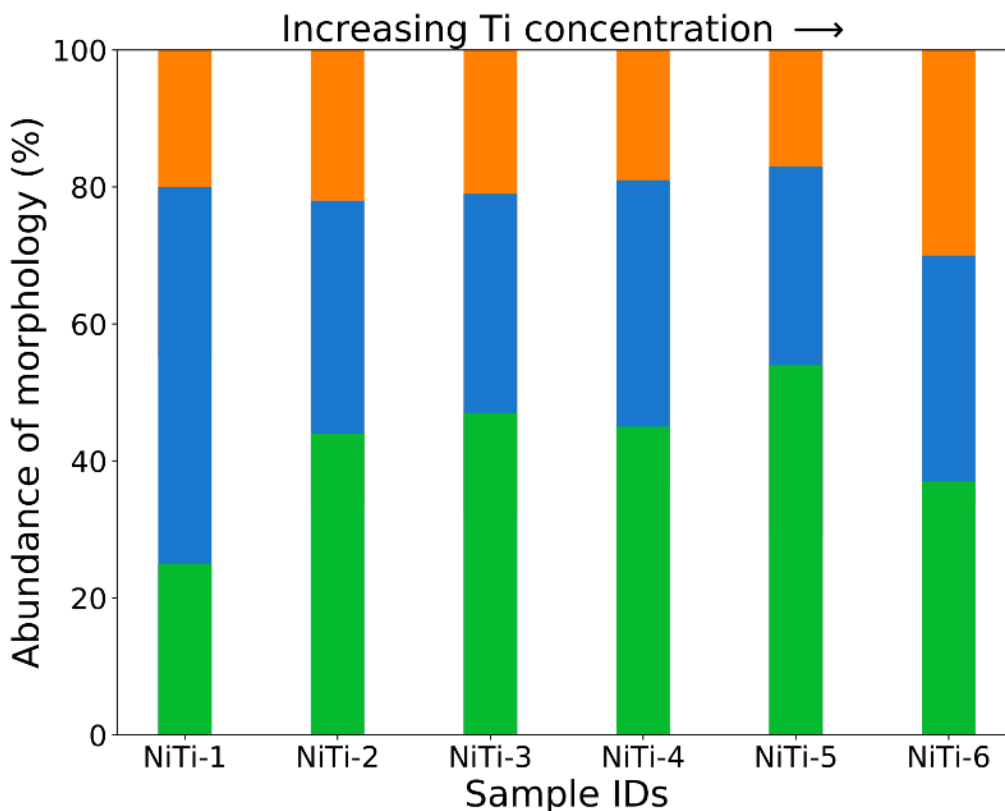


Figure 3-38. Statistical abundance of particle morphology for Ni-Ti co-doped TaC samples fixed Ni amount (20 at% calculated) and different Ti doping levels using metallic Ni and Ti as the precursors. Color legends: Orange – non-faceted particles; Blue – cuboctahedron particles; Green – cubic/truncated cubic particles.

3.3.8. Modeling-Assisted Discussion

In order to probe the effect of dopants on the surfaces, the dopant concentrations of the morphology modifiers, namely, Ni, Fe, Co, Ni-Ti, and Y are compared in the bulk using energy dispersive spectroscopy (EDS, penetration depth $\sim 1-2 \mu\text{m}$ below the surface) and near the surface using X-ray photoelectron spectroscopy (XPS, penetration depth $< 10 \text{ nm}$ below the surface) in Figure 3-39. The dopant with the greatest surface concentration enrichment (*i.e.*, elemental concentration by XPS is greater than EDS) is Ni followed by Fe, Y, and Co. Ti and Nb have a high solubility in the bulk, as shown by the high EDS concentrations. Due to the chemical similarity of Ti and Ta, TiC is expected to be mutually soluble with TaC, leading to its high

concentration in the bulk.³¹ As such, the formation of a bi-carbide solid solution in the bulk in the form of TiTa_3C_4 , which has a Ti concentration of 12.5 at.% is expected. This is within the range of the experimentally measured Ti concentration of ~2.2 to 18.5 at.% in the Ni-Ti co-doped system (refer to Table 3-1 for the dopant concentration in each sample determined by EDS). Henceforth, Ni-doping in TiTa_3C_4 will serve as the theoretical analog to Ni-Ti co-doping in TaC.

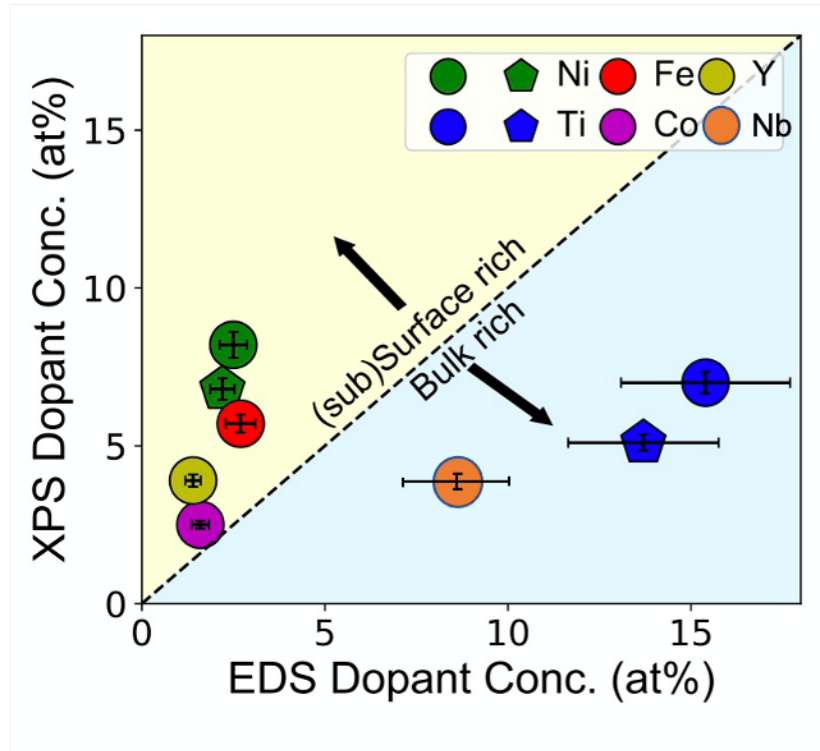


Figure 3-39. Plot of the dopant concentrations detected by X-ray photoelectron spectroscopy with respect to the concentration detected by energy dispersive spectroscopy. The samples chosen for comparison have the highest abundance of modified particles in each system, namely, Ni-4, Co-3, Fe-4 and NiTi-5. Shape legends: Pentagon – TiTa_3C_4 ; Circle – TaC.

Table 3-1. Dopant concentrations of TaC powders determined from energy dispersive spectroscopy. The dopant concentration of the Ni- and Ti-doped TaC powders represents the concentration of Ti as the concentration of Ni was fixed to be the same as Ni-4. All values are in atomic percent.

Sample Number	Ni-doped TaC	Co-doped TaC	Fe-doped TaC	Y-doped TaC	Nb-doped TaC	Ni-Ti co-doped TaC
1	0.9	0.9	0.5	0.6	4.4	2.2
2	1.4	1.6	1.2	1.0	7.8	4.1
3	1.7	1.9	2.2	1.3	-	8.0
4	2.5	2.3	2.7	1.6	-	12.4
5	4.1	2.6	4.0	2.2	-	16.4
6	5.7	3.4	4.2	-	-	18.5
7	-	-	4.8	-	-	-

Table 3-2. Dopant concentration of TaC powders determined from X-ray photoelectron spectroscopy. All values are in atomic percent.

Sample ID	XPS Dopant Conc.	Note
Ni-4	8.2	--
NiTi-4	6.8	Ni conc. in Ni-Ti co-doped TaC
NiTi-4	5.1	Ti conc. in Ni-Ti co-doped TaC
Y-3	3.9	--
Fe-4	5.7	--
Co-2	2.7	--
Ti-2	7.0	Ti conc. in Ti-doped TaC
Nb-2	4.3	--

To take a step further, the calculated surface segregation energies (E_{seg}^{surf}) for the TaC and TiTa_3C_4 {111} and {100} facets for the dopants considered in the study are plotted in Figure 3-41, while Figure 3-40 illustrates the slab models used to obtain the surface segregation energies. By comparing dopant stability in the surface and the bulk (defined as the energy difference between a doped and undoped cell), the location where the dopant will segregate can be determined. This is dictated by the segregation energy, which is given by:

$$E_{seg} = (E^{slab+X} - E^{slab})/2 - (E^{bulk+X} - E^{bulk}) \quad \text{Eq. 11}$$

The difference between E^{slab+X} and E^{slab} , the calculated total energies of the clean and doped slab cells respectively, represents dopant stability in the surface. Meanwhile the difference between E^{bulk+X} and E^{bulk} , the calculated total energies of the clean and doped bulk cells respectively, represents dopant stability in the bulk. The factor of 2 in the first term accounts for both surfaces being symmetrically doped. $E_{seg} < 0$ indicates a segregation tendency towards the surface, $E_{seg} \sim 0$ indicates no segregation tendency, and $E_{seg} > 0$ indicates a segregation tendency towards the bulk. Only dopants that segregate towards the surface are assumed to influence the surface energy and thus affect the morphology. Both the top-layer and sub-layer of the surface were investigated (see Figure 3-40), where the green-dashed box represents the surface, and the red-dashed box represents the sub-surface.

To simulate the experimental conditions where Ni and Ti were co-doped into TaC, TiTa_3C_4 slabs were generated from a fully relaxed bulk TiTa_3C_4 structure, which was in turn generated by substituting one Ta atom for Ti in the conventional unit cell of TaC [see Figure 3-40(c)-(d)]. Single substitution for both Ta and Ti atoms, one at a time, was performed for TiTa_3C_4 . The most dilute coverage of dopants were investigated, which can be calculated while maintaining slab systems of less than 200 atoms resulting in a coverage of $\frac{1}{4}$ and $\frac{1}{2}$ monolayers (number of dopants per unit

primitive slab) for the TaC and TiTa_3C_4 slabs, respectively. All slabs had a slab and vacuum layer 22 Å and 16 Å thick to prevent periodic interactions between the dopants and the two surfaces. All slab systems, including doped slabs, maintained symmetrically equivalent surfaces by ensuring Laue point group symmetry in the structures to avoid any dipole moments perpendicular to the surface.^{28,32-33}

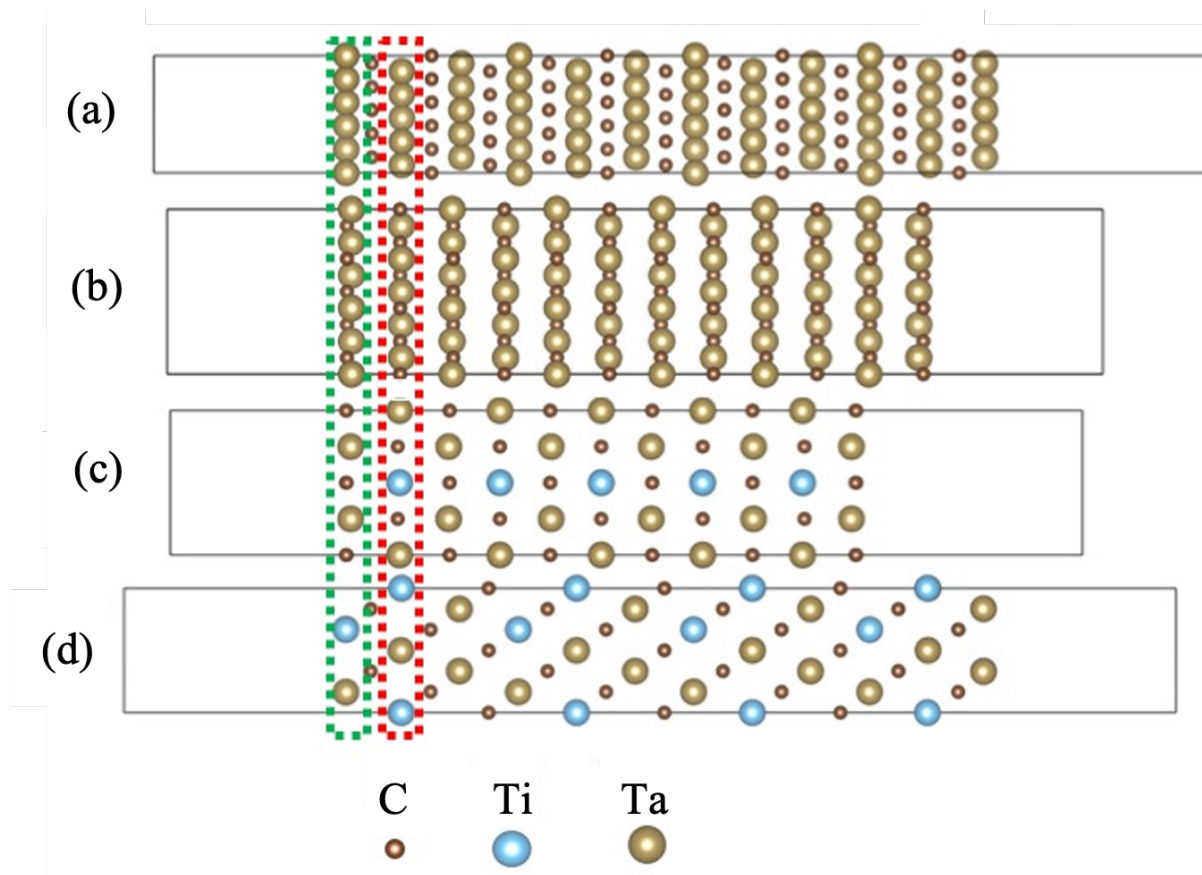


Figure 3-40. Slab models for (a) TaC (111) and (b) TaC (100) used to calculate segregation energies. Slab models for (c) TiTa_3C_4 (111) and (d) TiTa_3C_4 (100). The green (surface) and red (sub-surface) dashed boxes indicate the possible metallic (i.e., Ta and/or Ti) sites a dopant can substitute. The slab models were constructed using lattice transformations to orient the basal plane parallel to the Miller index plane of interest. The oriented unit cell was then expanded along the direction normal to the basal plane followed by a removal of half the atoms in the resulting supercell to generate a slab and vacuum layer. The most stable termination for the (111) TaC surface is a Ta-terminated nonstoichiometric slab, while the (100) surface is modeled with a Ta-C terminated stoichiometric slab (courtesy of Richard Tran, co-first author of Ref. 21).

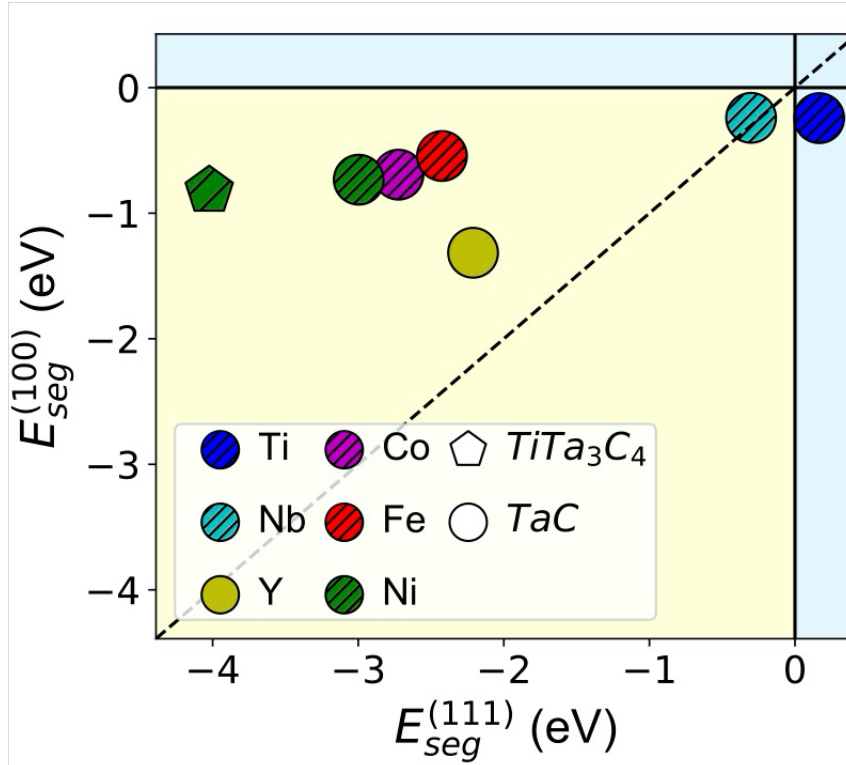


Figure 3-41. Calculated segregation energy for the (100) surface with respect to the (111) surface. Slab models for TaC (111), TaC (100), TiTa₃C₄ (111), and TiTa₃C₄ (100) used to calculate segregation energies are indicated in Figure 3-40. Shape legends: Pentagon – TiTa₃C₄; Circle – TaC (courtesy of Richard Tran, co-first author of Ref. 21).

A negative E_{seg}^{surf} indicates a driving force towards segregation into the surface (defined as the layer of atoms inside the green and red boxes in Figure 3-40). In agreement with the elemental analysis in experiments, Nb and Ti exhibit little to no preference to segregate to any surface since their segregation energies, illustrated in Figure 3-41, show values close to zero for both $E_{seg}^{(111)}$ and $E_{seg}^{(100)}$. In contrast, Ni, Fe, and Co are predicted to preferably segregate to the (111) surfaces. By comparing the $E_{seg}^{(111)}$ and $E_{seg}^{(100)}$, it is clear that the $E_{seg}^{(111)}$ values are less than -2 eV, whereas $E_{seg}^{(100)}$ is closer to -1 eV. In the case of the Ni-Ti co-doped samples, the E_{seg}^{surf} of Ni in the TiTa₃C₄ solution was calculated and it was demonstrated that Ni strongly tends to segregate to the (111) surface (see the green pentagon in Figure 3-41). This supports the experimental results that Ni,

Fe, and Co have higher concentrations in the surface relative to the bulk. Y also has a highly negative E_{seg}^{surf} according to the calculation. However, its microstructural expression makes the Y-doped TaC a special case to be discussed in the later paragraphs.

The surface atomic density (ρ) can be used to explain the selective surface segregation of dopants, as more open surfaces feel less strain from the doping atoms and therefore better facilitate segregation than close-packed surfaces.³⁴ This could be the major reason why the (111) surface ($\rho = 0.782$) generally has a lower E_{seg}^{surf} than the {100} surface ($\rho = 0.830$). This also implies that less stable surfaces are better at facilitating dopant segregation, as close-packed surfaces are generally more stable than open surfaces.

To rationalize the relative preference of cuboctahedron/cube (including truncated cube) formation, enthalpy maps of R as a function of $\Delta\mu_C$ (y-axis) and $\Delta\mu_X$ (x-axis) where X is the incorporated dopant in TaC are plotted in Figure 3-42. The yellow dashed line serves as a guide to partition the maps to where non-cubic/cuboctahedrons (white region), and cubes/truncated cubes (blue region) form. The larger the chemical potential window of the blue region (indicated by the percentage values), the more favorable the formation of cubes/truncated cubes becomes. It should be noted that the enthalpy map does not consider thermodynamic roughening and should only be used to compare the feasibility of two types of particle formation. Dopant segregation has two effects. First, the surface dopants modify the range of $\Delta\mu_C$ and $\Delta\mu_X$ where TaC is stable at the surface. Second, the surface dopants also modify the surface energies of TaC, and hence R , as a function of $\Delta\mu_C$ and $\Delta\mu_X$. The blue region occupies 52.7% of the map for Fe-doping [Figure 3-42(c)], but only 40.5% and 41.9% for Ni- and Co-doping respectively [Figure 3-42(a) and (b)], which indicates that the formation of cubes/truncated cubes is relatively more favorable with Fe doping. Meanwhile, the probability of forming cubes/truncated cubes (which requires R to be as

close to 1.73 as possible) for Fe-doping is also higher than Ni and Co doping due to the larger blue region. Ni-doping in TiTa_3C_4 will lead to a similarly large window for $\Delta\mu$ for the formation of cubic particles, but only under a low Ti content ($\Delta\mu_{\text{Ti}} \leq -2.25 \text{ eV}$) and a deficiency of carbon content in the surface. Since there is no presence of Ti-containing secondary phase in the Ni-Ti co-doped samples meaning that Ti resides in the bulk, and all the samples are slightly non-stoichiometric with respect to the carbon content, the enthalpy map reflects the experimental observations nicely. Moreover, the enthalpy map in Figure 3-42(d) shows that with Y doping, only cubic morphologies are possible. This is consistent with the statistical abundance shown in Figure 3-22.

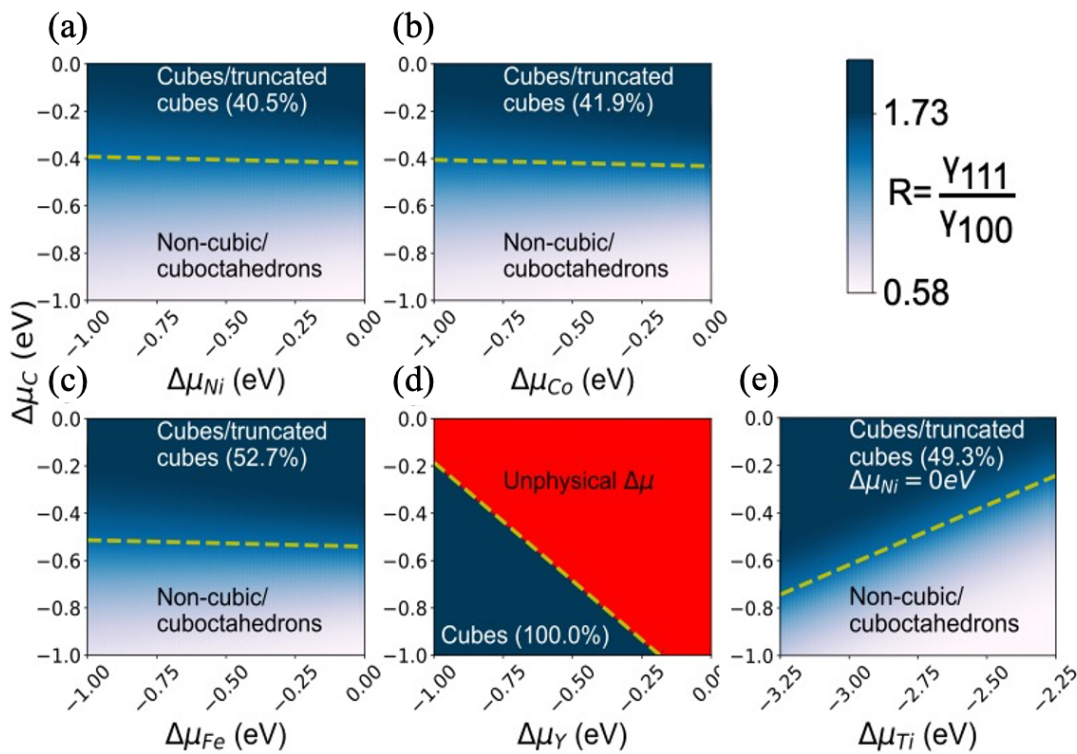


Figure 3-42. Calculated enthalpy maps of R as a function of $\Delta\mu_{\text{C}}$ and $\Delta\mu_{\text{X}}$ for (a) Ni in TaC; (b) Co in TaC; (c) Fe in TaC; (d) Y in TaC; (e) Ti in TiTa_3C_4 with $\Delta\mu_{\text{Ni}} = 0 \text{ eV}$. The yellow dashed line indicates $R=1.15$ for the onset of cuboctahedrons and partitions the enthalpy map into two regions. The region below is the $\Delta\mu$ window for the formation of (truncated) octahedrons and the region above is the $\Delta\mu$ window for the formation of (truncated) cubes. The color bar on the upper right corresponds to the value of R on the maps (courtesy of Richard Tran, co-first author of Ref. 21).

Since only the dopants that segregate towards the surface will induce morphology modification, surface segregation is a prerequisite for influencing γ . This is further supported by the notion that both Nb and Ti have little to no segregation preference towards the surface which results in no signs of morphological modification in particles synthesized from Nb and Ti-doped TaC as revealed in Figure 3-23 and Figure 3-43 below. We can therefore attribute the considerably lower percentage of polyhedrons in the Co-doped system relative to the Ni, Fe-doped, and Ni-Ti co-doped systems to its comparatively low concentration on the surface (<3 at.%), as revealed by XPS.

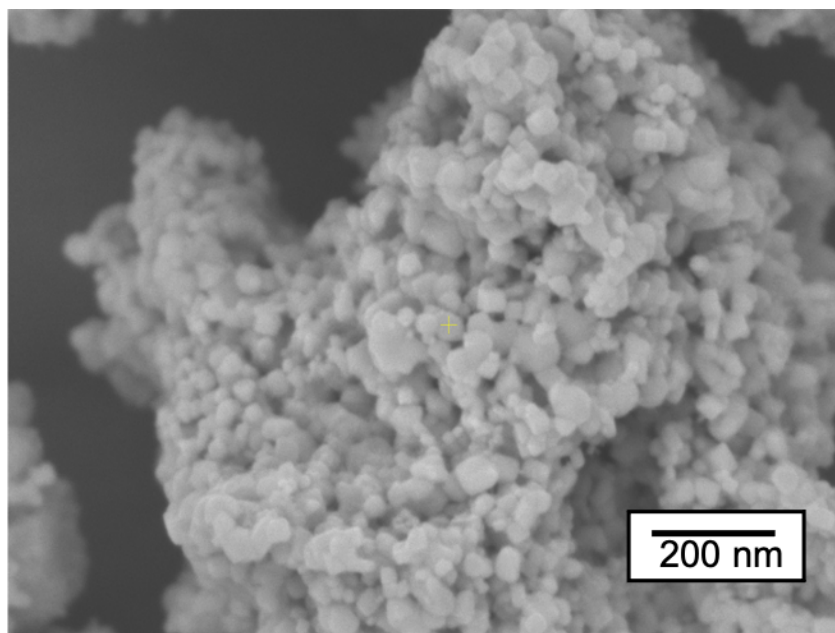


Figure 3-43. Scanning electron micrograph of Ti-doped TaC sample showing no sign of faceted particles with 15 at% calculated amount of Ti (Ti-2) using metallic Ti as the precursor.

(Sub)-surface segregation is necessary, but not sufficient for dopant interaction with surrounding atoms and morphology modification. Nie *et al.* previously suggested that doping of Ni in TiC may lead to *p-d* orbital hybridization between Ni and C at the (100) surface, which will further reduce its surface energy, thus resulting in more cubic particles.⁸ To investigate the effect

of p - d hybridization between the C and dopant atoms, the Crystal Orbital Hamiltonian Populations (COHPs) for each dopant bond on the {100} and {111} surfaces was calculated with the help of the Lobster code.^{35,36} The negative integrated COHP (-ICOHP) was used to quantitatively gauge the amount of covalent (dopant d and carbon p -orbital interactions) and metallic (dopant d and Ta d -orbital interactions) contributions to dopant bond strength (see Table 3-3 for percentage covalency of each dopant). It was observed that for Fe doping in TaC and Ni doping in TiTa_3C_4 that the majority contribution to bond strength is covalent (over 50%) in the (100) surface and metallic in the (111) surface. This dopant-induced majority covalency in the (100) surface stabilizes it over the (111), thus explaining the significantly higher yield of cubic nanoparticles for Fe-doped and Ni-Ti co-doped TaC compared to Ni and Co doping. Yttrium, however, has the lowest percentage of polyhedrons despite having a higher magnitude of segregation than Co due to its significantly higher atomic strain energy in TaC. This is because Y has less hybridization with its neighboring carbon atoms relative to the other dopants, as indicated by the minority bond contribution being covalent despite the significant decrease in γ .

Table 3-3. Percentage of covalency for the dopant bonds at the surface and the corresponding metal atom that was substituted in the undoped surface. The remainder percentage represents metallicity. Ni* indicates Ni substituting Ti in TiTa_3C_4 .

Dopant	(hkl)	% Covalency
Co	(111)	50.30
	(100)	54.54
Fe	(111)	49.67
	(100)	54.55
Ni	(111)	45.90
	(100)	41.39
Ni*	(111)	46.18
	(100)	53.27
Y	(111)	46.12
	(100)	42.73

Furthermore, the magnitude of Y segregation is not as strong as Ni and Fe according to the XPS results. Y is known to immediately react with surrounding oxygen to form oxides and subsequently be removed by acid washing. Y also enhances the diffusion of oxygen to induce severe formation of Ta-oxides [see the XRD patterns in Figure 3-11(c)]. This not only significantly decreases the amount of surface Y, but also creates more impurity phases and structural defects that are not favorable for the facet development of TaC particles. The formation of oxides with dopants, however, is beyond the scope of computation calculations in this work, and it is likely the cause to a lower computed E_{seg}^{surf} for Y than what the experiments suggest.

Another phenomenon worth discussing is that a decreasing yield in morphology-modified particles is seen as the dopant concentration in TaC increases beyond a certain amount (see Figures for the statistical abundance of particles). For the Ni and Co-doped systems, C atoms may be more favorable to bind onto the (111) surfaces due to the strong $d-p$ hybridization as the concentration of Ni and Co further increase. According to the enthalpy maps shown in Figure 3-42, an increase in surface C content will lead to fewer cuboctahedron particles due to the destabilization of the (111) facets, which explains its decrease in samples Ni-4 to Ni-6 and Co-3 to Co-6. In the case of Fe-doping, the binding energy for Fe-C is the strongest among other dopants. The excess amount of Fe, as its concentration increases, will potentially lead to the formation of iron carbide compounds on the surface, in addition to the segregated surface dopants. Although none of the XRD patterns of the Fe-doped samples shows the presence of an iron carbide phase, it is probable that the amount iron carbide is under the detection limit of XRD. According to the enthalpy map, it shows that a decrease in surface Fe and C will decrease the abundance of cubic particles, leading to a peak population in sample Fe-4. Despite the fact that Ti primarily segregates into the bulk region to form a $TiTa_3C_4$ solution, once a significant amount of $TiTa_3C_4$ has formed, the saturation

of Ti in the bulk will lead to some extent of surface segregation as the Ti content further increases. Again, the enthalpy maps show that an increase in surface Ti will lead to fewer cubic particles due to the stabilization of the Ti-rich (111) facet, which explains its decrease in samples NiTi-5 to NiTi-6.

3.4. Conclusions

A series of doping elements have been explored in order to study their effects on the particle morphology of TaC nanoparticles synthesized via a non-aqueous solvothermal method. Both undoped and doped TaC nanoparticles were successfully produced with high repeatability and good phase purity. For undoped TaC, it was observed that its morphology can be more faceted by reducing the reaction temperature to mitigate thermodynamic roughening. For doped TaC, Zr, Hf, Nb, and Ti are among the dopants that have no noticeable effect to modify the morphology of synthesized particles, while Ni, Co, Fe, and Ni-Ti are the ones demonstrated to be the effective morphology modifiers. Ni and Co doped TaC show the majority of their morphology to be cuboctahedron. Fe doped and Ni-Ti co-doped TaC show both cuboctahedron and cubic morphologies. Y doped TaC show only cubic morphology but with only a small population. The EDS and XPS elemental analysis hints that dopant segregation to the surfaces is one of the critical factors for the dopants to influence the particle morphology. By combining the experimental and computational efforts, it is clarified that the onset of morphology modification is due to the surface segregation of dopants and their interaction with the neighboring carbon atoms via *d-p* hybridization, which reduces the facet growth rate and prevents thermodynamic roughening. Ni and Co doping favors cuboctahedrons while Fe doping favors cuboctahedron and cubic geometries due to its stronger hybridization effect with neighboring C at the (100) surface. Ti dopants will

form a ternary solution with the TaC host whereby the intrinsic growth rate of the (100) is lower than the (111) facets due to the lack of Ti atoms on surface of the latter. Y doping segregates strongly into both facets, but has weaker *d-p* hybridization. Such dopants are likely to form cubes, albeit with a lower percentage of total polyhedrons. Figure 3-44 below provides a graphic summary of the dopant-induced morphology control.

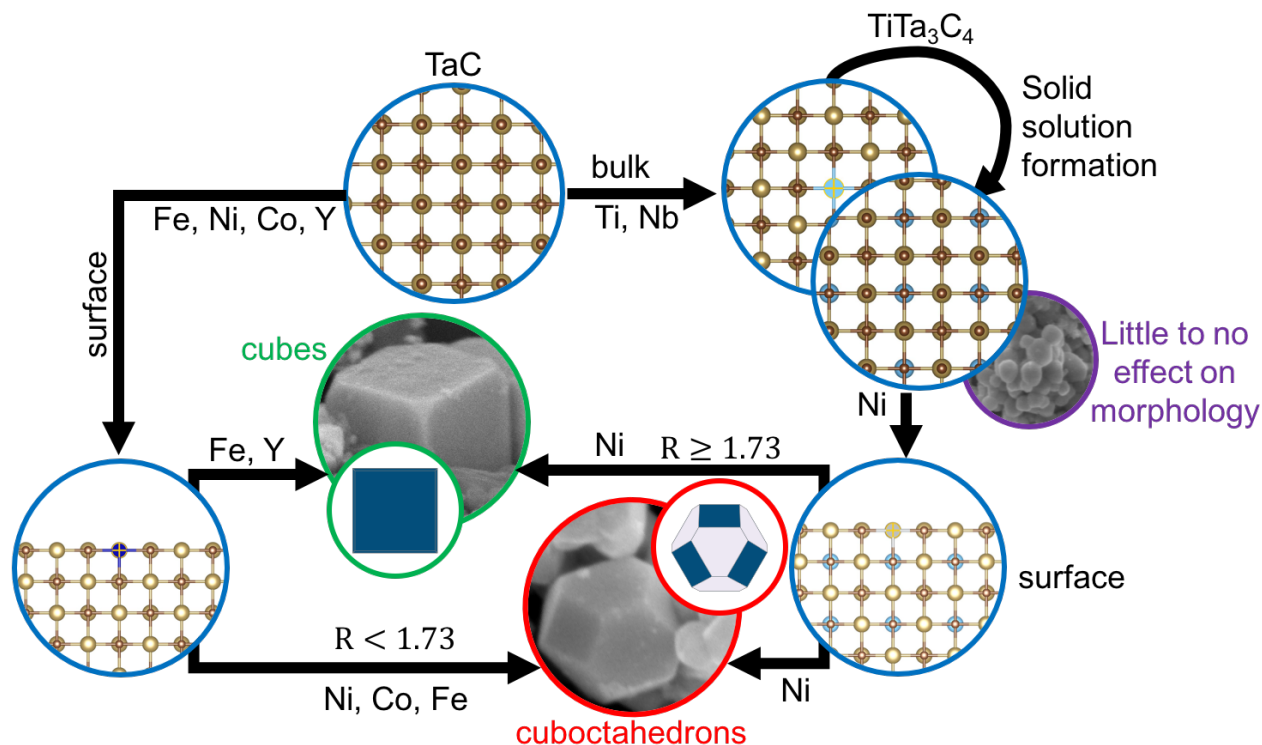


Figure 3-44. Summary of the dopant-induced morphology selectivity of TaC nanoparticles.

The mechanisms embedded in this study are expected to be widely applicable to other combinations of dopants and ceramic powders synthesized using similar high-temperature reaction approaches. For example, if one seeks to produce highly-faceted (V, Nb, Hf, Zr)-carbide nanoparticles with *fcc* crystal structure, doping strategies hereby described can be applied to have remarkable impact. To think beyond, rare earth elements, other than Y herein discussed, may also be effective in changing the growth habits of crystals based on surface segregation and dopant-

host atomic orbital hybridization. Future studies shall be directed to explore more combinations of dopants and host ceramic materials in order to further elucidate the mechanism behind morphology evolution and optimize the formation of specific shapes.

This chapter, in part, has been accepted for publication titled “Morphology Control of Tantalum Carbide Nanoparticles through Dopant Additions” in the Journal of Physical Chemistry C, 2021, where the dissertation author was the primary investigator and the co-first author of this paper. The paper is co-authored by R. Tran (co-first author), S. Lee, A. Bandera, M. Herrera, X.-G. Li, S.P. Ong, and O.A. Graeve.

3.5. References

1. A. Varma and J.P. Lebrat, “Combustion Synthesis of Advanced Materials,” *Chem. Eng. Sci.*, **47** [9-11] 2179-94 (1992).
2. D.L. Price, J.M. Wills, and B.R. Cooper, “Linear-Muffin-Tin-Orbital Calculation of TaC(001) Surface Relaxation,” *Phys. Rev. B*, **48** [20] 15301-10 (1993).
3. G.V. Samsonov, “How the Defect Content of the Carbon Sublattice Influences the Properties of Refractory Transition-Metal Carbides,” *Inorg. Mater.*, **9** [12] 1893-8 (1973).
4. B.-R. Kim, K.-D. Woo, J.-M. Doh, J.-K. Yoon, and I.-J. Shon, “Mechanical Properties and Rapid Consolidation of Binderless Nanostructured Tantalum Carbide,” *Ceram. Int.*, **35** [8] 3396-400 (2009).
5. X. Dan, C. Wang, X. Xu, X. Cheng, M. Fronzi, L. Bi, and X.S. Zhao, “Improving the Sinterability of CeO₂ by Using Place-Selective Nanocubes,” *J. Eur. Ceram. Soc.*, **39** [14] 4429-34 (2019).
6. J.G. Chen, “Carbide and Nitride Overlayers on Early Transition Metal Surfaces: Preparation, Characterization, and Reactivities,” *Chem. Rev.*, **96** [4] 1447-98 (1996).
7. M. Yao, Q. Li, G. Hou, C. Lu, B. Cheng, K. Wu, G. Xu, F. Yuan, F. Ding, Y. Chen, “Dopant-Controlled Morphology Evolution of WO₃ Polyhedra Synthesized by RF Thermal Plasma and Their Sensing Properties,” *ACS Appl. Mater. Inter.*, **7** [4] 2856-66 (2015).

8. J. Nie, Y. Wu, P. Li, H. Li and X. Liu, "Morphological Evolution of TiC from Octahedron to Cube Induced by Elemental Nickel," *Cryst. Eng. Comm.*, **14** 2213-21 (2012).
9. S. Jin, P. Shen, D. Zhou, and Q. Jiang, "A Common Regularity of Stoichiometry-Induced Morphology Evolution of Transition Metal Carbides, Nitrides, and Diborides during Self-Propagating High-Temperature Synthesis," *Cryst. Growth Des.*, **12** [6] 2814-24 (2012).
10. D.E. Grove, U. Gupta, and A.W. Castleman Jr., "Effect of Carbon Concentration on Changing the Morphology of Titanium Carbide Nanoparticles from Cubic to Cuboctahedron," *ACS Nano*, **4** [1] 49-54 (2010).
11. D.E. Grove, U. Gupta, and A.W. Castleman Jr., "Effect of Hydrocarbons on the Morphology of Synthesized Niobium Carbide Nanoparticles," *Langmuir*, **26** [21] 16517-21 (2010).
12. P. Kaghazchi, "Carbon-induced Ru nanorod formation," *RSC Adv.*, **4** [4] 1646-9 (2014).
13. E. Osei-Agyemang, J.F. Paul, R. Lucas, S. Foucaud, and S. Cristol, "Stability, equilibrium morphology and hydration of ZrC(111) and (110) surfaces with H₂O: a combined periodic DFT and atomistic thermodynamic study," *Phys. Chem.*, **17** [33] 21401-13 (2015).
14. M.T. Tang, Z.W. Ulissi, and K. Chan, "Theoretical Investigations of Transition Metal Surface Energies under Lattice Strain and CO Environment," *J. Phys. Chem. C*, **122** [26] 14481-7 (2018).
15. A. Vojvodic and C. Ruberto, "Trends in bulk electron-structural features of rochslat early transition-metal carbides," *J. Phys.: Condens. Matter.*, **22** 375501 (2010).
16. A.L. Bowman, "The variation of lattice parameter with carbon content of tantalum carbide," *J. Phys. Chem.*, **65** 1596-8 (1965).
17. J.P. Kelly and O.A. Graeve, "Mechanisms of pore formation in high-temperature carbides: case study of TaC prepared by spark plasma sintering," *Acta Mater.*, **84** 472-83 (2015).
18. G. Wulff, "Zur Frage der Geschwindigkeit des Wachstums und der Auflösung der Krystallflagen," *Zeitschrift für Krystallographie und Mineralogie*, **34** [5/6] 449–530 (1901).

19. W.K. Burton, N. Caberera, F.C. Frank, "The Growth of Crystals and the Equilibrium Structure of Their Surfaces," *Philos. Trans. R. Soc. A*, **243** [866] 299-358 (1951).
20. J.P. Kelly, R. Kanakala, and O.A. Graeve, "A Solvothermal Approach for the Preparation of Nanostructured Carbide and Boride Ultra-High-Temperature Ceramics," *J. Am. Ceram. Soc.*, **93** [10] 3035-8 (2010).
21. T. Ren, R. Tran, S. Lee, A. Bandera, M. Herrera, X.-G. Li, S.P. Ong, and O.A. Graeve, "Morphology Control of Tantalum Carbide Nanoparticles through Dopant Additions," Accepted (2021).
22. G. Kresse, and J. Furthmüller, "Efficient Iterative Schemes for Ab initio Total-energy Calculations Using a Plane-wave Basis Set," *Phys. Rev. B: Condens. Matter*, **54** [16] 11169–86 (1996).
23. W. Kohn, and L.J. Sham, "Self-consistent Equations Including Exchange and Correlation Effects," *Phys. Rev. B*, **140** [4A] 1133–8 (1965).
24. M. Hacene, A. Anciaux-Sedrakian, X. Rozanska, D. Klahr, T. Guignon, and P. Fleurat-Lessard, "Accelerating VASP Electronic Structure Calculations Using Graphic Processing Units," *J. Comput. Chem.*, **33** [32] 2581–9 (2012).
25. P.E. Blochl, "Projector Augmented-wave Method," *Phys. Rev. B*, **50** [24] 17953–79 (1994).
26. J. Perdew, K. Burke, and M. Ernzerhof, "Generalized Gradient Approximation Made Simple," *Phys. Rev. Lett.*, **77** [18] 3865–388 (1996).
27. A. Jain, S.P. Ong, G. Hautier, W. Chen, W.D. Richards, S. Dacek, S. Cholia, D. Gunter, D. Skinner, G. Cedar, and K.A. Persson, "Commentary: The Materials Project: A Materials Genome Approach to Accelerating Materials Innovation," *APL Mater.*, **1** [1] 011002 (2013).
28. W. Sun and G. Ceder, "Efficient Creation and Convergence of Surface Slabs," *Surf. Sci.*, **617** 53–9 (2013).
29. J. Rogal, and K. Reuter, "Ab Initio Atomistic Thermodynamics for Surfaces : A Primer," *Experiment, Modeling and Simulation of Gas-Surface Interactions for Reactive Flows in Hypersonic Flights*, Ch. 2, RTO, Neuilly-sur-Seine, 2010.
30. S. Zaima, Y. Shibata, H. Adachi, C. Oshima, S. Otani, M. Auno, and Y. Ishizawa, "Atomic Chemical Composition and Reactivity of the TiC(111) Surface," *Surf. Sci.*, **157** 380-92 (1985).

31. A.I. Gusev, A.A. Rempel, and A.J. Magerl, *Disorder and Order in Strongly Nonstoichiometric Compounds: Transition Metal Carbides, Nitrides and Oxides*; Ch. 10. Springer, New York, 2013.
32. R. Tran, Z. Xu, B. Radhakrishnan, D. Winston, W. Sun, K.A. Persson, and S.P. Ong, “Data Descriptor: Surface Energies of Elemental Crystals,” *Sci. Data*, **3** 1–13 (2016).
33. P.W. Tasker, “The Stability of Ionic Crystal Surfaces,” *J. Phys. C: Solid State Phys.*, **12** 4977–84 (1979).
34. M.A. Gibson, *Segregation and embrittlement in metallic interfaces: bounds, models, and trends*; Ph.D. Dissertation. Massachusetts Institute of Technology, (2016).
35. S. Maintz, V.L. Deringer, A.L. Tchougréeff, and R. Dronskowski, “LOBSTER: A tool to extract chemical bonding from plane-wave based DFT,” *J. Comput. Chem.*, **37** [11] 1030–35 (2016).
36. W. Sun, C.J. Bartel, , E. Arca, , S.R. Bauers, , B. Matthews, , B. Orvañanos, B.-R. Chen, M.F. Toney, L.T. Schelhas, W. Tumas, J. Tate, A. Zakutayev, S. Lany, A.M. Holder and G. Ceder, “A map of the inorganic ternary metal nitrides,” *Nat. Mater.*, **18** [7] 732–9 (2019).

Chapter 4

Prospects for Future Research

4.1. Selection of Growth Habit Modifier

Over the course of this work, many means of changing the crystal growth behavior of inorganic materials have been discussed. Depending on different materials systems and synthesis approaches, the type of growth habit modifiers ranges from organic monomers, long-chain polymers to ionic/elemental species. Usually, for certain molecules/atoms to have an observable impact on the growth habit of a crystal, they need to have strong interaction with the crystal surfaces, altering their growth kinetics and/or surface thermodynamics. For the TaC system herein focused, there is still plenty of room to be explored on other candidates for morphology modification. For example, large rare earth (RE) elements may all tend to segregate towards the surface layers due to the strain effect. If one can find a RE element that has strong orbital hybridization with carbon, then it will be a promising morphological modifier in addition to the ones that have been investigated in this study. For the current study where a high-temperature synthesis technique is involved, it will also be interesting to search for compounds that are capable of interacting with crystal surfaces at elevated temperatures so that they may serve as the high-temperature surface capping agents to change the morphology of the final product.

4.2. Experimental Techniques

Revealing the fundamentals of crystal growth at high temperatures can be experimentally challenging, as most of the high-temperature reactions are essentially rapid combustion of reacting species with little flexibility to have full control of the reaction conditions. For instance, the solvothermal method for the synthesis of TMCs only takes tens of seconds from the beginning of

ignition to completion. Therefore, if sophisticated tools can be utilized to capture the growth characteristics at different time frames during the reaction, the understanding of how particles are grown under the impact of growth habit modifiers can be more directly observed. In fact, this has been experimentally achieved by Liao *et al.* on the growth of Pt nanocubes in a liquid cell using high-resolution transmission electron microscopy.¹ The solution-based growth of Pt nanocubes was directly observed in real-time, with the nucleation being initialized by irradiating the precursor solution with the electron beam. However, this is not yet possible to directly observe the growth of UHTC crystals due to their high synthesis temperatures. Nevertheless, it is still worth to try. For example, rapid quenching of the reaction to potentially obtain the product features in that specific time frame, followed by microscopic characterization on each sample gathered at each stage of the reaction. This would require dedicated equipment with precise control of reaction conditions. This concept can be beneficial to further probe into the formation mechanisms of faceted TaC (or other UHTC particles) synthesized by solvothermal method. As a type of self-sustaining high-temperature syntheses, solvothermal method can be considered as a meta-stable condition due to its fast reaction time and large temperature gradient. If the reaction can be somehow kept at a high enough temperature for a considerably long period with sufficiently slow cooling afterwards, particle morphologies at equilibrium state can be obtained, and the competing effects from kinetics (e.g., doping) and thermodynamics can be explicitly unfolded.

In addition, computational methods have shown powerful capability in explaining the complicated phenomena in the world of controlled crystal growth, as demonstrated in Chapter 3. Thus, further research efforts shall be made based on computational calculations to predict suitable morphology modifiers and to get to the bottom of the reasons behind the change of growth habits.

The overall progress in designing new materials with unique particle morphologies and microstructures can also be accelerated.

4.3. Study of Sintering Behaviors and Properties

As addressed in the Motivation of Study section in Chapter 1, this work is fundamentally driven by the hypothesis that “highly-faceted UHTC particles will have better mechanical properties upon sintering by SPS.” Therefore, a thorough study on the sintering behavior of morphology-modified particles shall be proposed. Frankly, this aspect does not necessarily have to be based on UHTCs. Almost any inorganic materials can be selected as the model systems, as long as their particle morphology can be effectively altered. Surprisingly, by the time this dissertation was written, there were still not many published works that provide comprehensive studies on the correlations between particle morphology and bulk mechanical properties. Moreover, many contradictory results have been reported on the densification mechanisms in SPS, particularly on whether there is any plasma generated during the current flow across the particles.²⁻

⁴ By densifying highly-faceted particles in SPS, it may help clarify the actual mechanisms taking place during the whole process as the sharp edges and corners of particles can serve as the origin for plasma discharge, if there will be any. This certainly makes it a significant playground for the science and engineering communities to explore.

4.4. Conclusions

Controlled synthesis of UHTC particles with selected morphology is so far still in the early stage of research. While many questions on this topic remain unsolved, it is not difficult for the researchers to discover new directions and solve some of them. With a deepened understanding

of the formation mechanisms, the selection of morphology modifiers can be made more straightforward by combining experimental and computational approaches. Plenty of space exists for people to answer the unknowns such as “how the morphology of AlN particles can be tailored?” and “how will the change in morphology of ZrC affect its creep resistance?” These topics are to be seen of great development in scientific communities in the near future.

4.5. Reference

1. H.-G. Liao, D. Zhrebetsky, H. Xin, C. Czarnik, P. Ercius, H. Elmlund, M. Pan, L.-W. Wang, and H. Zheng, “Facet Development during Platinum Nanocube Growth,” *Science*, **345** [6199] 916-9 (2014).
2. G. Xie, O. Ohashi, T. Yoshioka, M. Song, K. Mitsuishi, H. Yasuda, K. Furuya, and T. Noda, “Effect of Interface Behavior between Particles, on Properties of Pure Al Powder Compacts by Spark Plasma Sintering,” *Mater. Trans.*, **42** [9] 1846-9 (2001).
3. O. Yanangisawa, H. Kuramoto, K. Matsugi, and M. Komatsu, “Observation of Particle Behavior in Copper Powder Compact during Pulsed Electric Discharge,” *Mater. Sci. Eng. A*, **350** [1-2] 184-9 (2003).
4. Z. Zhang, Z. Liu, J. Lu, X. Shen, F. Wang, and Y. Wang, “The Sintering Mechanism in Spark Plasma Sintering – Proof of the Occurrence of Spark Discharge,” *Scr. Mater.*, **81** 56-9 (2014).

Chapter 5

Conclusions

In this study, the principles of crystal growth are elaborated. The growth of crystals is governed by both kinetic and thermodynamic mechanisms, forming various particle shapes. The fundamental principle that governs the crystal growth habit under equilibrium conditions is the difference in the relative growth rate of facets based on their corresponding surface energies. In certain conditions, the facet development can also be largely impacted by the kinetically controlled growth mechanisms. Under these principles, the controlled synthesis of inorganic particles can be achieved in various ways, including surface capping, concentration tuning, temperature/time monitoring, as well as external doping. The state-of-the-art research on topics related to the morphology-controlled syntheses of nanoparticles are reviewed. A large pool of examples, including metallic nanoparticles and ceramic nanoparticles, are presented in detail. The morphology control of metallic nanoparticles has been very widely studied, their syntheses were well-defined, and the formation mechanisms were comprehensively revealed. While for ceramic materials, their morphology control is often more complicated, and the quantity of published reports is still relatively handful. Nevertheless, the potential of morphology control of ceramic particles is tremendous.

Aiming at filling the gaps in the research on UHTCs, TaC was chosen as the model system to explore the potential of controlling its particles morphology and understanding the fundamental mechanisms of its shape formation. TaC is attractive due to its high melting temperature, excellent chemical stability and exceptional hardness. A modified solvothermal synthesis approach was employed to fabricate phase-pure and highly-crystalline TaC nanoparticles. This method offers fast reaction time with minimal energy input, making it possible for the scale-up production. To

manipulate the morphology of synthesized TaC nanoparticles, metallic dopant was incorporated in TaC during synthesis, and this strategy was proven to be successful. Summarized by statistics, the single-doping systems, including Ni, Co, and Fe-doped TaC, and the co-doping system Ni-Ti co-doped TaC demonstrated the strongest effectiveness in modifying the TaC particle morphology. The general morphology for doped TaC was altered from round/irregular shape to well-defined highly-faceted cubes/cuboctahedrons with about 80% of abundance, while that of the undoped TaC was only about 10%. With the combination of experimental and computational methods, it was found that the onset of morphological modification is due to surface segregation of dopants and their interaction with the neighboring carbon atoms via $d-p$ hybridization, which reduces the growth rate to prevent thermodynamic roughening. By coupling the statistical abundance of particles and the enthalpy maps of R (the surface energy ratio between (111) and (100) facets) with respect to the chemical potentials, the relative abundance of different types of faceted particles is rationalized. Cuboctahedrons is favored by Ni and Co-doping, whereas both cuboctahedrons and cubic geometries are favored by Fe-doping due to its higher carbon binding energy. For the Ni-Ti co-doped system, Ti forms a solid solution within TaC and the intrinsic growth rate of the (100) is lower than the (111) facets due to the lack of Ti atoms on the surface of the latter. Further, the addition of Ni to the Ti-TaC solid solution prevents the thermodynamic roughening, leading to cubic and cuboctahedron geometries. It is also found that an excess amount of dopants destabilize the crystal facets, which results in fewer faceted particles. In the case of Y-doping, cubes are likely to form but with a much lower yield. This is due to the lack of $d-p$ hybridization, despite its strong segregation into both (100) and (111) surfaces because of the large atomic strain energy. The mechanisms described in this study are expected to be generally applicable to other ceramic materials fabricated with high-temperature synthesizing methods.

In conclusion, the morphology control of ceramic materials is an expansive field to be further explored by the science and engineering communities. Novel techniques, analyses, and ideas involving both experimental and computational materials scientists are expected to be powering the research of this topic to the next level beyond. This study sets a unique example for the fellow researchers to use for reference.

- END -